DISS. ETH NO. 30474

DEVELOPMENT OF PET AND SPECT TRACERS FOR MONITORING LEGUMAIN AND CD80 IN CANCER AND OTHER IMMUNE-RELATED CONDITIONS

A thesis submitted to attain the degree of

DOCTOR OF SCIENCES

(Dr. sc. ETH Zurich)

presented by

SEVERIN KILIAN LUSTENBERGER

MSc ETH in Pharmaceutical Sciences,
ETH Zurich

born on 02.02.1994

accepted on the recommendation of

Prof. Dr. Stefanie D. Krämer
Dr. Linjing Mu
Prof. Dr. Roger Schibli
Prof. Dr. Margret Schottelius
Dr. Luca Gobbi

2024

To my wife, Patricia, and our daughter, Hilda: your love and support have been my greatest source of strength and inspiration. You are my life.

Acknowledgments

The completion of this dissertation would not have been possible without the unwavering support, guidance, and encouragement of numerous individuals, to whom I am profoundly grateful.

First and foremost, I would like to extend my deepest gratitude to **Prof. Dr. Stefanie Krämer**, whose scientific support and mentorship have been invaluable throughout this journey. I could not have wished for a more exceptional supervisor and research partner. Your guidance has not only fostered my intellectual growth but has also allowed me to flourish as an individual. Your openness to my unconventional ideas encouraged me to explore new avenues, for which I am eternally thankful.

I am equally indebted to **Dr. Linjing Mu**, whose belief in my potential and continuous mentorship have been a constant source of motivation. Your insights and direction have significantly shaped the trajectory of my research.

A special thank you goes to **Prof. Dr. Roger Schibli** for the opportunity to work in his lab and for his scientific support, which has been instrumental to the success of this project. Your leadership and expertise have provided a strong foundation for my work.

I am incredibly fortunate to have collaborated with a remarkable group of students: **Fabienne Landolt**, **Andrea Lubina**, **Makar Pobiyakho**, **Michael Cselovsky**, **Omar Mohamad**, and **Luca Camenzind**. Your diverse perspectives and dedication have greatly enriched our lab work, and I have learned immensely from each of you.

To **Bruno Mancosu**, I am deeply grateful for your willingness to share your expertise and for the many enriching conversations that broadened my understanding across various subjects.

My sincere thanks go to **Claudia Keller** for her meticulous work in ensuring the reproducibility of our animal studies. Your expertise has been nothing short of astounding.

I also wish to acknowledge **Dr. Claudia Castro**, whose initiation of this project and instruction in essential methodologies laid the groundwork for my research. Your contributions were pivotal in the early stages of this journey.

My heartfelt thanks to **Aro Delparente** for your unwavering support during our trips to Geneva for measurements and for your assistance with animal work. Your companionship and dedication have been immensely appreciated.

A special mention goes to **Dr. Gregory Holtzhauer**, a former senior PhD colleague whose readiness to answer questions and offer guidance was invaluable.

I am also grateful to **Alain Blanc**, **Dr. Martin Béhé**, **Dr. Michal Grzmil**, **Dr. Jürgen Grünberg** and **Stefan Imobersteg** for their steadfast support of my project at PSI. A special thanks goes to **Dr. Rich Williams**, **Dr. Björn Bartels** and **Dr. Luca Gobbi** for their pleasant collaboration. Additionally, I extend my thanks to **Dr. Christoph Bauer** for his dedication to the radioluminescence measurements and to **Victor Romero Escalante Sanchez** for his assistance with animal experiments.

To my **lab mates at ETH and PSI**, your continuous support and camaraderie have made the challenges of research more manageable and the successes more fulfilling. I am grateful to have shared this journey with you.

I would also like to express my appreciation to the **Halin and Leroux labs** for their expertise and for granting me access to their instruments, which were critical to the completion of my experiments.

A special thank you to the **Pharmaceutical Scientists' Association** for your professional support and for the enjoyable moments that added much-needed balance to the intensity of research life.

To **Michele Capelli**, my lunch companion and cherished friend, your support and friendship have been invaluable, both professionally and personally.

Finally, I wish to express my deepest love and gratitude to my wife, **Patricia Lustenberger**. Your unwavering support and understanding have been the cornerstone of my perseverance. This achievement would not have been possible without you by my side.

Thank you all for your contributions, encouragement, and unwavering support.

Contents

Abstract

Purpose

The asparagine endopeptidase legumain and the co-stimulatory molecule CD80 have key but distinctly different functions in the progression of cancer and Alzheimer's disease (AD). Tumor-associated macrophages express both proteins. The expression of legumain by M2 macrophages is linked to tumor progression, while CD80 presentation on M1 macrophages is typically associated with T-cell activation. In AD, legumain is highly expressed in activated M1 microglia and contributes to the formation of amyloid plaques and neurofibrillary tangles. Both proteins are potential biomarkers for diagnosing and treating cancer and AD. This dissertation aimed to characterize CD80 and legumain in mouse models of disease and contribute to developing PET and SPECT tracers for their non-invasive imaging.

Main findings

For animal studies pertaining to cancer, the mice were inoculated with CT26 mouse colon carcinoma cells or MDA-MB-468 human breast cancer cells. The tumor microenvironment was modulated by the administration of the chemotherapeutic agent decitabine.

Fluorescence activity assays and qPCR revealed high activity and mRNA levels of legumain in CT26 tumors and kidneys, suitable for PET imaging, while decitabine treatment did not affect legumain levels in CT26 tumors. MDA-MB-468 tumors had lower legumain RNA but higher legumain activity compared to CT26 tumors. Based on fluorescence microscopy, M2 macrophages, associated with legumain, were also present in CT26 tumor tissue slices. *In vitro* fluorescence assays with compound **3** yielded a low nanomolar K_i, similar to compounds **1** and **2**. [^{11}C]**1** and [^{11}C]**2** showed tumor accumulation in PET and biodistribution after dissection but were rapidly metabolized with no observed specific binding. [^{11}C]**3** was more stable *in vivo* as evaluated by reverse-phase, column-switch HPLC and showed specific binding in the kidney and spleen, both rich in legumain, but had low accumulation in CT26 and MDA-MB-468 tumors. A weak blocking effect of [^{11}C]**3** was seen in CT26 tumors *in vitro*, but not *in vivo*.

In a pilot study using APP/PS1 transgenic mice, higher legumain and amyloid precursor mRNA expression was observed in their brain tissue compared to wild-type mice. Western blot showed similar levels of zymogen and activated legumain in wild-type and transgenic mice. Legumain activity was higher in the brain tissue of transgenic mice than in muscle tissue from healthy wild-type mice. The legumain-targeting tracer [^{11}C]CC11m showed uptake in the brain tissue of wild-type mice in PET. The expected BP of [^{11}C]CC11m, based on legumain activity and CC11m binding affinity in the brain tissue, was low.

The CD80-targeting tracers ^{99m}Tc-CACM-1 and ^{99m}Tc-CACM-2 were evaluated in CT26 tumor-bearing mice. Both tracers showed high affinity for CD80 in SPR and were used in SPECT imaging, revealing higher accumulation in tumor tissue compared to muscle, especially with ^{99m}Tc-CACM-2. However, high accumulation was also observed in other tissues, and co-injection of excess unlabeled protein did not affect uptake. Both tracers suffered from high renal and liver uptake.

Radioluminescence microscopy was combined with fluorescence microscopy in a standard immunohistochemical workflow, showing a homogeneous signal distribution on CT26 tumor cryosections. The radioluminescence signal correlated with the added activity and

qualitatively overlapped with tissue edges in the bright-field and fluorescence channels. The binding of ^{64}Cu-NODAGA-abatacept was likely nonspecific due to the high concentration used, substantially exceeding the K_D of abatacept for CD80.

Principal conclusions

Legumain and CD80 are potential biomarkers for the diagnosis, prognosis and treatment adaptation in the context of cancer and AD. Both are expressed by resident macrophages of the respective tissues. Our preclinical studies have shown that the P1-Asn peptidomimetic PET tracer [^{11}C]**3** binds to legumain in the kidney and the spleen in a specific manner. However, the accumulation of [^{11}C]**3** in the tumor tissue was not blocked by **3** in excess, possibly due to the presence of competing endogenous substrates, reducing the specific binding of the tracer. Our pilot study with [^{11}C]CC11m showed distribution to the brain of healthy mice, indicating blood-brain-barrier penetration. Furthermore, the brain tissue of APP/PS1 transgenic mice contained pro- and active-legumain as well as activated microglia cells. Future developments of legumain tracers may be based on P1-Asn peptidomimetic that, in the case of AD, should be able to cross the blood-brain-barrier. The use of alkyne-based, irreversible legumain PET tracers might alleviate the issue of endogenous substrate binding. For use in AD, one should use a blood-brain-barrier penetrant P1-Asn peptidomimetics. The CD80-targeting SPECT tracers ^{99m}Tc-CACM-1 and ^{99m}Tc-CACM-2 accumulate in CT26 tumors. However, high uptake in liver and kidney leaves room for improvement. Future studies should focus on optimizations with regard to kidney and liver uptake. Radioluminescence microscopy could be implemented in a standard immunohistochemical staining workflow and might be used to concurrently image radiotracer binding and another biomarker of choice in tissue slices. The method needs to be adapted based on the needs for radiotracer development.

Zusammenfassung

Zweck

Die Asparagin-Endopeptidase Legumain und das co-stimulatorische Molekül CD80 haben zentrale, aber deutlich unterschiedliche Funktionen in der Entwicklung von Krebs und der Alzheimer-Krankheit (AD). Tumor-assoziierte Makrophagen exprimieren beide Proteine. Die Expression von Legumain durch M2-Makrophagen korreliert mit der Tumorprogression, während die Präsentation von CD80 auf M1-Makrophagen typischerweise mit der T-Zell-Aktivierung assoziiert ist. Bei AD ist Legumain in aktivierten M1-Mikroglia hoch exprimiert und trägt zur Bildung von Amyloid-Plaques und neurofibrillären Tangles bei. Beide Proteine sind potenzielle Biomarker für die Diagnose und Behandlung von Krebs und AD. Diese Dissertation zielte darauf ab, CD80 und Legumain in Mausmodellen der jeweiligen Krankheit zu charakterisieren und zur Entwicklung von PET- und SPECT-Tracern für deren nicht-invasive Bildgebung beizutragen.

Wichtigste Ergebnisse

Für Tierstudien im Zusammenhang mit Krebs wurden die Mäuse mit CT26-Mauskolonkarzinomzellen oder MDA-MB-468 menschlichen Brustkrebszellen inokuliert. Das Tumormikromilieu wurde durch die Verabreichung des Chemotherapeutikums Decitabin moduliert.

Fluoreszenzaktivitätsassays und qPCR zeigten eine hohe Aktivität und mRNA-Spiegel von Legumain in CT26-Tumoren und Nieren, geeignet für PET-Bildgebung, während die Decitabin-Behandlung die Legumain-Spiegel in CT26-Tumoren nicht beeinflusste. MDA-MB-468-Tumoren hatten niedrigere Legumain-RNA, aber höhere Legumain-Aktivität im Vergleich zu CT26-Tumoren. Basierend auf Fluoreszenzmikroskopie waren auch M2-Makrophagen, die mit Legumain assoziiert sind, in CT26-Tumorgewebeschnitten vorhanden. *In vitro* Fluoreszenzassays mit Verbindung **3** ergaben einen niedrigen nanomolaren K_i, ähnlich wie bei den Verbindungen **1** und **2**. [^{11}C]**1** und [^{11}C]**2** zeigten Tumorakkumulation in PET und Biodistribution nach der Sektion, wurden jedoch schnell metabolisiert, ohne spezifische Bindung zu zeigen. [^{11}C]**3** war *in vivo* stabiler, wie durch RP-HPLC mit Säulenschaltung bewertet, und zeigte eine spezifische Bindung in Niere und Milz, beide reich an Legumain, jedoch eine geringe Akkumulation in CT26- und MDA-MB-468-Tumoren. Ein schwacher Blockierungseffekt von [^{11}C]**3** wurde *in vitro* in CT26-Tumoren beobachtet, aber nicht *in vivo*.

In einer Pilotstudie mit APP/PS1-transgenen Mäusen wurde eine höhere Legumain- und Amyloidvorläufer-mRNA-Expression im Gehirngewebe im Vergleich zu Wildtypmäusen beobachtet. Western Blot zeigte ähnliche Zymogen- und aktivierte Legumain-Spiegel in Wildtyp- und transgenen Mäusen. Die Legumain-Aktivität war im Gehirngewebe transgener Mäuse höher als im Muskelgewebe gesunder Wildtypmäuse. Der Legumain-targetierende Tracer [^{11}C]CC11m zeigte eine Aufnahme im Gehirngewebe von Wildtypmäusen in PET. Der erwartete BP von [^{11}C]CC11m, basierend auf der Legumain-Aktivität und der CC11m-Bindungsaffinität im Gehirngewebe, war gering.

Die CD80-targetierenden Tracer ^{99m}Tc-CACM-1 und ^{99m}Tc-CACM-2 wurden bei CT26-tumortragenden Mäusen untersucht. Beide Tracer zeigten in SPR eine hohe Affinität zu CD80 und wurden in SPECT-Bildgebung eingesetzt, wobei eine höhere Akkumulation im Tumorgewebe im Vergleich zu Muskelgewebe festgestellt wurde, insbesondere mit ^{99m}Tc-CACM-2. Allerdings wurde auch in anderen Geweben eine hohe Akkumulation

beobachtet, und die gleichzeitige Injektion eines Überschusses an unmarkiertem Protein hatte keinen Einfluss auf die Aufnahme. Beide Tracer litten unter einer hohen Aufnahme in Nieren und Leber.

Radiolumineszenzmikroskopie wurde mit Fluoreszenzmikroskopie in einem standardmässigen immunhistochemischen Workflow kombiniert, was eine homogene Signalverteilung auf CT26-Tumor-Kryoschnitten zeigte. Das Radiolumineszenzsignal korrelierte mit der hinzugefügten Aktivität und überlappte qualitativ mit den Geweberändern in den Hellfeld- und Fluoreszenzkanälen. Die Bindung von ^{64}Cu-NODAGA-Abatacept war wahrscheinlich unspezifisch aufgrund der hohen verwendeten Konzentration, die den K_D von Abatacept für CD80 erheblich überschritt.

Hauptschlussfolgerungen

Legumain und CD80 sind potenzielle Biomarker für die Diagnose, Prognose und Anpassung der Behandlung im Zusammenhang mit Krebs und AD. Beide werden von ansässigen Makrophagen der jeweiligen Gewebe exprimiert. Unsere präklinischen Studien haben gezeigt, dass der P1-Asn-peptidomimetische PET-Tracer [^{11}C]**3** spezifisch an Legumain in der Niere und der Milz bindet. Die Akkumulation von [^{11}C]**3** im Tumorgewebe wurde jedoch nicht durch Überschuss von **3** blockiert, möglicherweise aufgrund der Anwesenheit konkurrierender endogener Substrate, die die spezifische Bindung des Tracers verringern. Unsere Pilotstudie mit [^{11}C]CC11m zeigte eine Verteilung im Gehirn von gesunden Mäusen, was auf eine Blut-Hirn-Schranken-Penetration hinweist. Darüber hinaus enthielt das Hirngewebe von APP/PS1-transgenen Mäusen sowohl Pro- als auch aktives Legumain sowie aktivierte Mikrogliazellen. Zukünftige Entwicklungen von Legumain-Tracern könnten auf P1-Asn-Peptidomimetika basieren, die im Falle von AD in der Lage sein sollten, die Blut-Hirn-Schranke zu überwinden. Der Einsatz von alkinbasierten, irreversiblen Legumain-PET-Tracern könnte das Problem der Bindung endogener Substrate lindern. Für den Einsatz bei AD sollten blut-hirn-schranken-penetrierende P1-Asn-Peptidomimetika verwendet werden. Die auf CD80 zielenden SPECT-Tracer ^{99m}Tc-CACM-1 und ^{99m}Tc-CACM-2 akkumulieren in CT26-Tumoren. Die hohe Aufnahme in Leber und Niere schafft jedoch Spielraum für Verbesserungen. Zukünftige Studien sollten sich auf Optimierungen in Bezug auf die Aufnahme in Nieren und Leber konzentrieren. Die Radiolumineszenzmikroskopie könnte in einen standardmässigen immunhistochemischen Färbeprotokoll integriert werden und könnte verwendet werden, um gleichzeitig die Bindung von Radiotracern und weiterer Biomarker nach Wahl in Gewebeschnitten abzubilden. Details zur Anwendung der Radiolumineszenzmikroskopie im Zusammenhang mit der Radiotracerentwicklung hängen von den Anforderungen der jeweiligen Studie ab.

Chapter 1

General introduction

1.1 The immune system

The immune system is a network of cells, tissues, organs and soluble components that protects an organism from a wide variety of disease-causing agents such as viruses, parasites and cancer cells. The immune system can be divided into two main branches: the innate immune system and the adaptive immune system. The innate immune system comprises preconfigured responses to pathogens, while the adaptive immune system, as the name implies, adapts to pathogens as they are encountered by the host. A network of vascularization and nodes amenable to immune cell migration and development forms the lymphatic system. The lymphatic system comprises primary lympoid organs that provide the site for lymphocyte development and maturation, and secondary lymphoid organs, which provide the environment for lymphocytes to interact with antigens. Many different cell types play a role in the immune system of mammals. For the purpose of this thesis, we will focus on two cell types: T cells and macrophages [132].

1.1.1 T cells

T cells are lymphocytes that play an integral role in the adaptive immune response. They are characterized by the presentation of T-cell receptors (TCR) on their cellular surface. The TCR recognizes antigens (usually peptides) that are presented on the surface of other cells and bound to either major histocompatibility complex (MHC) class I or MHC class II receptors, depending on the type of T cell. MHC class I receptors are expressed by all nucleated cells and MHC class II receptors are specific to antigen presenting cells (APCs). T cell activation through the TCR is mediated by the binding of co-stimulatory molecules on the surface of the T cell (e.g., CTLA-4) and on APCs (e.g., CD80). T cells have many different functions in the immune system. An essential role is to kill cells that are potentially harmful to the body. Cytotoxic T cells express the CD8 protein on their surface and can directly kill cells that present foreign antigens on their surface such as virus-infected cells or cancer cells. T helper cells express the CD4 protein on their surface and can increase the activity of other immune cells. Regulatory T cells are a distinct population of T cells that prevents immune cells from acting against self-antigens and maintaining overall immune tolerance [132].

1.1.2 Macrophages

Macrophages are a cell type that is part of the innate immune system. Macrophages patrol the body, engulf and digest particles and pathogens that are recognized as foreign. They are ubiquitously found throughout the body and differ and in their form depending on the residence tissue [132]. Examples in mammals include liver-resident macrophages, called Kupffer cells, microglia specific to the brain and macrophages in tumors, known as tumor-associated macrophages (TAMs) [99, 146]. In their role as APCs, macrophages present peptides from phagocytosed antigens on MHC class II molecules to T helper cells. In the process of interacting with T cells, macrophages rely not only on the MHC class II molecules, but also on co-stimulatory molecules, such as CD80 and CD86 that bind to CD28 and CTLA-4 on the surface of T cells. In this way, macrophages modulate T helper cell activation and can facilitate full effector function. Classically, macrophages have been divided into two categories (depending on their polarization): M1 and M2 macrophages [128]. In a simplified view, M1 macrophages are pro-inflammatory and

M2 macrophages are anti-inflammatory. Macrophage polarization is a dynamic process that involves a complex network of signaling pathways, transcriptional epigenetic and post-transcriptional regulatory mechanisms [30]. The plasticity of macrophage polarization and findings of mixed phenotypes *in vivo* have led to criticism of the M1/M2 classification model [133]. However, the dichotomic polarization model provides a useful framework to understand macrophage function in the context of immune-related diseases.

1.2 Immune-related diseases

While the immune system plays a critical role in defending against numerous diseases, it can, under certain conditions, exert detrimental effects on the host. There are many maladies that are related to a malfuction of the immune system. Two with high prevalence and societal impact are cancer and Alzheimer's disease (AD).

1.2.1 Immune mechanisms in cancer

Cancer is a group of diseases characterized by uncontrolled cell growth with the potential to invade healthy tissues [6]. Although uncontrolled cell proliferation is the defining feature of cancer, the immune system is also fundamentally involved in its development and progression. Avoiding immune destruction and tumor-promoting inflammation are two hallmarks of cancer directly linked to the immune system [67]. Immune cells, together with stromal cells, blood vessels and the extracellular matrix, surround the cancerous cells and provide a tumor-specific hypoxic and slightly acidic milleu, the so-called tumor microenvironment (TME). Early on in the development of a tumor, a reciprocal relationship between the TME and the tumor cells is established. The TME varies in composition between different types of cancer and between different lesions within the same patient. Different types of immune cells infiltrate the tumor microenvironment (TME) to varying extents, resulting in three main categories of TMEs: *i)* immune infiltrated, characterized by immune cells homogeneously distributed throughout the tumor tissue, *ii)* immune excluded, where T cells are primarily found in the periphery of the tumor, and *iii)* immune silent, which is devoid of any immune cell infiltration [11]. Immune infiltrated tumors are characterized by the presence of tumor-infiltrating lymphocytes (TILs). The presence of TILs is linked to a more favorable prognosis in many types of cancer, through not universally. Additionally, the type, function and location of TILs in the TME has an impact on tumor progression [55]. Activation of T cells in the TME is mediated by the interaction with other cells. Through hypoxia and the secretion of cytokines, the TME promotes the polarization of macrophages toward the immunosuppressant M2 type. Clinically, such TAMs can represent a large proportion of the tumor mass [11]. The presence of such M2 TAMs is associated with a poor prognosis in many types solid tumors. M2 TAMs accelerate cancer progression through modulating cell growth, contributing to extracellular matrix degradation, promoting of angiogenesis and manipulating T cell activity [110]. M2 TAMs interact with their surroundings through the secretion of signaling peptides and proteins. For instance, secreted interleukin-6 and interleukin-10 are growth factors, that support the proliferation of cancer cells and matrix-metalloproteinases (MMPs) are enzymes that degrade the extracellular matrix and promote angiogenesis [110].

1.2.2 Alzheimer's disease and immune system dysfunction

AD is a neurodegenerative disease that is clinically characterized by progressive cognitive decline. The main pathological hallmarks of AD are the accumulation of amyloid-β (Aβ) plaques and neurofibrillary tangles in the brain [98]. However, targeting Aβ plaques and neurofibrillary tangles therapeutically has led to limited success [195]. Epidemiological studies and genetic evidence point to neuroinflammation as an important risk factor for AD. Microglia, the resident macrophages of the brain, can be activated by Aβ prior to the formation of plaques [121]. Microglia activation can create a positive feedback loop, leading to more Aβ plaques and subsequently more activation. The mechanisms through which microglia activation may be damaging to the brain are manifold. As part of the inflammatory response, microglia generate neurotrophic factors, potentially contributing to the demise of neurons. Activation disrupts the housekeeping function of microglia, aggravating the disease pathology. Furthermore, the activation of microglia can lead to the formation of neurofibrillary tangles characteristic for tau pathology [74]. The role of microglia in AD is a subject of intense research. Different proteins expressed by microglia have been associated with a high AD risk [175]. It was suggested that the role of microglia, similar to the one of macrophages in other diseases, is dependent on the larger disease context [73]. Similar to TAMs in cancer, activated microglia in AD can be polarized to the M1 or M2 type [65,215]. While the immunosuppressant M2 type is associated with disease progression in cancer, immunosuppression is neuroprotective in AD and thus beneficial. In contrast, M1 activated microglia produce inflammatory cytokines and chemokines, reactive oxygen species and nitric oxide, contributing to neurological damage [140].

1.3 Molecular imaging

Molecular imaging is the imaging-probe-aided visualization of *in vivo* biological processes at molecular and cellular scale [10]. The term encompasses methods such as magnetic resonance imaging (MRI) and spectroscopy, optical imaging, ultrasound and radiotracer imaging. Positron emission tomography (PET) and single photon emission computed tomography (SPECT) are radiotracer imaging techniques that are highly sensitive and widely used in the clinics. Both techniques allow to obtain functional information about a process of interest based on the localization of a radiotracer *in vivo*. They are often used in conjunction with anatomical imaging techniques such as computed tomography (CT) or MRI. SPECT and PET differ fundamentally in the type of tracers that are used. SPECT tracers emit γ-rays and are directly detected by a γ-camera. On the other hand, PET tracers are β-particle (positrons) emitting. The location of the parent nuclide is inferred based on annihilation photons [170]. In principal, any nuclide that fulfills the aforementioned criteria can be used for PET or SPECT imaging. However, the choice of nuclide is influenced by a range of factors such as the physical half life and the chemical properties. The most frequently used nuclides for PET imaging are ^{18}F and ^{11}C. ^{18}F has a radioactive decay half life of $\sim$110 min and ^{11}C has a half life of $\sim$20 min [4]. In both cases, the respective stable isotopes are widely used in medicinal chemistry and can readily be incorporated into drug-like molecules. In clincal use, [^{18}F]fluoredeoxyglucose (FDG), a glucose analog, is a major tool for diagnosis. For imaging with large molecules such as antibodies, the use of ^{89}Zr or ^{64}Cu is common and other radiometals such as ^{43}Sc and ^{44}Sc are emerging [114]. Radiometals are typically conjugated to the targeting macromolecule using a metal-complexing chelator. There is a plethora of different polydendate bifunctional

chelators available. Examples include DTPA, EDTA, DOTA, NOTA, and others. For SPECT, the most commonly used nuclides are ^{123}I, ^{111}In and ^{99m}Tc. ^{99m}Tc has a favorable half life of 6 hours, can be produced using a generator and subsequently incorporated using a chelator or a His_6-tag [4, 79].

1.3.1 PET and SPECT in cancer

The discovery that FDG accumulates in tumors has revolutionized cancer imaging. To this day, FDG-PET is widely used as a tool in cancer diagnosis. In addition to FDG, many other tracers have since been developed for PET and SPECT imaging in cancer. SPECT imaging in clincal oncology has been employed to identify tumors overexpressing particular proteins. Notable examples include somatostatin receptors, prostate-specific membrane antigen, and gastrin-releasing peptide receptors. All of them are targets of ^{99m}Tc-labeled peptides [166]. Past efforts have largely been focused on the tumor cells themselves. However, the TME is now recognized as an important imaging target [207]. Examples of TME imaging targets such as fibroblast associated protein (FAP), CD8, and programmed death-ligand 1 (PD-L1) are expressed by cancer-associated fibroblasts, CD8-positive T cells, and antigen presenting cells, respectively. In an effort to harness the targeting specificity of monoclonal antibodies, the field of immunoPET has emerged. Numerous antibodies and antibody fragments are in clinical use in support of cancer diagnosis and therapy [208]. For instance, ^{89}Zr-labeled atezolizumab, an anti-PD-L1 antibody, has been used to image PD-L1 expression in different types of cancer [17, 208]. Functional imaging tracers beyond FDG have been established to inspect the TME. To visualize the hypoxic conditions in the TME, imaging agents such as ^{18}F-fluoromisonidazole and ^{18}F-fluoroazomycin arabinoside are in clincical use [23]. Acidosis, another hallmark of the TME, is harnessed for imaging by use of ultra pH-sensitive nanoprobes manufactured from a NOTA chelator and a PEG-*b*-PEPA polymer labeled with ^{64}Cu [163]. PET radiotracers to image enzymes such as MMPs, typically overexpressed by M2 TAMs of the TME, have recently gained momentum. A number of ^{11}C and ^{18}F-labeled MMP inhibitors have been explored in clinical trials [162, 180].

1.3.2 PET and SPECT in AD

While SPECT plays a minor role in the imaging of AD, PET has been a major tool in the diagnosis and monitoring of the disease. Aside from the established FDG brain imaging, molecular imaging in AD has evolved around the visualization of Aβ plaques and neurofibrillary tangles. The first in-patient PET study to visualize Aβ plaques was conducted using ^{11}C-labeled Pittsburgh compound B (PIB) [13]. Since then, three tracers, namely ^{18}F-florbetapir, ^{18}F-florbetaben, and ^{18}F-flutemetamol, have been approved by the FDA for clinical use [98]. It has been suggested that this is due to Aβ accumulation in the brain in some cases decades prior to the onset of functional changes measurable by FDG PET [85]. Although Aβ has provided useful outcome measures in AD, limited therapeutic success of anti-Aβ drugs and the presence of large Aβ deposits in 33 % of cognitively normal, elderly individuals leave room for improvement [13, 168]. For the imaging of tau pathology, the PET ligand ^{18}F-flortaucipir has been developed and approved by the FDA for clinical use [86, 98]. In contrast to Aβ PET, tau PET is highly predictive of subsequent cognitive decline, irrespective of symptomatic status [5, 70]. In recent years, monitoring neuroinflammation using PET has gained interest. The most thoroughly investigated

target mitochondrial translocator protein (TSPO), is expressed in different cell types of the central nervous system. The detection of TSPO by PET has been linked to microglia activation in AD patients [222]. Other emerging targets that are more specific for microglia cells and have ^{11}C and ^{18}F-labeled tracers in development include colony-stimulating factor 1 receptor, cyclooxygenases and cannabinoid receptor type 2. There is also a growing body of evidence that builds upon the investigation of extra- and peri-cellular neuroinflammation targets such as reactive oxygen species and matrix MMPs [222].

1.4 Promising PET and SPECT imaging targets

There are many potential targets for PET and SPECT imaging in the context of immune-related conditions. In this work, we will focus on legumain and CD80.

1.4.1 Legumain

Legumain is a cysteine protease and is primarily located in late endosomes and early lysosomes of eukaryotic cells. In mammals, legumain is highly abundant in kidney and spleen tissue, and is expressed, albeit at a lower level, in other tissues throughout the body. Depending on the context, alternative names are used for legumain such as asparaginyl endopeptidase (AEP) and δ-secretase. Due to its His-148-Gly-spacer-Ala-Cys-189 motif, legumain is classified as a member of clan CD and the C13 family of cysteine proteases. It is the only known protease with Asn and Asp specificity at the P1 position. The main physiological function of legumain is the digestion of proteins in the lysosome. In this context, legumain plays an important role in the processing of self and foreign proteins for presentation on MHC class II molecules. A multitude of other functions have been ascribed to legumain and are subject of ongoing research. Legumain is expressed as a zymogen with a molecular weight of 56 kDa and undergoes activation at acidic pH. Autocatalytic processing at pH $\leq$ 5.5 of the proenzyme results in the formation of a 46/47 kDa intermediate active legumain. Further downstream processing yields a 36 kDa legumain variant. Activated legumain is stable at pH $\leq$ 6 and irreversibly inactivated at neutral pH. However, complexation with intregrins on the cellular surface and cystatin, an endogenous legumain inhibitor, can stabilize the protease at neutral pH, preventing it from irreversible structural changes. At pH $\sim$5.8, legumain specifically cleaves Asn residues C-terminally. Asp cleavage is exclusively observed at pH $<$ 4, and is thus physiologically negligible.

Under pathophysiologic conditions, legumain is found outside the lysosome in the cytoplasm, the nucleus, or in the extracellular space [35]. Legumain cleaves many endogenous substrates including other proteases such as cathepsins and MMPs [182]. Specifically in the context of cancer, legumain expression has been linked to tumor progression and metastasis in different tumors such as ovarian, breast, prostate, colorectal and gastric cancer [60, 134, 144, 201, 203]. The non-canonical localization of legumain has been widely observed in tumor tissue including the TME [182]. For instance, pro- and active legumain were found in the nucleus and cytosol of colorectal cancer cells [71, 72]. In large B cell lymphoma, legumain was localized on the cellular surface and in the extracellular matrix [179]. Moreover, the same study found that legumain was overexpressed by M2 TAMs specifically in the TME [179]. In gastric cancer, the downregulation of legumain expression in TAMs reduced cancer cell proliferation and angiogenesis *in vitro* and *in*

vivo [203]. In experiments differentiating between M1 and M2 TAMs, more active legumain was found in M2 than M1 polarized macrophages [183].

In AD mouse models, legumain expression is associated with microglial activation and disease progression [204]. Legumain levels increase with age in wild type mice and are significantly higher in mice with known AD-related mutations [204, 218]. In the human brain, legumain is abnormally activated in AD patients and is upregulated in microglia specifically upon acute inflammation [84,218]. Similar to cancer, non-canonically located legumain was identified in AD [14, 219]. In *in vitro* and *in vivo* studies, legumain cleavage of APP, the precursor of Aβ and tau has been shown [218, 219]. The prevention of legumain-mediated tau cleavage in P301S AD mice, led to ameliorated synaptic and cognitive function [219]. Similar effects were observed in mice expressing uncleavable APP [218]. The causal implication of legumain in cancer and AD makes it an interesting target for therapy.

Based on the narrow substrate specificity in P1 position, a series of azaAsn inhibitors with the α carbon replaced by a nitrogen has been developed in the early 2000s [141]. Since then, developments have included epoxide and michael acceptor containing moieties specifically targeting the active site Cys-189 [152]. The P1-Asn mimicking approach has culminated in reversibly binding cyano-warhead equipped and irreversibly binding alkyne compounds with favorable pharmacokinetic properties [40, 81, 101, 138, 139, 152]. Importantly, these active-site targeting inhibitors only bind to activated legumain, in which the active site is sufficiently accessible. An entirely different pharmacophore for legumain inhibition was discovered in a high-throughput screen with mouse kidney lysates and a $> 50\,000$ compound library [217]. The inhibitor was termed compound 11, bound to a regulatory exosite in addition to the active site and has since been further optimized [112]. Existing inhibitors and known substrates of legumain build the foundation of legumain-specific PET tracer development. Several legumain PET tracers have been explored preclinically. A group of molecules makes use of the physiological localization of legumain in lysosomes through lysosome-targeting. These lysosome-targeting tracers undergo intramolecular condensation upon legumain cleavage and are subsequently trapped within the lysosomes [159]. These ^{18}F tracers have since been optimized to reduce hepatic uptake and increase lysosomal targeting [118, 119]. Furthermore, the scaffold was coupled to a NOTA chelator and used for ^{68}Ga PET [80]. The tracers show more accumulation in MDA-MB-468 tumors with high legumain expression than in low-expression PC-3 tumors. The binding specificity of these tracers remains to be elucidated.

1.4.2 CD80

CD80 is a co-stimulatory membrane protein expressed on APCs [149]. The binding of T cells through the TCR to APCs is not sufficient to fully activate T cells [46]. CD28 is constitutively expressed on the surface of T cells and acts an an auxillary activator when binding to CD80 on APCs. Additionally, CTLA-4 is expressed on the surface of T cells and acts as a homologous, yet functiontionally opposite ligand for CD80 [127]. Thus, CTLA-4 competes with CD28 for the binding of CD80 and upon binding, reduces the required signal for T-cell activation. Additionally, CD80 and PD-L1, both expressed on the surface of APCs can interact and block the binding of PD-1 expressed on T cells to PD-L1 [150]. Notably, M1 polarized macrophages are characterized by high CD80 expression. CD80 is expressed not only by APCs, but also by various types of tumor cells,

leading to suppression of T cell activation and thereby evading immune surveillance [192]. Low CD80 expression in the tumor tissue has been associated with poor outcome in tumors such as gastric cancer and thyroid carcinoma patients [48, 191]. In immune checkpoint inhibitor (ICI) therapy, co-inhibitory molecules like CTLA-4 and PD-L1 are blocked in order to reactivate T cells in the TME and enhance the immune response to cancer cells [189]. Although exact numbers vary depending on the study, $\sim$60 % of patients respond only partially or not at all to the ICI therapy with generally higher response rates in combination therapy than monotherapy [33, 189]. Furthermore, immune-related adverse events in the form of T cells reacting with self-antigens in healthy organs are a major concern [12, 54]. Efforts to image the immune checkpoint molecules CTLA-4, PD-1 and PD-L1 have shown high predicive power for clinical response in the case of PD-L1 immunoPET with ^{89}Zr-labeled anti-PD-L1 atezolizumab [17]. However, antibodies that possess therapeutically favorable properties such as a long biological half life , are not necessarily optimal for PET or SPECT imaging. In the case of monoclonal antibodies, the long biological half life in combination with poor tumor penetration, requires the patient to come back to the hospital for PET scanning after an extended span of time, during which they will be exposed unnecessarily to ionizing radiation. A vast amount of ligands different from antibodies such as andibody fragments, nanobodies, small proteins and peptides coupled to different PET radioisotopes are currently in preclinical and clinical development [22]. As it pertains to SPECT, molecules of similar structures labeled with ^{99m}Tc are in development [211, 216]. CD80 imaging offers an alternative approach to CTLA-4, PD-1 and PD-L1 imaging. CD80 is expressed on M1-polarized macrophages of the TME and is predictive for ICI therapy response [171]. Aside from efforts within our group, we are not aware of any CD80 radiotracers in development [24, 187].

1.5 Aim of the thesis

The body of work that makes up this dissertation revolved around the development of tracers for PET and SPECT imaging of legumain and CD80, respectively. Both targets are expressed in the context of immune-related diseases. Legumain is an emerging therapeutic target both in cancer and in AD. It is overexpressed in tissue-resident macrophages such as M2-type TAMs and M1-type microglia and, provided a pathologically acidic environment, is activated and processes several endogenous substrates. CD80 is an important co-stimulatory signaling molecule of the TME. Similar to legumain, it is expressed by macrophages, albeit by M1-type TAMs. CD80 is crucial for the activation of T cells, which form the cornerstone of ICI therapy. Immunotherapeutic efforts to conquer cancer and AD could benefit greatly from the non-invasive detection of such biomarkers allowing for disease characterization in research and diagnosis and monitoring in the clinics. The specific goals of this thesis were:

- Characterization and modification of CD80 and legumain expression in cancer and AD mouse models using various biological methods
- Development (and continued development) of legumain- and CD80 targeting radiotracers followed by evaluation *in vitro* and *in vivo*

Furthermore, we have attempted the implementation of radioluminescence microscopy into the immunohistochemical staining workflow typically used in radiotracer development.

Chapter 2

Towards imaging the immune state of cancer by PET: Targeting legumain with ^{11}C-labeled P1-Asn peptidomimetics carrying a cyano-warhead

Author Statement

Severin K. Lustenberger: Conceptualization, Methodology (performed all experiments except acquisition of PET scans), Analysis (performed all data analysis), Writing (wrote first draft and corrected version), Project administration; **Claudia A. Castro Jaramillo**: Conceptualization, Funding acquisition, Methodology (pilot experiments) **Lena A. Bärtschi**: Methodology (supported experiments); **Rich Williams and his research group**: Materials/Data (providing precursor and reference compounds; measuring IC_{50} of Compounds), Writing (review); **Roger Schibli**: Supervision, Providing infrastructure, Writing (review); **Linjing Mu**: Supervision, Funding acquisition, Methodology (supported experimental planning), Analysis (supported data analysis), Writing (review), Project administration; **Stefanie D. Krämer**: Supervision, Funding acquisition, Methodology (supported experimental planning), Analysis (supported data analysis), Writing (review), Project administration

Published
Funding: This work was funded by the Swiss Cancer Research foundation, KFS-4900-08-2019

2.1 Background

Cancer remains one of the leading causes of death in high-income countries [49]. In search of effective treatments, the therapeutic focus has increasingly shifted from targeting cancer cells to targeting the tumor microenvironment (TME). This gave rise to therapeutic approaches with T-cell activity-modulating immune checkpoint inhibitors (ICI). These therapies leverage the involvement of T cells in the immune response to cancer through the targeting of CTLA-4, PD-1 or PD-L1. In recent years, the adoption of ICI therapy has substantially improved the prognosis for a sub-population of patients [68]. However, low response rates and immune-related adverse events necessitate an extension of treatment strategies beyond the established, leveraging other components of the TME [33,36]. Tumor-associated macrophages (TAM) of the anti-inflammatory M2 phenotype dampen the potential of T cells to attack tumor cells [205]. Various proteins expressed by TAMs have been studied as possible targets for the therapeutic modulation of the immune response. Immune-modulating strategies include the depletion of TAMs at the tumor site and the reprogramming of anti-inflammatory M2 to tumoricidal M1 type macrophages [148, 161]. Legumain, a lysosomal cysteine endopeptidase, is ubiquitously expressed across the body. Legumain specifically hydrolyzes substrates C-terminally to Asn residues (P1 position) in the Ala-Ala-Asn motif [35, 83]. In patients suffering from ovarian, breast, prostate, colorectal or gastric cancer, legumain expression correlates with tissue invasion and metastasis, a hallmark of tumor progression [60, 67, 134, 144, 201, 203]. Legumain facilitates extracellular matrix (ECM) remodeling through activation of metalloproteinases and cathepsins or by direct proteolysis of ECM components [29, 131, 181, 213]. M2 TAMs show elevated expression levels of legumain and its inhibition suppresses tumor progression in M2 TAM-dependent diffuse large B cell lymphomas in mice carrying human xenografts [179].

Consequently, legumain has been explored as a therapeutic target and prodrug-activator in the context of various tumor types. Based on the narrow substrate specificity of legumain, compounds containing nonproteinogenic amino acids and peptidomimetics have been developed. Such compounds were used to inhibit legumain and deliver chemotherapeutic payloads to the tumor [152]. Efforts in the development of activity-based inhibitors culminated in the synthesis of P1-Asn peptidomimetics equipped with an electrophilic cyano-warhead. In the presence of active-site Cys-189, these compounds form a reversible covalent bond, thereby inhibiting the enzyme [40, 81, 138, 139].

Medical imaging of legumain may offer a method to support immunotherapy in oncology [169]. Multiple attempts to image legumain have been undertaken in the course of the last decade. These include fluorescence imaging, MRI with contrast agents and positron emission tomography (PET) [31, 41, 58, 108, 111, 220]. PET enables clinically relevant deep tissue visualization. Recently, nanoparticle-based, ^{18}F- and ^{68}Ga-labeled PET tracers were developed to visualize legumain-expressing xenografts in tumor-bearing mice. The tracer relies on intracellular intramolecular condensation and macrocyclization based on legumain activity, resulting in lysosomal trapping [80, 118, 119, 159].

In this work, we aimed to develop a legumain-targeting PET tracer based on P1-Asn peptidomimetics amenable to ^{11}C-labeling and with suitable binding affinity for PET imaging. We chose two inhibitors with IC_{50} values of 3.85 nM (**1**) and 6.05 nM (**2**), respectively, as depicted in Figure 2.1. These inhibitors were developed and characterized as previously described [138]. We established the radiolabeling for [^{11}C]**1** and [^{11}C]**2**, characterized a CT26 tumor mouse model *in vitro* regarding the expression and activity

of legumain and evaluated both tracers *in vivo* in CT26 tumor-bearing mice by PET.

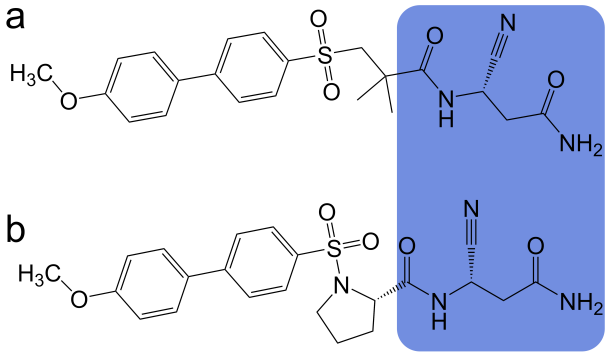

Figure 2.1: Chemical structures of **a** compound **1** and **b** compound **2**. The P1-Asn mimicking moiety is highlighted in blue.

2.2 Methods

2.2.1 Cell culture

The murine colon carcinoma cell line CT26.WT (ATCC CRL-2638) was obtained from the American Type Culture Collection. The cells were cultured in Roswell Park Memorial Institute (RPMI) 1640 medium with GlutaMAX-I and 25 mM HEPES (Gibco, Life Technologies, US) supplemented with 10 % fetal calf serum (FCS, Life Technologies, US), 10 000 U/ml penicillin and streptomycin (PS, Gibco, Life Technologies, US) at 5 % CO_2 and 37 °C. At 80-95 % confluence, cells were detached with 0.05 % trypsin-EDTA solution (Gibco, Life Technologies, US) and split 1 to 7 for sub-culture.

2.2.2 Mouse tumor inoculation

Animal studies were approved by the Zurich Cantonal Veterinary Office, Switzerland (license ZH28/2018), and conducted according to Swiss Animal Welfare legislation. Female BALB/c mice (Charles River Laboratories, Sulzfeld, DE) were housed at 22 °C with a 12-hour light-dark cycle and unlimited access to food and water. At the age of 14 weeks, the mice were inoculated subcutaneously in the right shoulder region with 8 * 10^5 CT26 cells re-suspended in 100 µl Matrigel (BD Biosciences, US). Experiments were performed 7-12 days after CT26 cell inoculation when tumors were clearly visible but no larger than 1.76 cm^3.

2.2.3 Fluorescence microscopy

Dissected CT26 tumors were embedded in OCT compound mounting medium (Avantor, US), cut to 10 µm slices with a cryotome, thaw-mounted on microscopy slides and stored at -80 °C. For fluorescent staining, slices were thawed, left to dry and washed (3 * 5 min) in phosphate-buffered saline (PBS, Gibco, Life Technologies, US). Tissue was encircled with a hydrophobic pen (Dako, DK) and fixed in 4 % paraformaldehyde in PBS for 10 min. Tissue was washed (3 * 5 min) in PBS and incubated in 5 % (w/v) powdered, skimmed milk in PBS on a benchtop rocker for 30 min. All subsequent incubation steps were performed protected from light on a benchtop rocker. Tissue was washed (3 * 5 min) in PBS and incubated with primary antibodies in PBS for 120 min. Tissue was washed (3 * 5 min) in PBS and incubated with secondary antibodies in PBS for 30 min. Tissue

was washed (3 * 5 min) in PBS and incubated with DAPI (BioLegend, US) 1:2 000 in PBS for 5 min. Tissue was washed (1 * 5 min) and sections were left to dry for 30 min. Cover slip was mounted with mounting medium (Mowiol, Kuraray, JP) and left to dry for 30 min. Slides were stored at 5 °C for up to 4 weeks prior to image acquisition. For macrophage staining, rat CD206 targeting primary antibody (MA5-16871, Thermo Fisher Scientific, US) 1:500 and goat Alexa Fluor 647 IgG secondary antibody (A21247, Thermo Fisher Scientific, US) 1:300 were used. For legumain staining, rabbit legumain targeting primary antibody (bs-3907R, Bioss, US) 1:100 and donkey Alexa Fluor 488 IgG secondary antibody (406416, BioLegend, US) 1:500 were used. Slides were scanned with a slide scanner (Pannoramic 250, 3DHistech, HU). Software provided by the manufacturer was used for image processing (3DHISTECH's Slide Converter version 2.3.2 and SlideViewer version 2.6).

2.2.4 Flow cytometry

CT26 tumors were dissected and washed with PBS, pH 7.4 (Gibco, Life Technologies, US). Tissue was chopped and incubated in 0.1 mg/ml DNAse I (11284932001, Roche, CH) and 1 mg/ml collagenase IV (1704-019, Gibco, US) in PBS at 37 °C, shaking for 2 h. Tissue was homogenized using a micropipette and forced through a 70 µm cell strainer (Corning, US). Single cell suspension was spun down at 500 * g for 5 min at 5 °C and re-suspended in culture medium based on RPMI 1640 with GlutaMAX-I and 25 mM HEPES (Gibco, Life Technologies, US) supplemented with 10 % heat-inactivated FCS and 10 000 U/ml penicillin and streptomycin (PS, Gibco, Life Technologies, US). For counting, cells were diluted 1:1 with 0.4 % trypan blue solution (Gibco, US), transferred to a counting chamber slide (Thermo Fisher Scientific, US) and inserted in an automated cell counter (Countess, Thermo Fisher Scientific, US). 100 000-400 000 cells per well were transferred to U-bottom 96-well plates (Greiner, AT) and spun down at 500 * g for 5 min at 5 °C. After removal of the supernatant, the cells were re-suspended in cell viability dye (Zombie Aqua, BioLegend, US) 1:1 000 in FACS buffer (2 mM EDTA in PBS containing 2 % (v/v) FCS) for 15 min and washed with FACS buffer. For fixation, cells were re-suspended in 1 % paraformaldehyde in FACS buffer and incubated for 10 min at 4 °C. After washing with FACS buffer, cells were permeabilized in permeabilizer solution (0.04 % (v/v) Triton x-100 in FACS buffer) and incubated for 20 min at 4 °C. Cells were washed with permeabilizer solution and re-suspended in Fc receptor blocking solution (Trustain FcX) 1:500 in permeabilizer solution followed by 10 min of incubation at 4 °C. Cells were washed with permeabilizer solution and incubated in permeabilizer solution containing antibody for 45 min at 4 °C. Cells were washed with FACS buffer (2 x) and re-suspended in FACS buffer. Measurements were performed on a flow cytometer (CytoFLEX S, Beckman Coulter, US). Compensation beads (UltraComp eBeads Plus, Thermo Fisher Scientific, US) were used to generate a compensation matrix for the given fluorophores. Isotype controls, fluorescence-minus-one samples and unstained cells were used to assist gating. PE conjugated rat CD206-targeting antibody (141705, BioLegend, US) 1:400 in FACS buffer was used to detect M2 macrophages. Gating and data processing were performed in R (R-project [160]) using open-source packages [3, 51–53, 66, 130, 151].

2.2.5 Gene expression analysis

CT26 tumors were dissected and washed with RNA-preserving solution (RNAlater, Thermo Fisher Scientific, US). For RNA extraction, tissue was transferred to RNA extraction

solution (TRIzol, Thermo Fisher Scientific, US) and homogenized using a bead-mill system (Qiagen, DE). The homogenate was centrifuged (12 000 * g, 10 min, 4 °C) and the uppermost phase was mixed with chloroform. After centrifugation (same conditions as above), the aqueous phase was mixed with isopropanol and incubated for 10 min. The samples were centrifuged (same conditions as above) and the resulting pellet was washed with 75 % ethanol and centrifuged (8 000 * g, 5 min, 4 °C). The wash was repeated, the sample pellets were centrifuged (15 000 * g, 2 min, 4 °C) and left to dry for 1-2 h. The pellet was dissolved in RNAse-free water. Concentration and quality of the RNA extract were determined using a microvolume spectrophotometer (NanoDrop, Thermo Fisher Scientific, US). For reverse transcription, RNA extract was incubated with wipeout buffer (QuantiTect Reverse Transcription kit, Qiagen, DE) for 2 min at 42 °C. Reverse transcriptase, reverse transcription buffer and reverse transcription prime mix (QuantiTect Reverse Transcription kit, Qiagen, DE) were added and the solution was incubated for 15 min at 42 °C followed by 3 min at 95 °C. Real-time quantitative polymerase chain reaction (RT-qPCR) was performed using cDNA from the previous step, gene specific primers and qPCR Master Mix (GoTaq qPCR Master Mix, Promega, US). Primers for qPCR were custom-made oligonucleotides (Microsynth, CH): legumain (Lgmn, NCBI Gene: 19141), forward 5'-GTG ATC AAC CGA CCT AAC G-3', reverse 5'-ATT CTC TGG AGT CAC ATC CTC-3'; ATP synthase beta chain (Atp5b, NCBI Gene: 8617357), forward 5'-GGT TCA TCC TGC CAG AGA CTA-3', reverse 5'-AAT CCC TCA TCG AAC TGG ACG-3'; cytochrome c1 (Cyc1, NCBI Gene: 66445), forward 5'-TAG CTA AGG ATG TCG CCAC-3', reverse 5'-TCA ACA ACA TCT TGA GAC CCA-3'; β-actin (Actb, NCBI Gene: 11461), forward 5'-GTG ACG TTG ACA TCC GTA AAG-3', reverse 5'-GCC GGA CTC ATC GTA CTC C-3'. On a real-time PCR system (Quantstudio 7 Flex, Thermo Fisher Scientific, US), 10 µl of total volume were run through 40 cycles with the hold stage temperature at 95 °C for 2 min and a PCR stage consisting of 95 °C for 15 s (denaturation) and 60 °C for 60 s (annealing/extension). Melt curve stage was included for quality control on a single well level. Lgmn was normalized to Actb1, Cyc1 and Atp5b levels [139]. Data processing was performed in R using open-source packages [209].

2.2.6 Legumain activity and estimation of binding potential

Tissues were dissected and washed with assay buffer consisting of 20 mM citric acid, 60 mM Na_2HPO_4, 1 mM EDTA, 0.1 % (m/v) CHAPS, 4 mM DTT at pH 5.8. Tissue was homogenized using a Polytron (Kinematica, US), and centrifuged at 19 000 * g, 4 °C for 20 min to precipitate debris. Protein content of the lysate was determined using the BCA assay, with bovine serum albumin for calibration [104]. Legumain activity was measured with a fluorescence assay [87]. In brief, samples of tissue lysate with total protein concentrations ranging from 382.0 to 11 325.2 µg/ml were prepared. The substrate Z-Ala-Ala-Asn-AMC (Bachem, CH) was added to the samples to reach a substrate concentration of 10 µM. Fluorescence was measured at excitation 340 nm and emission 460 nm every minute over 5 h. The activity was determined from the slope of the initial linear increase in fluorescence and normalized to the protein content of the tissue sample. Data processing was performed in R using open-source packages [209].
The density of legumain, corresponding to the maximal possible specific binding of legumain- targeting tracer per mg protein in the tissue ($B_{\max}$ in nmol/mg) was estimated based on the measured legumain activity in comparison to recombinant mouse legumain of known concentration (R&D Systems, US). To estimate the expected binding potential (BP)

of a tracer in tissue with Equation 2.1, B_{max} (nmol/mg) was transformed to B_{max} in nmol per 1 000 cm^3 tissue (nM), assuming a protein content of mouse tissue of 0.23 g/cm^3 [188], i.e., B_{max} in nmol/mg was multiplied by 2.3 * 10^5 mg/l to get B_{max} in nM.

$$\mathrm{BP} = \frac{B_{\mathrm{max}}(\mathrm{nM})}{K_{\mathrm{i}}(\mathrm{nM})} \tag{2.1}$$

K_i in Equation 2.1 was estimated from the IC_{50} of the inhibitor, i.e., 3.85 nM for **1** and 6.05 nM for **2** (determined according to [27]), the substrate concentration at which IC_{50} was determined, i.e., 10 µM [139] and the K_M reported for human legumain, i.e., 25.7 µM [153] according to the Cheng-Prusoff equation (Equation 2.2).

$$K_{\mathrm{i}} = \frac{\mathrm{IC}_{50}}{1 + \frac{[S]}{K_{\mathrm{M}}}} \tag{2.2}$$

2.2.7 Radiochemistry

Generation of [^{11}C]CH_3OTf

Proton bombardment of a target filled with N_2 fortified with 0.5 % O_2 in a Cyclone 18/9 cyclotron (18-MeV, IBA, BE) afforded [^{11}C]CO_2 by $^{14}N(p, \alpha)^{11}C$ nuclear reaction. For the conversion to [^{11}C]CH_3I, nickel-based catalytic reduction of [^{11}C]CO_2 with hydrogen was performed to form [^{11}C]CH_4, which was followed by iodination to afford [^{11}C]CH_3I. [^{11}C]CH_3I was further converted to [^{11}C]CH_3OTf by passing through a silver triflate column at elevated temperatures (190 °C).

Radiosynthesis

Approx. 1 mg precursor was dissolved in 500 µl acetone containing 3 µl 5 M NaOH. The generated [^{11}C]CH_3OTf was bubbled into the solution with constant stirring followed by incubation for 3 min at 70 °C. The reaction was quenched with water and the crude solution was injected into a semi-preparative HPLC column (Symmetry C18 Prep Column 5 µm 7.8 * 50 mm, Waters, US). A solvent gradient of 85-50 % phosphoric acid (0.1 % (v/v) in water) and 15-50 % acetonitrile over 7 min was applied. The flow rate was 4 ml/min. The product was collected with the help of a UV detector and a radio detector (Gabi Star, Elysia-Raytest, DE), diluted with water (8 ml) and purified using an activated (5 ml ethanol, 10 ml water) C18 cartridge (Sep-Pak C18 light, Waters, US). The cartridge was washed with 5 ml water and the product was eluted with 0.5 ml ethanol into a sterile vial. 9.5 ml saline solution (NaCl 0.9 %, B.Braun, DE) was added to obtain an isotonic product containing 5 % ethanol. Nitrogen was used as a propellant. For quality control, HPLC was performed with 50 µl of the solution injected into a reverse phase HPLC column (ACE 3 C18 3 µm 50 * 4.6 mm, ACE, UK). A solvent gradient was applied with A (0.1 % phosphoric acid in water/acetonitrile 95/5) and B (water/acetonitrile 5/95) from A/B 80/20 to 10/90 over 10 min. The flow rate was 1.2 ml/min. The molar activity was determined based on linear regression with reference compound measured with a UV detector (Gabi Star, Elysia-Raytest, DE) at 254 nm wavelength.

2.2.8 *In vitro* autoradiography

Frozen tissue slices as described for fluorescence microscopy were thawed and incubated with PBS for 10 min. Tissue was submerged in PBS containing 1 % (v/v) FCS for 2 h, followed by PBS or PBS with the addition of 4 µM reference compound **1** (blocking conditions) for 15 min at 2-8 °C. After this pre-conditioning, the slices were incubated for 30 min with 4 nM [^{11}C]**1** or [^{11}C]**2** in PBS (baseline conditions) or in PBS containing 4 µM reference compound **1** (blocking conditions) at 2-8 °C. Standards were prepared by dilution of tracer solution with PBS. Tissues were washed in ice-cold PBS (3 * 3 min) and water (1 * 5 sec) and left to dry. The slices were exposed to a photostimulable phosphor plate (BAS IP MS 2025, Fujifilm, JP) for 45-60 min and images were acquired using a phosphoimager (BAS-5000, Fujifilm, JP). Tissue images were cropped to rectangle including tissue and background. Gray-scale pixel intensity arrays were reduced to values above 20th percentile prior to plotting. Image processing was done with open-source imaging software [173], python community modules [69, 125, 199] and R open-source packages.

2.2.9 *In vivo* metabolism

Tracer (4.1 MBq to 139.7 MBq, 1.0 to 5.2 nmol/kg) was injected via lateral tail vein in CT26 tumor-bearing BALB/c mice. Animals were euthanized by decapitation under anesthesia (2-3 % isoflurane in oxygen/air, 1/1) and tissues were dissected. Blood was collected, plasma was separated for analysis by centrifugation at 5 000 * g for 3 min, and proteins were precipitated with an equal volume of ice-cold acetonitrile and centrifugation at 5 000 * g, 4 °C for 5 min. Tumor samples were homogenized in matching volumes of PBS using a Polytron (Kinematica, US), and centrifuged at 5 000 * g, 4 °C for 5 min. Supernatants were filtered through 0.45 µm pore size filters and analyzed by UPLC. A reverse phase UPLC column (Acquity UPLC BEH C18 1.7 µm 2.1 * 50 mm, Waters, US) was used. The mobile phase was 15-60 % acetonitrile over 2.5 min. The plates were exposed to a photostimulable phosphor plate for 1.5 h and images were acquired using the phosphorimager.

2.2.10 PET/CT scans

Tumor-bearing mice were anesthetized with 2-3 % isoflurane in oxygen/air (1/1) 10 min prior to PET acquisition. PET/CT scans were performed on a small-animal PET/CT scanner (Super Argus, Sedecal, ES) with an axial field of view of 4.8 cm and a spatial resolution of 1.6-1.7 mm (full width at half maximum) [61]. Respiratory rate was kept at $\sim$60 min^{-1} through adjustment of isoflurane concentration. Body temperature was kept at 37 °C using heated air. Tracer was injected into tail vein at the indicated time point and dose, and PET data were acquired in list mode. Anatomical information was obtained by CT following each PET acquisition. PET data were reconstructed with 2D ordered-subsets expectation maximization (2D-OSEM), applying random scatter correction and decay correction but no correction for attenuation, and analyzed with PMOD v4.2 software (PMOD Technologies Ltd., Zurich, Switzerland). Volumes of interest for the tumor, liver and reference region (muscle) on the contralateral side of the tumor were drawn manually in PMOD on the basis of the PET and CT images. SUVs were calculated as the ratio of regional averaged radioactivity in Becquerel per cubic centimeter and injected radioactivity in Becquerel per gram body weight, multiplied by 1 cm^3 per g body weight.

Image analysis was performed in python using community modules [15,69,82,117,125,212] and R open-source packages. All radioactivity was decay-corrected to the time point of injection to the animal.

2.2.11 Biodistribution after dissection

Following PET acquisition, tumor-bearing mice were euthanized through decapitation under anesthesia. Tissues were dissected and radioactivity determined with a gamma counter (Wizard 3", PerkinElmer, US). Data analysis was performed in R using open-source packages [209].

2.2.12 Statistical analysis

Statistical differences in radiotracer uptake or SUV ratios were analyzed by two-tailed paired or unpaired Student's t test, as indicated. Differences with $p < 0.05$ were considered significant. Average values are shown with standard deviations (SD) or data range in case of $n = 2$.

2.3 Results

2.3.1 Legumain mRNA expression, activity and association with M2 macrophages in CT26 tumors

The relative abundance of legumain in CT26 tumors was inferred using mRNA from 6 mice. Muscle and kidney of the same mice were analyzed as control tissues for low and high legumain expression, respectively [27]. Legumain expression in the CT26 tumors was similar as in kidney and expression in both tumor and kidney was significantly higher than in muscle, as shown in Figure 2.2. To quantify legumain in its active form, legumain activity was determined in CT26 tumor, kidney and muscle whole tissue lysates from 4 additional mice. In agreement with the mRNA expression, the legumain activity was significantly higher in tumor and kidney than muscle (Figures 2.2 and 2.11). The estimated density of legumain ($B_{\max}$) in muscle, kidney and tumor tissue was ~ 0 (-1.6 $\pm$ 0.81 pmol/mg), 62.9 $\pm$ 23.4 pmol/mg and 40.7 $\pm$ 19.1 pmol/mg, respectively. Assuming 0.23 g protein per cm^3 this corresponds to 14 471 $\pm$ 5 381 nM and 9 352 $\pm$ 4 387 nM in kidney and tumor, respectively. The K_i values of **1** and **2** as calculated with Equation 2.2 from the IC_{50} were 2.77 nM and 4.36 nM, respectively. The respective theoretical BP in tumor (Equation 2.1) are 3 376 $\pm$ 1 584 for **1** and 2 145 $\pm$ 1 006 for **2**.
The qualitative colocalization of M2 macrophages with extracellular legumain was assessed using fluorescent microscopy of CT26 tumor cryosections. Images based on whole section scans showed the occurrence of M2 macrophages (CD206 positive) along with extracellular legumain in the tumor periphery as shown in 2.3. The negative control stained with secondary antibody and without primary antibody is shown in Figure 2.12. Flow cytometry yielded that 5.1 $\pm$ 1.9 percent of viable cells in tumor samples ($n = 4$ mice) were M2 macrophages. The gating strategy is shown in Figure 2.13.

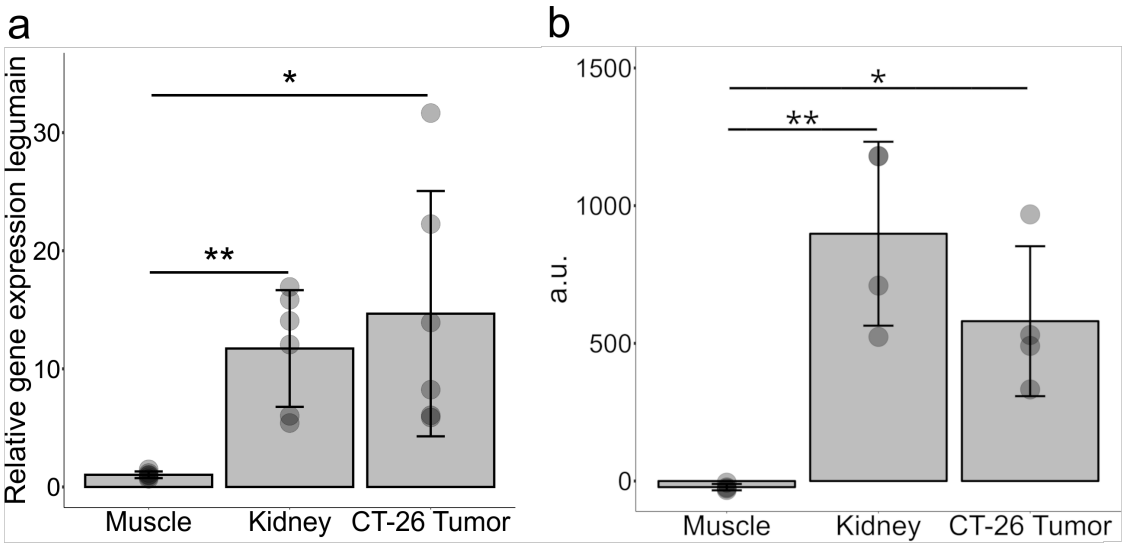

Figure 2.2: **a** mRNA levels of tissue from CT26 tumor-bearing mice ($n = 6$ mice, 1 sample each). Expression levels of Lgmn were quantified by RT-qPCR relative to Actb1, Cyc1 and Atp5B. **b** Legumain activity in total lysate of dissected tissues from CT26 tumor-bearing mice ($n = 4$ mice, 1 sample each). Legumain activity was measured as the conversion rate of the non-fluorescent substrate to the fluorescent product and normalized to the sample protein content. Significance compared with muscle tissue was analyzed with paired student's t tests, without correction for multiple comparisons. Bars, means; symbols, individual values; error bars, SD. *, $p < 0.05$; **, $p < 0.01$; a.u., arbitrary units.

2.3.2 Radiochemistry

Structures and reaction schemes for [^{11}C]**1** and [^{11}C]**2** are shown in Figure 2.4. The respective compound molar activities ranged from 40.6 to 383.2 GBq/µmol and from 12.9 to 271.1 GBq/µmol across 11 and 13 productions, respectively. The radiochemical purity was above 95 % for each production (Figures 2.14 and 2.15)

2.3.3 *In vitro* autoradiography with CT26 tumor slices

The binding of [^{11}C]**1** and [^{11}C]**2** to CT26 tumor tissue was characterized by *in vitro* autoradiography with tumor slices. Figure 2.5 shows the heterogeneous binding of both tracers in the tumor slices. The binding pattern was similar for the two tracers comparing slices from the same tumor, indicating that the heterogeneity in binding was reproducible. To characterize the mechanism of binding, additional slices were exposed to excess (4 µM) unlabeled **1**, added 15 min before and together with the tracers (blocking condition). A reduction in signal under blocking condition would indicate saturable, i.e., specific, binding of the tracer.

2.3.4 PET with CT26 tumor-bearing mice

Motivated by the *in vitro* heterogenous binding to the tumor slices and despite the lack of its blocking, we evaluated [^{11}C]**1** and [^{11}C]**2** as PET tracers *in vivo*. Pilot PET experiments in CT26 tumor-bearing mice indicated that the tumor/muscle ratios of both

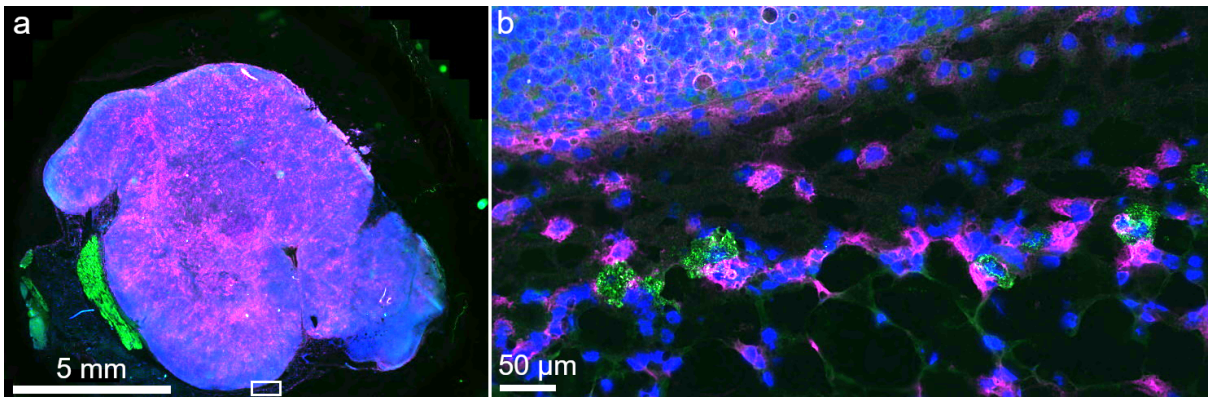

Figure 2.3: Representative fluorescence microscopy images of **a** CT26 tumor tissue slice. Cryosection stained with polyclonal anti-legumain primary antibody (green), monoclonal anti-CD206 primary antibody (purple; M2 macrophages) and DAPI (blue; nuclei). **a** Complete section for overview. **b** Magnification of tumor periphery, corresponding to the white frame in **a**.

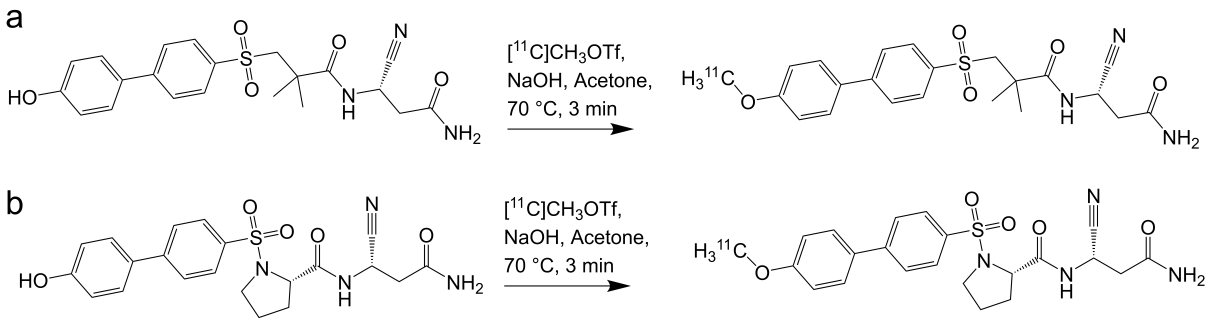

Figure 2.4: Synthesis of **a** [^{11}C]**1** and **b** [^{11}C]**2**.

tracers increased over time and only became constant ∼60 min post injection (p.i.), with tumor TACs peaking later and then decreasing slower than muscle TACs (total $n = 12$; one animal died during the scan). These data are not shown as some of these animals were pre-treated for other research questions. Based on these scans, we chose scan times from 60 to 150 min p.i. for the detailed evaluation of the two tracers. The injected activity (molar mass) at scan start of baseline scans from 60-150 min p.i. was 6.5-11.5 MBq (4.6-11.7 nmol/kg, $n = 4$ animals) of [^{11}C]**1** and 11.1-13.3 MBq (45.1-59.5 nmol/kg, $n = 3$ animals) of [^{11}C]**2**. The injected activity (molar mass) at scan start under blocking conditions, i.e., with excess (4.2 µmol/kg) respective unlabeled compound from 60-150 min p.i. was 13.4 and 16.3 MBq (21.2 and 12.7 nmol/kg, $n = 2$ animals) of [^{11}C]**1** and 5.3-14.3 MBq (17.5-35.9 nmol/kg, $n = 3$ animals) of [^{11}C]**2**. The PET images averaged from 60-150 min p.i. showed accumulation of radioactivity in the tumor periphery (Figures 2.6 and 2.17) besides high uptake in the abdomen. Co-injection of excess (4.2 µmol/kg) respective unlabeled reference compound did not alter the result, in agreement with the *in vitro* autoradiography results. Figures 2.7 and 2.8 show the time-activity curves (TAC) of tumor, muscle (reference tissue) and liver as well as the tumor/muscle activity ratios of all scans from 60-150 min p.i.. SUVs in tumor and muscle did not substantially change over the duration of the scan. Blocking reduced the SUV of [^{11}C]**2** in tumor and muscle (significant for muscle) but not in [^{11}C]**1**. The respective tumor/muscle ratio was not reduced by blocking for either tracer.

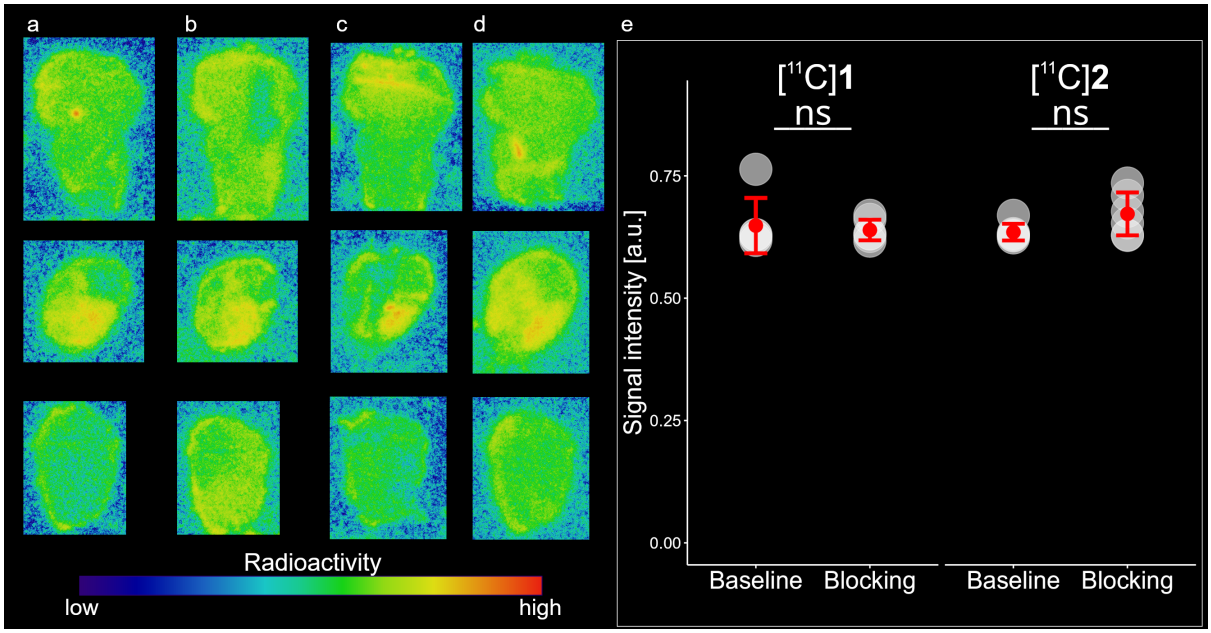

Figure 2.5: *In vitro* autoradiography with CT26 tumor slices (representative slices from 3 mice out of 6 mice; slices of one tumor per row in **a** to **d**). **a** Slices incubated with 4.0 nM [^{11}C]**1** (baseline condition) and **b** co-incubated with 4000 nM unlabeled **1** (blocking condition), in the same experiment. **c** Slices incubated with 4.0 nM [^{11}C]**2** (baseline condition) and **d** co-incubated with 4000 nM **1** (blocking condition), in the same experiment. **e** Quantification for 6 slices per tracer and condition (6 mice in total). Baseline and blocking conditions were compared with student's t tests, without correction for multiple comparisons. White symbols, median activity of the individual slices; red symbols, mean of medians; red error bars, SD. ns, no significant difference.

2.3.5 Biodistribution after dissection

The distribution of [^{11}C]**1** and [^{11}C]**2** was furthermore determined from the dissected tissues after euthanasia following the PET scans. The results are shown in Figures 2.9 (as SUV) and 2.10 (as percent injected dose per gram tissue, %ID/g). At 155 min p.i., liver uptake was highest among the analyzed tissues for both tracers, followed by spleen and kidneys, tissues with high legumain expression [27]. Radioactivity was significantly higher in tumor than muscle for both tracers. The resulting tumor/muscle ratios were 3.42 ± 0.47 for [^{11}C]**1** (n = 6) and 3.86 ± 0.63 for [^{11}C]**2** (n = 6) without significant difference between the tracers. No significant difference was seen between baseline and blocking conditions.

2.3.6 Tracer *in vivo* metabolism

To assess tracer metabolic stability *in vivo*, plasma, CT26 tumors and urine were collected after euthanasia at 10 min (both tracers), 20 min ([^{11}C]**1**) and 40 min ([^{11}C]**1**) p.i.. Tumors were homogenized, proteins were precipitated, and the supernatants were analyzed by reverse phase UPLC. The chromatograms are shown in Figure 2.16. The retention time (RT) of both references (intact tracers) was 2.9 min. Plasma and tumor homogenates contained a highly hydrophilic radiometabolite (RT 0.3 min) with higher concentration than the parent tracers already 10 min p.i. For both tracers, an additional radiometabolite, slightly

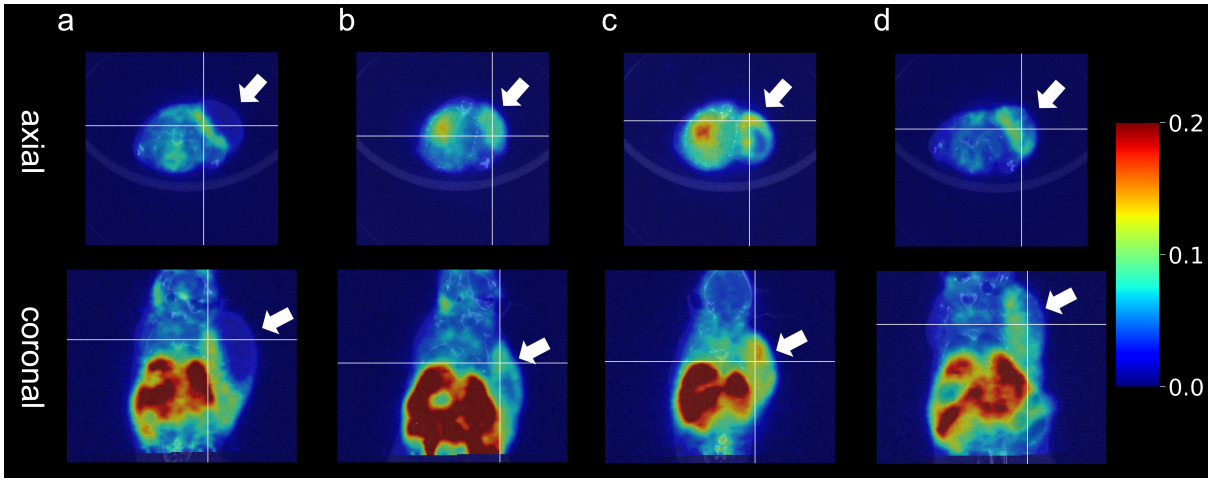

Figure 2.6: Representative PET images of CT26 tumor-bearing mice (60-150 min p.i., averaged) superimposed on CT (axial, coronal, as indicated). CT26 tumors on right shoulder (arrow). **a** Mouse injected with [^{11}C]**1** and **b** co-injected with 4.2 µmol/kg **1**. **c** Mouse injected with [^{11}C]**2** and **d** co-injected with 4.2 µmol/kg **2**. Crosshair indicates image planes. Mouse weights and activity (mass) at injection: **a** 19.7 g, 49.7 MBq (4.6 nmol/kg); **b** 18.9 g, 124.9.MBq (12.7 nmol/kg); **c** 18.8 g, 85.0 MBq (47.3 nmol/kg); **d** 22.2 g, 110.0 MBq (35.9 nmol/kg). PET, color bar and corresponding SUV are depicted on the right. CT, gray scale. The TACs of tumor, muscle and liver are shown in Figures 2.7 and 2.8. PET images of all scanned mice are shown in Figure 2.17.

more polar than the parent tracer (RT: 2.6 min), did not exceed tracer concentrations in plasma and tumor at the studied time points (Figure 2.16). At 40 min p.i. (tested for [^{11}C]**1** only), only the radiometabolite with RT 0.3 min was detectable in plasma and tumor homogenate. [^{11}C]**1** and its two radiometabolites were detected in urine at all analyzed time points, while for [^{11}C]**2** only the highly polar radiometabolite was detected in urine at 10 min p.i.. These data indicate that both tracers are rapidly metabolized *in vivo*. It should be noted that covalently bound tracer or covalently bound radiometabolite would not be detected in the analyzed supernatant.

2.4 Discussion

We attempted to use a warhead-equipped inhibitor for the imaging of legumain by PET. Previous approaches involved the legumain recognition motif Ala-Ala-Asn and make use of the legumain proteolytic function with the aim of increased tracer uptake and retention [58, 80, 118, 119, 159]. Both of our tracers [^{11}C]**1** and [^{11}C]**2** accumulated peripherally in CT26 tumors. However, accumulation was not reduced by injection of unlabeled reference compound in excess, which would have proven specific binding.

Our results show similarly high legumain mRNA expression in the kidney and CT26 tumor tissues, substantially higher than in muscle. High legumain levels in kidney and CT26 tumors are in accordance with previous findings [27]. In addition to target expression, we assessed target accessibility for our tracers. *In vivo*, legumain undergoes activation in multiple steps which alters both its ligase and protease activity [35]. In the case of our active-site targeting P1-Asn peptidomimetics, we estimated accessibility based on legumain protease activity. In agreement with the expression results, protease activity

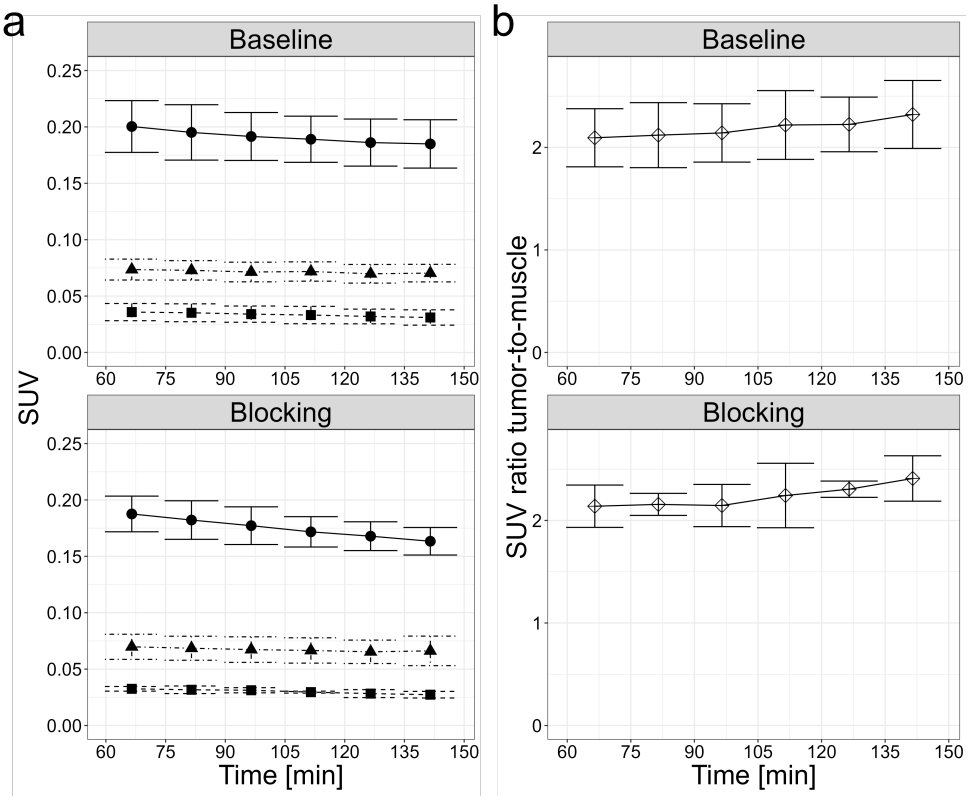

Figure 2.7: Quantification based on PET scans with [^{11}C]**1**. **a** TACs for baseline ($n = 4$ animals) and blocking ($n = 2$ animals) conditions, as indicated. See Figure 2.6 for details. Circles, liver; squares, muscle; triangles, tumor. **b** Resulting SUV ratio tumor-to-muscle over time for baseline and blocking conditions, as indicated. Shown are means with error bars indicating SD (baseline) or individual values (blocking). Data from the scans shown in Figures 2.6 and 2.17.

was high and at similar levels in kidney and tumor homogenates but negligible in muscle homogenate. High contrast in PET imaging requires a high enough BP, which is given by the ratio between B_{max} and K_D. The calculated K_i of **1** (2.77 nM) and **2** (4.36 nM) and the tumor B_{max} of 40.7 ± 19.1 pmol/mg fulfill this criterion [39]. Examples for comparison are folate-receptor targeting with a K_D of 2.09 nM at a B_{max} of 14.7 pmol/mg and PD-L1 targeting with a K_D of 59.9 nM at a B_{max} of 5.43 pmol/mg [102, 135]. Based on our estimated BP, high accumulation of our legumain-targeting PET tracers would be expected in the CT26 tumors.

Indeed, both *in vitro* autoradiography and *in vivo* PET scans showed accumulation of our tracers (or radiometabolites) in the tumor periphery where legumain-expressing pro-tumorigenic M2 macrophages constituted a sizable proportion of the total cell population. However, the lack of blocking by excess unlabeled reference compound both *in vitro* and *in vivo* questions the specific binding of our tracers to legumain in tissues. Through their electrophilic cyano-warhead, both **1** and **2** are engineered to act in reversible covalent fashion on Cys-189 in the legumain catalytic triad [35]. In principle, cross reactivity of the cyano-warhead with other cysteine proteases, such as cathepsin S, cathepsin B, caspase 3, caspase 8, and ubiquitin-specific peptidase cannot be ruled out [47, 107, 138]. However, legumain is the only known asparagine-specific mammalian cysteine protease, rendering legumain P1-Asn peptidomimetic structures unlikely to interact with other

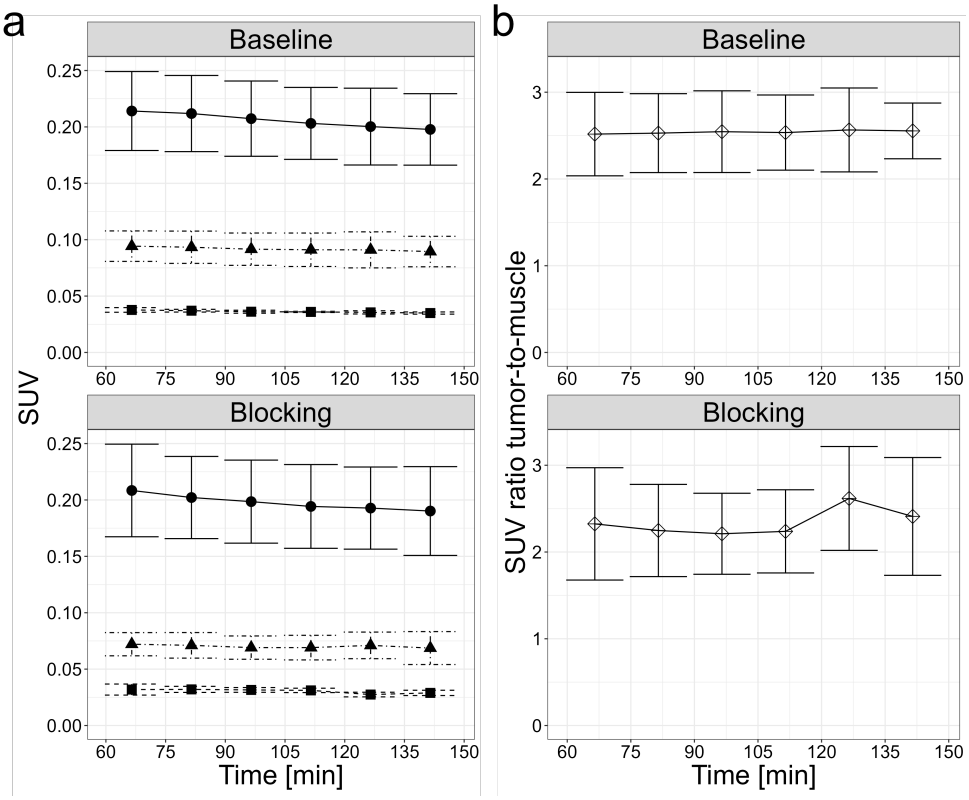

Figure 2.8: Quantification based on PET scans with [^{11}C]**2**. **a** TACs for baseline ($n = 3$ animals) and blocking ($n = 3$ animals), as indicated. See Figure 2.6 for details. Circles, liver; squares, muscle; triangles, tumor. **b** Resulting SUV ratio tumor-to-muscle over time for baseline and blocking conditions, as indicated. Shown are means with error bars indicating SD (baseline) or individual values (blocking). Data from the scans shown in Figures 2.6 and 2.17.

proteases [184]. To counteract potentially slow kinetics of the covalent tracer binding, we added a pre-incubation step with excess unlabeled **1** under blocking conditions to the autoradiography protocol. However, this did not reduce tracer binding, indicating that slow covalent binding to the target was not the cause for the lack of blocking. The lack of blocking by excess unlabeled **1** may be the result of impaired accessibility of the target or lack of covalent bond formation. Regarding legumain accessibility: legumain activity and conformational stability are sensitive to the chemical milieu [35]. Specifically, legumain is conformationally inactivated at neutral pH [35]. However, the slightly acidic conditions of the tumor microenvironment likely stabilize active legumain [194]. Preserved activity in our *ex vivo* activity assay indicates that legumain is conformationally stable with protease activity in the target tissue. Regarding a potential lack of covalent bond: our tracers would still bind to legumain, based on the target-specific P1-Asn peptidomimetic structure. However, the overall affinity would be magnitudes weaker in the absence of the covalent bond. The high B_{max} observed in tumor and kidney may still allow some contrast in imaging. In this scenario, blocking with 4 µM unlabeled compound (autoradiography) may be inefficient and would require much higher concentrations. Our *in vitro* and *in vivo* results would be in agreement with such a scenario. We can furthermore not rule out competition for the binding to legumain by the many endogenous substrates [35]. A final possible reason for the lack of blocking may be an underestimation of the target

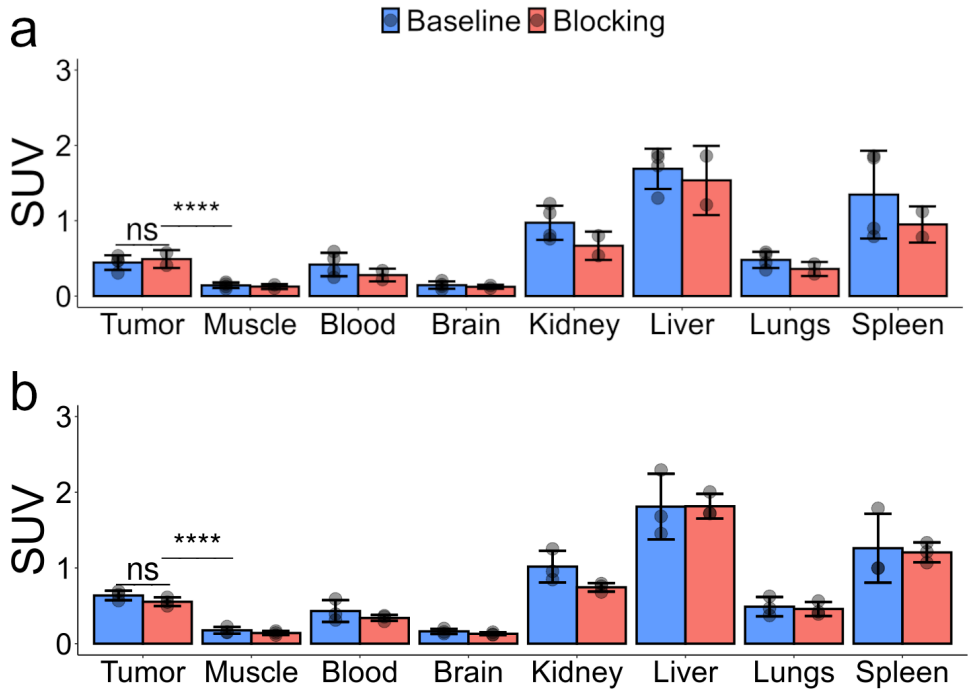

Figure 2.9: Biodistribution (SUV) after dissection at 155 min p.i. of the mice studied by PET (Figures 2.6 to 2.8 and 2.17). **a** [^{11}C]**1** and **b** [^{11}C]**2**. Blue bars, baseline conditions (tracer only). Red bars, blocking conditions (tracer co-administered with excess **1**(**a**) or **2**(**b**)). Points, individual values; error bars, SD for $n \geq 3$ or individual values for $n = 2$. Significance between tumor and muscle with combined baseline and blocking SUV was analyzed as indicated (horizontal lines above error bars) with student's t tests, without post hoc corrections for multiple comparisons; $n = 6$ for both tracers (combined baseline and blocking). ****, $p < 0.0001$; ns, no significant differences between baseline and blocking condition, for any tissue (only indicated for tumor). The same data is expressed as %ID/g in Figure 2.10.

abundance in case the tracers bind to the zymogen as well and not only the activated enzyme. In this case, the target could exceed the amount of blocking compound both *in vitro* and *in vivo*, resulting in inefficient blocking.

In vivo, compounds [^{11}C]**1** and [^{11}C]**2** were rapidly metabolized, yielding a highly polar radiometabolite which may have unspecifically accumulated in the tumor, not affected by our blocking conditions. Given the structure of the two compounds, it is likely that they are subject to *O*-[^{11}C]demethylation by cytochrome P450 enzymes [190]. This process yields reactive [^{11}C]formaldehyde, which either binds to e.g., proteins, can be reduced to [^{11}C]methanol or oxidized to [^{11}C]formic acid and eventually [^{11}C]CO_2 [90]. However, we are not aware of any [^{11}C]methylated PET tracer with accumulation of the released [^{11}C]formaldehyde (or its further metabolites) in the target region.

The poor metabolic stability is a substantial drawback of our tracers anyway, potentially reducing their chance for specific binding. Before further investigating the binding mode of our tracers, we aim to improve the metabolic stability by optimizing the chemical structure. This will allow to address the binding mode(s) to the active enzyme and the zymogen *in vitro* and *in vivo* in more detail. In this context, it is noteworthy, that none

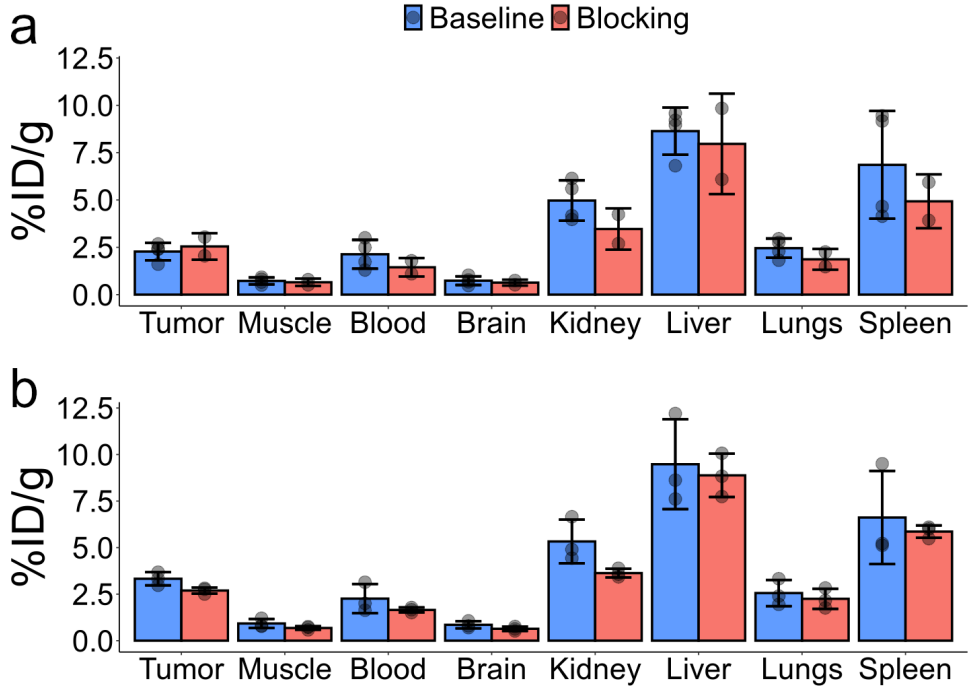

Figure 2.10: Biodistribution (%ID/g) after dissection at 155 min p.i. of the mice studied by PET (Figures 2.6 to 2.8 and 2.17). **a** [^{11}C]**1** and **b** [^{11}C]**2**. Blue bars, baseline conditions (tracer only). Red bars, blocking conditions (tracer co-administered with excess **1**(**a**) or **2**(**b**)). Points, individual values; error bars, SD for $n \geq 3$ or individual values for $n = 2$. For both tracers (combined baseline and blocking) $n = 6$. %ID/g, percentage of injected dose per gram tissue. The same data is expressed as SUV in Figure 2.9. For significance indication see Figure 2.9.

of the previous studies with legumain-targeting PET tracers have shown blocking by legumain inhibition *in vivo* [80, 118, 119, 159].

2.5 Conclusions

The CT26 tumor model provides high legumain expression and activity, ideal for the development of legumain-targeting PET tracers of the P1-Asn peptidomimetic type. Two such legumain-targeting tracers were synthesized with high radiochemical purity and molar activity. For both tracers, radioactivity accumulated in the CT26 tumor. However, their poor in vivo stability and the absence of a blocking effect dampen the prospects of the developed tracers. Structural modifications to improve the *in vivo* stability will allow to address the mechanism(s) of target binding and further development of legumain-targeting PET tracers.

2.6 Supplementary material

2.6.1 Legumain activity

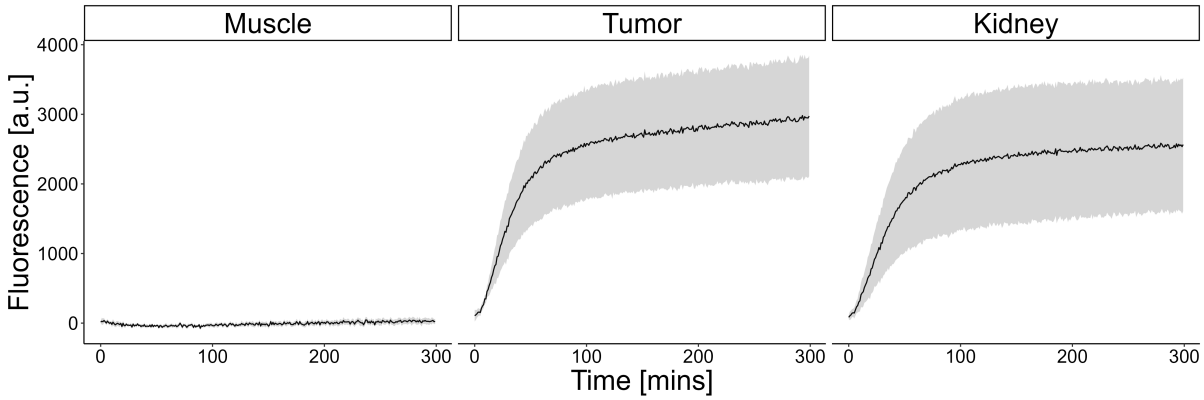

Figure 2.11: Conversion rate of the non-fluorescent substrate to the fluorescent product in total tissue lysate of dissected tissues from CT26 tumor-bearing mice ($n = 4$ mice, 1 sample each; tissues as indicated). Solid line, mean values; error bands, SD. a.u., arbitrary units.

2.6.2 Fluorescence microscopy

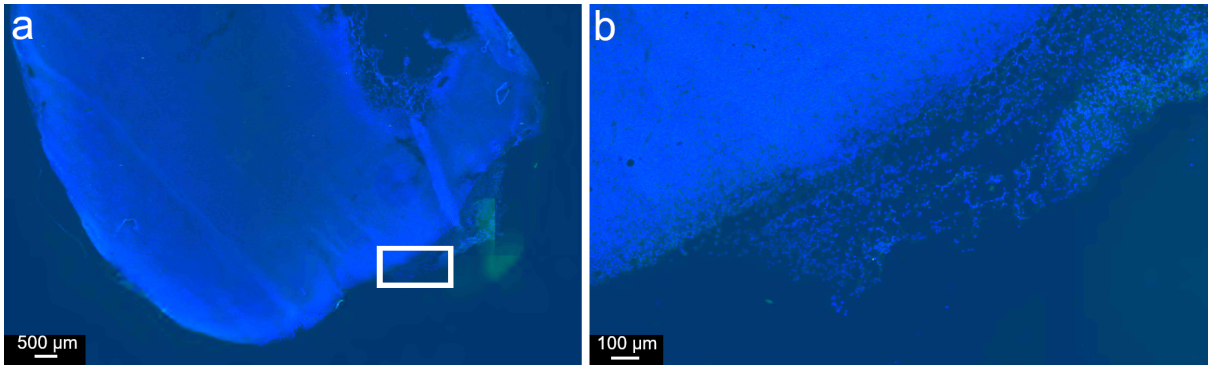

Figure 2.12: Representative fluorescence microscopy images of a CT26 tumor tissue slice. Cryosection stained with Alexa Fluor 488 IgG secondary antibody (green) and DAPI (blue; nuclei). **a** Complete section for overview. **b** Magnification of tumor periphery, corresponding to the white frame in **a**.

2.6.3 Flow cytometry

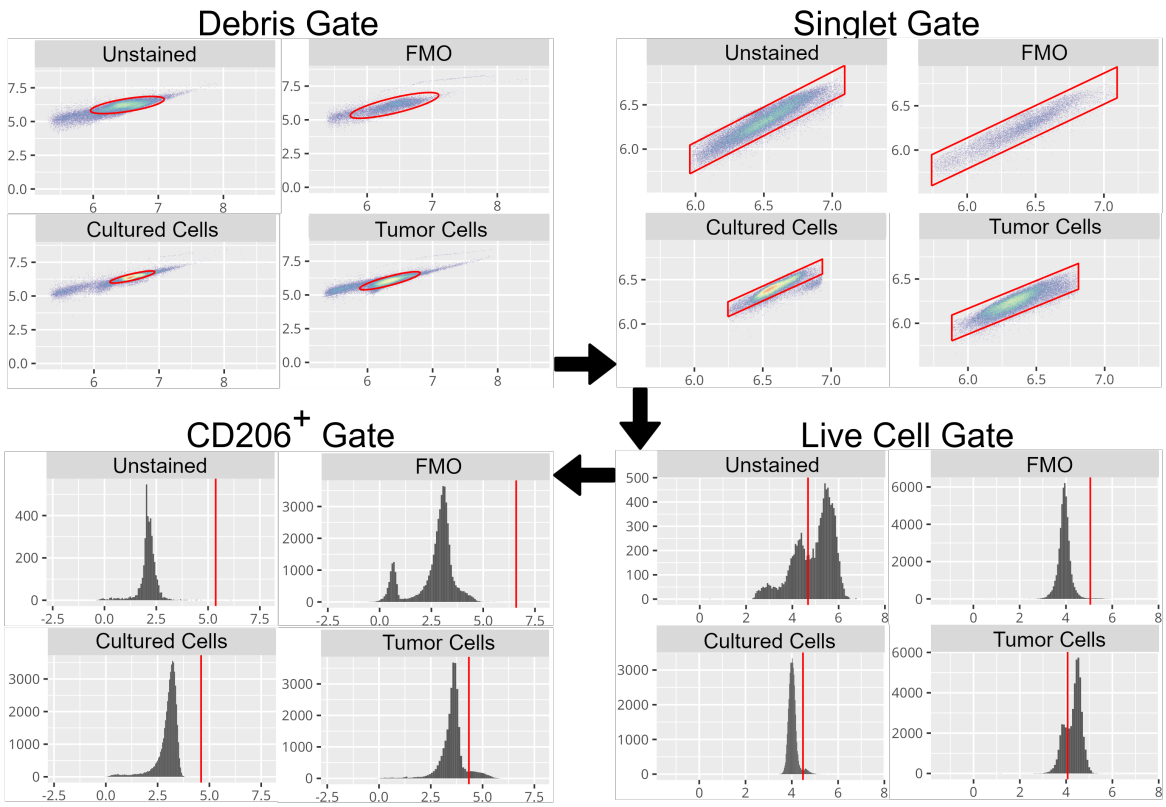

Figure 2.13: Flow cytometry gating strategy of CT26 cells isolated from dissected tumors or cultured *in vitro*. Unstained, unstained CT26 tumor cells exhibit no fluorescent dye labeling; FMO, CT26 tumor cells stained solely with a viability dye; Tumor Cells, CT26 tumor cells stained with both a viability dye and anti-CD206 antibody; Cultured Cells, cultured CT26 cells stained with both a viability dye and anti-CD206 antibody. Debris Gate, based on k-means clustering of data points in channels FSC-A vs. SSC-A, data points within the red circle are identified as cells. Singlet Gate, based on linear correlation of data points in channels FSC-A vs. FSC-H, cells within the red parallelogram are identified as individual, single cells. Live Cell Gate, based on minimum between two Zombie Aqua channel intensity histogram maxima, single cells to the left of red separating line are identified as viable. $CD206^+$ Gate, based on minimum between two CD206 channel intensity histogram maxima, viable cells to the right of red separating line are classified as M2 macrophages.

2.6.4 RP HPLC chromatograms

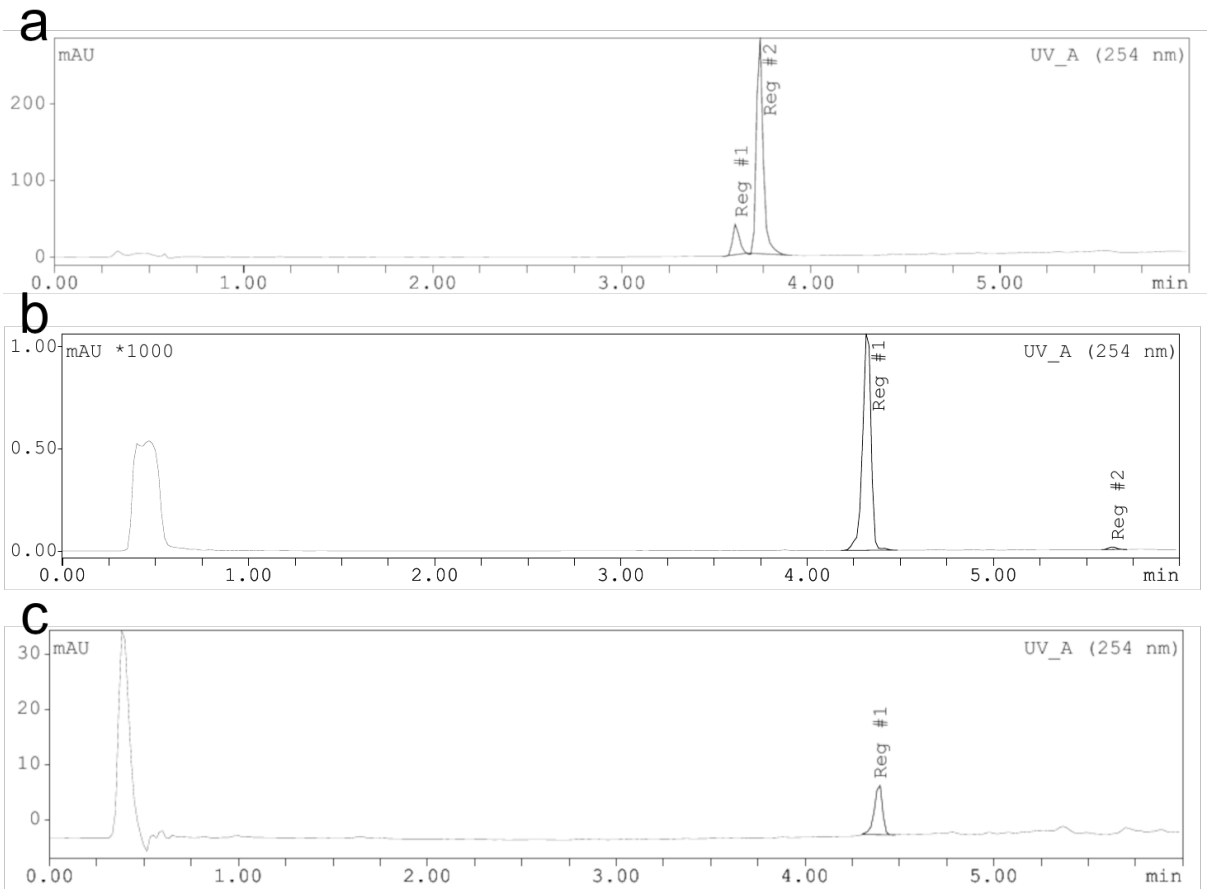

Figure 2.14: Reverse phase HPLC chromatograms for purity and identity of **1** and **1** precursor. UV signal measured at 254 nm. Retention time and % of total integrated area were determined. **a**, **1** precursor, Reg 1: 3.62 min (11.97 %), Reg 2: 3.73 min (88.03 %). **b**, **1** reference, Reg 1: 4.32 min (98.91 %), Reg 2: 5.65 min (1.09 %). **c**, [^{11}C]**1**, Reg 1: 4.38 min (100 %).

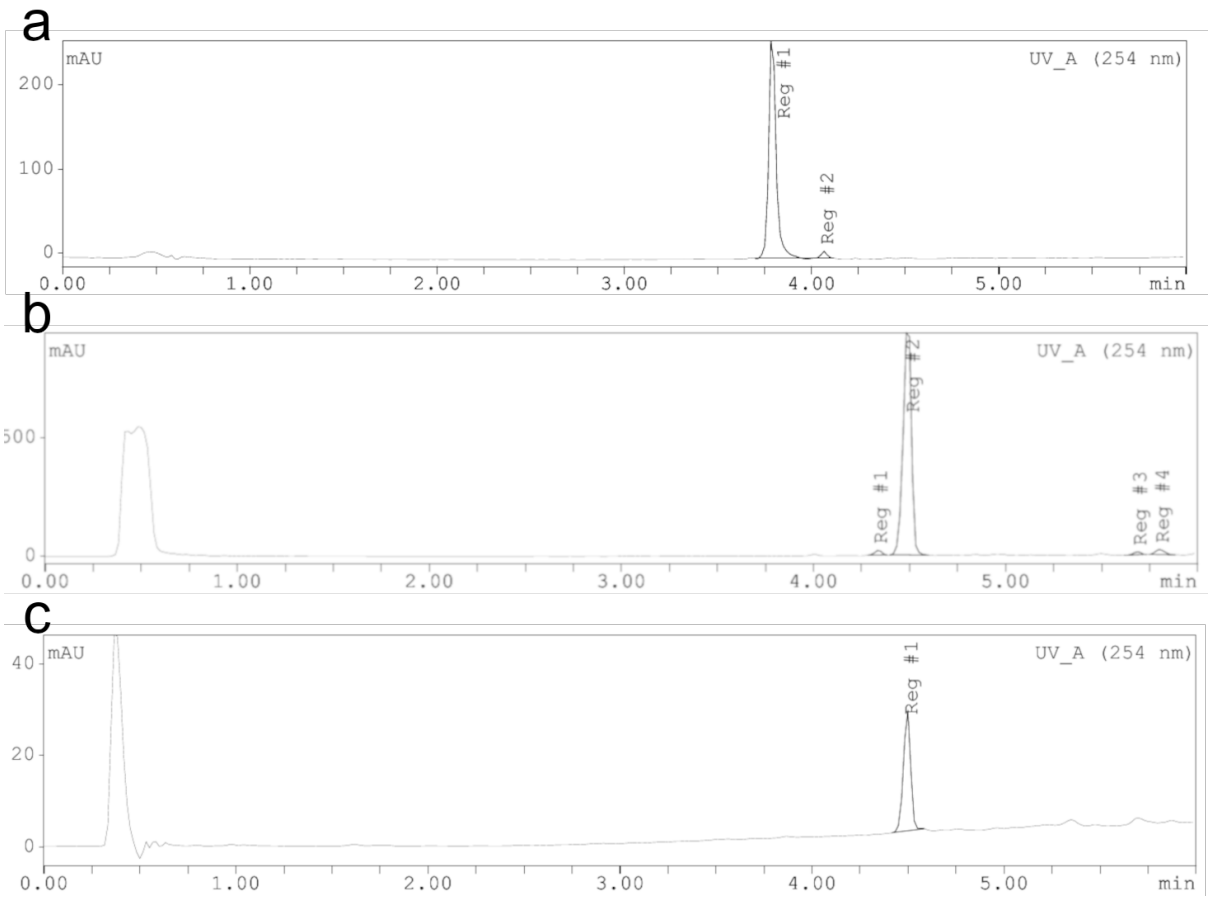

Figure 2.15: Reverse phase HPLC chromatograms for purity and identity of **2** and **2** precursor. UV signal measured at 254 nm. Retention time and % of total integrated area were determined. **a**, **2** precursor, Reg 1: 3.80 min (97.85 %), Reg 2: 4.07 min (2.15 %). **b**, **2** reference, Reg 1: 4.33 min (1.59 %), Reg 2: 4.48 min (95.23 %), Reg 3: 5.68 min (1.00 %), Reg 4: 5.80 min (2.18 %). **c**, [^{11}C]**2**, Reg 1: 4.50 min (100 %).

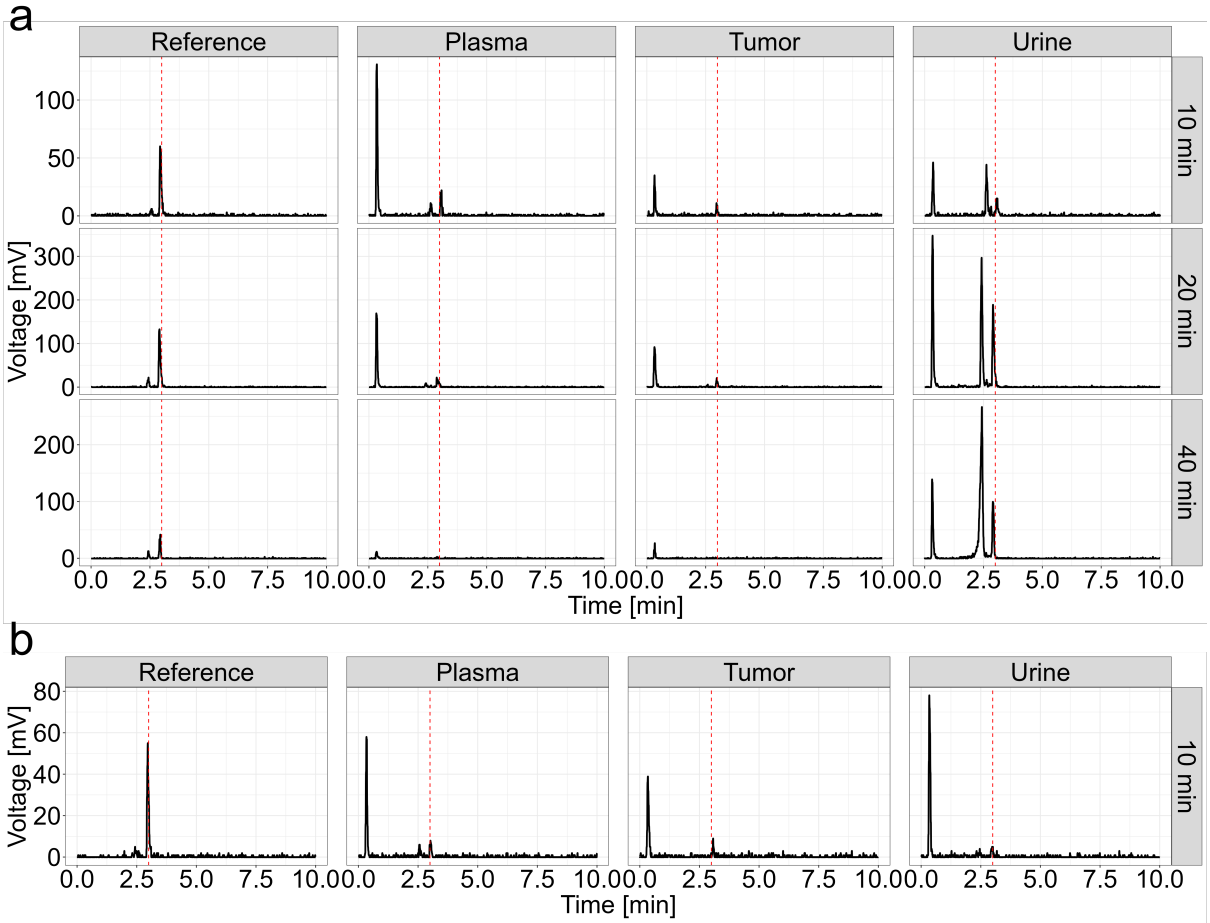

Figure 2.16: *In vivo* metabolism study with **a** [^{11}C]**1** and **b** [^{11}C]**2** in CT26 tumor-bearing BALB/c mice. Reverse phase radio-UPLC analysis of tissue homogenate samples 10-40 min p.i. (as indicated) of tracer. Proteins were precipitated before analysis. The experiment was performed once for each timepoint compound combination. Reference, tracer in formulated solution for intravenous injection (5 % EtOH in saline) kept at room temperature for the indicated duration. Dashed line indicates parent compound peak.

2.6.5 Identity ^{13}C / ^{1}H NMR, HRMS

N-[(1S)-3-amino-1-cyano-3-oxopropyl]-3-[4-(4-hydroxyphenyl)phenyl]sulfonyl-2,2-dimethylpropanamide
^{13}C NMR (101 MHz, $(CD_3)_2CO$) δ[ppm] 175.25, 171.46, 159.18, 146.82, 140.47, 131.10, 129.48, 129.09, 127.64, 119.30, 116.87, 64.82, 42.48, 38.69, 37.66, 25.96, 24.96.
HRMS (ESI^+, m/z) calc. for $C_{21}H_{23}N_3Na_1O_5S_1$ 452.1251 (M + Na) found 452.1248.

N-[(1S)-3-amino-1-cyano-3-oxopropyl]-3-[4-(4-methoxyphenyl)phenyl]sulfonyl-2,2-dimethylpropanamide
^{13}C NMR (101 MHz, $(CD_3)_2CO$) δ[ppm] 175.25, 161.35, 146.53, 140.72, 132.16, 129.40, 129.13, 127.84, 119.30, 115.42, 64.84, 55.74, 42.49, 38.69, 37.68, 25.97, 24.98.
HRMS (ESI^+, m/z) calc. for $C_{22}H_{26}N_3O_5S_1$ 444.1588 (M + H) found 444.1590.

(2S)-N-[(1S)-3-amino-1-cyano-3-oxopropyl]-1-[4-(4-hydroxyphenyl)phenyl]sulfonylpyrrolidine-2-carboxamide
^{13}C NMR (101 MHz, $(CD_3)_2CO$) δ[ppm] 172.03, 170.77, 159.19, 146.45, 135.37, 130.99, 129.41, 129.33, 127.71, 119.24, 116.89, 63.17, 50.29, 38.18, 35.61, 31.38, 25.01.
HRMS (ESI^+, m/z) calc. for $C_{21}H_{23}N_4O_5S_1$ 443.1384 (M + H) found 443.1387.

(2S)-N-[(1S)-3-amino-1-cyano-3-oxopropyl]-1-[4-(4-methoxyphenyl)phenyl]sulfonylpyrrolidine-2-carboxamide
^{1}H NMR (500 MHz, $(CD_3)_2CO$) δ[ppm] 8.38 (d, J = 8.9 Hz, 1H), 7.98-7.94 (m, 2H), 7.91-7.87 (m, 2H), 7.75-7.70 (m, 2H), 7.10-7.06 (m, 2H), 5.22 (dd, J = 14.6, 6.6 Hz, 1H), 4.18 (dd, J = 8.7 Hz, 3.4 Hz, 1H), 3.87 (s, 3H), 3.54-3.49 (m, 1H), 3.32-3.26 (m, 1H), 2.91 (dd, J = 6.4, 2.6 Hz, 2 H), 2.00-1.94 (m, 1H), 1.79-1.89 (m, 1H), 1.70-1.68 (m, 1H), 1.70-1.61 (m, 1H).
HRMS (ESI^+, m/z) calc. for $C_{22}H_{25}N_4O_5S_1$ 457.1540 (M + H) found 457.1536.

2.6.6 PET scans

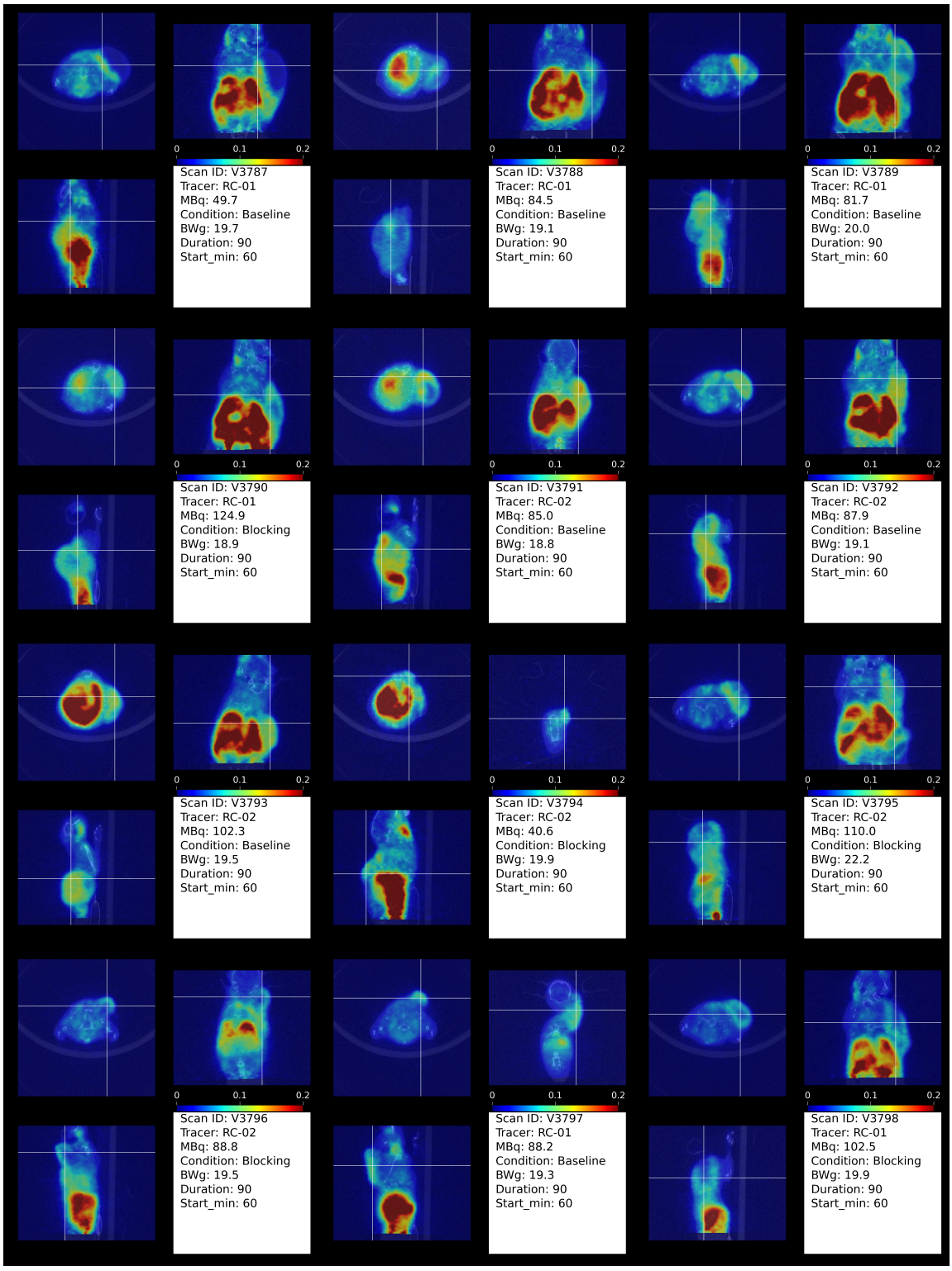

Figure 2.17: Mouse PET images (60-150 min p.i., averaged) superimposed on CT (axial, coronal, sagittal). CT26 tumors on right shoulder. Baseline condition, mouse injected with [^{11}C]**1** or [^{11}C]**2**. Blocking condition, tracer co-injected with 4.2 µmol/kg of the respective unlabeled compound. Crosshairs indicate image planes (in tumor region). PET, color bar for the corresponding SUV. CT, gray scale. MBq, activity at injection in MBq; BWg, body weight in g; Duration, duration of the scan in min; Start_min, start of the scan after injection in min; The TACs of tumor, muscle and liver are shown in Figures 2.7 and 2.8.

Chapter 3

Optimizing ^{11}C-labeled P1-Asn peptidomimetic PET tracers carrying a cyano-warhead to target legumain in the tumor microenvironment

Author Statement

Severin K. Lustenberger: Conceptualization, Methodology (performed all experiments except ^{1}H NMR acquisition and PET scans), Analysis (performed all data analysis), Writing (wrote first draft and corrected version), Project administration; **Björn Bartels**: Supervision, Materials/Data (precursor, reference compound, transfected HEK293 cells, ^{1}H NMR data), Methodology (supported experimental planning), Analysis (supported data analysis), Writing (review), Conceptualization (development of legumain inhibitor); **Makar Pobiyakho**: Methodology (supported experiments); **Roger Schibli**: Supervision, Providing infrastructure, Writing (review); **Claudia A. Castro Jaramillo**: Funding acquisition; **Luca Gobbi**: Supervision, Materials/Data (precursor, reference compound, transfected HEK293 cells, ^{1}H NMR data), Methodology (supported experimental planning), Analysis (supported data analysis), Writing (review), Conceptualization (development of legumain inhibitor); **Linjing Mu**: Supervision, Funding acquisition, Methodology (supported experimental planning), Analysis (supported data analysis), Writing (review), Project administration; **Stefanie D. Krämer**: Supervision, Funding acquisition, Methodology (supported experimental planning), Analysis (supported data analysis), Writing (review), Project administration

Funding: This work was funded by the Swiss Cancer Research foundation, KFS-4900-08-2019

3.1 Background

Legumain, a lysosomal cysteine endopeptidase, is overexpressed in various solid cancer types, and its expression correlates with tissue invasion and metastasis [60, 134, 144, 182, 201, 203]. Tumor-associated macrophages (TAMs) of the pro-tumorigenic M2 phenotype express legumain at high levels in human tumor tissue and human cell xenografts [147, 179]. Similarly, primary and metastatic 4T1 mouse breast cancers are infiltrated by legumain-expressing M2 TAMs [116]. A causal role of legumain in cancer progression is implicated by several findings. For instance, the inhibition of M2 TAMs by legumain-activated prodrugs led to tumor ablation in 4T1-tumor-bearing mice [116]. In another *in vivo* study, specifically inhibiting legumain in TAM-dependent diffuse large B cell lymphomas in human xenografted mice dampened tumor growth [179]. To monitor legumain levels *in vivo*, several PET tracers have been explored [80, 118, 119, 159]. These PET tracers rely on lysosomal targeting and subsequent intramolecular condensation triggered by legumain cleavage, leading to lysosomal trapping. Legumain is expressed in its zymogen form and undergoes activation through multiple steps at an acidic pH [35]. Its protease function, which contributes to tumor progression, is only exhibited by its active form. Consequently, PET tracers targeting legumain in its active form provide information on the invasiveness and progression potential of a cancer lesion. Although established tracers are specific for activated legumain, their detection capabilities are limited to the intra-lysosomal space. However, in cancer legumain relocalizes peri- and intracellularly to the extracellular space, the cellular surface and the nucleus [60, 72, 115]. Considering the pivotal role of non-lysosomal legumain, tracers that allow the detection of active legumain independent of its localization may be preferable.

To detect activated legumain irrespective of its localization, we develop legumain-targeting PET tracers that interact with the active site Cys-189 leading to the formation of a covalent bond. In our previous study, we established the P1-Asn peptidomimetic legumain PET tracers [^{11}C]**1** and [^{11}C]**2** (Figure 3.1) [120]. Those tracers were readily synthesized with high radiochemical purity and molar activity and accumulated in legumain-positive tumors. However, tracer accumulation was lower than expected based on legumain activity. Both compounds were rapidly metabolized *in vivo* with high ratios of radiometabolite(s) to parent tracer. In addition, competition with an excess of reference compound did not reduce the radioactivity in the tumors, possibly as a result of the high signal from radiometabolite(s) devoid of specific binding.

In an effort to assess the use of P1-Asn peptidomimetics with extended residence time as legumain PET tracers, we have developed [^{11}C]**3**, which is based on a scaffold with improved microsomal stability and strong binding affinity to legumain (Figure 3.1) [101]. Taking into account the differences in legumain expression by M2 macrophages in tumors, we implemented three tumor models with differing M2 contribution. We inoculated immunodeficient mice with human MDA-MB-468 tumors, in which due to a lack of T cell interaction, M2 contribution is reduced compared to immunocompetent mouse tumor models [19]. We furthermore inoculated immunocompetent mice with mouse colon carcinoma (CT26) tumor cells to achieve a higher M2 macrophage participation [32]. In a third model, we administered low-dose decitabine to CT26 tumor-bearing mice, potentially elevating M2 macrophage contribution compared to the untreated CT26 tumor-bearing mice [38, 214].
We established the radiolabeling of [^{11}C]**3**, checked the metabolic stability, evaluated the

affinity to mouse and human legumain *in vitro* and explored the use for *in vivo* PET in tumor-bearing mice. To investigate whether tracer accumulation was related to M2 macrophages and activated legumain, we studied PET in the three tumor models with different M2 macrophage levels.

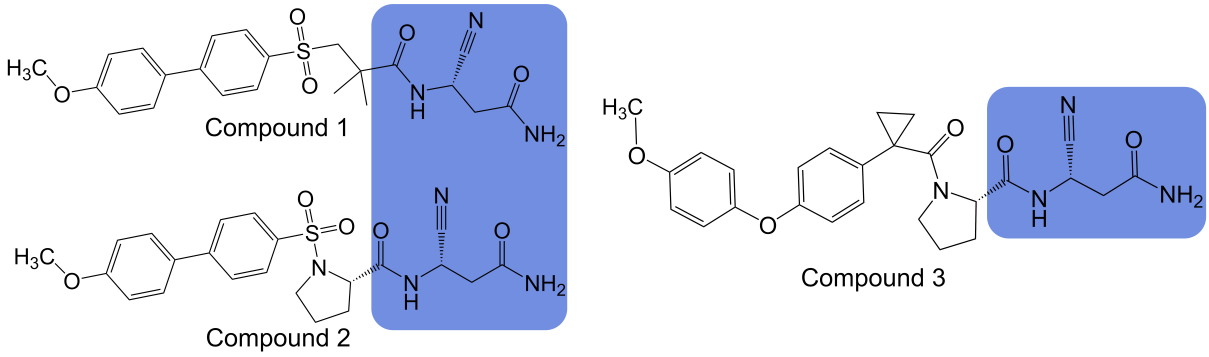

Figure 3.1: Chemical structures of legumain-targeting P1-Asn peptidomimetics **1**, **2** [120, 138] and **3**. The P1-Asn mimicking moiety is highlighted in blue.

3.2 Methods

3.2.1 Cell culture

The murine colon carcinoma cell line CT26.WT (ATCC CRL-2638) was obtained from the American Type Culture Collection. Human breast carcinoma MDA-MB-468 cells (ACC 738) were obtained from the Leibniz Institute DSMZ. CT26 cells were cultured in Roswell Park Memorial Institute (RPMI) 1640 medium with GlutaMAX-I and 25 mM HEPES (Gibco, Life Technologies, US), and MDA-MB-468 cells were cultured in Dulbecco's Modified Eagle Medium (DMEM) with GlutaMAX and high glucose (Gibco, Life Technologies, US). Both cell culture media were supplemented with 10 % fetal calf serum (FCS, Life Technologies, US), 10 000 U/ml penicillin and streptomycin (PS, Gibco, Life Technologies, US). Cells were maintained as described in [120].

3.2.2 Mouse tumor inoculation

Female BALB/c and BALB/c nude mice, obtained from Charles River Laboratories (Sulzfeld, DE), were housed at 22 °C with a 12-hour light-dark cycle and had unlimited access to food and water. At the age of 14 weeks, mice were inoculated subcutaneously in the right shoulder region with either 8 * 10^5 CT26 cells or 4 * 10^6 MDA-MB-468 cells resuspended in 100 µl matrigel (BD Biosciences, US). The studies were conducted 7-12 days post CT26 cell inoculation and 15-20 days post MDA-MB-468 cell inoculation when tumors were clearly visible but no larger than 1.76 cm^3.

3.2.3 Decitabine treatment

CT26 tumor-bearing mice were injected intraperitoneally with 1 mg/kg body weight decitabine (CAY-11166-5, Cayman, US) in 200 µl phosphate-buffered saline, pH 7.4 (PBS, Gibco, Life Technologies, US) or PBS only (vehicle control) [200]. Intraperitoneal

injections were performed on 4 consecutive days starting 3 days after CT26 cell inoculation. Animals were scanned and dissected 3-7 days after the treatment ended.

3.2.4 Gene expression analysis

CT26 and MDA-MB-468 tumor tissues were dissected and washed with RNA preserving solution (RNAlater, Thermo Fisher Scientific, US). For RNA extraction, tissue was transferred to RNA extraction solution (TRIzol, Thermo Fisher Scientific, US) and homogenized using a bead-mill system (Qiagen, DE). The homogenate was centrifuged (12 000 * g, 10 min, 4 °C) and the uppermost phase was mixed with chloroform. After centrifugation (same conditions as above), the aqueous phase was mixed with isopropanol and incubated for 10 min. The samples were centrifuged (same conditions as above) and the resulting pellet was washed with 75 % ethanol and centrifuged (8 000 * g, 5 min, 4 °C). The wash was repeated, the sample pellets were centrifuged (15 000 * g, 2 min, 4 °C) and left to dry for 1-2 h. The pellet was dissolved in RNAse-free water. Concentration and quality of the RNA extract were determined using a microvolume spectrophotometer (NanoDrop, Thermo Fisher Scientific, US). For reverse transcription, RNA extract was incubated with wipeout buffer (QuantiTect Reverse Transcription kit, Qiagen, DE) for 2 min at 42 °C. Reverse transcriptase, reverse transcription buffer and reverse transcription prime mix (QuantiTect Reverse Transcription kit, Qiagen, DE) were added and the solution was incubated for 15 min at 42 °C followed by 3 min at 95 °C. Real-time quantitative polymerase chain reaction (RT-qPCR) was performed using cDNA from previous step, gene specific primers and qPCR Master Mix (GoTaq qPCR Master Mix, Promega, US). Primers for qPCR were custom-made oligonucleotides (Microsynth, CH): mouse legumain (Lgmn, NCBI Gene: 19141), forward 5'-GTG ATC AAC CGA CCT AAC G-3', reverse 5'-ATT CTC TGG AGT CAC ATC CTC-3'; human legumain (LGMN, NCBI Gene: 5641) forward 5'ATA ATT ATA GGC ACC AGG CAG-3', reverse 5'-CAAC GAT CTG TTC GTC AGG-3'; mouse cytochrome c1 (Cyc1, NCBI Gene: 66445), forward 5'-TAG CTA AGG ATG TCG CCA C-3', reverse 5'-TCA ACA ACA TCT TGA GAC CCA-3'; human cytochrome c1 (CYC1, NCBI Gene: 1537), forward 5'-TCT CTT CCT TGG ACC ACA C-3', reverse 5'-GTC TTG AAC CTC CAC CTC C-3'; ATP synthase beta chain (Atp5b, NCBI Gene: 8617357) forward 5'-GGT TCA TCC TGC CAG AGA CTA-3', reverse 5'-AAT CCC TCA TCG AAC TGG ACG-3'. On a real-time PCR system (Quantstudio 7 Flex, Thermo Fisher Scientific, US), 10 µl of total volume were run through 40 cycles with hold stage temperature at 95 °C for 2 min and a PCR stage consisting of 95 °C for 15 s (denaturation) and 60 °C for 60 s (annealing/extension). Melt curve stage was included for quality control on a single well level. Normalization of Legumain to Cytochrome C1 or both ATP synthase beta chain and Cytochrome C1 was performed. To calculate the standard deviation for each ratio error propagation according to Equation 3.1 was applied. Data processing was performed in R (R-project) using open-source packages [160, 209].

$$\sigma_R = \frac{\mu_A}{\mu_B}\sqrt{(\frac{\sigma_A}{\mu_A})^2 + (\frac{\sigma_B}{\mu_B})^2} \tag{3.1}$$

3.2.5 Legumain activity and estimation of binding potential

Inhibition of legumain in mouse tissue

Tissues were dissected and washed with assay buffer consisting of 20 mM citric acid, 60 mM Na_2HPO_4, 1 mM EDTA, 0.1 % (m/v) CHAPS, 4 mM DTT at pH 5.8. Tissue was homogenized using a Polytron (Kinematica, US), and centrifuged at 19 000 * g, 4 °C for 20 min to precipitate debris. Protein content of the lysate was determined using the BCA assay, with bovine serum albumin for calibration [104]. Legumain activity was measured with a fluorescence assay [87]. In brief, samples of tissue lysate with total protein concentrations ranging from 3.06 to 15.69 mg/ml were prepared. The substrate Z-Ala-Ala-Asn-AMC (Bachem, CH) was added to the samples and the fluorescence was measured at excitation 340 nm and emission 460 nm every minute over 5 h. To calculate the percentage inhibition, the slope of the initial linear increase in fluorescence was determined and normalized from 0 to 100 % based on the highest fluorescence value for each tissue type. Percentage inhibition was then calculated as described in Equation 3.2.

$$\%\text{Inhibition} = (1 - \frac{\text{Slope}_{\text{withInhib}}}{\text{Slope}_{\text{noInhib}}}) * 100 \tag{3.2}$$

IC_{50}

To obtain the conversion rate, the slope of the initial linear increase in fluorescence was determined and normalized to the protein content of the tissue sample.
To determine the IC_{50} and the K_i of compound **3**, a stock solution (2.10 mM in 3.3 % DMSO, 6.5 % ethanol, 90.2 % saline) was diluted with assay buffer to get to concentrations ranging 0.4 - 1 285.7 nM in the sample wells. Human and mouse recombinant legumain (R&D Systems, US) were diluted to 0.14 ng/µl assay concentration. The IC_{50} was determined based on the assay [27]. Data was normalized from 0 to 100 % based on the highest fluorescence value for each type of legumain. A linear segment of the normalized data was used to determine the slope of fluorescence vs. time. The mean of the slopes for each type of legumain-inhibitor concentration was then used to determine the IC_{50} according to the Hill equation (Equation 3.3) [75] where Response is the measured slope per inhibitor concentration, $\text{Min}_{\text{Response}}$ is the minimum response set to 0, and $\text{Max}_{\text{Response}}$ is the maximum slope determined by nonlinear regression.

$$\text{Response} = \text{Min}_{\text{Response}} + (\text{Max}_{\text{Response}} - \text{Min}_{\text{Response}}) * \frac{\text{IC}_{50}}{\text{IC}_{50} + \text{Concentration}_{\text{Inhibitor}}} \tag{3.3}$$

B_{max} and BP

The density of legumain, corresponding to the maximal possible specific binding of legumain-targeting tracer per mg protein in the tissue (B_{max} in nmol/mg) was estimated based on the measured legumain activity in comparison to recombinant mouse legumain of known concentration (R&D Systems, US). To estimate the expected binding potential (BP) of a tracer in the tissue with Equation 3.4, B_{max} (nmol/mg) was transformed to B_{max} in nmol per 1 000 cm^3 tissue (nM), assuming a protein content of mouse tissue of 0.23 g/cm^3 [188], i.e., B_{max} in nmol/mg was multiplied by 2.3 * 10^5 mg/l to get B_{max} in nM.

$$\mathrm{BP} = \frac{B_{\max}(\mathrm{nM})}{K_{\mathrm{i}}(\mathrm{nM})} \tag{3.4}$$

K_{i} in Equation 3.4 was estimated from the IC_{50} of the inhibitor, the substrate concentration at which IC_{50} was determined, and the K_{M} reported for human legumain, i.e., 25.7 µM [153] according to the Cheng-Prusoff equation (Equation 3.5).

$$K_{\mathrm{i}} = \frac{\mathrm{IC}_{50}}{1 + \frac{[S]}{K_{\mathrm{M}}}} \tag{3.5}$$

All data processing was performed in R using open-source packages [209].

3.2.6 Radiochemistry

Generation of [^{11}C]CH_3OTf

Proton bombardment of a target filled with N_2 fortified with 0.5 % O_2 in a Cyclone 18/9 cyclotron (18-MeV, IBA, BE) afforded [^{11}C]CO_2 by $^{14}N(p, \alpha)^{11}C$ nuclear reaction. For the conversion to [^{11}C]CH_3I, nickel-based catalytic reduction of [^{11}C]CO_2 with hydrogen was performed to form [^{11}C]CH_4, which was followed by iodination to afford [^{11}C]CH_3I. [^{11}C]CH_3I was further converted to [^{11}C]CH_3OTf by passing through a silver triflate column at elevated temperatures (190 °C).

Radiosynthesis

Approx. 1 mg precursor was dissolved in 500 µl acetone containing 3 µl 5 M NaOH. The generated [^{11}C]CH_3OTf was bubbled into the solution with constant stirring followed by incubation for 3 min at 70 °C. The reaction was quenched with 1.8 ml water and the crude solution was injected into a semi-preparative HPLC column (Symmetry C18 Prep Column 5 µm 7.8 * 50 mm, Waters, US). A solvent gradient of 80-20 % phosphoric acid (0.1 % (v/v) in water) and 20-80 % acetonitrile over 10 min was applied. The flow rate was 4 ml/min. The product was collected with the help of a UV detector and a radio detector (Gabi Star, Elysia-Raytest, DE), diluted with water (8 ml) and purified using an activated (5 ml ethanol, 10 ml water) C18 cartridge (Sep-Pak C18 light, Waters, US). The cartridge was washed with 5 ml water and the product was eluted with 0.5 ml ethanol into a sterile vial. 9.5 ml saline solution (NaCl 0.9 %, B.Braun, DE) was added to obtain an isotonic product containing 5 % ethanol. Nitrogen was used as a propellant. For quality control, HPLC was performed with 50 µl of the solution injected into a reverse phase HPLC column (ACE 3 C18 3 µm 50 * 4.6 mm, ACE, UK). A solvent gradient was applied with A (0.1 % phosphoric acid in water/acetonitrile 95/5) and B (water/acetonitrile 5/95) from A/B 80/20 to 10/90 over 10 min. The flow rate was 1.2 ml/min. The molar activity was determined based on linear regression with reference compound measured with a UV detector (Gabi Star, Elysia-Raytest, DE) at 254 nm wavelength.

3.2.7 *In vivo* stability of [^{11}C]3

Tracer (52.7 MBq, 24.1 nmol/kg for 10 min time point and 65.0 MBq, 7.8 nmol/kg for 45 min time point) was injected via lateral tail vein in CT26 tumor-bearing BALB/c

mice. Animals were euthanized by decapitation under anesthesia by 2-3 % isoflurane in oxygen/air (1/1) and tissues were dissected. Blood was collected, plasma was separated for analysis, by centrifugation at 5 000 * g for 3 min. Tissue samples were homogenized in matching volumes of PBS using a Polytron (Kinematica, US), and centrifuged at 5 000 * g, 4 °C for 5 min. In plasma, urine and tissue samples, proteins were precipitated with 2/3 volumes of ammonium sulfate in water (3M) and removed by centrifugation at 5 000 * g, 4 °C for 5 min. Supernatants were filtered through 0.45 µm pore size filters and analyzed by column-switch radio HPLC according to the description in the literature [76]. A reverse phase HPLC column (Luna 5u C18, 5 µm 4.6 * 250 mm, Phenomenex, US) was used. The mobile phase was phosphoric acid (0.1 % (v/v) in water)/acetonitrile 50:50 over 15 min.

3.2.8 *In vitro* autoradiography

Dissected tissues and pellets from harvested cells were embedded in OCT compound mounting medium (Avantor, US), cut to 20 µm slices with a cryotome, thaw-mounted on microscopy slides and stored at -80 °C. Slices were thawed and submerged in MES buffer (0.5 M, pH 5.5) containing 1 % (v/v) FCS for 2 h, followed by MES or MES with the addition of reference compound (cold tracer, 4 µM) for 15 min. After this pre-conditioning, the slices were incubated for 30 min with 4 nM [^{11}C]tracer in MES (baseline conditions) or in MES containing reference compound (cold tracer, 4 µM; blocking conditions). Tissues were washed in MES (3 * 5 min) and in water (1 * 5 sec) and left to dry. The slices were exposed to a photostimulable phosphor plate for 45-60 min and images were acquired using a phosphoimager (BAS-5000, Fujifilm, JP). Images were cropped to rectangles including tissue and background. For quantification, mean (tissues) or sum (cell pellets) of slice activity based on gray-scale images (Figures 3.14 and 3.15) was calculated. To calculate the standard deviation for each ratio error propagation according to Equation 3.1 was applied. Image processing was done with open-source imaging software [173], python community modules [69, 125, 199] and R open-source packages [209].

3.2.9 PET/CT Scans

Tumor-bearing mice were anesthetized with 2-3 % isoflurane in oxygen/air (1/1) 10 min prior to PET acquisition. PET/CT scans were performed on a small animal PET/CT scanner (Super Argus, Sedecal, ES) with an axial field of view of 4.8 cm and a spatial resolution of 1.6-1.7 mm (full width at half maximum) [61]. Respiratory rate was kept at $\sim$60 min^{-1} through adjustment of isoflurane concentration and body temperature at 37 °C using heated air throughout the scan. PET scan was started and tracer was injected 1 min after scan start. PET data were acquired in list mode for dynamic analysis 0-60 min p.i.. Anatomical information was obtained by CT following each PET acquisition. PET data were reconstructed with 2D ordered-subsets expectation maximization (2D-OSEM) protocol by applying random scatter correction and decay correction but no correction for attenuation, and analyzed with PMOD v4.2 software (PMOD Technologies Ltd., Zurich, Switzerland). Volumes of interest for the tumor, kidney and reference region (muscle) on the contralateral side of the tumor were drawn manually in PMOD on the basis of the PET and CT images. SUVs were calculated as the ratio of regional averaged radioactivity in Becquerel per cubic centimeter and radioactivity at injection in Becquerel per gram body weight. For ratios that were obtained based on two samples from the same animal, the standard deviation was calculated directly from ratios. For ratio calculations where tissues

from different animals had to be used to calculate individual ratios, error propagation according to Equation 3.1 was applied to obtain standard deviation. Image analysis was performed in python using community modules [15, 69, 82, 117, 125, 212] and R open-source packages [209]. All radioactivity was decay-corrected to the time point of injection to the animal.

3.2.10 Biodistribution after dissection

Following PET and CT acquisition, tumor-bearing mice were euthanized through decapitation still under anesthesia. Tissues were dissected and radioactivity determined with a gamma counter (Wizard 3", PerkinElmer, US). Data analysis was performed in R using open-source packages [209].

3.2.11 Statistical analysis

Statistical differences in radiotracer uptake or SUV ratios were analyzed by two-tailed paired or unpaired Student's t test, as indicated. Differences with $p < 0.05$ were considered significant. Average values are shown with standard deviations or data range for $n < 3$.

3.3 Results

3.3.1 Legumain inhibition by compound 3

Inhibition of legumain in mouse tissue

We first investigated the inhibitory potential of compound **3** at a concentration of 1000 nM in tissue lysates with high legumain expression and recombinant human legumain. The total lysates of CT26 tumors and kidneys from CT26 tumor-bearing mice ($n = 4$ mice, 1 sample each), as recently described ([120]) showed a legumain inhibition of 84.78 % ± 5.04 % in tumor tissue lysate and 84.53 % ± 5.49 % in kidney tissue lysate. Human recombinant legumain ($n = 1$) was inhibited 81.93 % (Figure 3.2).

IC_{50} of compound 3

The IC_{50} of compound **3** was determined with human and mouse recombinant legumain and 10 µM fluorigenic legumain substrate Z-Ala-Ala-Asn-AMC. IC_{50} were 24.4 ± 1.7 nM and 40.3 nM ± 6.9 nM, respectively (Figure 3.3). The calculated K_i of compound **3** based on Equation 3.5 were 18.2 ± 1.3 nM with human and 30.2 ± 5.1 nM with mouse recombinant legumain.

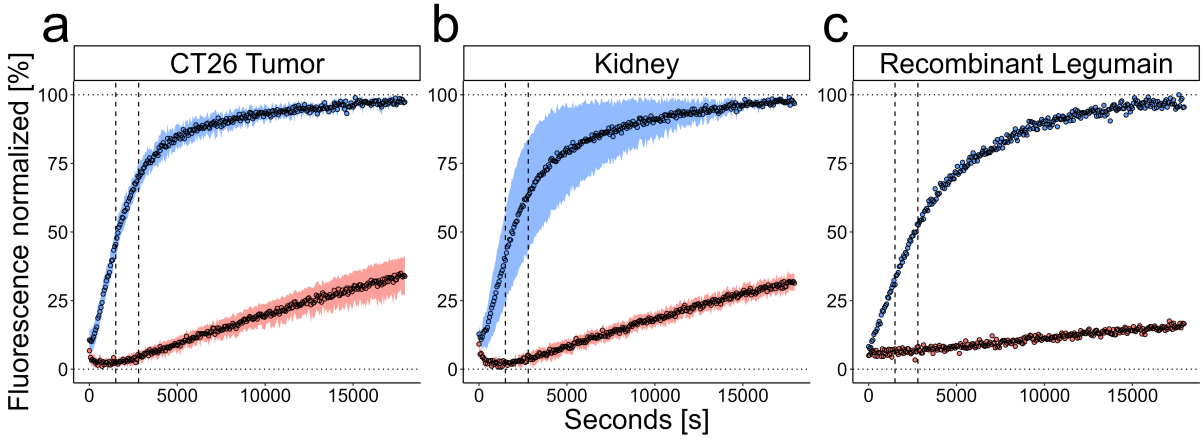

Figure 3.2: Inhibition of legumain activity was measured using the fluorescence of a fluorogenic legumain substrate (10 µM) in mouse CT26 tumor tissue (**a**), mouse kidney tissue (**b**) and human recombinant legumain (**c**). Legumain activity was measured in tissues ($n = 4$) and human recombinant legumain ($n = 1$) in the presence (red) or absence (blue) of 1000 nM compound **3**. Symbols, mean data points; ribbons, SD; horizonal dotted lines, 0 and 100 % activity relative to maximum value. Slopes to calculate legumain activity were determined between the two vertical dashed lines.

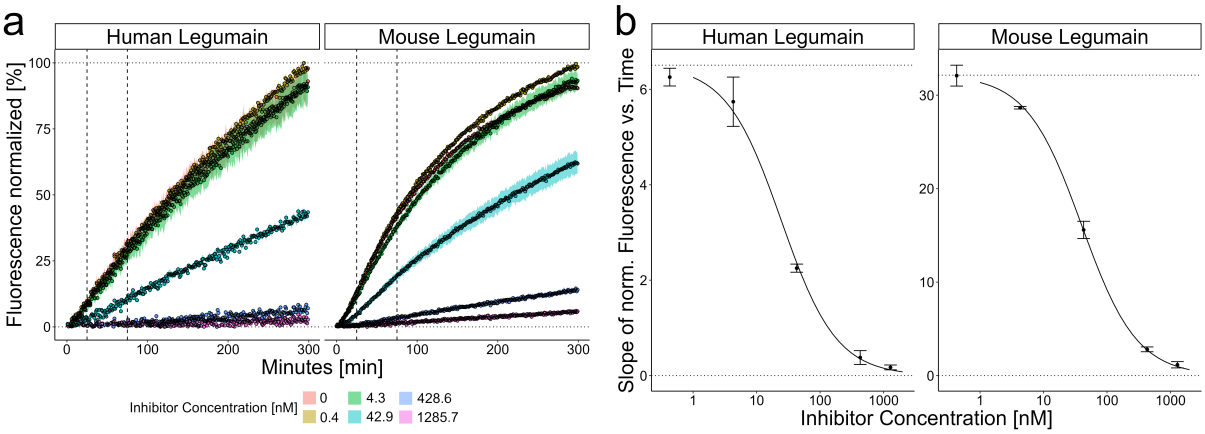

Figure 3.3: IC_{50} of compound **3** toward human and mouse legumain. **a** Legumain activity of recombinant human and mouse legumain was measured as the increase in fluorescence of a fluorogenic legumain substrate (10 µM) over time. Colors represent inhibitor concentrations as indicated in the Figure ($n = 3$ independent experiments). Symbols, mean of data; ribbons, SD of data. Dotted lines, 0 and 100 % activity relative to maximum value. Slopes to calculate legumain activity were determined between the two vertical dashed lines. **b** IC_{50} plots based on **a**. Symbols, mean of slopes ($n = 3$); error bars, SD of slopes. Dotted lines, minimum and maximum slope based on non-linear fitting; solid lines, fit functions (Equation 3.3). Note that 0 nM is not covered by the logarithmic range of the x-axis.

3.3.2 Radiochemistry

The reaction scheme for the synthesis of [^{11}C]**3** is shown in Figure 3.4. The molar activity ranged from 44.0 to 920.7 GBq/µmol and the radiochemical purity was above 95 % for

each production (Figure 3.13).

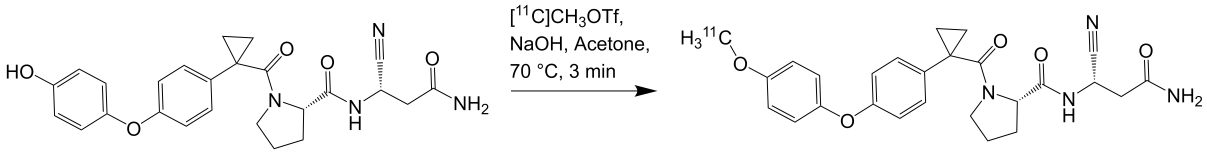

Figure 3.4: Synthesis of [^{11}C]**3**.

3.3.3 *In vivo* stability of compound [^{11}C]3

Our recently investigated legumain-targeting PET tracers, [^{11}C]**1** and [^{11}C]**2**, were rapidly metabolized *in vivo* with higher levels of a polar radiometabolite than parent tracer already 10 min post injection (p.i.). As shown in Figure 3.5, [^{11}C]**3** was more stable *in vivo* than [^{11}C]**1** and [^{11}C]**2** [120], with higher levels of parent tracer than radiometabolites 10 min p.i.. At 45 min p.i., [^{11}C]**3** was still detectable in plasma. No unbound tracer was detectable in tumor homogenate 10 or 45 min p.i..

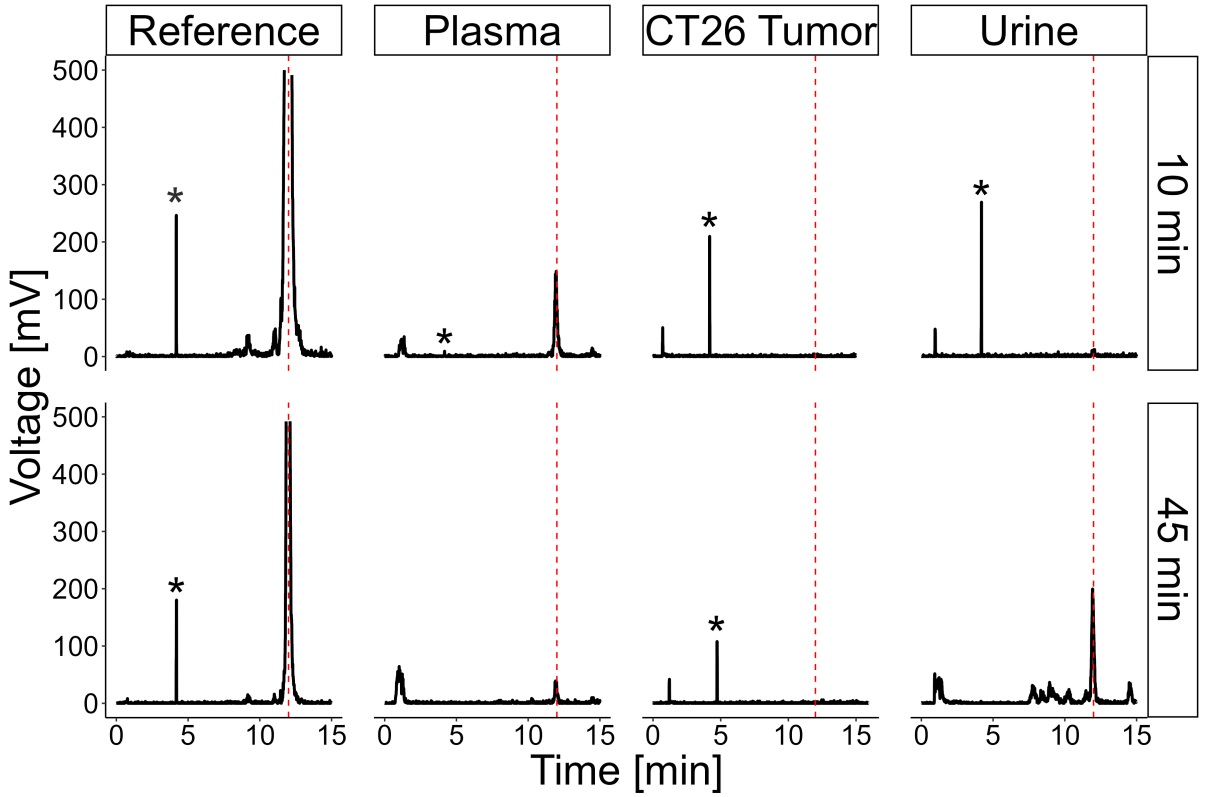

Figure 3.5: *In vivo* metabolism study with [^{11}C]**3** in CT26-tumor bearing BALB/c mice. Reverse phase, column-switch radio HPLC analysis of tissue homogenate samples at 10 and 45 min p.i. of [^{11}C]**3**, as indicated. Proteins were precipitated before analysis. The experiment was performed once for each time point. Reference, tracer in formulated solution for intravenous injection (5 % EtOH in saline) kept at room temperature for the indicated duration. Dashed line, retention time of [^{11}C]**3**; asterisk, method artifact peak.

3.3.4 *In vitro* autoradiography with compound [^{11}C]3

To characterize the binding of compound [^{11}C]**3** to legumain, irrespective of tissue-specific factors, we conducted *in vitro* autoradiography on legumain-overexpressing HEK 293 cell pellets. Pellet slices were incubated with 4.0 nM [^{11}C]**3** (baseline condition, $n = 3$), and co-incubated with 4 µM unlabeled compound **3** (blocking condition, $n = 3$). Images and quantification results are shown in Figure 3.6. To account for folding of the pellet slices, we used the sum of activity of the tissue slice area (Figure 3.14) for quantification. Blocking conditions reduced the binding of [^{11}C]**3** by 29 ± 13 % ($p = 0.030$) compared to baseline conditions. Preincubation of cell pellets under acidic conditions to further activate legumain did not have an effect both under baseline and blocking conditions (data not shown). To investigate the binding of compound **3** in tissue, specifically, we performed *in vitro* autoradiography using CT26 tumor, kidney, muscle and spleen slices (4 slices each from 2 mice). Baseline and blocking conditions, identical to the ones used for cell pellet autoradiography, were compared (Figure 3.7). Because there was less slice-folding and slice areas varied across tissues, tissue slice area mean activities were used for quantification (Figure 3.15). In the tissue autoradiography experiments, the total activity in organ tissues correlated well with legumain expression based on the literature, with the highest expression in the kidney, followed by spleen and lower expression in the muscle [27]. Under blocking conditions, a 10 ± 8 % ($p = 0.024$) reduction in activity was observed in CT26 tumor tissue relative to baseline conditions. The blocking to baseline ratios in kidney (0.97 ± 0.12), muscle (1.12 ± 0.12) and spleen (0.93 ± 0.14) were not significantly different from 1. Furthermore, the tumor slices were subject to heterogeneous activity distribution, which was conserved across slices from the same tumor.

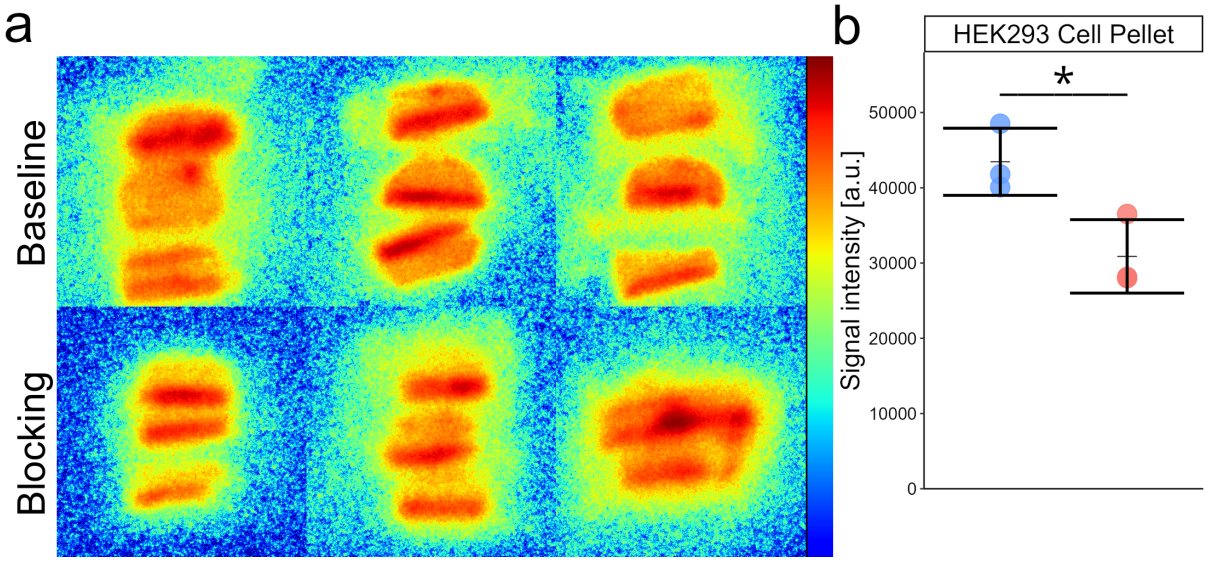

Figure 3.6: *In vitro* autoradiography with legumain overexpressing HEK 293 cell pellet slices ($n = 3$); **a** Slices incubated with 4.0 nM [^{11}C]**3** (baseline condition) and co-incubated with 4 µM unlabeled compound **3** (blocking condition), in the same experiment. Scalebar, red, high activity; blue, low activity. Note: Pellet slices were folded and partially overlapping. **b** Quantification for the slices shown in **a**. Baseline (blue) and blocking (red) conditions were compared with student's t tests. Symbols, sum of activity of tissue slice area; thin black bars, mean of sums; black error bars, SD.

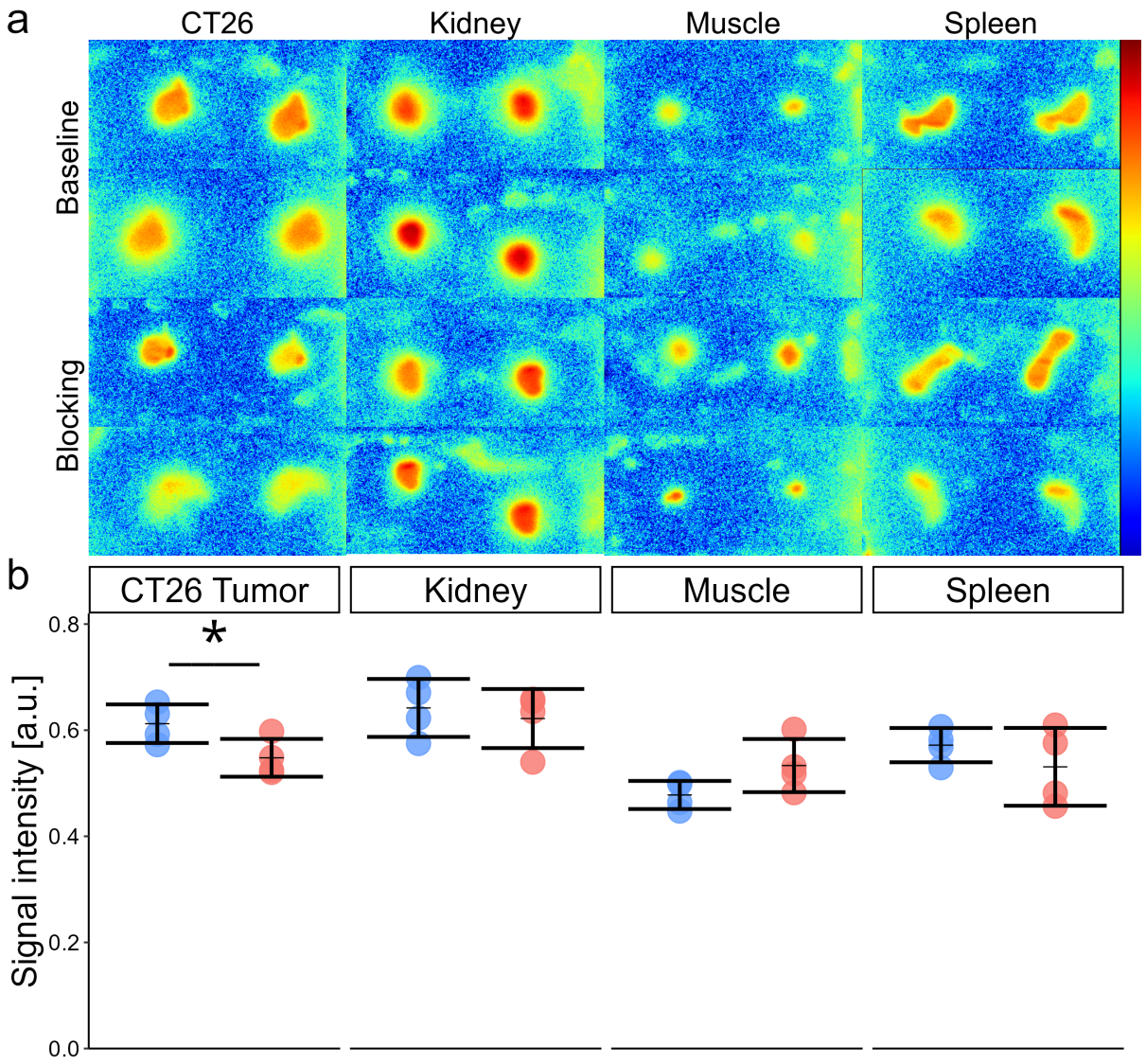

Figure 3.7: *In vitro* autoradiography with CT26 tumor, kidney, muscle and spleen slices (4 slices from 2 mice per tissue); **a** Slices incubated with 4.0 nM [^{11}C]**3** (baseline condition) and co-incubated with 4 µM unlabeled compound **3** (blocking condition), in the same experiment. Scalebar, red, high activity; blue, low activity. **b** Quantification of the slices shown in **a**. Baseline (blue) and blocking (red) conditions were compared with student's t tests, without correction for multiple comparisons. Symbols, mean activity of tissue slice area; thin black bars, mean of means; black error bars, SD. *, $p < 0.05$.

3.3.5 Legumain mRNA expression and activity

To assess legumain expression in the tumor models, we used qPCR. The comparison of cultured CT26 cells ($n = 1$) to MDA-MB-468 cells ($n = 1$) showed a 9.67-fold higher target expression in MDA-MB-468 cells (significance not tested). In the tumor tissue, the image was inverted. CT26 tumor tissue ($n = 6$) had a 7.09 ± 7.01-fold ($p = 0.031$) higher legumain expression than MDA-MB-468 tumor tissue ($n = 8$). In a separate experiment, legumain expression ratios in tissues from decitabine-treated to PBS-treated mice with 4 samples each were 1.57 ± 0.66 (not significant) in kidney tissue, 3.00 ± 2.01 ($p = 0.012$)

in CT26 tumor tissue and 1.29 ± 0.98 (not significant) in muscle tissue.

Legumain activity was compared in total lysate of dissected tissue from CT26 tumor-bearing mice treated with PBS (vehicle) or low-dose decitabine and MDA-MB-468 tumor-bearing mice. In contrast to the qPCR results, the legumain activity in CT26 tumor tissue of PBS-treated mice ($n = 2$) was 47 ± 17 % (significance not tested) lower than in MDA-MB-468 tumor tissue ($n = 2$). Between CT26 tumor tissue from PBS-treated mice ($n = 2$) and decitabine-treated mice, a ratio of 1.26 ± 0.45 was found (significance not tested).

The estimated density of active legumain ($B_{\max}$) and the theoretical, estimated binding potential (BP), both calculated from the activity assay, are shown in Table 3.1. The K_i of compound **3** experimentally determined with recombinant mouse legumain (30.2 ± 5.1 nM) was used to calculate the BP (Equation 3.4). A protein density of 0.23 g per cm^3 was assumed for the tissue.

Table 3.1: Mouse legumain density and binding capacity of compound **3** in tissue.

Tissue	**Treatment**	$B_{\max}$ **[pmol/mg]**	**BP**	**n (tissues)**
CT26 Tumor	PBS	8.54 ± 0.48	66.56 ± 12.57	2
CT26 Tumor	Decitabine	6.79 ± 2.39	52.92 ± 10.00	4
MDA-MB-468 Tumor	none	16.06 ± 5.10	125.20 ± 23.65	2
Kidney	Decitabine	24.26 ± 10.38	189.10 ± 35.71	3

3.3.6 PET with tumor-bearing mice

Influence of tumor type and blocking

Having evaluated [^{11}C]**3** *in vitro* binding and *in vivo* stability, we proceeded with PET imaging in mice. The injected activity (molar mass) of [^{11}C]**3** in CT26 tumor-bearing mice was 8.2-10.1 MBq (2.26-4.15 nmol/kg, $n = 3$ animals), 7.5-9.0 MBq (1.24-6.58 nmol/kg, $n = 3$ animals) in CT26 tumor-bearing mice co-injected with 4 µmol/kg compound **3** (blocking conditions) and 4.8-6.1 MBq (1.1-1.9 nmol/kg, $n = 3$ animals) in MBA-MB-468 tumor-bearing mice (Figure 3.8 and 3.9). The absence of co-injection with 4 µmol/kg compound **3** is referred to as baseline conditions.

All tumors were clearly visible in the PET images (Figure 3.8). In agreement with the tissue autoradiography, tracer accumulation was higher in the periphery of the CT26 tumors than in the core. Peripheral accumulation was absent in MDA-MB-468 tumors. As observed in earlier studies with P1-Asn peptidomimetic tracers, all PET scans showed high uptake in the abdomen [120]. In the PET, the SUV averaged over the duration of the scan (0-60 min) from the images looked higher in CT26 tumors compared to MDA-MB-468 tumors (Figure 3.8). The time-activity-curves (TACs) are shown in Figure 3.10. When analyzing the TACs of SUV ratio kidney-to-muscle for each animal a 8.17 ± 2.40 ($n = 15$, $p = 10^{-8}$) difference from 1 was found. The TACs ratio tumor-to-muscle was 1.27 ± 0.21 ($n = 15$, $p = 2 * 10^{-4}$). Evaluating the TACs of non-treated CT26 tumor-bearing mice ($n = 5$) in comparison to MDA-MB-468 tumor-bearing mice ($n = 3$), the SUV ratio CT26-to-MDA-MB-468 in tumors was 1.27 ± 0.30 (not significant) from 0-60 min and 1.25 ± 0.33 from 30-60 min (not significant). The SUV ratio tumor-to-muscle comparison

of baseline ($n = 10$) to blocking ($n = 5$) conditions did not show a significant difference over all time points or from 30-60 min alone. In contrast, the SUV ratio kidney-to-muscle comparison of baseline ($n = 10$) to blocking ($n = 5$) conditions over all time points yielded a significant difference of 1.78 ± 1.80 ($p = 4 * 10^{-5}$).

Influence of decitabine treatment in the CT26 tumor model

To assess the effect of low-dose decitabine treatment on [^{11}C]**3** accumulation, we injected an activity (molar mass) of 11.8 and 12.2 MBq (8.16 and 4.37 nmol/kg, $n = 2$ animals) in CT26 tumor-bearing, decitabine-treated mice. 9.4 and 10.2 MBq (2.10 and 2.56 nmol/kg, $n = 2$ animals) of tracer were injected in PBS-treated mice. Under blocking conditions, an excess of 4 µmol/kg compound **3** was co-injected in decitabine-treated mice injected with an activity (molar mass) of 9.2 and 12.3 MBq (1.67 and 3.20 nmol/kg, $n = 2$ animals) (3.9). Data from non-treated mice were included as PBS-treated when evaluating decitabine- vs PBS-treated mice. The SUV ratio decitabine-to-PBS including baseline and blocking decitabine-treated ($n = 4$) and non-treated ($n = 8$) mice was not significantly different from 1 in tumors or kidney (Figure 3.9 and 3.10). The tumors from decitabine-treated mice were smaller than. Notably, no low-activity tumor core was present in the decitabine-treated mice.

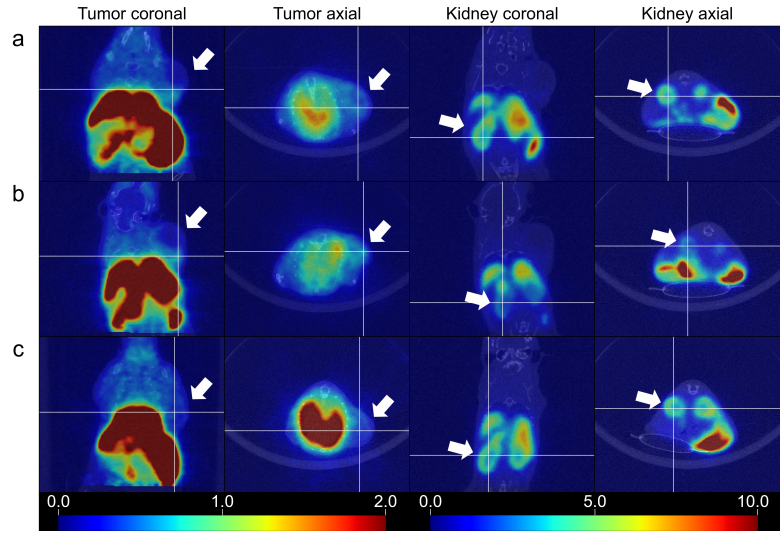

Figure 3.8: Representative PET images of tumor-bearing mice (0-60 min p.i., averaged) superimposed on CT (coronal, axial as indicated). Tumors on right shoulder (arrow), kidney (arrow). **a** CT26 tumor-bearing mouse injected with [^{11}C]**3** and **b** co-injected with 4 µmol/kg compound **3**. **c** MDA-MB-468 tumor-bearing mouse injected with [^{11}C]**3**. Crosshair indicates image planes. Mouse weights and activity at time of injection: **a** 18.3 g, 10.1 MBq (3.15 nmol/kg); **b** 18.9 g, 9.0 MBq (1.24 nmol/kg); **c** 18.6 g, 5.9 MBq (1.91 nmol/kg). PET, color bars and corresponding SUV (averaged 0-60 min of scan) are depicted at the bottom left (tumor) and right (kidney). CT, gray scale. The corresponding TACs and TAC ratios are shown in Figure 3.10. PET images of all scanned mice are shown in Figures 3.16 and 3.17.

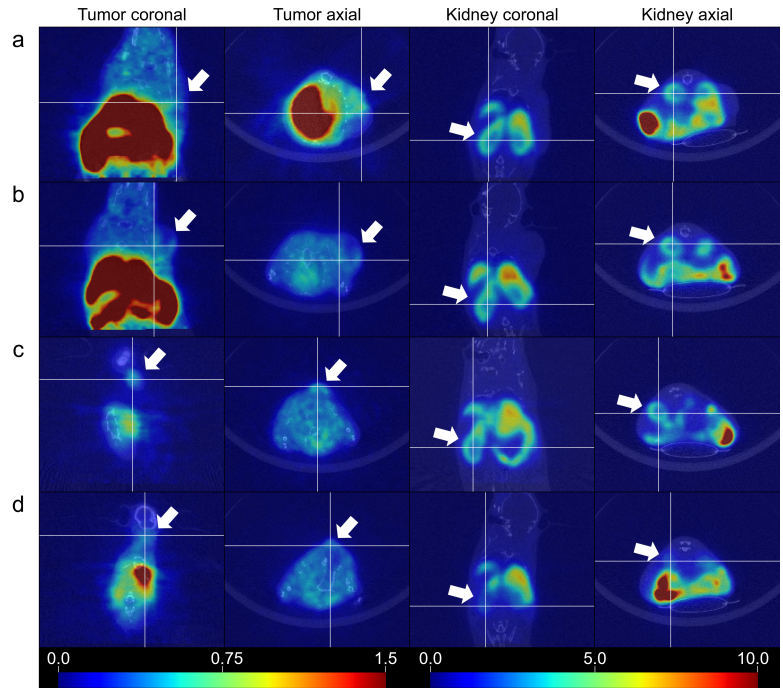

Figure 3.9: Representative PET images of CT26 tumor-bearing mice (0-60 min p.i., averaged) superimposed on CT (coronal, axial as indicated). Tumors on right shoulder (arrow), kidney (arrow). **a** Vehicle-treated tumor-bearing mouse injected with [^{11}C]**3** and **b** non-treated tumor-bearing mouse injected with [^{11}C]**3** and co-injected with 4 µmol/kg compound **3**. **c** Decitabine-treated tumor-bearing mouse injected with [^{11}C]**3** and **d** co-injected with 4 µmol/kg compound **3**. Crosshair indicates image planes. Mouse weights and activity at time of injection: **a** 21.1 g, 9.4 MBq (2.10 nmol/kg); **b** 20.4 g, 8.2 MBq (4.15 nmol/kg); **c** 19.5 g, 12.2 MBq (4.37 nmol/kg); **d** 19.1 g, 12.3 MBq (3.20 nmol/kg). PET, color bars and corresponding SUV (averaged 0-60 min of scan) are depicted at the bottom left (tumor) and right (kidney). CT, gray scale. The corresponding TACs and TAC ratios are shown in Figure 3.10. PET images of all scanned mice are shown in Figures 3.16 and 3.17.

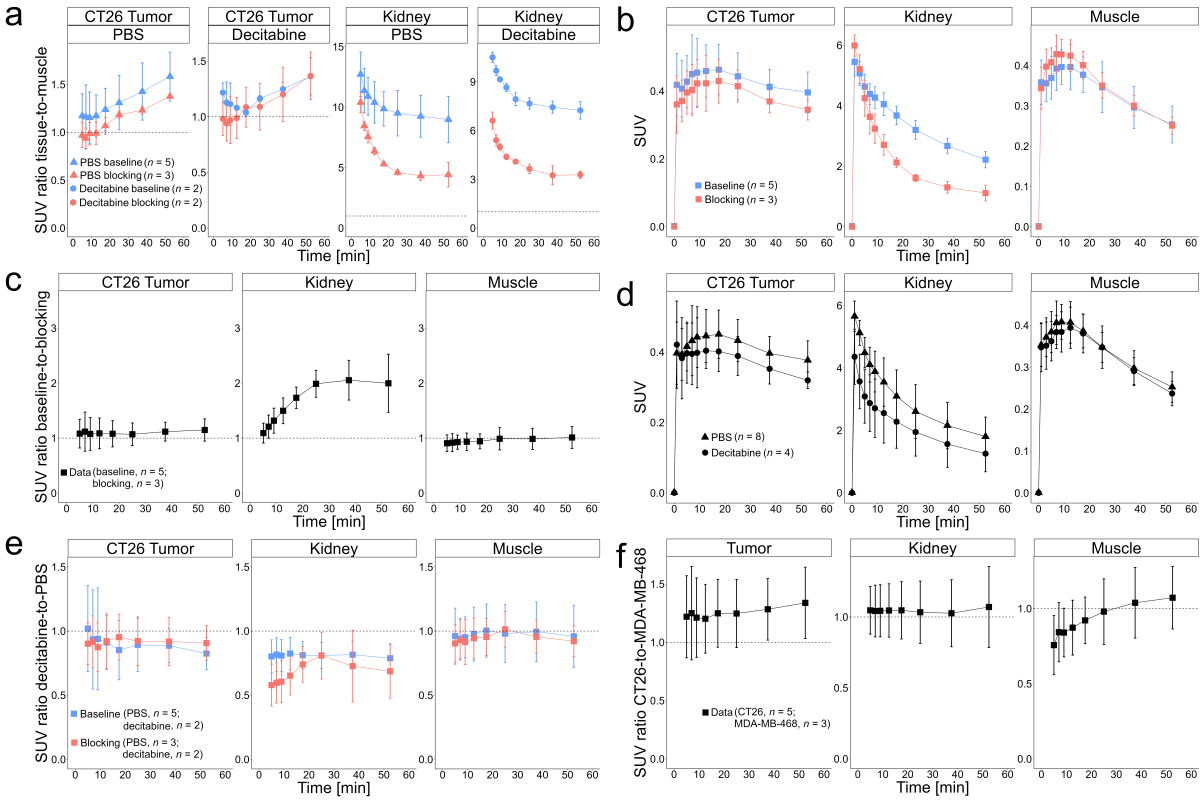

Figure 3.10: Time-activity and time-activity ratio curves from PET scans with [^{11}C]**3**. **a** SUV ratios tissue-to-muscle, **b** SUV over time, **c** SUV ratios baseline-to-blocking over time, **d** SUV over time, **e** SUV ratios decitabine-to-PBS over time, **f** SUV ratios MDA-MB-468-to-CT26 tumor over time. Symbols, mean; error bars, SD for $n \geq 3$ or value range for $n < 3$. Conditions and number of samples as indicated. Dashed lines indicate ratio of 1. The scans shown in Figure 3.8 and 3.9 are included in these data.

3.3.7 Radioactivity distribution in dissected tissues

Following the PET scans, animals were euthanized, and tissues dissected to determine the distribution of [^{11}C]**3**. The results are shown in Figures 3.11 (as SUV) and 3.12 (as percent injected dose per gram tissue, %ID/g). At 65 min p.i., liver uptake was highest among all analyzed tissues (data not shown). When analyzing the SUV ratio kidney-to-muscle for each animal a 20.94 ± 10.32 ($n = 15$, $p = 3 * 10^{-6}$) difference from 1 was found. Doing the same for the spleen, revealed a 4.16 ± 1.04 ($n = 15$, $p = 1 * 10^{-8}$) SUV ratio spleen-to-muscle. Across tumor types and conditions, the SUV ratio tumor-to-muscle was 2.53 ± 0.66 ($n = 15$, $p = 4 * 10^{-7}$).

Influence of tumor type and blocking

Assessing the SUV ratio tumor-to-muscle for the specific tumor types separately, yielded 2.95 ± 0.37 in CT26 baseline ($n = 5$, $p = 3 * 10^{-4}$), 2.23 ± 0.31 MDA-MB-468 baseline ($n = 4$, $p = 0.004$) and 2.74 ± 0.92 in CT26 blocking ($n = 3$, not siginificant). When comparing non-treated CT26 tumor-bearing mice ($n = 5$) to MDA-MB-468 tumor-bearing mice ($n = 4$), the SUV ratio CT26-to-MDA-MB-468 in tumors was 1.62 ± 0.35 ($p = 0.002$). Comparing baseline ($n = 10$) to blocking ($n = 5$) conditions with CT26 non-treated, PBS-treated and decitabine-treated mice taken together, a SUV ratio baseline-to-blocking

of 0.97 ± 0.09 (not significantly different from 1) was found in the tumors. In contrast, the SUV ratio baseline-to-blocking comparison in the spleen yielded a difference of 1.45 ± 0.15 ($p = 0.003$) and 3.14 ± 1.22 ($p = 3 * 10^{-6}$) in the kidney .

Influence of decitabine treatment in the CT26 tumor model

The SUV ratio decitabine-to-PBS including baseline and blocking decitabine treated ($n = 3$) and non-treated ($n = 8$) mice was not significantly different from 1 in tumor, kidney, and spleen.

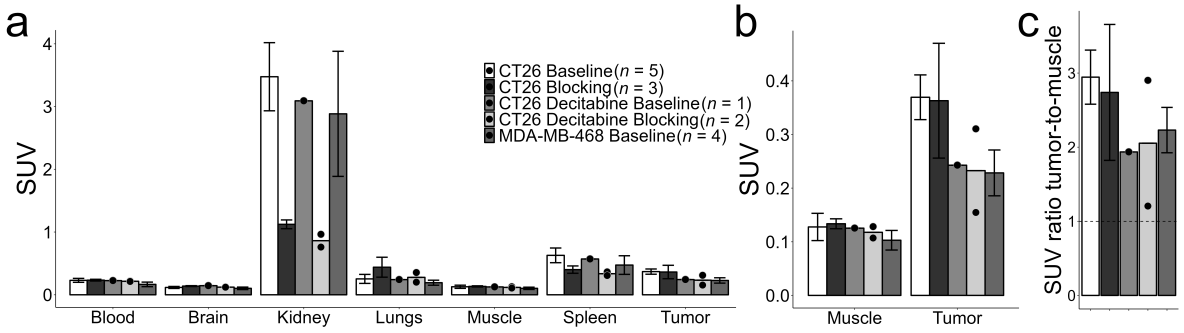

Figure 3.11: Biodistribution (SUV) after dissection at 65 min p.i. of the mice studied by PET (Figures 3.8 and 3.9). **a** SUV of tissues from tumor-bearing mice injected with [^{11}C]**3** (baseline conditions) or co-injected with 4 µmol/kg compound **3** (blocking conditions). **b** Enlarged comparison between muscle and tumor tissue. **c** SUV ratios tumor-to-muscle. Dashed line indicates ratio of 1. Error bars, SD ($n \geq 3$); symbols, individual values ($n < 3$). The same data is expressed as %ID/g in Figure 3.12.

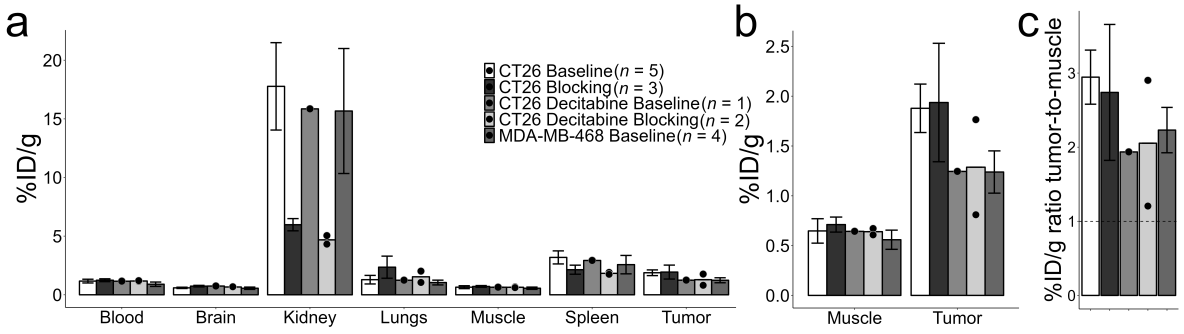

Figure 3.12: Biodistribution (%ID/g) after dissection at 65 min p.i. of the mice studied by PET (Figures 3.8 and 3.9). **a** %ID/g of tissues from tumor-bearing mice injected with [^{11}C]**3** (baseline conditions) or co-injected with 4 µmol/kg compound **3** (blocking conditions). **b** Enlarged comparison between muscle and tumor tissue. **c** %ID/g tissue ratios tumor-to-muscle. Dashed line indicates ratio of 1. Error bars, SD ($n \geq 3$); symbols, individual values ($n < 3$). %ID/g, percentage of injected dose per gram tissue. The same data is expressed as SUV in Figure 3.11. For significance indicators see Figure 3.11.

3.4 Discussion

We developed the legumain PET tracer [^{11}C]**3**, a P1-Asn peptidomimetic with strong affinity for legumain and better *in vivo* stability than our previous legumain-targeting tracers [^{11}C]**1** and [^{11}C]**2** [120]. [^{11}C]**3** accumulated in legumain-overexpressing cells and tissues *in vitro* and was blockable with an excess of compound **3**. Although quantifiable, the blocking effect size was moderate. In agreement with the literature, tissue slices from spleen and kidney showed higher total activity than muscle [27]. The CT26 tumor slice autoradiographs showed an accumulation that was, as expected based on previous studies and our legumain activity assays, between the kidney and muscle slices [120].

In PET and radioactivity measurements following the scans, [^{11}C]**3** accumulated more in tumors, kidney and spleen than in the muscle. Moreover, we observed a blocking effect when co-injecting [^{11}C]**3** with 4 µM **3** in kidney and spleen. This *in vivo* finding stands in contrast to what was observed with the previously developed tracers [^{11}C]**1** and [^{11}C]**2** and may be due to the increased stability [120]. The calculated K_i of compound **3** for human (18.2 ± 1.3 nM) and mouse (30.2 ± 5.1 nM) recombinant legumain are weaker than typically expected for a tracer to be suitable for PET imaging. The high B_max in the tumor tissues should, however, still allow for an adequate BP in the 10-100 range. As to why we did not observe a blocking effect in the tumors is unclear. Legumain is found extracellularly in the tumor microenvironment, where it is involved in the degradation of the extracellular matrix [35]. There may be competition with endogeneous substrates that are highly expressed in the tumor microenvironment such as cathepsins and fibronectin [35, 43, 145]. Active legumain in the kidney and spleen may be in the presence of less such endogenous substrates. One strategy to mitigate competition with endogenous substrates involves the development of irreversible binders, such as alkyne compounds, rather than reversible binders equipped with a cyano warhead like [^{11}C]**3** [101]. [^{11}C]**3** may be used in a context where endogeneous substrates are less of a concern.

Interestingly, the CT26 tumors had discernable tracer accumulation hotspots, which were conserved across cryosections from the same tumor. We observed such hotspots during the investigation of [^{11}C]**1** and [^{11}C]**2** as well [120]. The two tumor types showed a different tracer distribution. While in CT26, accumulation was higher in the periphery than the core, the distribution was homogeneous throughout the MDA-MB-468 tumors. The heterogeneity in tracer accumulation could be due to the presence of tertiary lymphoid structures (TLS), commonly found in human cancers [174]. These peripheral clusters of immune cells, are often populated by M2 macrophages, which would explain the high tracer accumulation [142]. The accumulation in the tumor periphery as seen in PET, further supports this hypothesis. The abrogated M2 macrophage contribution in the MDA-MB-468 immunocompromised tumor model and the resulting reduced local legumain expression could explain the lack of peripheral accumulation observed in PET with MDA-MB-468 tumor-bearing mice. However, our approach does not allow for the distinction between legumain expressed by macrophages and legumain stemming from other sources. The SUV in CT26 tumors, based on the dissected tissue, was 62 ± 35 % higher than in MDA-MB-468 tumors. This difference was not observed in the PET. There is a visible trend in the TACs showing the PET to be more similar to the measurements of the dissected tissue toward the end of the scan.

The discrepancy between legumain expression in cells and accumulation of legumain-targeting tracers *in vivo* emphasizes the effect of the cellular environment on legumain

expression. Monocultured cancer cells may exhibit a completely different expression pattern *in vitro* than *in vivo*. To study the effect of the decitabine on the whole tumor microenvironment, we treated CT26 tumor-bearing mice with a low-dose regimen of decitabine. Decitabine treatment has been shown to increase M2 polarization in macrophages [214]. Our application of a low-dose treatment regimen in mice as employed by others [200], did neither alter legumain RNA expression in the tumors nor the accumulation of [^{11}C]**3**. Decitabine is a nucleoside analogue and might have a direct effect on the tumor cells and other cell types in addition to M2 macrophages [38].

3.5 Conclusions

The newly developed legumain PET tracer [^{11}C]**3** showed high accumulation and blocking in healthy tissues with high legumain expression, indicating specific targeting of legumain. However, accumulation in the tumor was lower than expected and not blocked, potentially resulting from legumain occupancy by endogenous substrates.

3.6 Supplementary material

3.6.1 RP HPLC chromatograms

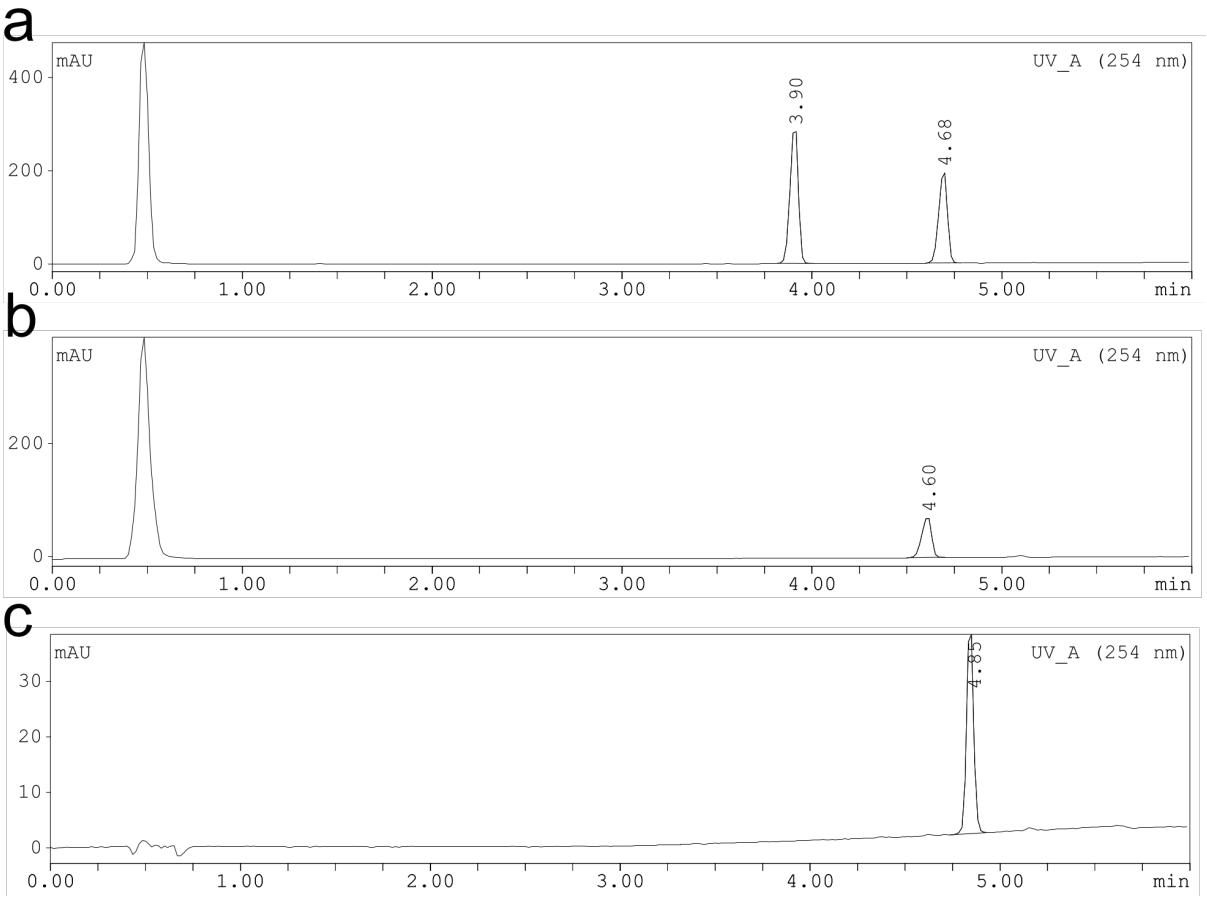

Figure 3.13: Reverse phase HPLC chromatograms for purity and identity. UV signal measured at 254 nm. Retention time and, where applicable, % area were determined. **a**, **3** precursor 3.90 min, compound **3** reference 4.68 min. **b**, **3** reference 4.60 min (100 %). **c**, [^{11}C]**3** 4.83 min (100 %).

3.6.2 Autoradiography quantification masks

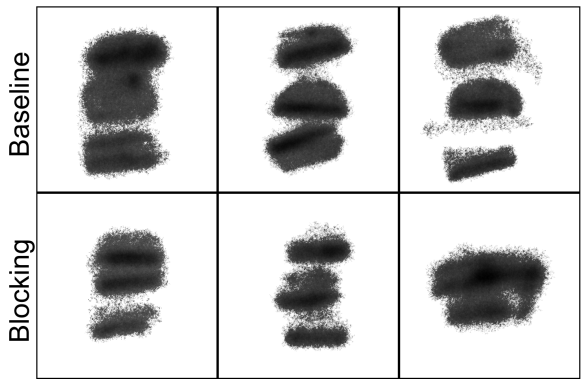

Figure 3.14: Tissue slice areas used for quantification in Figure 3.6.

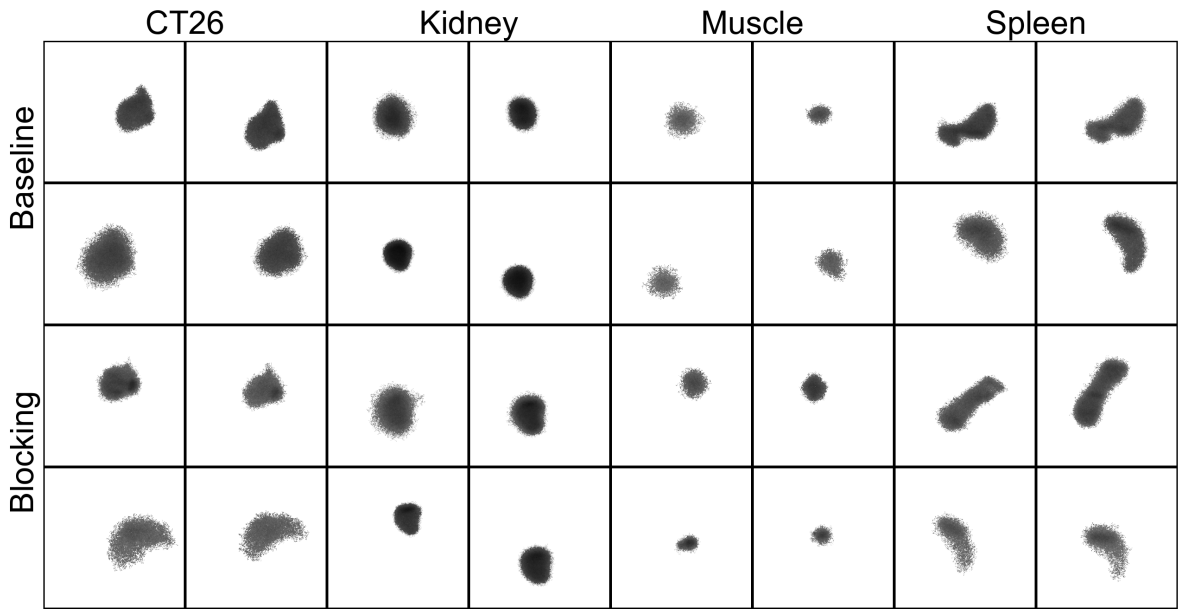

Figure 3.15: Tissue slice areas used for quantification in Figure 3.7.

3.6.3 Identity ^{1}H NMR, HRMS

(2S)-N-[(1S)-3-amino-1-cyano-3-oxopropyl]-1-[1-[4-(4-methoxyphenoxy)phenyl]cyclopropanecarbonyl]pyrrolidine-2-carboxamide
^{1}H NMR (400 MHz, DMSO-d6) δ[ppm] 8.71 (d, J = 8.3, 1H); 7.61 (s, 1H); 7.25-7.18 (m, 2H), 7.17 (s, 1H); 7.04-6.91 (m, 4H); 6.88-6.80 (m, 2H); 4.91 (q, J = 7.3, 1H), 4.27 (dd, J = 5.1, 8.73, 1H); 3.75 (s, 3H); 3.23-3.14 (m, 1H); 2.70 (dd, J = 15.4, J = 8.3, 1H); 2.61 (dd, J = 15.6, J = 6.3, 1H); 2.11-1.98 (m, 1H); 1.85-1.62 (m, 3H); 1.37-1.27 (m, 1H); 1.27-1.11 (m, 2H); 1.05-0.95 (m, 1H).
HRMS (ESI$^+$, m/z) calc. for $C_{26}H_{29}N_4O_5$ 477.2132 (M + H) found 477.2133.

(2S)-N-[(1S)-3-amino-1-cyano-3-oxopropyl]-1-[1-[4-(4-hydroxyphenoxy)phenyl]cyclopropanecarbonyl]pyrrolidine-2-carboxamide
^{1}H NMR (400 MHz, DMSO-d6) δ[ppm] 9.33 (s, 1H); 8.68 (d, J = 7.4, 1H); 7.60 (s, 1H); 7.22-7.12 (m, 2H); 6.90-6.84 (m, 2H) 6.84-6.73 (m, 4H); 4.91 (q, J = 7.4, 1H), 4.30-4.23 (m, 1H); 3.22-3.14 (m, 1H); 2.70 (dd, J = 15.9, J = 8.6, 1H); 2.60 (dd, J = 15.9, J = 7.1, 1H); 2.00-1.98 (m, 1H); 1.85-1.62 (m, 3H); 1.36-1.26 (m, 1H); 1.25-1.09 (m, 2H); 1.07-0.96 (m, 1H).
HRMS (ESI$^+$, m/z) calc. for $C_{25}H_{27}N_4O_5$ 463.1976 (M + H) found 463.1983.

3.6.4 PET scans

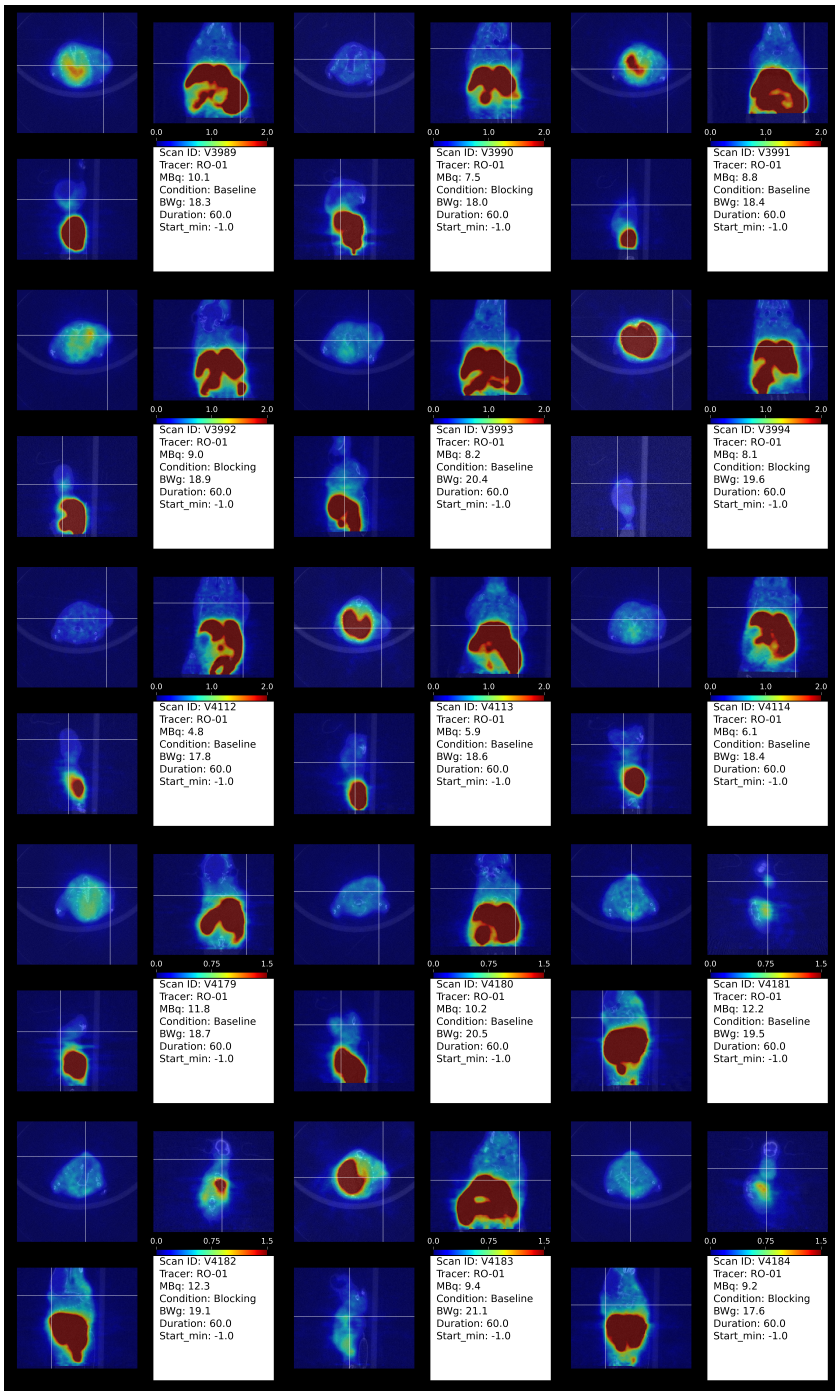

Figure 3.16: Mouse PET images (0-60 min p.i., averaged) superimposed on CT (axial, coronal, saggital). Tumors on right shoulder. Conditions as indicated. Baseline condition, mouse injected with [^{11}C]**3**; blocking condition, tracer co-injected with 4 µmol/kg of compound **3**. CT26 tumor-bearing mice (Scan ID: V3989, V3991, V3993, V3990, V3992, V3994); PBS-treated CT26 tumor-bearing mice (Scan ID: V4180, V4183); decitabine-treated CT26 tumor-bearing mice (Scan ID: V4179, V4181, V4182, V4184); MDA-MB-468 tumor-bearing mice (Scan ID: V4112, V4113, V4114). Crosshairs indicate image planes (in tumor region). PET, color bar for the corresponding SUV; CT, gray scale. MBq, activity at time of injection in MBq; BWg, body weight in g; Duration, duration of the scan in min; Start_min, start of the scan after injection in min. The TACs of tumor, muscle and kidney are shown in Figure 3.10. The same data sets as in Figure 3.17 are shown.

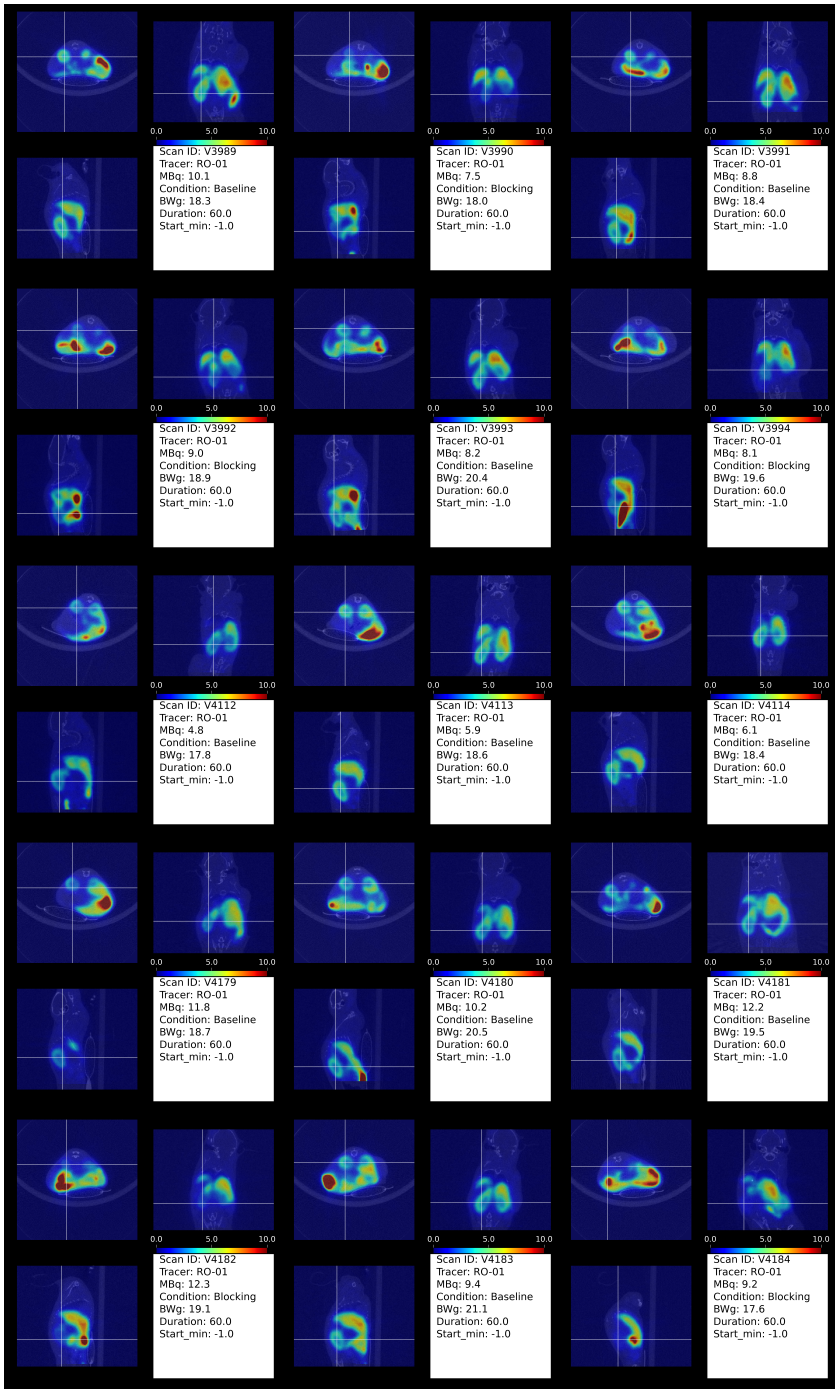

Figure 3.17: Mouse PET images (0-60 min p.i., averaged) superimposed on CT (axial, coronal, saggital) as in Figure 3.16, with focus on left kidney. Tumors on right shoulder. Conditions as indicated. Baseline condition, mouse injected with [^{11}C]**3**; blocking condition, tracer co-injected with 4 µmol/kg of compound **3**. CT26 tumor-bearing mice (Scan ID: V3989, V3991, V3993, V3990, V3992, V3994); PBS-treated CT26 tumor-bearing mice (Scan ID: V4180, V4183); decitabine-treated CT26 tumor-bearing mice (Scan ID: V4179, V4181, V4182, V4184); MDA-MB-468 tumor-bearing mice (Scan ID: V4112, V4113, V4114). Crosshairs indicate image planes (in left kidney region). PET, color bar for the corresponding SUV; CT, gray scale. MBq, activity at time of injection in MBq; BWg, body weight in g; Duration, duration of the scan in min; Start_min, start of the scan after injection in min. The TACs of tumor, muscle and kidney are shown in Figure 3.10.

Chapter 4

PET imaging of legumain in Alzheimer's disease: A pilot study in mice using ^{11}C-labeled CC11m

Author Statement

Severin K. Lustenberger: Conceptualization, Methodology (equal contribution to radiosynthesis and animal study, performed the other experiments except PET scans), Analysis (performed all data analysis), Writing (wrote first draft and corrected version), Project administration; **Claudia A. Castro Jaramillo**: Conceptualization, Methodology (equal contribution to radiosynthesis and animal study), Writing (review); **Michael Cselovsky**: Methodology (supported experiments); **Omar Mohamad**: Methodology (supported experiments); **Andrea Lubina**: Methodology (supported experiments); **Makar Pobiyakho**: Methodology (supported experiments); **Roger Schibli**: Supervision, Providing infrastructure, Writing (review); **Linjing Mu**: Supervision, Methodology (supported experimental planning), Analysis (supported data analysis), Writing (review), Project administration; **Stefanie D. Krämer**: Supervision, Funding acquisition, Methodology (supported experimental planning), Analysis (supported data analysis), Writing (review), Project administration

4.1 Background

Alzheimer's disease (AD) is a neurodegenerative disorder that clinically manifests as progressive cognitive decline. The risk of developing AD increases drastically with age, leading to a prevalence of 10-30 % in the population > 65 years of age [123]. The pathology of AD is characterized by neurofibrillary tangles and amyloid plaques, which are composed of the microtubule protein tau and insoluble amyloid-β (Aβ) peptides, respectively [123]. Genome-wide association studies have pinpointed most AD risk genes to macrophages of the brain, so-called microglia cells [42]. Legumain, a lysosomal cysteine endopeptidase, is upregulated in microglia upon acute inflammation caused by experimental strokes [84]. In AD mouse models, legumain expression correlates with microglial activation and disease progression [204]. Legumain, along with β- and γ-secretases, is part of an enzyme family involved in the processing of Aβ and tau [98]. Legumain, in the context of AD often called δ-secretase, hydrolyzes peptide bonds c-terminally to asparagine residues [35]. In studies examining brains from humans with AD, legumain was found to proteolytically cleave both amyloid precursor protein (APP), the precursor of Aβ, and tau [218, 219]. Moreover, an age-related increase in legumain expression and activation was observed in wild-type mice, along with high levels in brain tissue of 5xFAD, APP/PS1, and P301S transgenic mouse strains [218]. Legumain-cleavage of tau and APP in such established, transgenic, AD mouse models regulates the accumulation of Aβ plaques and tau tangles. The deletion of legumain in these mice reduced disease pathology and alleviated the symptoms of AD, suggesting a causal role of legumain in the pathogenesis of the disease [88, 218, 219].

In a landmark legumain inhibition study, the small molecule legumain ligand compound 11 reduced tau and APP cleavage, leading to reduced Aβ and tau pathology and restored synaptic function in 5xFAD and P301S mice [217]. More recently, the same group has optimized compound 11 to yield compound 11a, with improved oral bioavailability and *in vivo* pharmacokinetic properties [112]. A different approach to legumain inhibition makes use of P1-Asn peptidomimetic compounds, conceived and improved for applications in cancer [41, 81, 108, 138, 139]. The orally bioavailable, blood-brain-barrier (BBB) penetrant legumain inhibitor compound 18 has been developed based on the P1-Asn scaffold [101]. Compound 18 reduced the levels of cleaved tau fragments in P301L mice along with a decrease in legumain activation *in vivo*. The BBB-penetrant legumain inhibitors compound 11, compound 11a and compound 18 are shown in Figure 4.1.

Particularly in the field of AD, imaging probes have long been employed for disease diagnostics [98]. In addition to unspecific [^{18}F]FDG imaging, PET tracers specifically for Aβ and tau have been developed. ^{18}F-labeled Aβ PET tracers such as florbetapir, florbetaben and flutemetamol are clinically available and ^{11}C-labeled Pittsburgh compound B is frequently used in research [98]. To image tau, several PET tracers are in development, of which flortaucipir has been approved for clinical use [98]. Despite regulatory approval of these tracers, the use of Aβ plaques and tau tangles as biomarkers has been criticized because both are considered necessary but not sufficient to cause AD [57, 185, 186]. This is exemplified by the limited treatment success of therapies targeting Aβ and tau tangles [50]. Legumain, a key enzyme upstream of Aβ plaque and tau tangle formation, might be a more suitable target for AD imaging. In recent years ^{18}F- and ^{68}Ga-labeled legumain PET tracers based on lysosomal trapping have been developed [80, 118, 119, 159]. These nanoparticle-based tracers do, however, not cross the blood brain barrier likely due to their size and hydrophilicity. To our knowledge, there is currently no BBB-penetrant

legumain PET tracer available.

In this feasibility study, we focused on evaluating legumain expression and activity in APP/PS1 transgenic mice, a well-established AD mouse model [20, 165]. The study also centered on developing and optimizing methodologies for a potential BBB-penetrant legumain PET tracer, based on the *N*-methylated compound 11, which has a reported IC_{50} of 124 nM [217]. We synthesized [^{11}C]CC11m by *N*-methylation of compound 11 with [^{11}C]CH3OTf, and assessed its *in vivo* distribution using PET, complemented by tissue analysis post-scan [24].

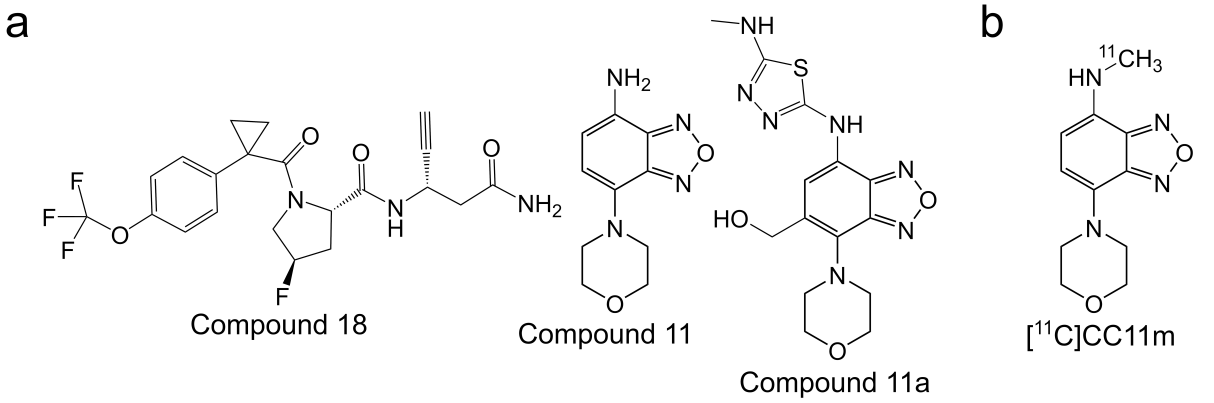

Figure 4.1: Chemical structures of likely BBB-penetrant legumain ligands. **a** Compound 18 [101], compound 11 [217], and compound 11a [112]. **b** Tracer [^{11}C]CC11m based on methylated compound 11.

4.2 Methods

4.2.1 Animal models

Animal studies were approved by the Zurich Cantonal Veterinary Office, Switzerland (licenses ZH011/22 and ZH028/22), and conducted according to Swiss Animal Welfare legislation. Studies were performed with B6C3-Tg(APPswe,PSEN1dE9)85Dbo/Mmjax, hemizygous mice abbreviated as APP/PS1 transgenic and their littermates C57BL/6J wild-type abbreviated as APP/PS1 wild-type, age 9-10 months. APP/PS1 mice were ordered from The Jackson Laboratory (Bar Harbor, US) and bred in-house in our animal facility. 3-4 months old BALB/cAnNCrl from Charles River Laboratories (Sulzfeld, DE) are abbreviated as BALB/c mice. The BALB/c mouse that underwent PET imaging was inoculated with a CT26 tumor because it was part of a different project (Chapter 2). All animals were housed at 22 °C with a 12-hour light-dark cycle and unlimited access to food and water.

4.2.2 Fluorescence microscopy

Brains were embedded in OCT compound mounting medium (Avantor, US), cut to 10 µm slices with a cryotome, thaw-mounted on microscopy slides and stored at -80 °C. For fluorescent staining, slices were thawed, left to dry and washed (3 * 5 min) in phosphate-buffered saline (PBS, gibco, Life Technologies, US). Tissue was encircled with

a hydrophobic pen (Dako, DK) and fixed in 4 % paraformaldehyde in PBS for 10 min. Tissue was washed (3 * 5 min) in tris-buffered saline with 0.1 % Tween (TBST) and incubated in 5 % (w/v) powdered, skimmed milk in TBST on a benchtop rocker for 30 min. All subsequent incubation steps were performed protected from light on a benchtop rocker. Tissue was washed (3 * 5 min) in and permeabilized TBST and incubated with primary antibodies in TBST for 120 min. Tissue was washed (3 * 5 min) in TBST and incubated with secondary antibodies in TBST for 30 min. Tissue was washed (3 * 5 min) in TBST and incubated with DAPI (BioLegend, US) 1:2 000 in TBST for 5 min. Tissue was washed (1 * 5 min) and sections were left to dry for 30 min. Cover slip was mounted with mounting medium (Mowiol, Kuraray, JP) and left to dry for 30 min. Slides were stored at 5 °C for up to 4 weeks prior to image acquisition. For microglia staining, rat IBA1 targeting primary antibody (MA5-38266, Thermo Fisher Scientific, US) 1:500 and goat Alexa Fluor 647 IgG secondary antibody (A21247, Thermo Fisher Scientific, US) 1:500 were used. For legumain staining, rabbit legumain targeting primary antibody (bs-3907R, Bioss, US) 1:100 and goat Alexa Fluor 488 IgG secondary antibody (A11008, Thermo Fisher Scientific, US) 1:500 were used. Images were acquired on a widefield microscope (Leica DMI6000B, DE). Image processing was done with open-source imaging software [173].

4.2.3 Gene expression analysis

Tissues were dissected and washed with RNA-preserving solution (RNAlater, Thermo Fisher Scientific, US). For RNA extraction, tissue was transferred to RNA extraction solution (TRIzol, Thermo Fisher Scientific, US) and homogenized using a bead-mill system (Qiagen, DE). The homogenate was centrifuged (12 000 * g, 10 min, 4 °C) and the uppermost phase was mixed with chloroform. After centrifugation (same conditions as above), the aqueous phase was mixed with isopropanol and incubated for 10 min. The samples were centrifuged (same conditions as above) and the resulting pellet was washed with 75 % ethanol and centrifuged (8 000 * g, 5 min, 4 °C). The wash was repeated, the sample pellets were centrifuged (15 000 * g, 2 min, 4 °C) and left to dry for 1-2 h. The pellet was dissolved in RNAse-free water. Concentration and quality of the RNA extract were determined using a microvolume spectrophotometer (NanoDrop, Thermo Fisher Scientific, US). For reverse transcription, RNA extract was incubated with wipeout buffer (QuantiTect Reverse Transcription kit, Qiagen, DE) for 2 min at 42 °C. Reverse transcriptase, reverse transcription buffer and reverse transcription prime mix (QuantiTect Reverse Transcription kit, Qiagen, DE) were added and the solution was incubated for 15 min at 42 °C followed by 3 min at 95 °C. Real-time quantitative polymerase chain reaction (RT-qPCR) was performed using cDNA from the previous step, gene specific primers and qPCR Master Mix (GoTaq qPCR Master Mix, Promega, US). Primers for qPCR were custom-made oligonucleotides (Microsynth, CH): legumain (Lgmn, NCBI Gene: 19141), forward 5'-GTG ATC AAC CGA CCT AAC G-3', reverse 5'-ATT CTC TGG AGT CAC ATC CTC-3'; Amyloid beta precursor protein (App, NCBI Gene: 11820), forward 5'-TGA ACC AGT CTC TGT CCC T-3', reverse 5'-TCT GAA GCA GCT CAT CGA C-3'; GLE1 RNA export mediator (Gle1, NCBI Gene: 74412), forward 5'-CAA ATG GAA CCC AGA GCA C-3', reverse 5'-ACC CTT CCA CTT TGA TCG C-3'. On a real-time PCR system (Quantstudio 7 Flex, Thermo Fisher Scientific, US), 10 µl of total volume were run through 40 cycles with the hold stage temperature at 95 °C for 2 min and a PCR stage consisting of 95 °C for 15 s (denaturation) and 60 °C for 60 s (annealing/extension). Melt curve stage was included for quality control on a single well

level. Lgmn and App were normalized to Gle1. Data processing was performed in R using open-source packages [209].

4.2.4 Protein expression analysis

Whole brains were dissected and perfused with RIPA buffer (25 mM Tris pH 7.4, 150 mM NaCl, 1 % (v/v) Triton x-100, 0.5 % (m/v) sodium deoxycholate detergent, 0.1 % (m/v) sodium dodecyl sulfate, protease inhibitor cOmpete tablets (Roche, CH), 1 mM phenylmethylsulfonyl fluoride in water). For protein extraction, the tissue was chopped and incubated for 2 h at 5 °C. The tissue lysate was centrifuged at 15 000 * g, 4 °C for 15 min. The supernatant underwent buffer exchange with PBS using 10K MWCO protein concentrators (Thermo Fisher Scientific, US) and protein concentration determination with Bradford reagent (Merck Millipore, US). For separation, 10 % acrylamide SDS gels were prepared and loaded with 30 µg of protein and stained protein molecular weight standards (Biorad, US). Electrophoresis took place under 200 V and 300 mA constant voltage for 1 h 15 min. The proteins were transferred to a PVDF membrane (Merck Millipore, US) under wet conditions and 100 V, 350 mA constant voltage for 1 h. Membranes were blocked in 5 % (w/v) powdered, skimmed milk in TBST for 45 min and incubated in primary antibody in TBST at 5 °C over night. Membranes were washed (3 * 5 min) in TBST and incubated with secondary antibody for 1 h. Membranes were washed (3 * 5 min) in TBST and incubated with peroxide luminol solution (1.25 mM luminol, 0.2 mM *p*-coumaric acid, 0.02 % (v/v) H_2O_2 in water) for 2 min. Protein bands were visualized based on chemiluminescence and white light exposure using a ChemiDoc XRS (Biorad, US). Rabbit legumain targeting primary antibody (bs-3907R, Bioss, US) 1:250, and rabbit anti-β-actin primary antibody (A2066, Sigma-Aldrich, US) 1:500 were used. Secondary antibodies were anti-rabbit HRP conjugated (A0545, MilliporeSigma, US) 1:2 000.

4.2.5 Legumain activity and estimation of binding potential

Tissues were dissected and washed with assay buffer consisting of 20 mM citric acid, 60 mM Na_2HPO_4, 1 mM EDTA, 0.1 % (m/v) CHAPS, 4 mM DTT at pH 5.8. Tissue was homogenized using a Polytron (Kinematica, US), and centrifuged at 19 000 * g, 4 °C for 20 min to precipitate debris. Protein content of the lysate was determined using the BCA assay, with bovine serum albumin for calibration [104]. Legumain activity was measured with a fluorescence assay [87]. In brief, a sample of tissue lysate with total a protein concentration of $\sim$12 000 µg/ml was prepared. The substrate Z-Ala-Ala-Asn-AMC (Bachem, CH) was added to the samples to reach a substrate concentration of 10 µM. Fluorescence was measured at excitation 340 nm and emission 460 nm every minute over 5 h. The activity was determined from the slope of the initial linear increase in fluorescence and normalized to the protein content of the tissue sample. Data processing was performed in R using open-source packages [209].

The density of legumain, corresponding to the maximal possible specific binding of legumain-targeting tracer per mg protein in the tissue (B_{max} in nmol/mg) was estimated based on the measured legumain activity in comparison to recombinant mouse legumain of known concentration (R&D Systems, US). To estimate the expected binding potential (BP) of a tracer in tissue with Equation 4.1, B_{max} (nmol/mg) was transformed to B_{max} in nmol per 1 000 cm^3 tissue (nM), assuming a protein content of mouse tissue of 0.23 g/cm^3 [188], i.e., B_{max} in nmol/mg was multiplied by 2.3 * 10^5 mg/l to get B_{max} in nM.

$$\mathrm{BP} = \frac{B_{\max}(\mathrm{nM})}{K_{\mathrm{i}}(\mathrm{nM})} \tag{4.1}$$

K_{i} in Equation 4.1 was estimated from the IC_{50} of the inhibitor, the substrate concentration at which IC_{50} was determined, i.e., 10 µM [139] and the K_{M} reported for human legumain, i.e., 25.7 µM [153] according to the Cheng-Prusoff equation (Equation 4.2).

$$K_{\mathrm{i}} = \frac{\mathrm{IC}_{50}}{1 + \frac{[S]}{K_{\mathrm{M}}}} \tag{4.2}$$

4.2.6 Radiochemistry

Generation of [^{11}C]CH_3OTf

Proton bombardment of a target filled with N_2 fortified with 0.5 % O_2 in a Cyclone 18/9 cyclotron (18-MeV, IBA, BE) afforded [^{11}C]CO_2 by $^{14}N(p, \alpha)^{11}C$ nuclear reaction. For the conversion to [^{11}C]CH_3I, nickel-based catalytic reduction of [^{11}C]CO_2 with hydrogen was performed to form [^{11}C]CH_4, which was followed by iodination to afford [^{11}C]CH_3I. [^{11}C]CH_3I was further converted to [^{11}C]CH_3OTf by passing through a silver triflate column at elevated temperatures (190 °C).

Radiosynthesis

Approx. 1 mg precursor (Cayman, US) was dissolved in 500 µl 1,1,1,3,3,3-Hexafluoro-2-propanol containing 3 µl 5 M NaOH. The generated [^{11}C]CH_3OTf was bubbled into the solution with constant stirring followed by incubation for 5 min at 50 °C. The reaction was quenched with water and the crude solution was injected into a semi-preparative HPLC column (Symmetry C18 Prep Column 5 µm 7.8 * 50 mm, Waters, US). A solvent gradient of 95-10 % trifluoroacetic acid (0.1 % (v/v) in water) and 5-90 % acetonitrile over 10 min was applied. The flow rate was 4 ml/min. The product was collected with the help of a UV detector and a radio detector (Gabi Star, Elysia-Raytest, DE), diluted with water (8 ml) and purified using an activated (5 ml ethanol, 10 ml water) C18 cartridge (Sep-Pak C18 light, Waters, US). The cartridge was washed with 5 ml water and the product was eluted with 0.5 ml ethanol into a sterile vial. 9.5 ml saline solution (NaCl 0.9%, B.Braun, DE) was added to obtain an isotonic product containing 5 % ethanol. Nitrogen was used as a propellant. For quality control, HPLC was performed with 50 µl of the solution injected into a reverse phase HPLC column (ACE 3 C18 3 µm 50 * 4.6 mm, ACE, UK). A solvent gradient was applied with A (0.1 % trifluoroacetic acid in water/acetonitrile 95/5) and B (water/acetonitrile 5/95) from A/B 100/0 to 20/80 over 13 min. The flow rate was 1.2 ml/min. The molar activity was determined based on linear regression with reference compound measured with a UV detector (Gabi Star, Elysia-Raytest, DE) at 254 nm wavelength.

4.2.7 PET scans and biodistribution after dissection

Mouse was anesthetized with 2-3 % isoflurane in oxygen/air (1/1) 10 min prior to PET acquisition. PET/CT scans were performed on a small-animal PET/CT scanner (Super Argus, Sedecal, ES) with an axial field of view of 4.8 cm and a spatial resolution of

1.6-1.7 mm (full width at half maximum) [61]. Respiratory rate was kept at ~ 60 min^{-1} through adjustment of isoflurane concentration. Body temperature was kept at 37 °C using heated air. Tracer was injected into tail vein at the indicated time point and dose, and PET data were acquired in list mode. Anatomical information was obtained by CT following each PET acquisition. PET data were reconstructed with 2D ordered-subsets expectation maximization (2D-OSEM), applying random scatter correction and decay correction but no correction for attenuation, and analyzed with PMOD v4.2 software (PMOD Technologies Ltd., Zurich, Switzerland). SUVs were calculated as the ratio of regional averaged radioactivity in Becquerel per cubic centimeter and injected radioactivity in Becquerel per gram body weight, multiplied by 1 cm^3 per g body weight. Image analysis was performed in python using community modules [15, 69, 82, 117, 125, 212] and R open-source packages. All radioactivity was decay-corrected to the time point of injection to the animal.

4.2.8 Statistical analysis

Statistical differences were analyzed by two-tailed unpaired Student's t test, as indicated. Differences with $p < 0.05$ were considered significant. Average values are shown with standard deviations (SD), data range in case of $n = 2$, and individual values in case of $n = 1$.

4.3 Results

4.3.1 Legumain and APP mRNA levels

To compare legumain and APP levels between APP/PS1 wild-type mice and APP/PS1 transgenic mice, we dissected whole-brain tissue from age-matched 10-month-old animals and analyzed mRNA levels by qPCR (Figure 4.2). APP/PS1 transgenic mice ($n = 5$) showed 2.85 ± 0.61-fold ($p = 0.002$) higher mRNA levels of APP, and 1.32 ± 0.19-fold ($p = 0.017$) higher mRNA levels of legumain than wild-type controls ($n = 7$).

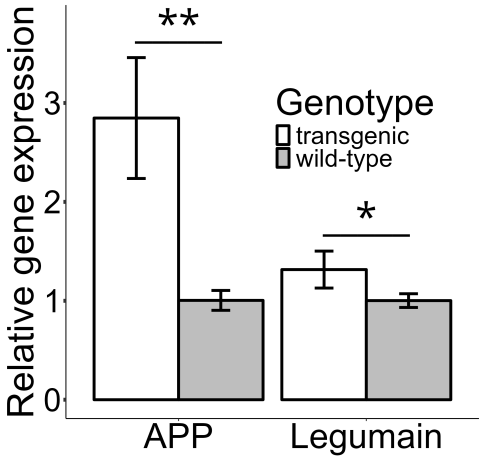

Figure 4.2: mRNA levels of brain tissue from APP/PS1 transgenic and wild-type mice. Expression levels of legumain (Lgmn) and APP (App) were quantified by RT-qPCR relative to Gle1. Fold-change of transgenic ($n = 5$) compared to wild-type ($n = 7$) is shown. Significance was analyzed with unpaired student's t tests, without correction for multiple comparisons. Bars, means; error bars, SD. *, $p < 0.05$; **, $p < 0.01$.

4.3.2 Prolegumain and active legumain

Legumain is expressed as a zymogen (prolegumain) and activated through autocatalytic cleavage [35]. We performed western blot analysis of whole-brain tissue lysates from

wild-type ($n = 4$) and APP/PS1 transgenic ($n = 4$) mice at age 10 months to see if both the prolegumain and the active form of legumain are present. As depicted in Figure 4.3, prolegumain was detected at $\sim$56 kDa and the active form at $\sim$46 kDa. β-actin was used as loading control. Furthermore, no difference in prolegumain or active legumain levels between wild-type and APP/PS1 transgenic mice was observed by visual comparison.

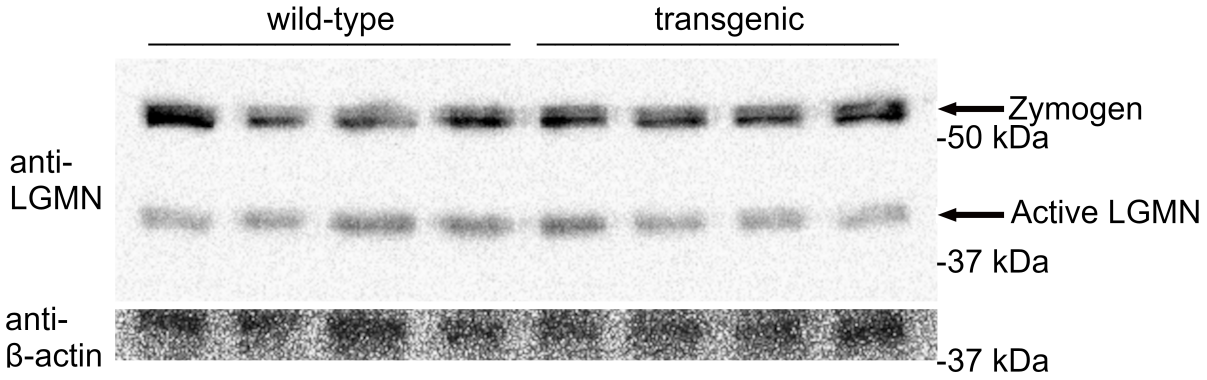

Figure 4.3: Zymogen and active form of legumain in wild-type and APP/PS1 transgenic mouse brain tissue lysate. Western blot with samples from wild-type ($n = 4$) and APP/PS1 transgenic ($n = 4$) mice (10 months of age). Anti-LGMN (upper panel), probed with polyclonal anti-legumain primary antibody; anti-β-actin (lower panel), probed with polyclonal anti-β-actin primary antibody; molecular weight marker, as indicated; genotype, as indicated; legumain form (zymogen or active), as indicated.

4.3.3 Legumain activity

To investigate legumain activity in APP/PS1 transgenic mice, we performed a legumain activity assay with whole-brain tissue lysates from 10-month-old mice. Figure 4.4 shows the measured conversion rate of non-fluorescent substrate to fluorescent product for brain tissue of APP/PS1 transgenic mice ($n = 1$) in comparison to muscle tissue of BALB/c wild-type mice ($n = 12$) and recombinant mouse legumain ($n = 3$). The estimated density of legumain ($B_{\max}$) in brain tissue of APP/PS1 transgenic mice was 0.65 pmol/mg ($n = 1$) and higher than in muscle tissue of BALB/c wild-type mice ($\sim$0 pmol/mg, $n = 12$). Assuming 0.23 g protein per cm^3, the density of legumain corresponds to a $B_{\max}$ of 149.5 nM. The K_{i} value of CC11m as calculated with Equation 4.2 from the IC_{50} of 124 nM [217] was 89.3 nM.

4.3.4 Fluorescence microscopy of legumain and activated microglia

Next, we wanted to qualitatively locate legumain and activated microglia cells in APP/PS1 transgenic mouse brain tissue in comparison to the wild-type. We performed fluorescence microscopy on brain cryosections of APP/PS1 transgenic ($n = 1$ animal) and wild-type ($n = 1$ animal) mice. As seen in Figure 4.5, microglia cells stained with anti-IBA1 antibody (red) are abundant in both tissues. Intra- and extracellular legumain staining (green) revealed larger clusters in APP/PS1 transgenic mouse brain tissue compared to wild-type.

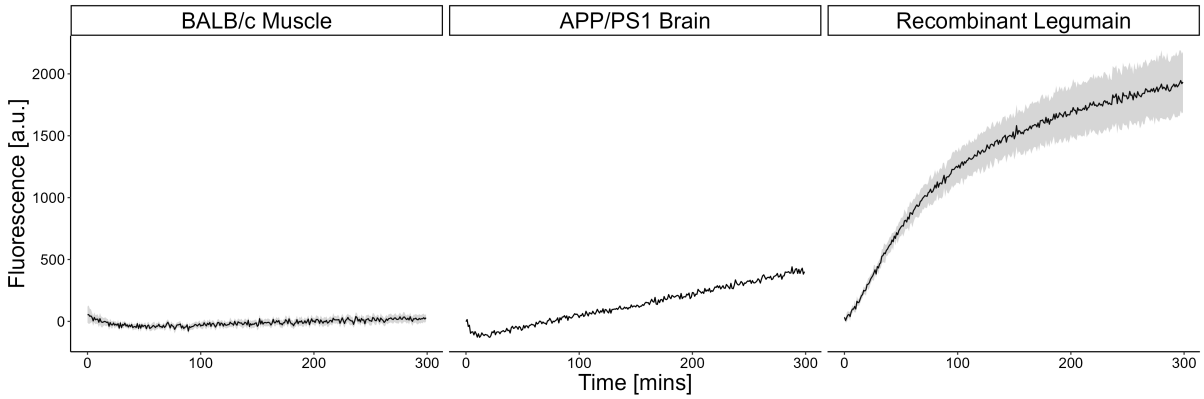

Figure 4.4: Conversion rate of the non-fluorescent substrate to the fluorescent product in total tissue lysate of dissected tissues (as indicated) from 4-month-old BALB/c wild-type ($n = 12$) mice, a 10-month-old APP/PS1 transgenic mouse ($n = 1$) and recombinant mouse legumain ($n = 3$). The tissues were permeabilized with TBST. Solid line, mean values; error bands, SD. a.u., arbitrary units.

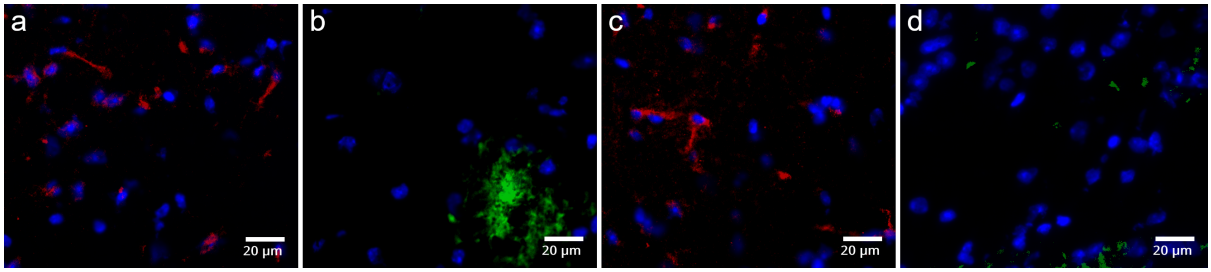

Figure 4.5: Representative fluorescence microscopy images of mouse brain cryosections. APP/PS1 transgenic mouse tissue stained with **a** monoclonal anti-IBA1 primary antibody (red; activated microglia) or **b** polyclonal anti-legumain primary antibody (green); APP/PS1 wild-type mouse tissue stained with **c** monoclonal anti-IBA1 primary antibody (red; activated microglia) or **d** polyclonal anti-legumain primary antibody (green). Nuclei were stained with DAPI and are shown in blue. Brain slices from one animal per group; 10 months of age.

4.3.5 Radiosynthesis of [^{11}C]CC11m

[^{11}C]CC11m was synthesized from commercially available compound 11 in a one-step reaction (Figure 4.6). The compound molar activity was 26.2 GBq/µmol and the radiochemical purity > 95 %.

4.3.6 PET/CT and biodistribution of [^{11}C]CC11m after dissection

To assess the *in vivo* distribution of [^{11}C]CC11m, we injected the tracer (9.45 MBq, 4.0 nmol/kg) into a 4-month-old BALB/c mouse and performed a PET scan. The mouse was dissected after the scan to obtain the tissue distribution (Figure 4.7). The scan shows high uptake in liver and kidneys and low uptake in the brain. Based on the biodistribution after dissection, the standardized uptake value (SUV) ratio tissue-to-muscle was 10.5 for the liver, 5.2 for the kidneys and 2.8 for the spleen. Both kidney and spleen express high levels of legumain in mice [27]. The brain SUV was 0.18 resulting in a SUV ratio

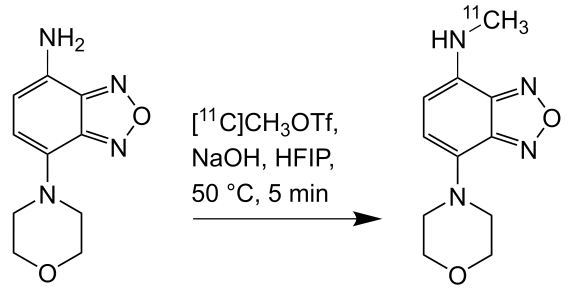

Figure 4.6: Synthesis of [^{11}C]CC11m.

brain-to-muscle of 1.3. The SUV ratio brain-to-blood was 0.5, which is higher than 0.05, the approximate cerebral blood volume ratio in whole-brain tissue, and indicates that the tracer can cross the BBB [109].

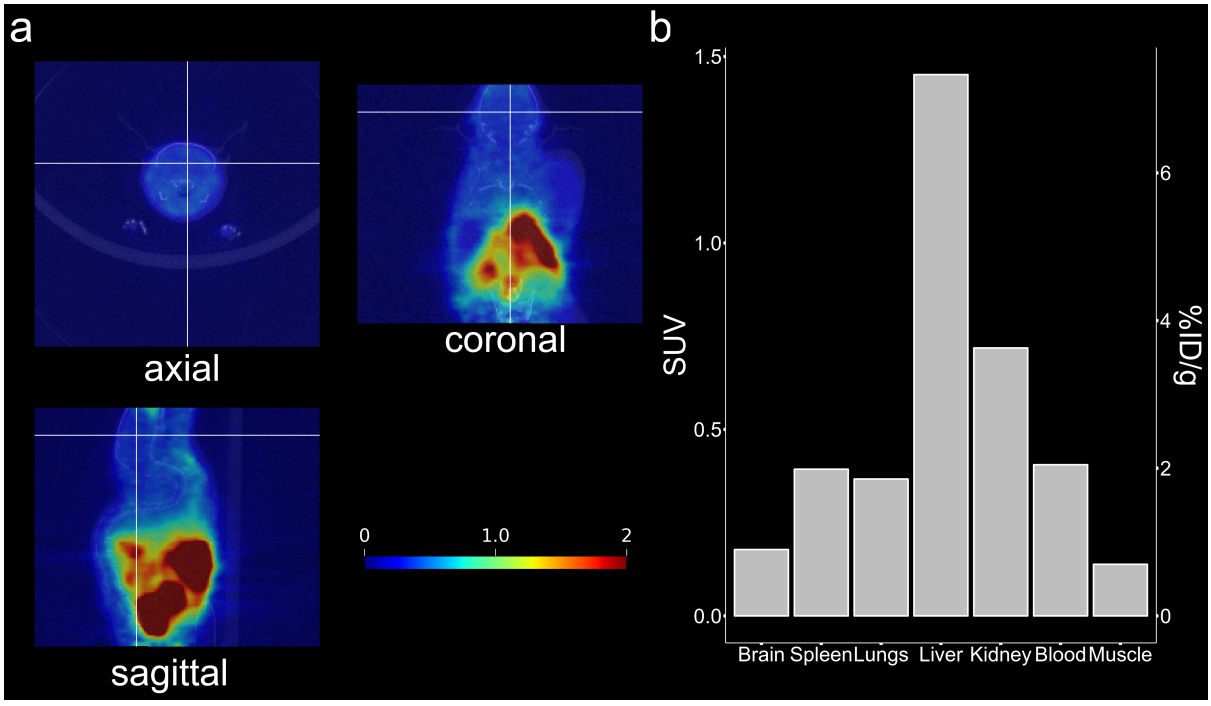

Figure 4.7: PET images and radioactivity distribution of [^{11}C]CC11m in a BALB/c mouse at 4 months of age. Mouse (19.8 g) injected with 9.45 MBq (4.0 nmol/kg) [^{11}C]CC11m. **a** PET images (0-60 min p.i., averaged from 0-60 min) superimposed on CT (axial, coronal, sagittal as indicated). Crosshair indicates image planes. PET, color bar and corresponding SUV are depicted on the bottom right. **b** Radioactivity distribution (SUV, left axis; %ID/g, right axis) after dissection 65 min p.i.. Note that the mouse carried a CT26 tumor as it was part of a different project (Chapter 2).

4.4 Discussion

In this pilot study, we evaluated the use of APP/PS1 transgenic mice for legumain-targeted PET. Furthermore, we synthesized the likely BBB-penetrant legumain ligand [^{11}C]CC11m and assessed its distribution *in vivo*.

We found that legumain RNA expression was higher in APP/PS1 transgenic mice than in wild-type controls at 10 months of age. Evidence suggests that legumain expression is

also elevated in wild-type animals at this age [217]. Using western blotting, we detected prolegumain ($\sim$56 kDa), and one form of active legumain ($\sim$46 kDa) in mouse brain lysates from APP/PS1 transgenic and wild-type mice. The molecular weight of the identified bands in the experiment is as expected based on the molecular weight of both legumain species reported in the literature [28, 35]. Visually, the amount of both prolegumain and active legumain was similar in wild-type and APP/PS1 transgenic mice, indicating that the ratio of activated legumain to prolegumain is approx. equal. We did not detect active legumain with a molecular weight of 36 kDa, as reported in mouse brain tissue from APP/PS1 transgenic mice by other groups [202, 218]. For the purpose of this study, we consider this finding negligible because both 46 kDa and 36 kDa legumain show identical protease activity [35].

Fluorescence microscopy of APP/PS1 brain slices showed a high abundance of activated microglia as indicated by IBA1 staining. This is in accordance with the literature according to which microglia activation is abundant in APP/PS1 mice [137]. The colocalization of legumain and microglia cells has been observed by others, it remains to be elucidated whether the legumain clusters in our fluorescence microscopy results are associated with microglia cells [210].

We found legumain in whole-brain tissue lysates from APP/PS1 mice to cleave fluorogenic substrate *in vitro* more efficiently than wild-type muscle tissue lysate from 4-month-old BALB/c mice. This indicates more active legumain in the brain than in the muscle, potentially translating into a difference in the PET signal. A comparison of whole-brain tissue lysates from APP/PS1 mice and wild-type mice was not conducted, because no difference was expected based on the western blot. Using the experimentally determined B_{max} (149.5 nM) and the estimated K_{i} of CC11m (89.3 nM), we calculated the binding potential according to Equation 4.1. The calculation resulted in a BP of 1.67, which is rather low compared to established neuroimaging PET tracers [56].

The PET scan with a 4-month-old BALB/c mouse showed high uptake in liver and kidneys. The biodistribution after dissection also revealed high uptake in the spleen which, together with the kidney, is among the organs with the highest legumain expression [27]. From the image, the brain signal of [^{11}C]CC11m is as high as in the muscle, indicating brain uptake. However, brain uptake could better be investigated using a mouse model with higher legumain expression in the brain.

Assessing the compound metabolization would be a crucial next step in the development of the legumain-targeting tracer. Finally, compound 11 binds allosterically in addition to binding to the active site [217]. An ideal tracer would bind exclusively to active legumain to avoid a dilution effect, as only the active form possesses the disease relevant protease activity and is present in significantly lower quantities than prolegumain [35]. To alleviate this problem, further developments in legumain PET neuroimaging might build upon BBB-penetrant P1-Asn peptidomimetics, which are specific for the active site of legumain and have strong affinity [101].

4.5 Conclusions

We investigated the use of tracer [^{11}C]CC11m with nanomolar binding affinity for *in vivo* PET imaging of legumain in APP/PS1 transgenic mice. While APP/PS1 transgenic mice express legumain in its active form in the brain, it is unclear as to whether the expression

is high enough to be detected with PET. While there is tracer uptake in the brain, the weak affinity in conjunction with the estimated $B_{\max}$ yields a BP close to 1, which is too low for PET imaging. Increasing tracer affinity and potentially adopting an animal model with a higher $B_{\max}$ would be paramount for the further studies. To specifically target active legumain, the development of a BBB-penetrant legumain PET tracer based on P1-Asn peptidomimetics would be more promising.

Chapter 5

SPECT imaging of CD80 using ^{99m}Tc-labeled CTLA-4-derived recombinant proteins

Author Statement

Severin K. Lustenberger: Conceptualization, Methodology (performed all experiments except for SPECT scan acquisition and experiments starting with ID 12** and SPR), Analysis (performed all data analysis), Writing (wrote first draft and corrected version), Project administration; **Claudia A. Castro Jaramillo**: Conceptualization, Funding acquisition, Methodology (SPR and SPECT scans with ID 10**), Writing (review); **Sandra Kreis**: Methodology (supported SPR); **Alain Blanc**: Methodology (supported experiments); **Jürgen Grünberg**: Materials/Data (protein production and purification); **Roger Schibli**: Supervision, Writing (review); **Martin Béhé**: Supervision, Writing (review); **Stefanie D. Krämer**: Supervision, Funding acquisition, Methodology (supported experimental planning), Analysis (supported data analysis), Writing (review), Project administration

Funding: This work was funded by the Swiss Cancer Research foundation, KFS-4900-08-2019

5.1 Background

Cancer is among the principal causes of death in the developed world [49]. In recent decades, cancer therapy has shifted from exclusively targeting the tumor cells to leveraging the cells in the tumor microenvironment (TME). So-called immune checkpoint inhibitors (ICIs) block co-inhibitory signals on cancer-killing T cells, thereby enabling the immune system to attack the tumor [189]. The two T cell surface proteins cytotoxic T lymphocyte antigen-4 (CTLA-4) and programmed cell death 1 (PD-1) along with its ligand PD-L1 are the targets of ICI therapy. CTLA-4 negatively regulates the activation of T cells through competing with CD28 for the co-stimulatory ligands CD80 and CD86 on antigen presenting cells [46,149]. PD-1 binds to PD-L1 and PD-L2, thereby inhibiting T cell activity. Consequently, CTLA-4 and PD-1 can cause T cell exhaustion and dormancy [167, 189]. Ipilimumab, a first-of-its-kind human anti-CTLA-4 monoclonal antibody, gained market approval from the FDA in 2011 for the treatment of melanoma [198]. In long-term studies, 22 % of treated patients with advanced melanoma benefited from a minimum extension of life span of 3 years [172]. In 2014, two fully human anti-PD1 mAbs pembrolizumab and nivolumab became the first FDA-approved anti-PD1 drugs [62]. Nivolumab improved survival from 42.1 % to 72.9 % in a group of patients in comparison to chemotherapy with dacarbazine [206]. Pembrolizumab administered to non-small-cell lung carcinoma patients, provided a 4.3-month increase in progression-free survival compared with platinum-based tumor therapy [164]. However, inconsistent responses to ICI therapy remain a persistent challenge. The overall response rate for various ICIs is $\sim$11 %, with patients generally maintaining their level of responsiveness throughout the treatment process [33]. Combination therapies increase response rates to levels exceeding 60 %. Unfortunately, the therapeutic success of such combination regimens is accompanied by toxicity-related adverse effects [105, 154]. A deeper understanding of the factors influencing ICI response and adverse effect profiles may enable practitioners to refine therapies, thereby improving response rates and mitigating adverse effects.

CD80, expressed on antigen presenting cells, plays a key role in ICI therapy through its interaction with CD28 and CTLA-4. Furthermore, CD80 can dimerize with PD-L1, extending the potential use to PD-1 targeting ICIs [221]. Clinically, high CD80 expression has been associated with high survival rates in nasopharyngeal carcinoma and was more frequently found in primary lesions compared to metastases of gastric carcinomas [26, 100]. In recent years, several studies have identified CD80 as a biomarker for disease progression and treatment response [7, 48, 171]. CD80 expression level detection is nonetheless absent in current clinical practice. The clinical need for standardized methods to monitor the expression and dynamics of such predictive biomarkers, has prompted the development of non-invasive imaging methods [103, 113].

Single-photon emission computed tomography (SPECT) imaging provides a non-invasive tool to detect and monitor the expression of CD80 in patients prior to treatment start and throughout the ICI therapy. In the past, our group has conducted proof-of-concept studies to image CD80/CD86 using ^{111}In-labeled belatacept in atherosclerosis, as well as ^{64}Cu-labeled abatacept in lipopolysaccharide-induced inflammation [126,187]. Both abatacept and belatacept are fusion proteins that consist of the Fc region of immunoglobulin IgG1 linked to the extracellular domain of CTLA-4 [1,2]. These molecules were specifically designed for therapeutic use, relying on a long plasma half-life, which is unsuitable for imaging purposes. Furthermore, CTLA-4-linked proteins bind to CD86 in addition to

CD80.

To address these shortcomings, we developed the small recombinant protein CACM-1 based on the extracellular domain of CTLA-4, devoid of the Fc region and introduced point mutations to improve the affinity and selectivity toward CD80 [24, 37]. In addition, we developed a dimeric version of CACM-1, termed CACM-2 (Figure 5.1). Both proteins were labeled with ^{99m}Tc for SPECT imaging. Herein, we present a detailed *in vivo* study of ^{99m}Tc-labeled CACM-1 and CACM-2. We performed SPECT scans of CT26 mouse colon carcinoma-bearing mice, which express CD80, with ^{99m}Tc-labeled CACM-1 and CACM-2 and monitored the biodistribution of the radiotracers.

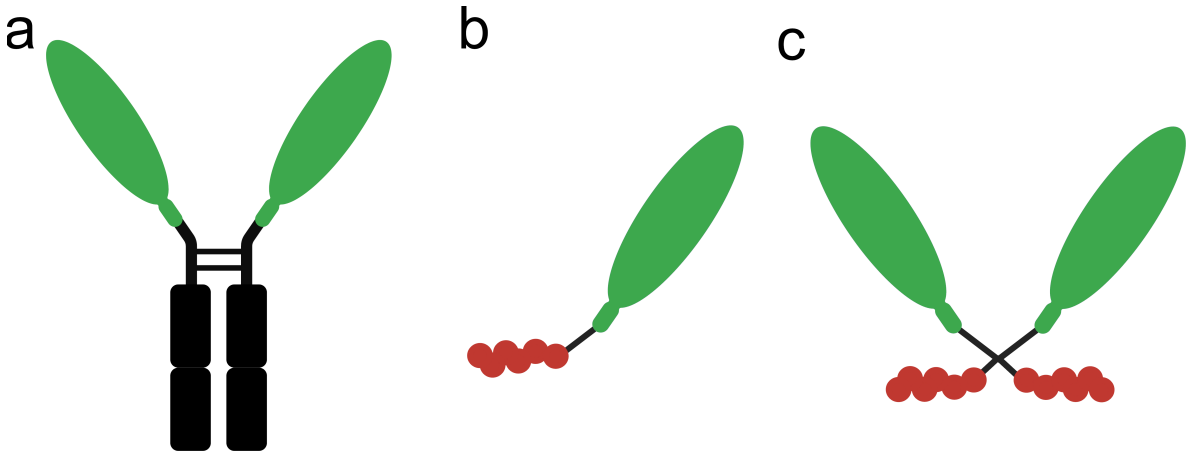

Figure 5.1: **a** Fc-fused, potency-optimized CTLA-4 moieties (green) [37]. **b** Affinity- and selectivity-improved, His_6-tagged (red) small recombinant protein CACM-1 (green, monomer) and **c** CACM-2 (green, dimer).

5.2 Methods

5.2.1 Cell culture

The murine colon carcinoma cell line CT26.WT (ATCC CRL-2638) was obtained from the American Type Culture Collection. The cells were cultured in Roswell Park Memorial Institute (RPMI) 1640 medium with GlutaMAX-I and 25 mM HEPES (gibco, Life Technologies, US). Culture medium was supplemented with 10 % fetal calf serum (FCS, Life Technologies, US), 10 000 U/ml penicillin and streptomycin (PS, gibco, Life Technologies, US) at 5 % CO_2 and 37 °C. At 80-95 % confluence, cells were detached with 0.05 % trypsin-EDTA solution (gibco, Life Technologies, US) and split 1 to 7 for sub-culture.

5.2.2 Mouse tumor inoculation

Animal studies were approved by the Zurich Cantonal Veterinary Office, Switzerland (licenses ZH28/2018, ZH28/2022), and conducted in accordance with Swiss Animal Welfare legislation. Female BALB/c and BALB/c nude mice, obtained from Charles River Laboratories (Sulzfeld, DE), were housed at 22 °C with a 12-hour light-dark cycle and had unlimited access to food and water. At the age of 14 weeks, mice were inoculated subcutaneously in the right shoulder region with either 8 * 10^5 CT26 cells or 4 * 10^6 MDA-MB-468 cells re-suspended in 100 µl matrigel (BD Biosciences, US). The studies

were conducted 7-12 days post CT26 cell inoculation and 15-20 days post MDA-MB-468 cell inoculation when tumors were clearly visible but no larger than 1.76 cm^3.

5.2.3 Flow cytometry

CT26 tumors were dissected and washed with PBS, pH 7.4 (gibco, Life Technologies, US). Tissue was chopped and incubated in 0.1 mg/ml DNAse I (11284932001, Roche, CH) and 1 mg/ml collagenase IV (1704-019, gibco, US) in PBS at 37 °C, shaking for 2 h. Tissue was homogenized using a micropipette and forced through a 70 µm cell strainer (Corning, US). Single cell suspension was spun down at 500 * g for 5 min at 5 °C and re-suspended in culture medium based on RPMI 1640 with GlutaMAX-I and 25 mM HEPES (gibco, Life Technologies, US) supplemented with 10 % heat-inactivated FCS and 10 000 U/ml penicillin and streptomycin (PS, gibco, Life Technologies, US). For counting, cells were diluted 1:1 with 0.4 % trypan blue solution (gibco, US), transferred to a counting chamber slide (Thermo Fisher Scientific, US) and inserted in an automated cell counter (Countess, Thermo Fisher Scientific, US). 100 000 - 400 000 cells per well were transferred to U-bottom 96-well plates (Greiner, AT) and spun down at 500 * g for 5 min at 5 °C. After removal of the supernatant, the cells were re-suspended in cell viability dye (Zombie Aqua, BioLegend, US) 1:1 000 in FACS buffer (2 mM EDTA in PBS containing 2 % (v/v) FCS) for 15 min and washed with FACS buffer. For fixation, cells were re-suspended in 1 % paraformaldehyde in FACS buffer and incubated for 10 min at 4 °C. After washing with FACS buffer, cells were re-suspended in Fc receptor blocking solution (Trustain FcX) 1:500 in FACS buffer followed by 10 min of incubation at 4 °C. Cells were washed with FACS buffer and incubated in FACS buffer containing antibody for 45 min at 4 °C. Cells were washed with FACS buffer (2 x) and re-suspended in FACS buffer. Measurements were performed on a flow cytometer (CytoFLEX S, Beckman Coulter, US). Compensation beads (UltraComp eBeads Plus, Thermo Fisher Scientific, US) were used to generate a compensation matrix for the given fluorophores. Isotype controls, fluorescence-minus-one samples and unstained cells were used to assist gating. FITC conjugated armenian hamster CD80-targeting antibody (104706, BioLegend, US) 1:500 in FACS buffer was used. Gating and data processing were performed in R using open-source packages [3, 51–53, 66, 130, 151].

5.2.4 Fluorescence microscopy

Dissected CT26 tumors were embedded in OCT compound mounting medium (Avantor, US), cut to 10 µm slices with a cryotome, thaw-mounted on microscopy slides and stored at -80 °C. For fluorescent staining, slices were thawed, left to dry and washed (3 * 5 min) in phosphate-buffered saline (PBS, gibco, Life Technologies, US). Tissue was encircled with a hydrophobic pen (Dako, DK) and fixed in 4 % paraformaldehyde in PBS for 10 min. Tissue was washed (3 * 5 min) in PBS and incubated in 5 % (w/v) powdered, skimmed milk in PBS on a benchtop rocker for 30 min. All subsequent incubation steps were performed protected from light on a benchtop rocker. Tissue was washed (3 * 5 min) in PBS and incubated with primary antibodies in PBS for 120 min. Tissue was washed w(3 * 5 min) in PBS and incubated with secondary antibodies in PBS for 30 min. Tissue was washed (3 * 5 min) in PBS and incubated with DAPI (BioLegend, US) 1:2 000 in PBS for 5 min. Tissue was washed (1 * 5 min) and sections were left to dry for 30 min. Cover slip was mounted with mounting medium (Mowiol, Kuraray, JP) and left to dry

for 30 min. Slides were stored at 5 °C for up to 4 weeks prior to image acquisition. For CD80 staining, rabbit CD80 targeting primary antibody (bs-2211R, Bioss, US) 1:100 and donkey Alexa Fluor 647 IgG secondary antibody (406414, BioLegend, US) 1:500 were used. Slides were scanned with a slide scanner (Pannoramic 250, 3DHistech, HU). Software provided by the manufacturer was used for image processing (3DHISTECH's Slide Converter version 2.3.2 and SlideViewer version 2.6).

5.2.5 Surface plasmon resonance

Binding kinetics were investigated using dextran-treated amine chips on a surface plasmon resonance (SPR) device (SPR-2, Sierra Sensors, DE). Ligands were immobilized using immobilization buffer (0.01 % (m/v) Tween-20 in PBS). The chip was equilibrated with 5 injection rounds of 100 mM HCl each followed by immobilization buffer. Activation of the chip was facilitated using 100 µl freshly prepared 1:1 mixture of 0.5 M 1-ethyl-3-(3-dimethylaminopropyl)carbodiimide and 0.2 M *N*-Hydroxysuccinimide. Subsequent injection of 20-40 µl 100 nM recombinant human CD80, mouse CD80, human CD86 or mouse CD86 from R&D Sytems (US) resulted in a response unit (RU) change of 150-250. Injection with 1 M ethanolamine deactivated unreacted chip surface. The protein-coated chip was kept under continuous flow of running buffer (0.01 % (m/v) Tween-20 in 50 mM trisaminomethane buffer, pH 7.4). Analytes were diluted with running buffer $\sim 10\,000$ x. For the measurement, 100 µl of each dilution was injected with an injection rate of 25 µl/min over 240 s. Non-linear fitting based on Langmuir isotherm (Equation 5.1) and analysis were performed in R using open-source packages [45, 209].

$$\text{Response} = \frac{\text{Response}_{\text{max}} \times \text{Concentration}_{\text{analyte}}}{K_{\text{D}} + \text{Concentration}_{\text{analyte}}} \tag{5.1}$$

5.2.6 Protein expression and purification

HEK-293 cells were obtained from the German Collection of Microorganisms (DE) and cultured in Dulbecco's modified Eagle's medium (DMEM) supplemented with 10 % fetal calf serum (FCS), 2 mM glutamine, 100 units/ml penicillin, 100 µg/ml streptomycin and 0.25 µg/ml fungizone (BioConcept, CH) at 37 °C, 5 % CO_2 and 95 % humidity. The DNA designed (Genewiz, DE) sequence as shown in Figure 5.13 was cloned into the HindIII/BamHI site of the mammalian expression vector pcDNA3.1(+) (Invitrogen, US) and transfected in HEK-293 cells. The amino acid sequence with stronger affinity and selectivity according to [37] is shown in 5.13. Clones were selected with Geneticin [64]. The proteins were separated from the medium using a Vivacell 250 filter with a cut off 10 000 MW (Sartorius DE). The proteins have a His_6 tag at the C-terminal end of the heavy chain for affinity purification via Ni-NTA agarose (Qiagen, NL) that was followed by size exclusion chromatography using a Superdex 75 column (Cytiva, US). The respective fractions were collected, pooled and stored at -20 °C. On the day of the experiment, the proteins were thawed and 10 µl of indicated fractions were analyzed on a 4-15 % gel without DTT (Figure 5.12). Laemmli buffer was added 1:1 and samples were incubated at 90 °C for 6 min. PBS was used as the running buffer. CACM-1 and CACM-2 were confirmed by comparison to a molecular weight marker (Biorad, US). Following confirmation, proteins were concentrated by ultracentrifugation in 10 000 MW spin columns (Thermo Fisher Scientific, US) at 2 000 * g for 20 min at 10 °C.

5.2.7 ^{99m}Tc production and radiolabeling

Using an established technetium labeling protocol, the His_6-tagged recombinant proteins were radiolabeled with ^{99m}Tc(I)-tricarbonyl with molar activity 12.1-28.1 GBq/µmol [197]. To prepare ^{99m}Tc(I)-tricarbonyl, pertechnetate ($^{99m}TcO_4^-$, 6 ml) eluted from a commercial generator (37.85 GBq, Mallinckrodt, NL) was added to a tricarbonyl kit (IsoLink, Mallinckrodt, NL) and heated to 95 °C for 20 min. The colorless, aqueous, technetium solution (pH 10-11) was brought to pH 6.5 by adding buffer solution (1 M HCl/0.6 M phosphate, 3/2 (v/v)). To perform the labeling, protein samples in PBS were mixed with technetium solution and incubated at 37 °C for 1 h. For the quality control, 1 µl labeling mixture was added to 50 µl PBS and analyzed by HPLC. A C18 reverse phase cartridge (Waters, US), UV detector (280 nm) and radiodetector were used. The mobile phase consisted of acetonitrile and 0.1 % (v/v) trifluoroacetic acid (TFA) in Milli-Q water. A solution gradient of 2-80 % acetonitrile and 98-20 % 0.1 % TFA over 5 min was applied. The flow rate was set to 1 ml/min.

5.2.8 SPECT/CT scans

Tumor-bearing mice were constrained and injected with tracer only (baseline conditions), and co-injected with 0.3 mg (0.750 µmol/kg, 0.375 µmol/kg) unlabeled reference compound (blocking conditions). Prior to starting the scans, mice were anesthetized with 2 % isofluorane in oxygen/air (1/1). Respiratory rate was kept at $\sim$60 min^{-1} through adjustment of isoflurane concentration and body temperature at 37 °C using heated air throughout the scan. Tracer was injected into tail vein at the indicated time point and dose. SPECT/CT scans were conducted with a four-head multiplexing multipinhole camera (NanoSpect/CT, Bioscan, US). The acquisition time per view depended on the injection-to-scan-time, resulting in varying scan times (Table 5.4). Anatomical information was obtained by CT following each SPECT acquisition. SPECT data were reconstructed with HiSPECT software (Scivis GmbH, DE), and images were generated with the Nucline Software (Bioscan, US). Image analysis was performed in python using community modules [69, 82, 117, 125, 212]. All radioactivity was decay-corrected to the time point of injection to the animal. Note: Scans performed with animals *post mortem* are listed in Table 5.4

5.2.9 Biodistribution after dissection

Following PET acquisition, tumor-bearing mice were euthanized through decapitation under anesthesia. Tissues were dissected and radioactivity determined with a gamma counter (Packard Cobra II Auto Gamma, PerkinElmer, US). To calculate the standard deviation of ratios between proteins error propagation according to Equation 5.2 was applied. Analysis was performed in R using open-source packages [209].

$$\sigma_R = \frac{\mu_A}{\mu_B}\sqrt{(\frac{\sigma_A}{\mu_A})^2 + (\frac{\sigma_B}{\mu_B})^2} \tag{5.2}$$

5.2.10 Statistical analysis

Statistical differences in radiotracer uptake or SUV ratios were analyzed by two-tailed paired or unpaired Student's t test, as indicated. Differences with $p < 0.05$ were considered

significant. Average values are shown with standard deviations and/or data range.

5.3 Results

5.3.1 CD80 expression in CT26 tumors

To determine the CD80 expression in CT26 tumors, we performed flow cytometry on cells isolated from dissected tumors ($n = 2$). The percentages of $CD80^+$ cells in the two samples were 2.75 % and 4.00 %, respectively. The gating stategy is depicted in Figure 5.10. To visualize CD80 expressing cells in the tissue, we performed fluorescence microscopy on cryosections of CT26 tumors. Images based on whole section scans showed the occurrence of $CD80^+$ cells sporadically throughout the tissue (Figure 5.2). The negative control stained with secondary antibody and without primary antibody is shown in Figure 5.11.

5.3.2 Fluorescence microscopy

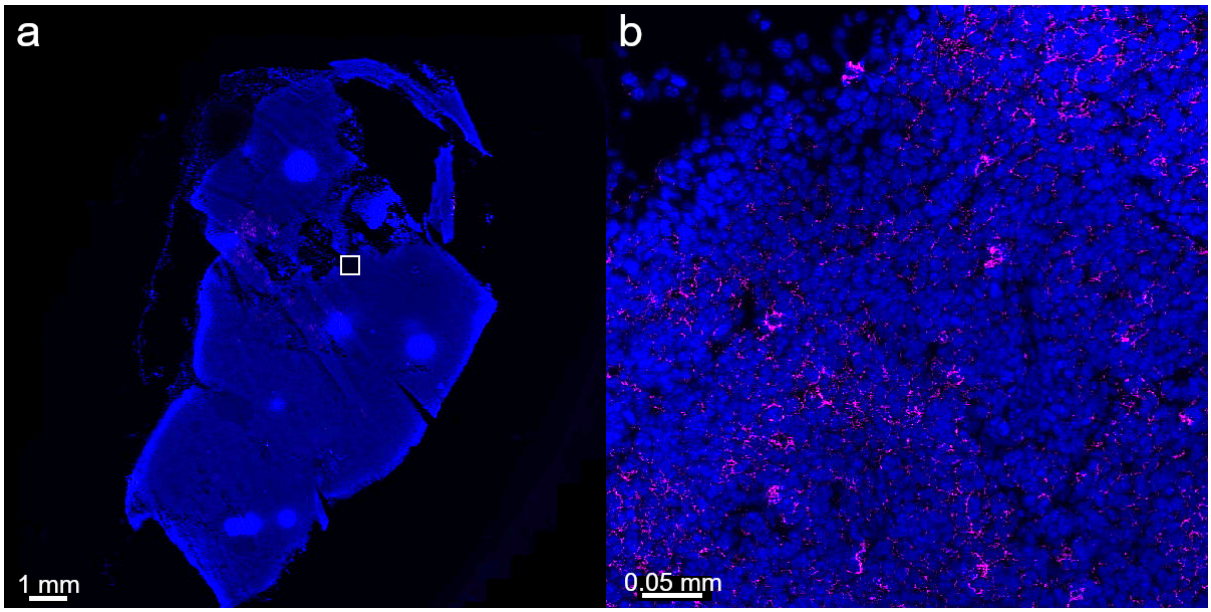

Figure 5.2: Representative fluorescence microscopy images of a CT26 tumor tissue slice. Cryosection stained with anti-CD80 primary antibody (purple; immune cells) and DAPI (blue; nuclei). **a** Complete section for overview. **b** Magnification of tumor periphery, corresponding to the white frame in **a**.

5.3.3 CACM-1 and CACM-2 radiolabeling with ^{99m}Tc

Radiolabeling of CACM-1 and CACM-2 with ^{99m}Tc was performed with ^{99m}Tc(I)-tricarbonyl at 37 °C for 1h [197]. The process is depicted in Figure 5.3. Assuming a molecular weight of 22 kDa (CACM-1) and 44 kDa (CACM-2), the molar activity was in the range of 12.1-28.1 GBq/µmol. The radiochemical purity for both proteins was above 95 % (Figure 5.15).

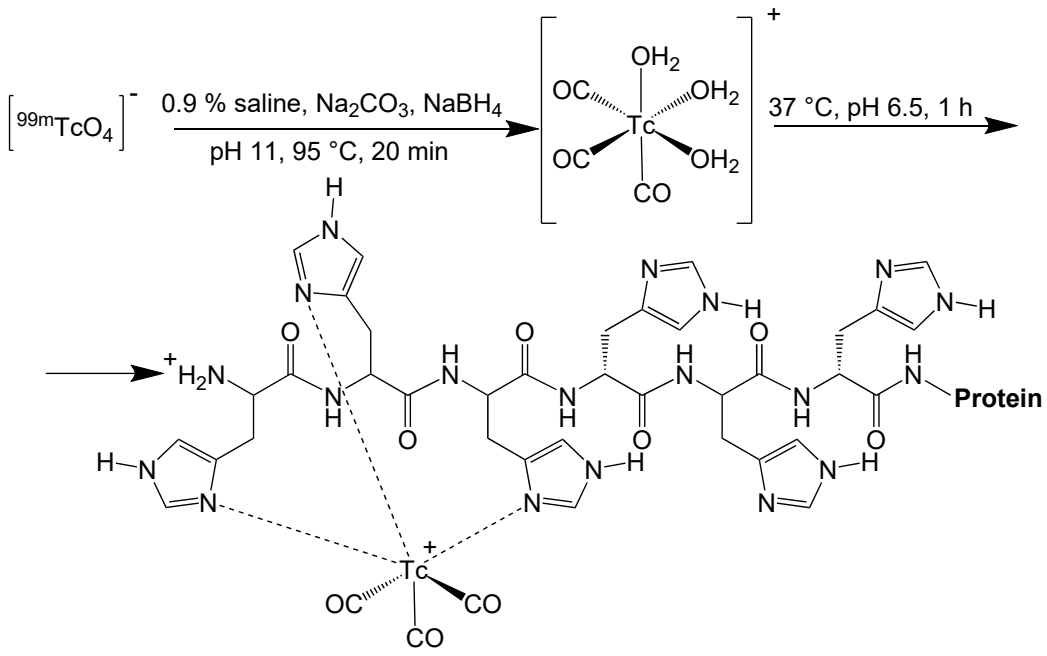

Figure 5.3: Conjugation procedure for ^{99m}Tc-CACM-1 and ^{99m}Tc-CACM-2.

Table 5.1: Dissociation constant (K_D [nM]) of CACM-1 and CACM-2 to mCD80, mCD86, hCD80 and hCD86. Determined by non-linear fit of SPR data according to Equation 5.1. One sample each. Non-linear fits are shown in Figure 5.14.

	mCD80	**mCD86**	**hCD80**	**hCD86**
CACM-1	45.8	831.8	3.6	62.2
CACM-2	10.3	1526.9	5.2	16.2

5.3.4 Surface plasmon resonance

By introducing point mutations to the CTLA-4 extracellular domain according to [37], we aimed at improving the affinity of the proteins toward CD80 and simultaneously weakening the affinity toward CD86. The affinities of CACM-1 and CACM-2 toward mouse CD80 (mCD80), mouse CD86 (mCD86), human CD80 (hCD80), and human CD86 (hCD86) were determined using surface plasmon resonance (SPR). The data was fitted to the Langmuir isotherm according to Equation 5.1. The fits as shown in 5.14 and the resulting K_D are listed in Table 5.1. Affinities toward hCD80 were stronger than toward mCD80 for both proteins. CACM-2 showed a stronger affinity toward mCD86 compared to CACM-1. CACM-1 had a 18-fold stronger affinity for mCD80 than for mCD86 and a 17-fold stronger affinity for hCD80 than for hCD86. In the case of CACM-1 the affinity for mCD80 was 148-fold stronger than for mCD86 and 3-fold stronger for hCD80 than for hCD86.

Table 5.2: Activity and dose ranges of scanned animals injected with ^{99m}Tc-CACM-1 or ^{99m}Tc-CACM-2. Molecule, protein injected; Condition, baseline (radiotracer only) or blocking (co-injection with excess protein); Time point, duration between injection and scan start; Activity range, range of injected activity in MBq or individual value if $n = 1$; Dose range, range of injected dose in nmol/kg or individual value if $n = 1$; n, number of animals. Note: Time points in the range 20-24 h are indicated as 24 h. Details on individual mice are listed in Table 5.4.

Molecule	**Condition**	**Time point [h]**	**Activity range [MBq]**	**Dose range [nmol/kg]**	**n**
CACM-1	Baseline	1	26.4	33.92	1
CACM-1	Baseline	4	6.1 - 26.4	7.10 - 37.46	4
CACM-1	Baseline	24	6.1 - 26.4	7.41 - 34.09	3
CACM-1	Block	4	5.4	34.44	1
CACM-1	Block	24	5.4	34.09	1
CACM-2	Baseline	1	22.9	28.56	1
CACM-2	Baseline	4	5.7 - 22.9	9.21 - 28.56	5
CACM-2	Baseline	24	5.7 - 22.9	9.46 - 27.51	3
CACM-2	Block	4	4.1 - 9.7	16.88 - 19.71	2
CACM-2	Block	24	5.1	18.04	1

5.3.5 SPECT with CT26 tumor-bearing mice

With the improved-affinity, ^{99m}Tc labeled CACM-1 and CACM-2, we performed SPECT/CT scans in CT26 tumor-bearing mice. The scans were conducted at 1 h, 4 h, and 24 h post injection (p.i.) of ^{99m}Tc-labeled CACM-1 or CACM-2 (baseline conditions). Where indicated, the tracer injection was accompanied by a 300 µg co-injection of the respective unlabeled protein (blocking conditions). The injected dose per time point (activity, molar mass) for both proteins is summarized in Table 5.2. Representative SPECT images of CT26 tumor-bearing mice injected with ^{99m}Tc-CACM-1 and ^{99m}Tc-CACM-2 are shown in Figure 5.4 and 5.5, respectively. All SPECT images are shown in Figure 5.16. From 1 h onward, there was high accumulation in the kidney and liver. At 4 h, activity accumulated visibly in the tumor. However, 24 h p.i., the activity in the tumor was similar to background (muscle) level. In the mice co-injected with 300 µg (0.75 µmol/kg) CACM-1, accumulation in the tumor was comparable to the baseline scans at 4 h and absent at 24 h p.i.. In contrast to ^{99m}Tc-CACM-1 injected mice, ^{99m}Tc-CACM-2 did not accumulate in the tumor at any time point (Figure 5.5). The activity was predominantly found in the liver and kidney. Co-injection of 300 µg (0.325 µmol/kg) CACM-2 did not alter the biodistribution of the tracer, as determined from the SPECT images. A panel of all scans is shown in Figure 5.17. Notably, scans at the same time point and comparable injected activity showed high interindividual heterogeneity in the tumor uptake (Figure 5.16 and 5.17).

5.3.6 Radioactivity distribution in dissected tissues

To further quantify the distribution of ^{99m}Tc-CACM-1 and ^{99m}Tc-CACM-2, we dissected the tissues of CT26 tumor-bearing animals 1 h, 4 h and 24 h p.i.. Kidney and liver tissue were excluded from the analysis due to SUV activity levels (> 50). Each animal

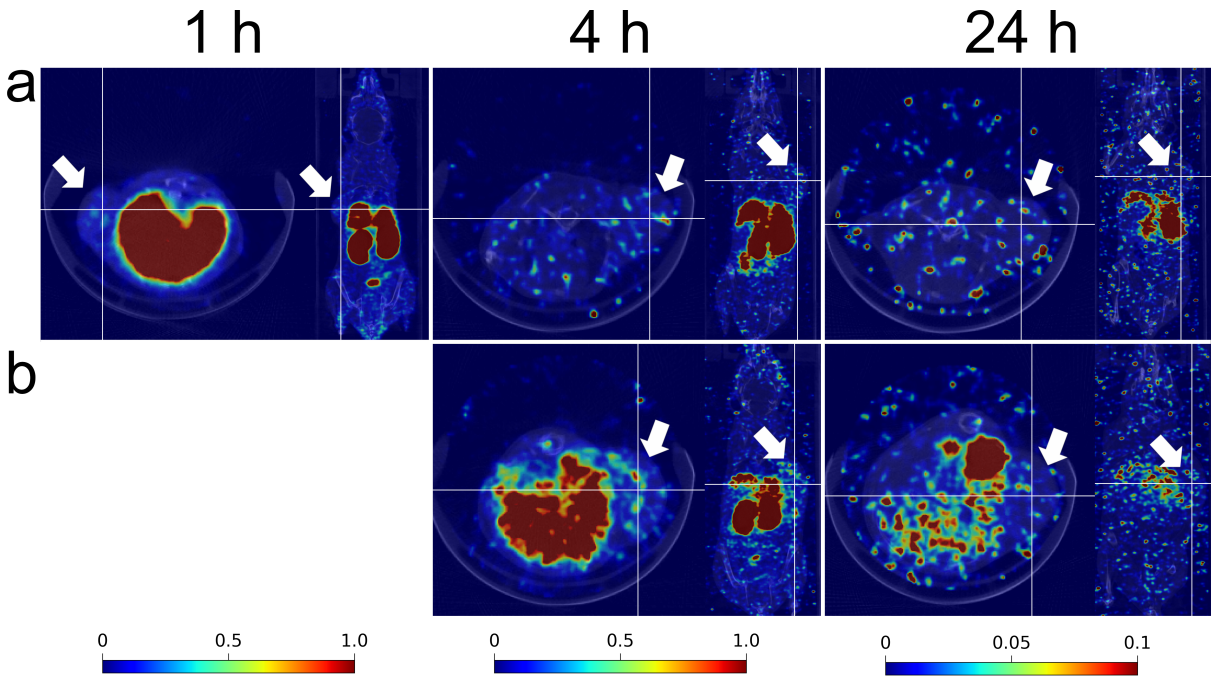

Figure 5.4: Representative SPECT images of ^{99m}Tc-CACM-1 in CT26 tumor-bearing mice (1, 4 and 24 h p.i., as indicated) superimposed on CT (axial, coronal). Tumors on shoulder (arrow). **a** Injected with ^{99m}Tc-CACM-1 and **b** co-injected with CACM-1 (0.75 µmol/kg). Mouse weights, activity at injection and scan duration: **a** 20.1 g, 26.4 MBq, 45 min (33.9 nmol/kg, 1 h); 20.1 g, 6.1 MBq, 40 min (33.9 nmol/kg, 4 h); 20.8 g, 6.1 MBq, 133 min (32.8 nmol/kg, 24 h). **b** 19.8 g, 5.4 MBq, 40 min (34.4 nmol/kg, 4 h); 20.0 g, 5.4 MBq, 133 min (34.1 nmol/kg, 24 h). SPECT, color bars and corresponding SUV are depicted at the bottom for each time point. CT, gray scale. SPECT images of all mice injected with ^{99m}Tc-CACM-1 are shown in Figure 5.16.

was injected with ^{99m}Tc-labeled protein alone (baseline conditions) or co-injected with unlabeled protein in excess (blocking conditions). The injected dose per time point (activity, molar mass) for both proteins is summarized in Table 5.3.

Mice injected with ^{99m}Tc-CACM-1 were co-injected with 0.75 µmol/kg CACM-1 under blocking conditions. The results are shown in Figures 5.6 (as SUV) and 5.7 (as percent injected dose per gram tissue, %ID/g). The SUV tumor-to-muscle ratio remained consistently above 1 at all time points. Specifically, at 1 h p.i. (3.78 ± 0.75, $p = 0.002$, $n = 6$ each tissue), 4 h p.i. (5.55 ± 0.66, $p = 10^{-6}$, $n = 6$ each tissue), and 24 h p.i. (4.56 ± 0.23, $p = 4{*}10^{-4}$, $n = 3$ each tissue). Additionally, the mean SUV spleen-to-muscle ratio at 1 h, 4 h, and 24 p.i., including animals under baseline and blocking conditions was 4.44 ± 1.48 ($p = 10^{-10}$, $n = 15$ each tissue). The mean SUV blood-to-muscle ratio was 1.51 ± 0.70 ($n = 15$ each tissue) and not significantly different from 1.

In the case of ^{99m}Tc-CACM-2, the mice were co-injected with 0.325 µmol/kg CACM-2 under blocking conditions. The results are shown in Figures 5.8 (as SUV) and 5.9 (as percent injected dose per gram tissue, %ID/g). The SUV tumor-to-muscle ratio was 3.03 ± 0.68 at 1 h p.i. ($p = 0.001$, $n = 7$ each tissue), 4.86 ± 1.36 at 4 h p.i. ($p = 0.003$, $n = 6$) and 5.56 ± 1.05 at 24 h p.i. ($p = 0.005$, $n = 3$ each tissue) and thus similar to ^{99m}Tc-CACM-1.

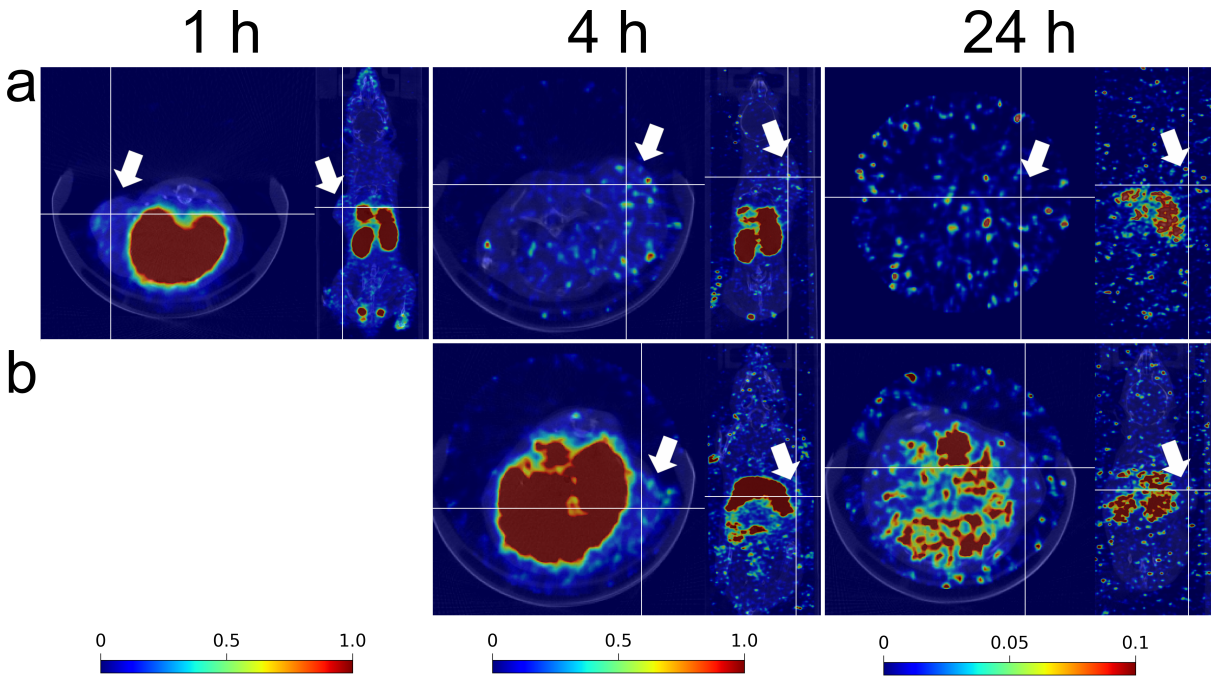

Figure 5.5: Representative SPECT images of ^{99m}Tc-CACM-2 in CT26 tumor-bearing mice (1, 4 and 24 h p.i., as indicated) superimposed on CT (axial, coronal). Tumors on shoulder (arrow). **a** Injected with ^{99m}Tc-CACM-2 and **b** co-injected with CACM-2 (0.325 µmol/kg). Mouse weights and activity at injection and scan duration: **a** 18.3 g, 22.9 MBq, 45 min (28.6 nmol/kg, 1 h); 18.8 g, 5.7 MBq, 40 min (18.1 nmol/kg, 4 h); 18.3 g, 5.7 MBq, 116 min (18.6 nmol/kg, 24 h). **b** 17.3 g, 4.1 MBq, 40 min (19.7 nmol/kg, 4 h); 18.9 g, 5.1 MBq, 133 min (18.0 nmol/kg, 24 h). SPECT, color bars and corresponding SUV are depicted at the bottom for each time point. CT, gray scale. SPECT images of all mice injected with ^{99m}Tc-CACM-2 are shown in Figure 5.17.

The SUV spleen-to-tumor ratio of ^{99m}Tc-CACM-2 (2.94 ± 0.64, $n = 16$) was higher ($p = 2 * 10^{-10}$) than in ^{99m}Tc-CACM-1 (0.96 ± 0.27, $n = 15$) including all time points and baseline as well as blocking conditions. Similarly, the mean SUV blood-to-muscle ratio was higher ($p = 8 * 10^{-7}$) in ^{99m}Tc-CACM-2 (7.66 ± 3.15, $n = 16$) than in ^{99m}Tc-CACM-1 (1.51 ± 0.70, $n = 15$) when all time points and baseline as well as blocking conditions were included.

Blocking the respective tracer in excess had no significant impact on the SUV at the tested time point (4 h, $n = 3$ each).

Table 5.3: Activity and dose ranges of animals injected with ^{99m}Tc-CACM-1 or ^{99m}Tc-CACM-2 and subsequently dissected to determine the activity distribution. Molecule, protein injected; Condition, baseline (radiotracer only) or blocking (co-injection with excess protein); Time point, duration between injection and euthanasia; Activity range, range of injected activity in MBq or individual value if $n = 1$; Dose range, range of injected dose in nmol/kg or individual value if $n = 1$; n, number of animals. Details on individual mice are listed in Table 5.4. Note: Time points in the range 20-24 h are indicated as 24 h.

Molecule	**Condition**	**Time point [h]**	**Activity range [MBq]**	**Dose range [nmol/kg]**	**n**
CACM-1	Baseline	1	3.2 - 6.5	32.62 - 38.96	6
CACM-1	Baseline	4	6.0 - 6.7	33.92 - 36.27	3
CACM-1	Baseline	24	5.5 - 6.5	37.88 - 38.52	3
CACM-1	Blocking	4	5.9 - 6.1	36.27 - 39.41	3
CACM-2	Baseline	1	2.6 - 6.5	16.88 - 18.83	6
CACM-2	Baseline	4	6.3 - 6.6	18.13 - 19.48	3
CACM-2	Baseline	24	6.1 - 6.2	17.94 - 19.82	3
CACM-2	Blocking	1	3.0	17.22	1
CACM-2	Blocking	4	5.2 - 5.7	18.04 - 18.23	3

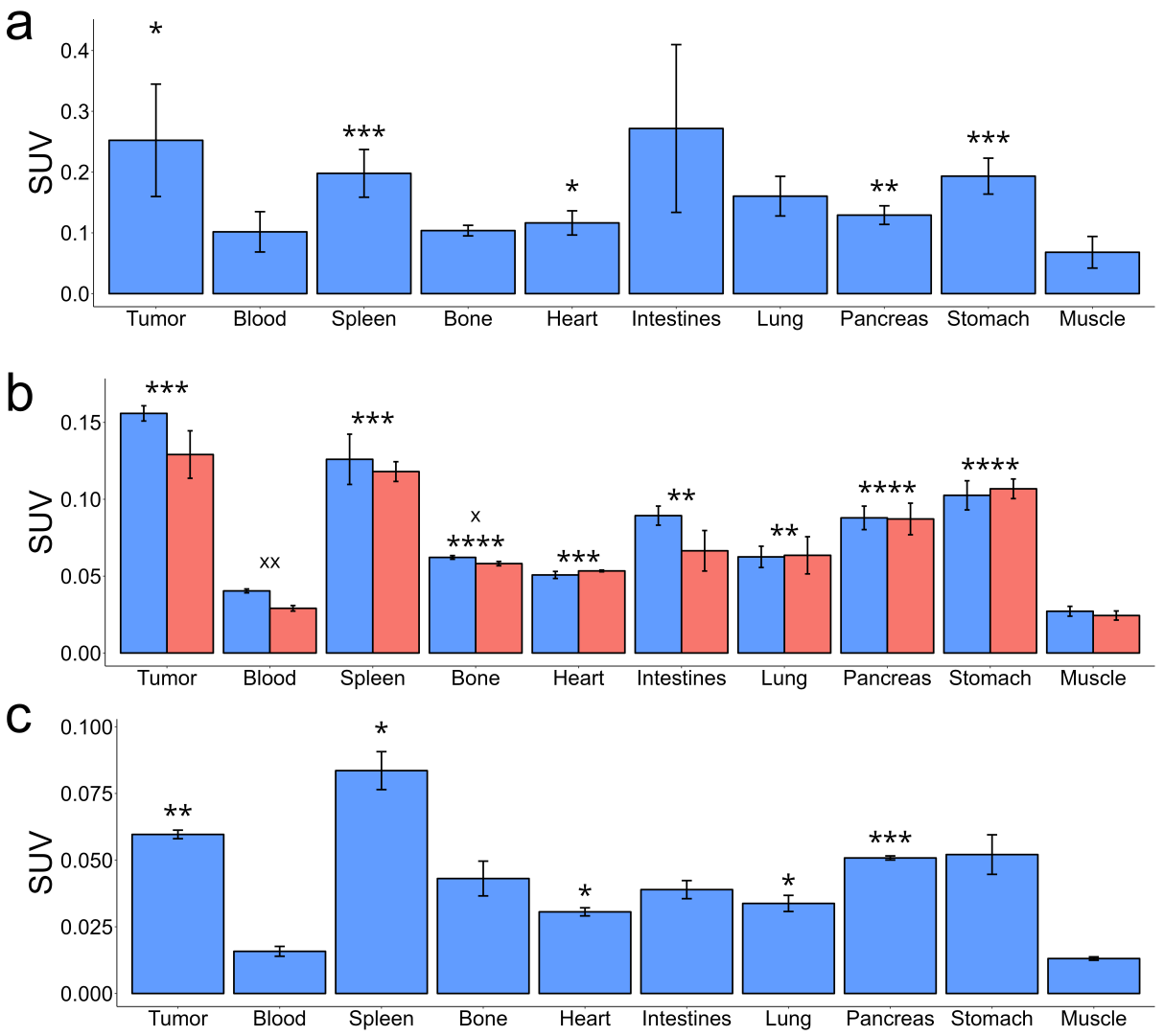

Figure 5.6: Biodistribution (SUV) of ^{99m}Tc-CACM-1 after dissection at 1 h (**a**), 4 h (**b**), and 24 h (**c**) p.i. of CT26 tumor-bearing mice. Mice studied by SPECT at 4 h and 24 h p.i. (Figure 5.4) were included. Blue bars, baseline conditions (tracer only). Red bars, blocking conditions (tracer co-administered with 0.75 µmol/kg CACM-1). Significance between each tissue and muscle with combined baseline and blocking SUV compared using student's paired t tests with Bonferroni correction is indicated by asterisks. Significance between baseline and blocking SUV using student's unpaired t tests without corrections for multiple comparisons is indicated by crosses. Error bars, SD; *, $p \leq 0.05$; **, $p \leq 0.01$; ***, $p \leq 0.001$; ****, $p \leq 0.0001$; x, $p \leq 0.05$; xx, $p \leq 0.01$; **a**, $n = 6$; **b**, $n = 3$ (baseline), $n = 3$ (blocking); **c**, $n = 3$. SUV, standardized uptake value. The same data is expressed as %ID/g in Figure 5.7. Note: Kidney and liver SUV were > 50 and not included in the plots.

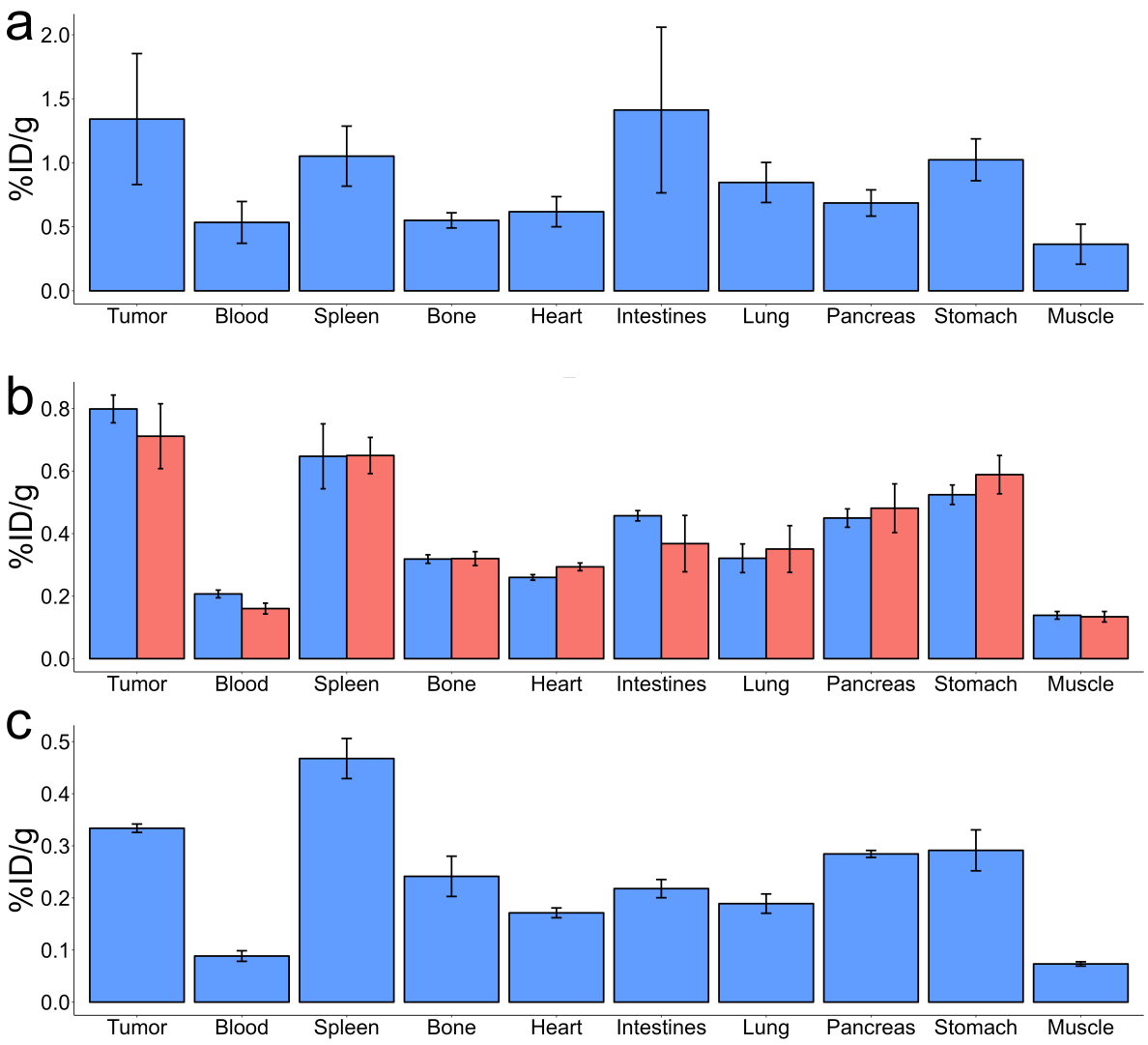

Figure 5.7: Biodistribution (%ID/g) of ^{99m}Tc-CACM-1 after dissection at 1 h (**a**), 4 h (**b**), and 24 h (**c**) p.i. of CT26 tumor-bearing mice. Mice studied by SPECT at 4 h and 24 h p.i. (Figure 5.4) were included. Blue bars, baseline conditions (tracer only). Red bars, blocking conditions (tracer co-administered with 0.75 µmol/kg CACM-1). Error bars, SD; %ID/g, percentage of injected dose per gram tissue. The same data is expressed as SUV in Figure 5.6. For significance see Figure 5.6. Note: Kidney and liver %ID/g were > 50 and not included in the plots.

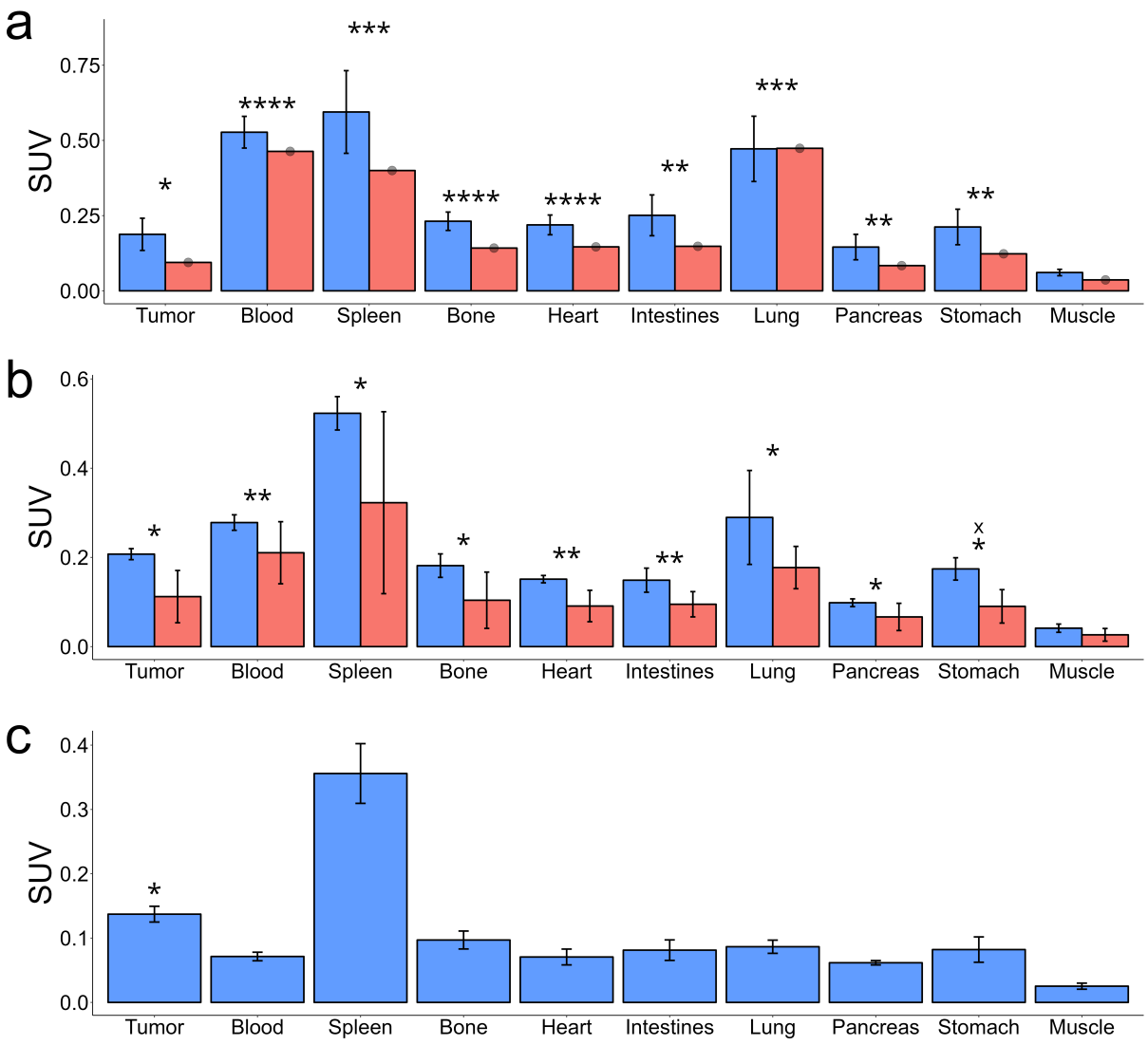

Figure 5.8: Biodistribution (SUV) of ^{99m}Tc-CACM-2 after dissection at 1 h (**a**), 4 h (**b**), and 24 h (**c**) p.i. of CT26 tumor-bearing mice. Mice studied by SPECT at 4 h and 24 h p.i. (Figure 5.4) were included. Blue bars, baseline conditions (tracer only). Red bars, blocking conditions (tracer co-administered with 0.325 µmol/kg CACM-2). Significance between each tissue and muscle with combined baseline and blocking SUV compared using student's paired t tests with Bonferroni correction is indicated by asterisks. Significance between baseline and blocking SUV using student's unpaired t tests without corrections for multiple comparisons is indicated by crosses. Error bars, SD; *, $p \leq 0.05$; **, $p \leq 0.01$; ***, $p \leq 0.001$; ****, $p \leq 0.0001$; x, $p \leq 0.05$; **a**, $n = 6$ (baseline), $n = 1$ (blocking); **b**, $n = 3$ (baseline), $n = 3$ (blocking); **c**, $n = 3$. SUV, standardized uptake value. The same data is expressed as %ID/g in Figure 5.9. Note: Kidney and liver SUV were > 50 and not included in the plots.

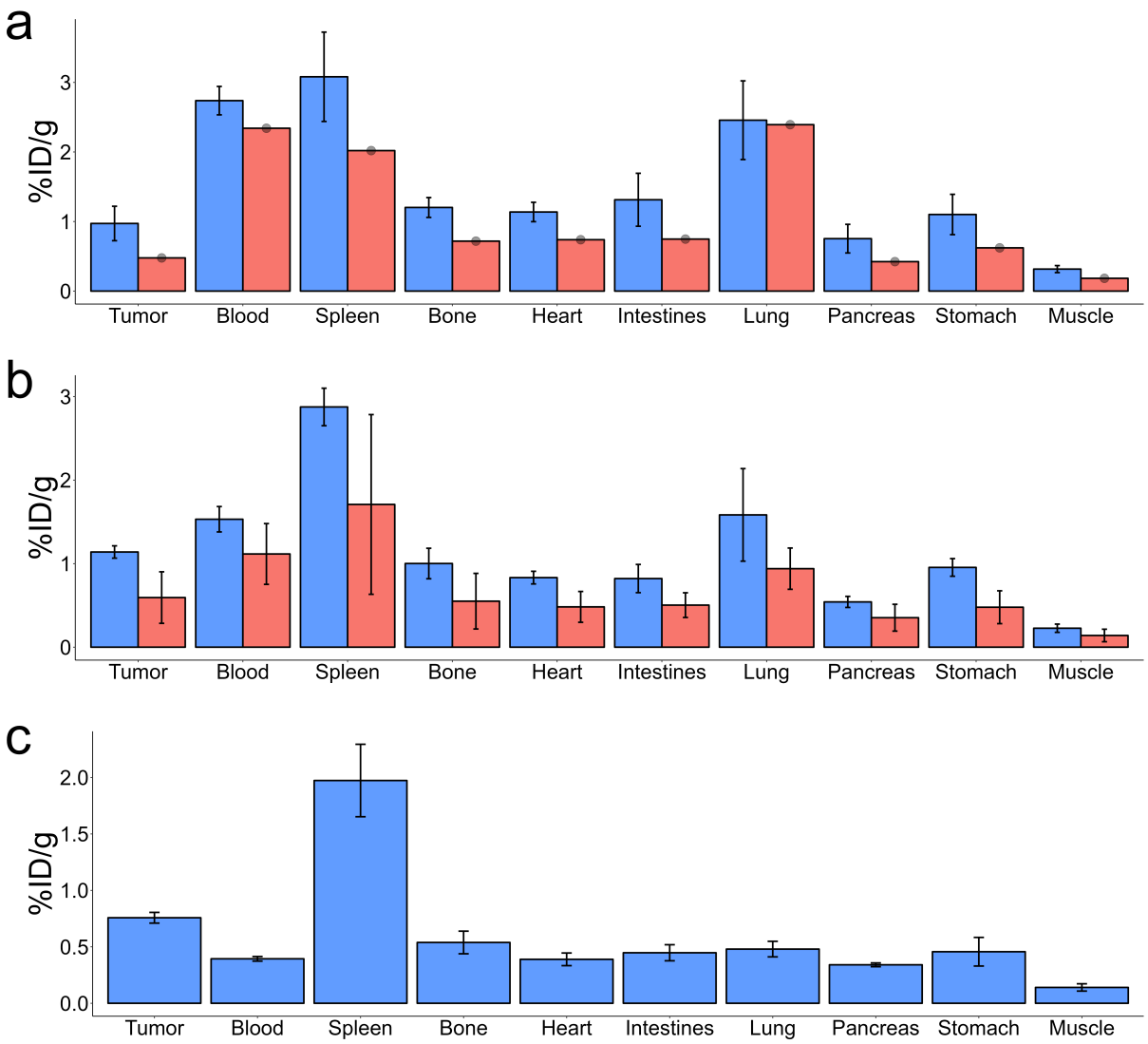

Figure 5.9: Biodistribution (%ID/g) of ^{99m}Tc-CACM-2 after dissection at 1 h (**a**), 4 h (**b**), and 24 h (**c**) p.i. of CT26 tumor-bearing mice. Mice studied by SPECT at 4 h and 24 h p.i. (Figure 5.4) were included. Blue bars, baseline conditions (tracer only). Red bars, blocking conditions (tracer co-administered with 0.325 µmol/kg CACM-2). Error bars, SD; %ID/g, percentage of injected dose per gram tissue. The same data is expressed as SUV in Figure 5.8. For significance see Figure 5.8. Note: Kidney and liver SUV were > 50 and not included in the plots.

5.4 Discussion

We have used the two novel proteins CACM-1 and CACM-2, previously developed by our group, for ^{99m}Tc SPECT imaging of CD80-expressing immune cells in CT26 tumor-bearing mice. Both proteins had yielded promising results *in vitro* [24]. CACM-1 and CACM-2 possessed strong affinity toward CD80 and selectivity over CD86. The SPECT scans and *ex vivo* biodistribution showed accumulation in the tumor compared to muscle tissue. However, other tissues were similarly high and administering unlabeled protein in excess did not alter the SUV. We confirmed the presence of CD80-expressing cells in CT26

tumors, as reported before by our group, by immunohistochemistry and flow cytometry.

Both proteins exhibited high renal and hepatic uptake. The His_6 tag used for protein purification and labeling in CACM-1 and CACM-2 has been shown to increase liver uptake in SPECT imaging tracers [79]. The small size of CACM-1 and CACM-2 (22 kDa and 44 kDa, respectively) might also contribute to the high kidney uptake due to excretion and reabsorption in the proximal tubules as it is commonly observed with such antibody fragments [196]. In contrast, negligible kidney uptake was reported for ^{64}Cu-abatacept, with a molecular weight of 92 kDa [1, 24].

While a SUV tumor-to-muscle ratio of > 3 across time points and for both ^{99m}Tc-CACM-1 and ^{99m}Tc-CACM-2 is indicative of successful CD80-targeting, the inability to block the ^{99m}Tc-labeled proteins with unlabeled proteins in excess opens up the question of binding specificity. One reason might be a high expression of CD80 leading to the inability of the unlabeled protein to block the labeled protein at the target site. This explanation cannot be ruled out due to the small amount of blocker (~ 20 times more unlabeled than labeled tracer). Determining the total density of receptors ($B_{\max}$) experimentally would be necessary to elucidate this finding.

Moreover, the enhanced permeability and retention (EPR) effect, which suggests an increased and non-specific accumulation of macromolecules in tumor tissue, might be involved [124]. An increased SUV blood-to-muscle ratio in ^{99m}Tc-CACM-2 compared to ^{99m}Tc-CACM-1 indicates impaired extravasation in the case of ^{99m}Tc-CACM-2 possibly due to the larger size.

Another explanation for the weak signal might be the molar activity range of 12.1-28.1 GBq/µmol, which led to small amounts of injected activity and in turn high scattering in SPECT, especially at 24 h p.i.. Low molar activity has been identified as an issue by others performing biomolecule-based ^{99m}Tc imaging [21].

^{99m}Tc is a widely used radionuclide for SPECT imaging and can be obtained from a ^{99}Mo/^{99m}Tc generator [89]. Our straightforward radiolabeling procedure makes use of the purification His_6 tag that is present CACM-1, CACM-2, and many other recombinantly produced proteins [78]. For ^{99m}Tc-CACM-1, the highest SUV tumor-to-muscle ratio was reached 4 h p.i., putting it in alignment with the half life of ^{99m}Tc, which is ~ 6 h [16]. Despite these promising results, low tumor uptake, high kidney and hepatic uptake and the inability to block the tracer with unlabeled protein in excess, prompt the need for further optimization of the proteins.

5.5 Conclusions

The CT26 tumor model provides a suitable platform for the *in vivo* evaluation of CD80-targeting proteins. The proteins CACM-1 and CACM-2 labeled with ^{99m}Tc can be used for SPECT imaging of CD80-expressing immune cells. The high SUV tumor-to-tissue ratio of ^{99m}Tc-CACM-1 renders it a more suitable candidate for further development than ^{99m}Tc-CACM-2. Further studies are needed to assess the binding specificity of the proteins and to optimize the biodistribution profile.

5.6 Supplementary material

5.6.1 Flow cytometry

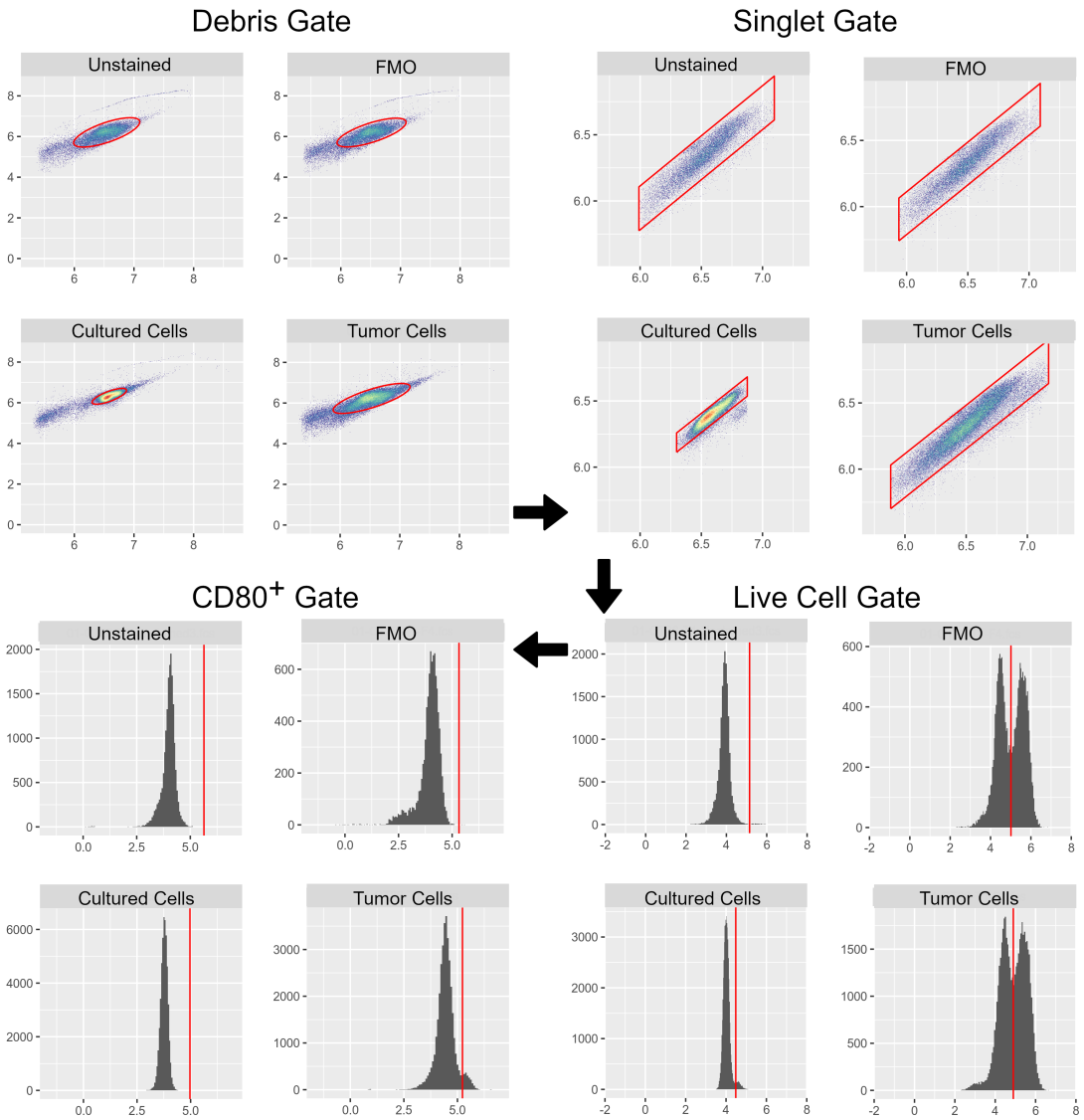

Figure 5.10: Flow cytometry gating strategy of CT26 cells isolated from dissected tumors or cultured *in vitro*. Unstained, unstained CT26 tumor cells exhibit no fluorescent dye labeling; FMO, CT26 tumor cells stained solely with a viability dye; Tumor cells, CT26 tumor cells stained with both a viability dye and anti-CD80 antibody; Cultured cells, cultured CT26 cells stained with both a viability dye and anti-CD80 antibody. Debris Gate, based on k-means clustering of data points in channels FSC-A vs. SSC-a, data points within the red circle are identified as cells. Singlet Gate, based on linear correlation of data points in channels FSC-A vs. FCS-H, cells within the red parallelogram are identified as individual, single cells. Live Cell Gate, based on minimum between two Zombie Aqua channel intensity histogram maxima, single cells to the left of red separating line are identified as viable. $CD80^+$ Gate, based on minimum between two CD80 channel intensity histogram maxima, viable cells to the right of red separating line are classified as CD80-expressing immune cells.

5.6.2 Fluorescence microscopy

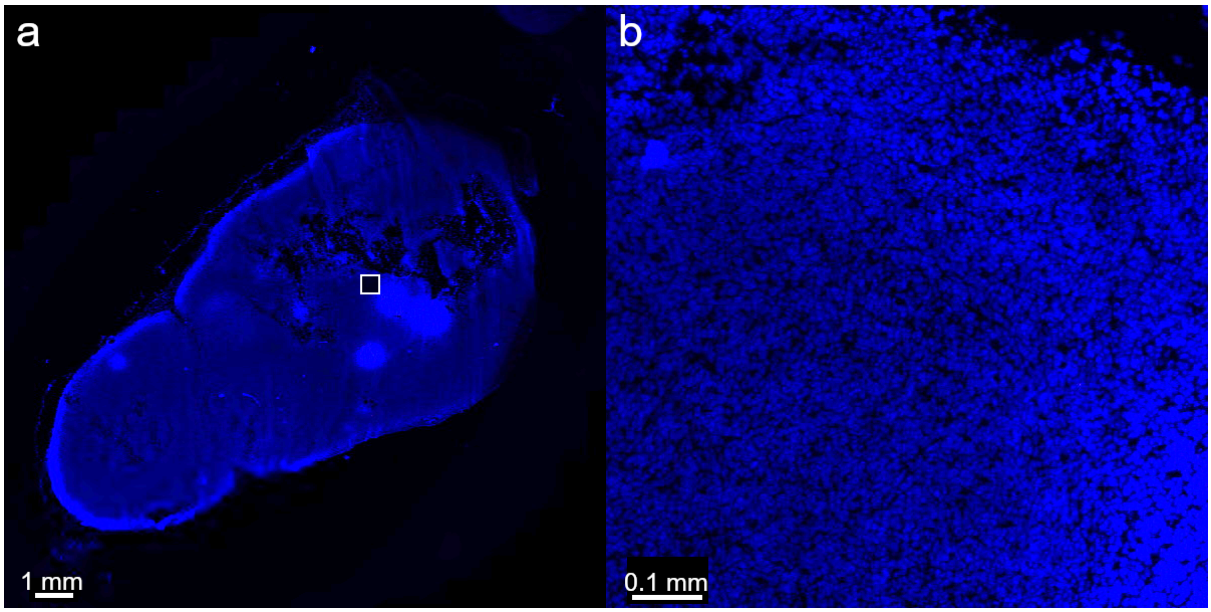

Figure 5.11: Representative fluorescence microscopy images of a CT26 tumor tissue slice. Cryosection stained with Alexa Fluor 647 IgG secondary antibody (purple) and DAPI (blue; nuclei). **a** Complete section for overview. **b** Magnification of tumor periphery, corresponding to the white frame in **a**.

5.6.3 Protein production and purification

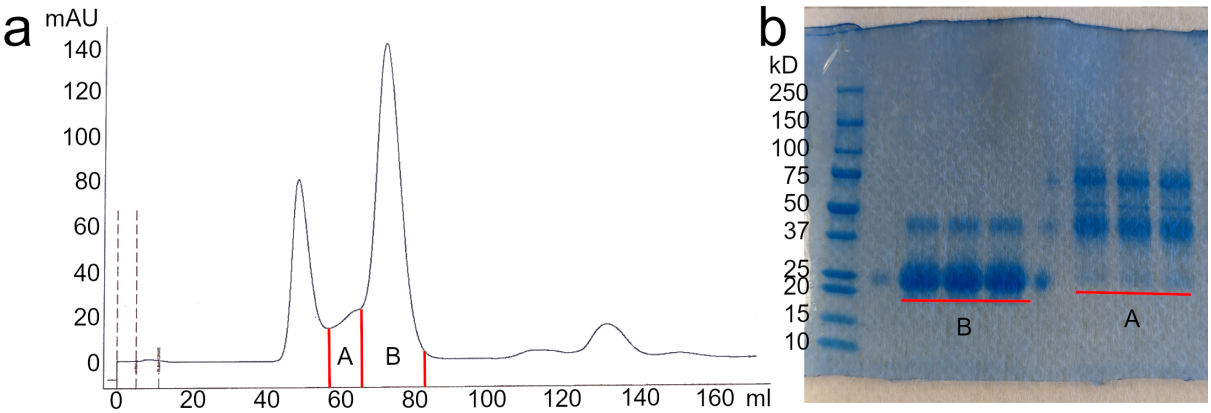

Figure 5.12: Analysis of products CACM-1 and CACM-2. **a** Fractionation SEC chromatogram with indication of fractions used for down-stream processing. A, CACM-2; B, CACM-1. The fractions were pooled and analyzed by SDS-PAGE. Note: Ticklabels were added after the chromatogram was recorded to improve readability. **b** SDS-PAGE gel of the pooled fractions right before radiolabeling. Lanes B, CACM-1; Lanes A, CACM-2.

MACLGFQRHKAQLNLATRTWPCTLLFFLLFIPVFCKAMHVAQPAVVLASSRGRASFVCEYTNPSKATEVRVTV
LRQADSQVTEVCAATYMMGNEATFLDDSICTGTASGNQVNLTIQGLRAQDTGLYICQVELMYPPPYYLGIGNG
TQIYVIAKEKKPSYNRGLCENAPNRARMEQKLISEEDLNMHTGHHHHHH

Figure 5.13: Amino acid sequence of CACM-1 and CACM-2. The signaling peptide is highlighted.

5.6.4 SPR

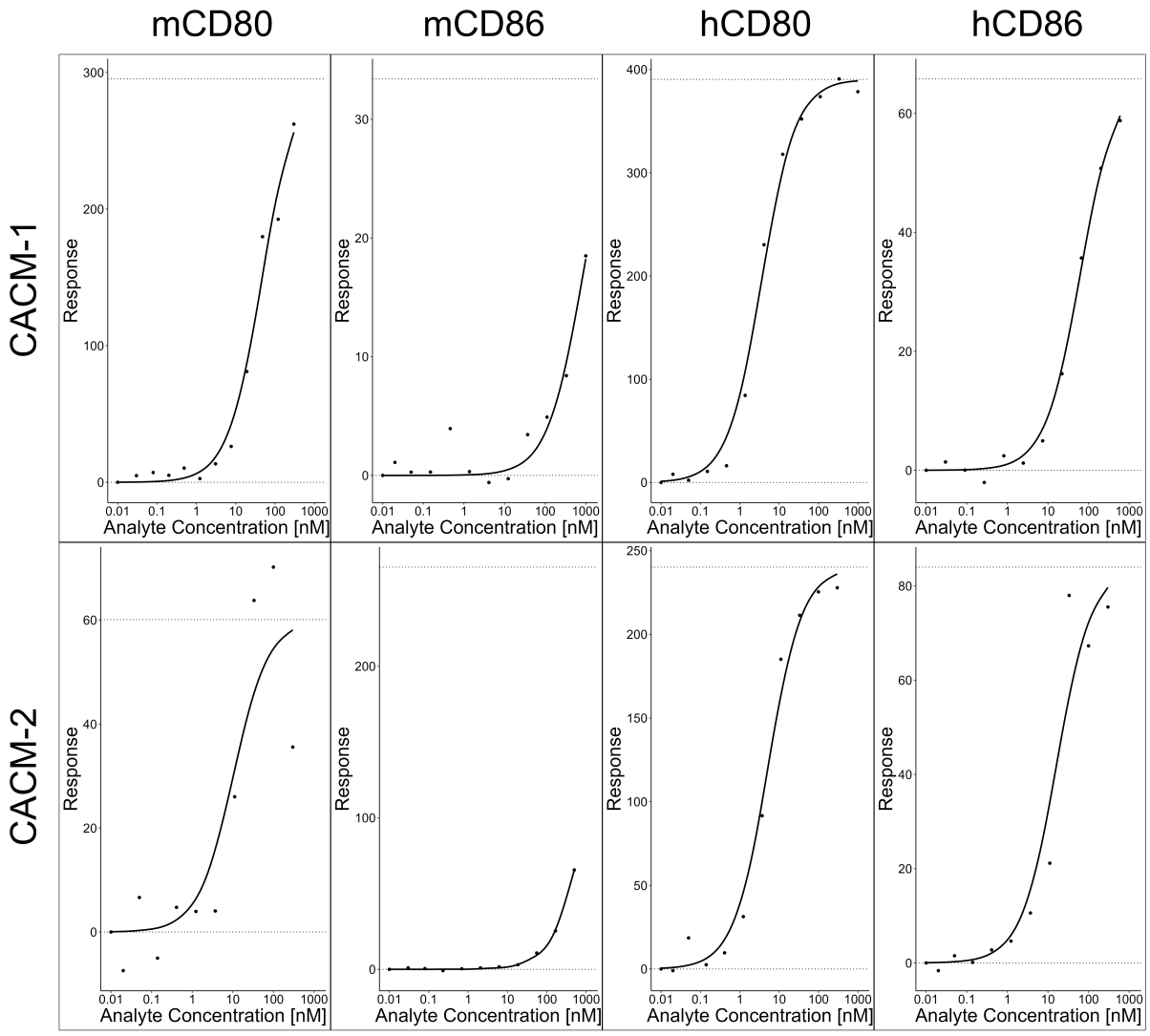

Figure 5.14: Analyte concentration vs. SPR response of CACM-1 and CACM-2 to mouse CD80 (mCD80), mouse CD86 (mCD86), human CD80 (hCD80) and human CD86 (hCD86). Symbols, data points; solid lines, non-linear fits; dotted lines, minimum and maximum response. Note: Each data point represents one measurement.

5.6.5 RP HPLC chromatograms

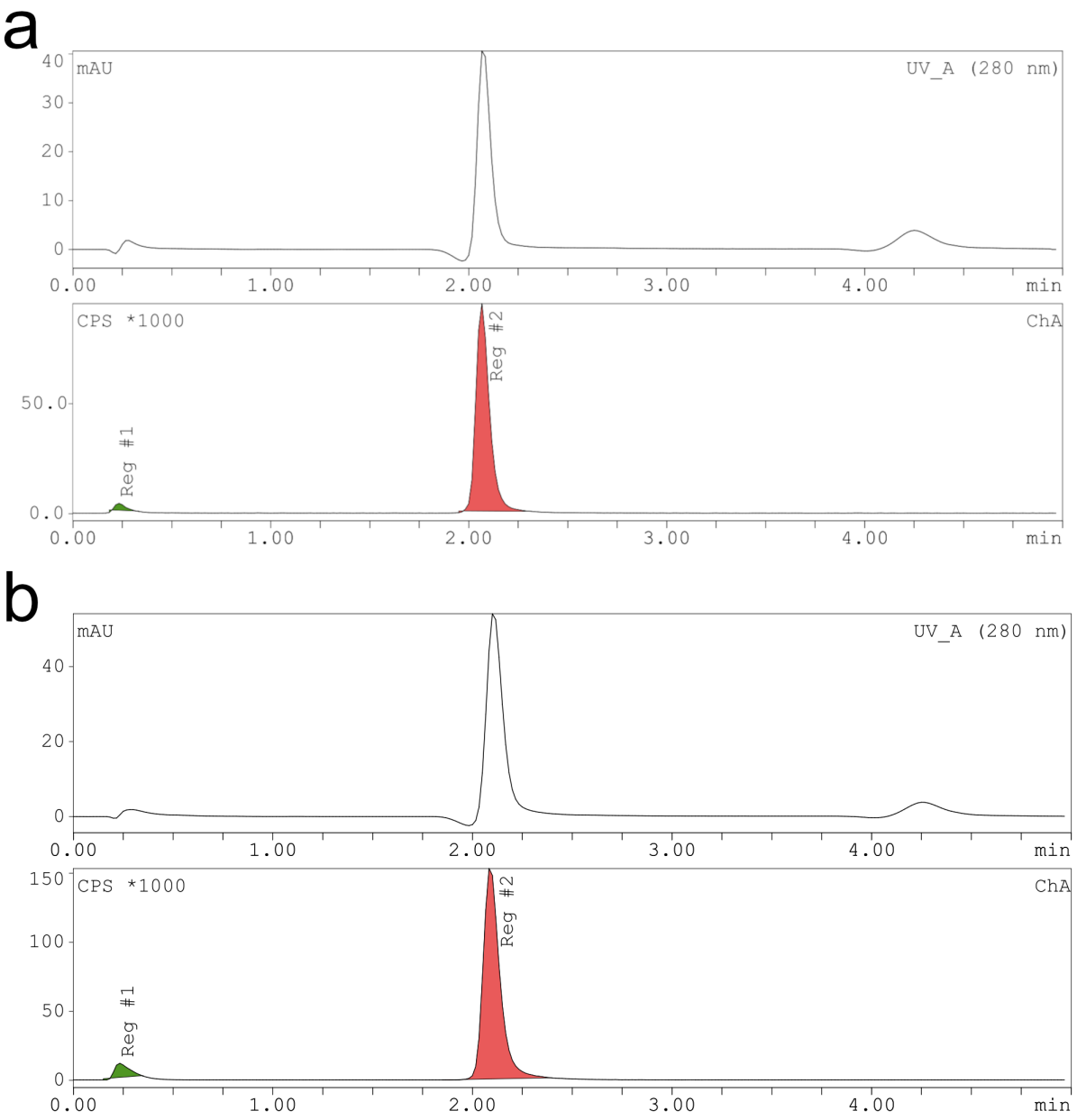

Figure 5.15: Reverse phase HPLC chromatograms of ^{99m}Tc-CACM-1 and ^{99m}Tc-CACM-2. UV signal measured at 280 nm. Retention time and, where applicable, % area were determined. **a**, ^{99m}Tc-CACM-1 2.07 min (97.75 %). **b**, ^{99m}Tc-CACM-2 2.10 min (95.00 %).

5.6.6 SPECT scans

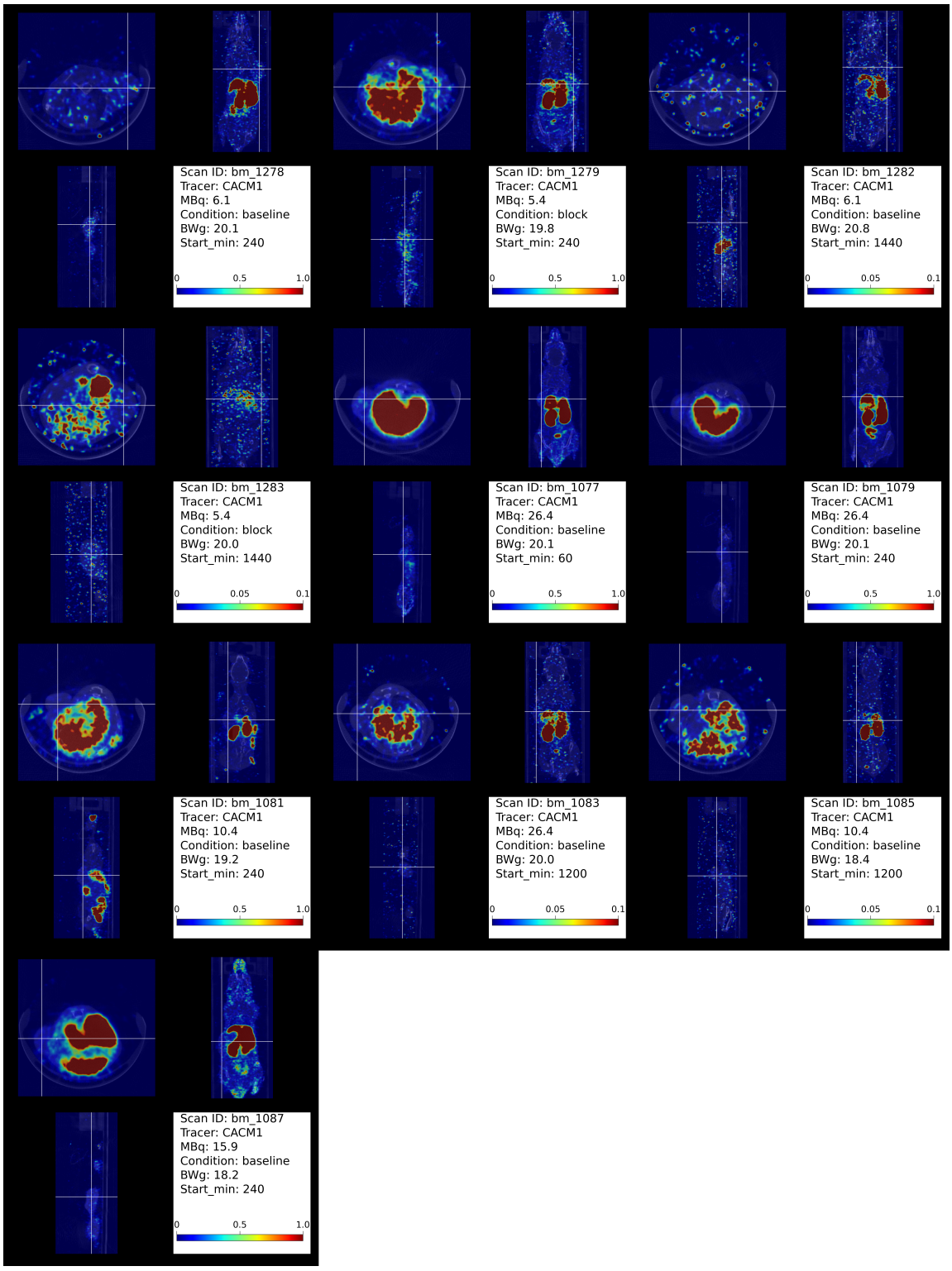

Figure 5.16: SPECT images of ^{99m}Tc-CACM-1 in CT26 tumor-bearing mice (1, 4 and 24 h p.i., as indicated) superimposed on CT (axial, coronal, saggital). CT26 tumors on shoulder. Baseline condition, mouse injected with ^{99m}Tc-CACM-1. Blocking condition, tracer co-injected with 0.75 µmol/kg CACM-1. Crosshairs indicate image planes (in tumor region). PET, color bar for the corresponding SUV; CT, gray scale. MBq, activity at injection in MBq; BWg, body weight in g; Start_min, start of the scan after injection in min.

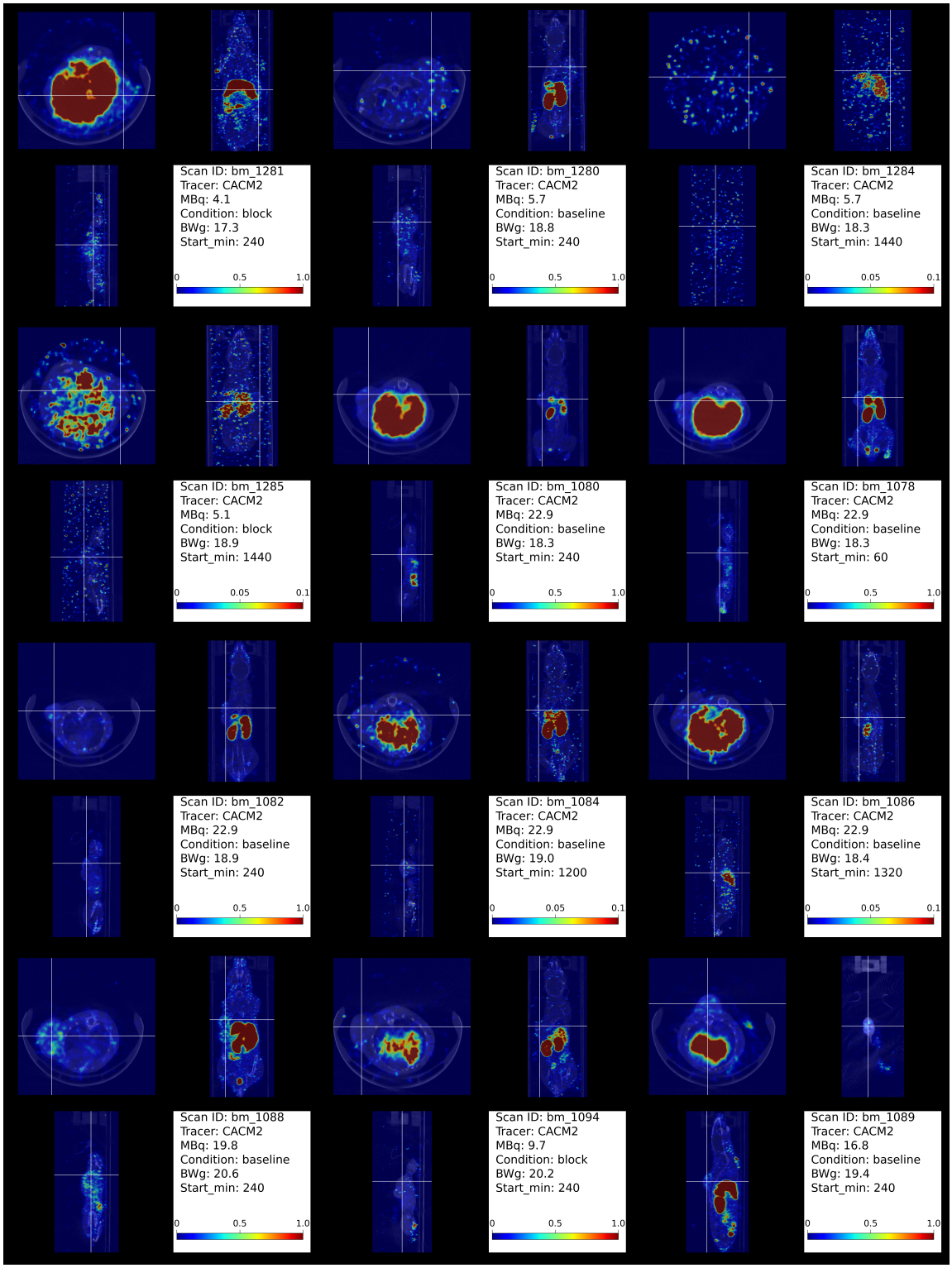

Figure 5.17: SPECT images of ^{99m}Tc-CACM-2 in CT26 tumor-bearing mice (1, 4 and 24 h p.i., as indicated) superimposed on CT (axial, coronal, saggital). CT26 tumors on shoulder. Baseline condition, mouse injected with ^{99m}Tc-CACM-2. Blocking condition, tracer co-injected with 0.325 µmol/kg CACM-2. Crosshairs indicate image planes (in tumor region). PET, color bar for the corresponding SUV; CT, gray scale. MBq, activity at injection in MBq; BWg, body weight in g; Start_min, start of the scan after injection in min.

5.6.7 Detailed information on mice

Table 5.4: Detailed information on mice that were summarized in Table 5.2 and 5.3. ID, unique identifier; Molecule, protein injected; Condition, baseline (radiotracer only) or blocking (radiotracer with excess protein); Time point, duration between injection and scan start or euthanasia in case of biodistribution; Activity, injected activity in MBq; Dose, injected dose in nmol/kg; Scan duration, duration of the scan in min; Experiment, type of experiment (SPECT or biodistribution).

ID	Molecule	Condition	Time point [min]	Activity [MBq]	Dose [nmol/kg]	Scan duration [min]	Experiment
1077	CACM-1	Baseline	60	26.4	33.92	45	SPECT
1078	CACM-2	Baseline	60	22.9	28.56	45	SPECT
1079	CACM-1	Baseline	240	26.4	33.92	45	SPECT
1080	CACM-2	Baseline	240	22.9	28.56	45	SPECT
1081	CACM-1	Baseline	240	10.4	7.10	45	SPECT
1082	CACM-2	Baseline	240	22.9	9.21	45	SPECT
1083	CACM-1	Baseline	1200	26.4	34.09	60	SPECT
1084	CACM-2	Baseline	1200	22.9	27.51	67	SPECT
1085	CACM-1	Baseline	1200	10.4	7.41	112	SPECT
1086	CACM-2	Baseline	1320	22.9	9.46	60	SPECT
1087	CACM-1	Baseline	240	15.9	37.46	40	SPECT
1088	CACM-2	Baseline	240	19.8	16.55	45	SPECT
1089	CACM-2	Baseline	240	16.8	17.57	45	SPECT
1094	CACM-2	Blocking	240	9.7	16.88	45	SPECT
1278	CACM-1	Baseline	240	6.1	33.92	40	SPECT
1279	CACM-1	Blocking	240	5.4	34.44	40	SPECT
1280	CACM-2	Baseline	240	5.7	18.13	40	SPECT
1281	CACM-2	Blocking	240	4.1	19.71	40	SPECT
1282	CACM-1	Baseline	1440	6.1	32.78	133	SPECT
1283	CACM-1	Blocking	1440	5.4	34.09	133	SPECT
1284	CACM-2	Baseline	1440	5.7	18.63	116	SPECT
1285	CACM-2	Blocking	1440	5.1	18.04	133	SPECT
1_1	CACM-1	Baseline	60	6.1	35.89	not applicable	Biodis
1_2	CACM-1	Baseline	60	6.5	32.62	not applicable	Biodis
1_3	CACM-1	Baseline	60	6.1	37.46	not applicable	Biodis
2_1	CACM-1	Baseline	240	6.7	33.92	not applicable	Biodis
2_2	CACM-1	Baseline	240	6.5	34.61	not applicable	Biodis
2_3	CACM-1	Baseline	240	6.0	36.27	not applicable	Biodis
3_1	CACM-1	Blocking	240	6.1	36.86	not applicable	Biodis
3_2	CACM-1	Blocking	240	6.0	36.27	not applicable	Biodis
3_3	CACM-1	Blocking	240	5.9	39.41	not applicable	Biodis
4_1	CACM-1	Baseline	1440	6.5	38.52	not applicable	Biodis
4_2	CACM-1	Baseline	1440	6.5	37.88	not applicable	Biodis
4_3	CACM-1	Baseline	1440	5.5	38.09	not applicable	Biodis
5_1	CACM-2	Baseline	60	6.5	17.13	not applicable	Biodis
5_2	CACM-2	Baseline	60	6.3	18.83	not applicable	Biodis
5_3	CACM-2	Baseline	60	6.3	17.85	not applicable	Biodis
6_1	CACM-2	Baseline	240	6.6	19.48	not applicable	Biodis
6_2	CACM-2	Baseline	240	6.5	18.13	not applicable	Biodis
6_3	CACM-2	Baseline	240	6.3	18.63	not applicable	Biodis
7_1	CACM-2	Blocking	240	5.2	18.04	not applicable	Biodis
7_2	CACM-2	Blocking	240	5.3	18.23	not applicable	Biodis
7_3	CACM-2	Blocking	240	5.7	18.04	not applicable	Biodis
8_1	CACM-2	Baseline	1440	6.1	17.94	not applicable	Biodis
8_2	CACM-2	Baseline	1440	6.2	18.83	not applicable	Biodis
8_3	CACM-2	Baseline	1440	6.1	19.82	not applicable	Biodis
9_1	CACM-2	Baseline	60	2.6	18.23	not applicable	Biodis
9_2	CACM-2	Baseline	60	3.1	17.57	not applicable	Biodis
9_3	CACM-2	Baseline	60	3.0	16.88	not applicable	Biodis
12_1	CACM-2	Blocking	60	3.0	17.22	not applicable	Biodis
10_1	CACM-1	Baseline	60	3.4	35.51	not applicable	Biodis
10_2	CACM-1	Baseline	60	3.3	38.96	not applicable	Biodis
10_3	CACM-1	Baseline	60	3.2	36.46	not applicable	Biodis

Chapter 6

Augmenting radiotracer development with radioluminescence microscopy: Integration in the immunohistochemical staining workflow

Author Statement

Severin K. Lustenberger: Conceptualization, Methodology (equal contribution to image acquisition, performed all other experimental steps except for PET scans), Analysis (performed all data analysis), Writing (wrote first draft and corrected version), Project administration; **Aro Delparente**: Methodology (equal contribution to image acquisition); **Luca Camenzind**: Methodology (supported image analysis); **Nicholas P. van der Meulen**: Materials/Data (provided $^{64}CuCl_2$); **Chiara Favaretto**: Materials/Data (provided $^{64}CuCl_2$); **Chrsitoph R. Bauer**: Conceptualization, Providing infrastructure, Methodology (equal contribution to image acquisition); **Roger Schibli**: Supervision, Providing infrastructure, Writing (review); **Stefanie D. Krämer**: Supervision, Funding acquisition, Methodology (supported experimental planning), Analysis (supported data analysis), Writing (review)

6.1 Background

Preclinical experiments are an essential part of PET tracer development. Autoradiography has long been used to evaluate the specificity and distribution of tracers *ex vivo* and *in vitro* [106]. To investigate tracer binding on a cellular level, microautoradiography can be used in parallel with immunohistochemical (IHC) methods well established in molecular biology. This can yield valuable information about the types of cells the tracer colocalizes with [158]. However, the two methods remain separate because the respective samples are differently prepared and comparison is thus limited.

In 2012, single-cell uptake of [^{18}F]fluorodeoxyglucose (FDG) was studied *in vitro* using a novel method termed radioluminescence microscopy (RLM) [157]. The original setup consisted of human ovarian cancer cells growing on a $CdWO_4$ scintillator plate and installed on a light-sensitive microscope. The γ-rays resulting from the annihilation of the emitted β-particles by the FDG would cause radioluminescence, i.e. produce visible light. The scintillator was used to further reduce the travel distance of β-particles. The light would be detected by the microscope, focusing on the scintillator surface [157]. RLM has been used in combination with fluorescence imaging in several studies [91, 92, 157].

The technique has since successfully been used and optimized in multiple *in vitro* studies and could be applied to other common PET isotopes such as ^{11}C , ^{68}Ga, ^{64}Cu and ^{124}I. [59, 94, 96, 155, 156, 176–178]. Furthermore, direct comparisons of *ex vivo* tissue from mice injected with ^{89}Zr-rituximab using storage-phosphor autoradiography and RLM have indicated superior resolution in RLM [136]. More recently, an RLM-based method was used to study patient-derived tumor organoids and correlate FDG uptake, live-dead stains and hematoxylin and eosin stains [92]. These examples show the versatility of RLM and its potential in augmenting established methods.

In preclinical tracer development, the combination of RLM with fluorescence microscopy specifically, would allow for a more comprehensive analysis of tracer binding and distribution on a cellular level. Cell-type specific tracer binding is crucial for the development of tracers in applications like immunoPET, where markers are expressed by a subpopulation of cells in the target tissue [208]. In current practice, the study of tracers in the context of other targets simultaneously under a fluorescence-capable microscope, requires the tracer to be fluorescently labeled. Antibodies and antibody fragments used as tracers for immunoPET can often be coupled to a fluorescent dye for colocalization studies. However, the coupling may be challenging and the resulting change in structure could influence the PKPD properties of the tracer. Furthermore, commercially available, fluorescently labeled antibodies typically lack a metal chelator for radiolabeling, which can lead to a disparity between the tracer and the antibody used for fluorescence imaging [170]. Labeling small molecule tracers with fluorescent dyes is even more problematic, due to the large size of fluorescent dyes relative to the molecule [63]. Combining the PET tracer *per se* with fluorescently labeled antibodies specific for other targets of interest in the same RLM session circumvents these issues.

In this proof-of-concept study, we aim to show that RLM can be included in a standard IHC staining workflow with the goal of contemporaneous image acquisition of tracer and IHC stain. A conceptual sketch is shown in Figure 6.1. We fluorescently labeled mouse colon carcinoma (CT26) tissue cryosections with a PE/Cy5 conjugated anti-F4/80 antibody and subsequently incubated the tissue with CD80-targeting ^{64}Cu-NODAGA-abatacept [187]. F4/80 is a macrophage specific marker and CD80 is differentially expressed

on various immune cells including macrophages. We acquired radioluminescence and fluorescence images of the stained tissues concurrently using a light-sensitive bioluminescence microscope and qualitatively assessed colocalization of the two markers. Furthermore, we explore the setup of an affordable, lensless RLM instrument for future studies [97].

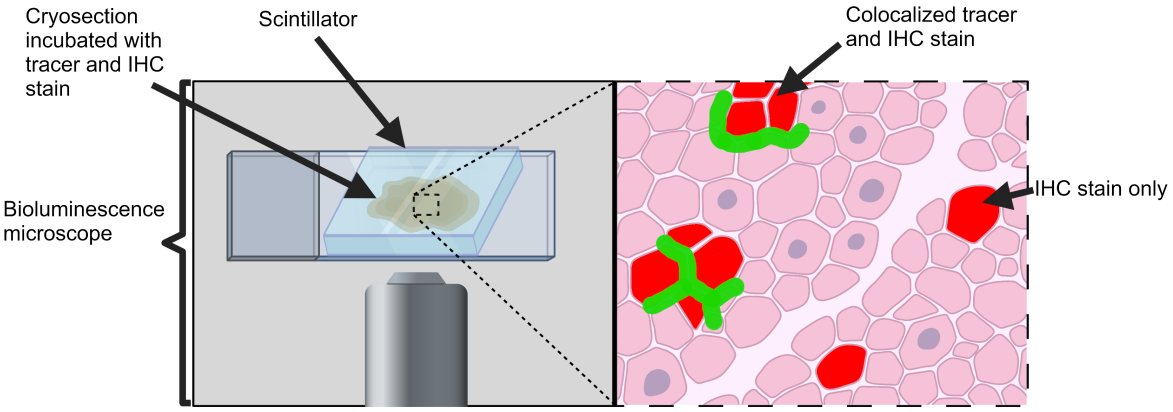

Figure 6.1: Conceptual sketch of the combined radioluminescence and fluorescence microscopy setup. A tissue slice is stained with one or more fluorescent antibodies and subsequently incubated with a radiolabeled tracer. The tissue is then imaged with a microscope capable of low-light image acquisition (for RLM) and fluorescence imaging.

6.2 Methods

6.2.1 Cell culture

The murine colon carcinoma cell line CT26.WT (ATCC CRL-2638) was obtained from the American Type Culture Collection. The cells were cultured in Roswell Park Memorial Institute (RPMI) 1640 medium with GlutaMAX-I and 25 mM HEPES (gibco, Life Technologies, US) supplemented with 10 % fetal calf serum (FCS, Life Technologies, US), 10 000 U/ml penicillin and streptomycin (PS, gibco, Life Technologies, US) at 5 % CO_2 and 37 °C. At 80-95 % confluence, cells were detached with 0.05 % trypsin-EDTA solution (gibco, Life Technologies, US) and split 1 to 7 for sub-culture.

6.2.2 Mouse tumor inoculation

Animal studies were approved by the Zurich Cantonal Veterinary Office, Switzerland (license ZH28/2018), and conducted according to Swiss Animal Welfare legislation. Female BALB/c mice (Charles River Laboratories, Sulzfeld, DE) were housed at 22 °C with a 12-hour light-dark cycle and unlimited access to food and water. At the age of 14 weeks, the mice were inoculated subcutaneously in the right shoulder region with 8 * 10^5 CT26 cells re-suspended in 100 µl Matrigel (BD Biosciences, US). Tumors where excised 7-12 days after CT26 cell inoculation when tumors were clearly visible but no larger than 1.76 cm^3. Animals were decapitated under anesthesia prior to dissection.

6.2.3 ^{64}Cu production, abatacept chelator conjugation and labeling

^{64}Cu was produced via the ^{64}Ni(p,n)^{64}Cu nuclear reaction. Abatacept (Bristol-Myers Squibb, US) conjugated with p-SCN-Benzyl-NODAGA (CheMatech MDT, France) was added to a 1:1 mix of ammonium acetate buffer (0.5 M, pH 5.5) and $^{64}CuCl_2$ (1093 MBq) in 400 µl 0.1 M HCl and incubated at 37 °C for 30 min [34]. The resulting molar activity of ^{64}Cu-NODAGA-abatacept was 45.2 ± 1.0 GBq/µmol. For quality control, the mixture was diluted with phosphate-buffered saline (PBS, gibco, Life Technologies, US) and analyzed by HPLC with a H_2O/MeOH gradient as mobile phase. A C18 reverse phase cartridge (Waters, US), UV detector (280 nm) and radiodetector were used.

6.2.4 IHC workflow integrated with RLM

Dissected CT26 tumors were embedded in OCT compound mounting medium (Avantor, US), cut to 10 µm slices with a cryotome, thaw-mounted on cover slips (porcine skin gelatin coated) and stored at -80 °C. Slices were thawed, treated with acetone (2 min), methanol (5 min) and washed (3 * 5 min) with PBS. The dried tissue was encircled with a hydrophobic pen (Dako, DK) and incubated with immunomix containing 1 % donkey serum, 1 % BSA, 0.05 % sodium azide and 0.1 % Triton X-100 in PBS for 1 h. All subsequent incubation steps were performed protected from light on a benchtop rocker. Tissue was washed (3 * 5 min) in PBS and incubated with PE/Cy5 conjugated rat anti-mouse F4/80 antibody (123111, Biolegend, US) 1:100 in PBS for 4 h at 4 °C. The tissue was washed (3 * 5 min) in PBS, ^{64}Cu-NODAGA-abatacept in a volume of 100 µl was added and followed by a 20 min incubation. The tissue was washed (3 * 5 min) and left to dry for ∼10 min. The 10 x 10 x 0.5 mm $CdWO_4$ scintillator plates (MTI Corporation, US) were mounted with mounting medium (Mowiol, Kuraray, JP) on the tissue. Images were acquired on an bioluminescence microscope (LV200, Olympus, JP). Image processing was done with open-source imaging software [173].

6.3 Results

The workflow for the combined RLM and IHC staining method is shown in Figure 6.2. In brief, tumors were excised from CT26 tumor-bearing mice and cryosectioned. The sections were mounted on a cell-adherence-treated cover slip. A standard IHC protocol with PE/Cy5 conjugated F4/80 antibody (1:100) was followed by the addition of ^{64}Cu-NODAGA-abatacept. The slices were then imaged using a light-sensitive bioluminescence microscope. A detailed description of the IHC workflow integrated with RLM can be found in Section 6.2.4. The experiment was conducted in three different locations spanning two days. First, cryosections were prepared at ETH in Zürich, then IHC and radiotracer staining followed at PSI in Villigen and finally, the RLM imaging was conducted over 2 days at the Bioimaging Center of the University of Geneva. Samples were measured to ensure the radio activity was below the legally allowed maximum for transfer using public transport.

Three different concentrations of abatacept were used for the experiments. The measured activity, abatacept concentration, abatacept-to-radionuclide-ratio and molar activity prior to adding the solution to the tissue are shown in Table 6.1. The activity

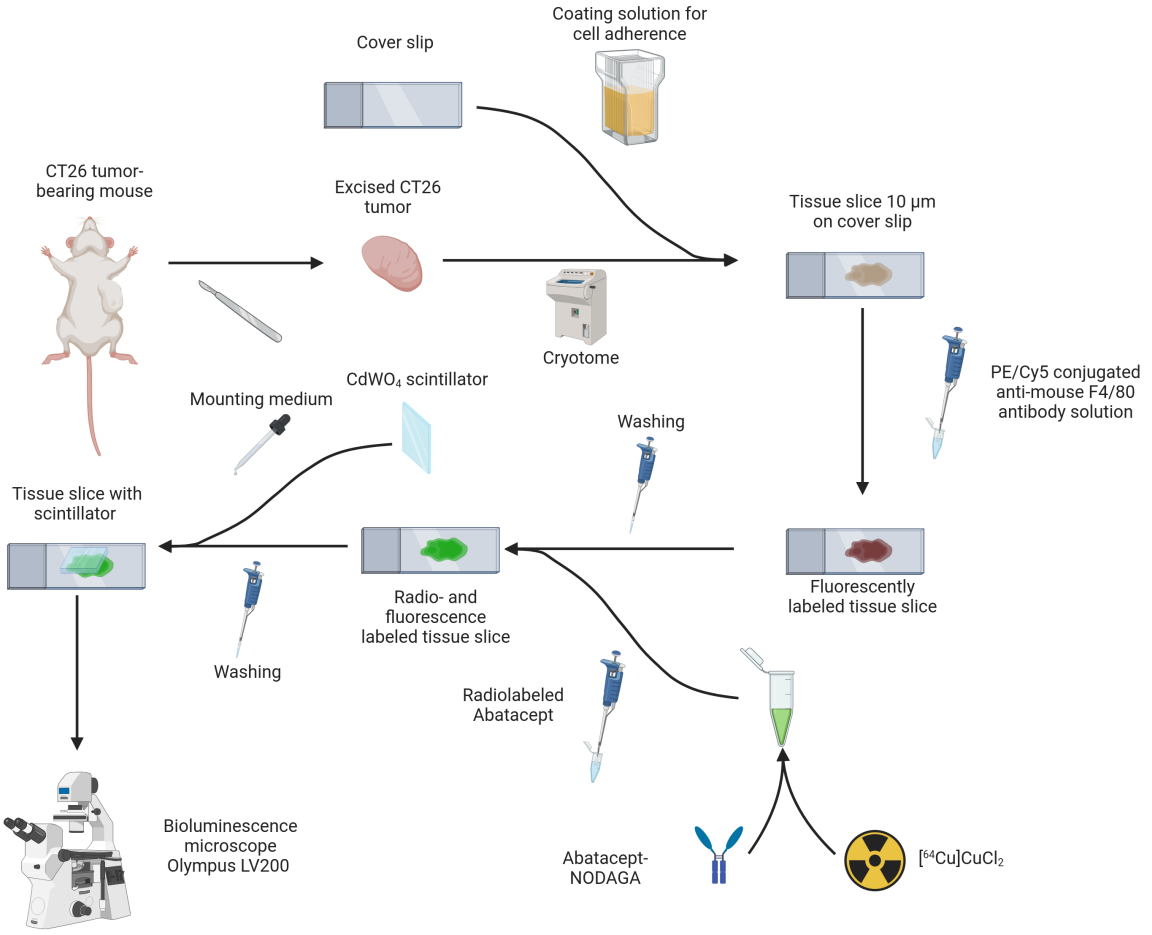

Figure 6.2: Overview of IHC staining workflow integrated with RLM.

measured on the slides after incubation with the radiotracer was < 0.4 MBq for each slide. The bright-field, radioluminescence and fluorescence images are shown in Figures 6.3, 6.4 and 6.5.

Table 6.1: Conditions of radiotracer incubation with CT26 tissue cryosections.

Measured activity [MBq]	**Abatacept conc. [uM]**	**Abatacept-to-radionuclide-ratio**	**Molar activity [GBq/µmol]**
44.86	10	183	44.60
23.44	5	201	46.36
4.71	1	201	44.50

The fluorescence images are brighter in the center than on the image edge and had high background signal. To evaluate the difference in the radioluminescence signal due to different ^{64}Cu-NODAGA-abatacept concentrations, we compared regions in the core of the tissue, that were incubated with either 10 µM or 1 µM tracer (Figure 6.3) and acquired radioluminescence images with 20 s exposure time. The signal of these regions $\sim$1 d after incubation was comparable in the fluorescence images, but visibly weaker in the 1 µM compared to the 10 µM ^{64}Cu-NODAGA-abatacept sample.

The tissue boundaries as defined by the bright-field images, were clearly visible in the fluorescence and radioluminescence (10 s exposure) channels 6.4.

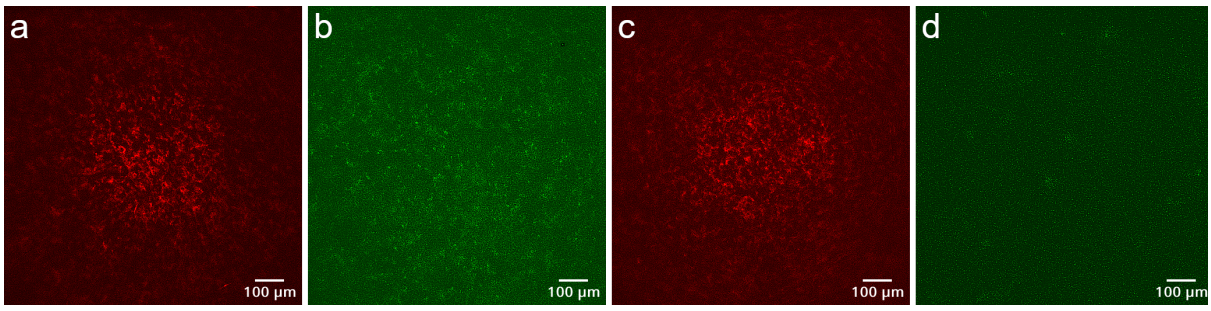

Figure 6.3: Comparison of fluorescence and radioluminescence in CT26 tumor tissue at different tracer concentrations. Tissue stained with ^{64}Cu-NODAGA-abatacept and fluorescent anti-F4/80 antibody with PE/Cy5 1 d prior to measurement **a**, **b** 10 µM, 44.86 MBq and **c**, **d** 1 µM, 4.71 MBq of ^{64}Cu-NODAGA-abatacept. **a**, **c** show red fluorescence channel, **b** and **d** show bioluminescence channel for radioactivity. Exposure time in the bioluminescence channel was 20 s.

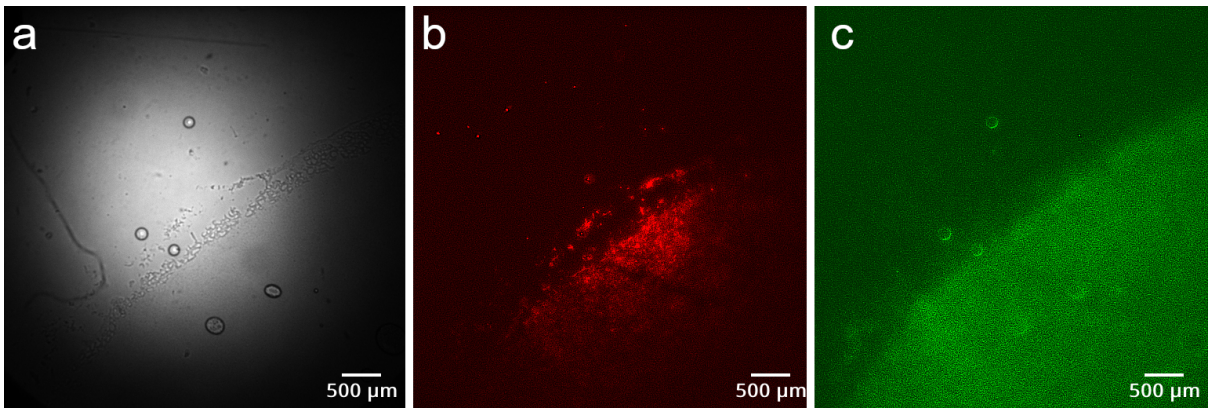

Figure 6.4: Edge of tissue discerned by bright-field, fluorescence and radioluminescence. Tissue stained with 5 µM ^{64}Cu-NODAGA-abatacept (23.44 MBq) and fluorescent anti-F4/80 with PE/Cy5 6 h pior to measurement. **a** bright-field channel, **b** red fluorescence channel, **c** bioluminescence channel for radioactivity. Exposure time in the bioluminescence channel was 10 s.

The composit image of radioluminescence and fluorescence showed a qualitative overlap of the two signals 6.5. However, no colocalization was found within the tissue between the fluorescence and radioluminescence signal upon quantitative analysis (data not shown). The averaged radioluminescence image (120 frames, 20 s exposure each) did not show heterogenous tracer uptake (Figure 6.5).

To explore the use of a lensless RLM setup as proposed by Klein et al. [97], we acquired a Raspberry Pi 4 compact computer and camera module for a total of $\sim$90 CHF (Figure 6.6). Open-source software modules are written in Python and are easily adaptable for imaging needs [97]. The camera lens needs to be manually removed prior to image acquisition.

6.4 Discussion

We combined radioluminescence microscopy with IHC staining in a standard IHC protocol. The method was tested on CT26 tumor cryosections stained with a PE/Cy5 conjugated anti-

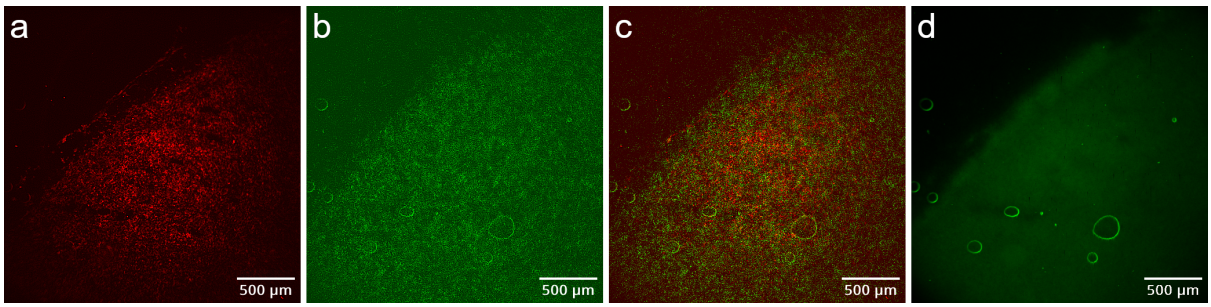

Figure 6.5: Colocalization of fluorescence and radioluminescence. Tissue stained with 5 µM ^{64}Cu-NODAGA-abatacept (23.44 MBq) and fluorescent anti-F4/80 with PE/Cy5 1 d pior to measurement. **a** red fluorescence channel, **b** bioluminescence channel for radioactivity (exposure time was 20 s), **c** composite image of **a** and **b**, **d** bioluminescence channel for radioactivity. The image (**d**) is a result of averaging the signal over 120 frames of 20 s exposure time each.

F4/80 antibody targeting macrophages and subsequently incubated with ^{64}Cu-NODAGA-abatacept targeting CD80. The radioluminescence signal was clearly visible in the tissue along with the fluorescence signal and marked the tissue boundaries. The signal intensity was dependent on the concentration of the radiotracer.

Implementing RLM in our IHC staining workflow was straightforward. We used cover slips instead of glass slides to reduce the distance between lense and scintillator surface. One might also use tissue sections on glass slides depending on the microscope used. Adding the radiotracer staining step right before mounting of the scintillator plate was not time critical and can be done subsequently to the fluorescent staining. We do not expect interference of the fluorescence signal with the radioluminescence channel during image acquisition due to the lack of a light source needed for fluorescence. Interference from the radioluminescence in the fluorescence channel is likely negligible because of a combination of very dim intensity of the radioluminescence signal and short acquisition times in fluorescence imaging.

RLM was developed primarily with single cell imaging in dishes and microfluidics in mind. In cell culture settings, where cells are sparsely seeded, spatial resolutions of 20-25 µm have been achieved [136]. Imaging tissue is more challenging due to the higher cell density. However, a comparison of autoradiography and RLM *ex vivo* on tissue slices and correlations with fluorescence stainings of patient-derived tumor organoids show the potential of RLM in the field of tracer development [92,136]. To achieve a sufficient spatial resolution for tissue imaging, the travel distance of the β-particles prior to annihilation should be as short as possible. To improve spatial resolution, Lu_2O_3:Eu instead of $CdWO_4$ scintillators could be used [176]. For tracer development, RLM could be used to identify cell populations and tissue regions on cryosections with high tracer binding and correlate the findings with IHC stainings.

Abatacept has strong affinity for CD80 and CD86, expressed on antigen-presenting cells, and F4/80 is typically found on macrophages [18,77,129]. Therefore, we expected to see clearly distinguishable, high ^{64}Cu-NODAGA-abatacept regions in the radioluminescence images that correlate with the anti-F4/80 fluorescence signal. While both channels showed accumulation on the tissue, we did not obtain a heterogeneous image but rather a homogeneously distributed radioluminescence signal. This is most prominent in the

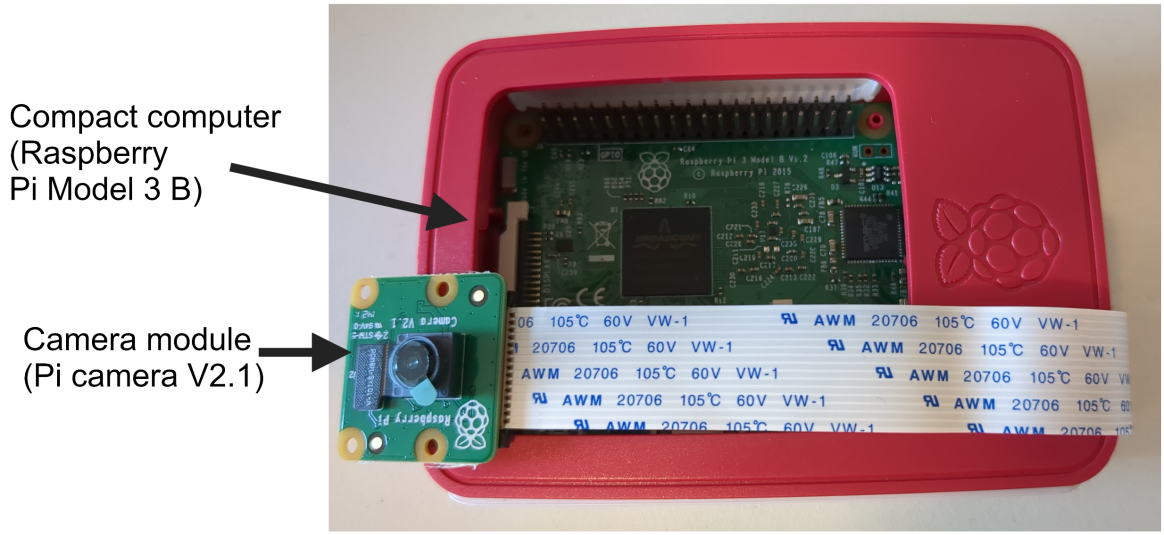

Figure 6.6: Essential equipment needed for a lensless RLM setup according to Klein et al. [97]. Raspberry Pi 4 compact computer and camera module acquired for a total of $\sim$90 CHF. Lense can be removed from the camera module to allow for direct imaging on the CMOS detector.

averaged image shown in Figure 6.5, where hot spots were visible. The exposure time was $\geq$ 20 s, which is longer than the recommended $<$ 1 s usually used in RLM studies [94]. To get a discernable signal, it is recommended to capture multiple frames, each with an exposure time of 10-100 ms, process each frame separately and then combine them. RLM image reconstruction algorithms such as ionization track analysis have been developed specifically for this purpose [8]. The radioluminescence imaging lacked specificity due to the concentration of the tracer being much higher than the K_D of $\sim$2 nM [187]. The washing step prior to mounting the scintillator may have been insufficient to remove unbound tracer and alleviate the problem of unspecific binding. Lower concentrations of ^{64}Cu-NODAGA-abatacept should be used to test specificity in blocking studies with non-radioactive Cu-NODAGA-abatacept in excess. Furthermore, the treatment of the tissue for IHC staining might have had an impact on radiotracer binding. Control experiments with cryosections that were not stained with the anti-F4/80 antibody should be conducted to assess the impact of the staining on tracer binding.

The fluorescence images were bright in the center and dark toward the edges. This is likely due to instrument limitations. The Olympus LV200 that was used for this experiment is primarily a bioluminescence microscope and lacks capabilities that one would expect from a fluorescence microscope. For instance, samples are illuminated using a transillumination source leading to high background as visible in our images. As an alternative, a microscope setup specifically designed for RLM has been proposed and used with single cell and organoid samples [92,94,95]. The drawback of such custom solutions is that they require expertise in optics and electronics and are not readily available. Recently, a lensless microscope for radioluminescence imaging based on off-the-shelf parts for a price of 100 USD has been evaluated in *in vitro* tracer uptake studies [97]. For such a lensless microscope, the samples are placed directly on the CMOS detector without the need for a scintillator or a lense. We have acquired the necessary equipment for such a setup and will evaluate its performance in future studies. There are multiple

projects revolving around fluorescence imaging using a compact computer and camera module [25, 143]. However, these projects typically employ bandpass filters and use lenses, between sensor and samples, preventing their direct implementation for RLM. Alternatively, fluorescence could potentially be imaged in conjunction with RLM through use of the built-in Bayer array or coating the CMOS pixels with a bandpass filter [93]. Through the use of open-source software, the acquisition settings could easily be adapted to a RLM and fluorescence imaging combined setup. Further adjustments for use with stained tissue would be necessary.

6.5 Conclusions

As a proof-of-concept, we have included radioluminescence microscopy of ^{64}Cu-NODAGA-abatacept into an IHC staining workflow with PE/Cy5 conjugated anti-F4/80 antibody. The subsequently acquired images using a light-sensitive bioluminescence microscope showed a homogeneous radioluminescence signal. The fluorescence images likely suffered from high unspecific binding and high background signal. Future experiments should address the high background by using lower tracer concentrations in the range of the K_{D}, and assess specific binding in blocking studies. The field of RLM is rapidly evolving and the use of a lensless RLM setup could be a cost-effective alternative to be applied for simultaneous imaging of radioluminescence and fluorescence in cryosections.

6.6 Supplementary material

6.6.1 Quality Control

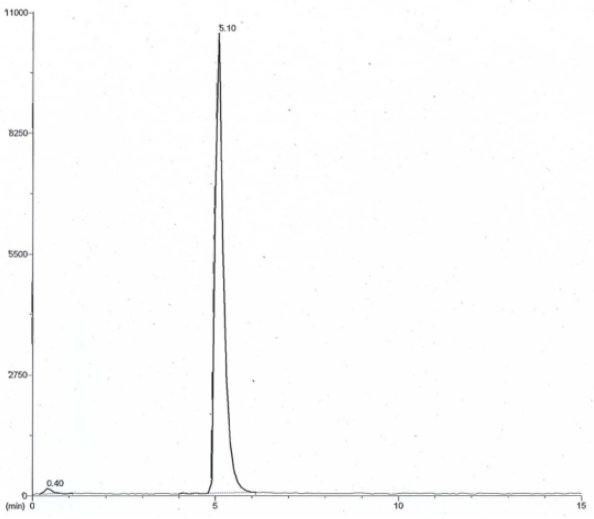

Figure 6.7: Reverse phase HPLC chromatograms of ^{64}Cu-NODAGA-abatacept. Retention time and, where applicable, % area were determined. ^{64}Cu-NODAGA-abatacept 5.1 min (99 %).

Chapter 7

Conclusion and outlook

The immune system has gained attention in different fields of therapy. Among the most widespread diseases of the developed world, cancer and AD have been identified as immune-related [42, 49, 68, 123]. The immune system is a result of innate mechanisms and adaptation to external stimuli. This leads to inter-individual heterogeneity in immune responses, that need to be taken into account when developing therapies [132].

Molecular imaging using PET and SPECT allows to visualize and quantify immune-relevant components based on their molecular properties. Radiotracers can be developed to target specific proteins that are up- or down-regulated in the tissue of interest to visualize changes in the immune response. This allows for the detailed characterization and tailored treatment approaches for patients suffering from immune-related diseases [10].

The complex interplay between different cell types embedded in an extracellular milieu is characteristic for the TME [11]. Specifically immune cells play a crucial role in the development and progression of many tumor types. The inhibition of the immune response through cells such as macrophages by means of their polarization toward an M2-type phenotype is associated with a poor prognosis. M2 macrophages offer a plethora of different potential targets that have been causally linked to tumor progression [110]. The asparagine endopeptidase legumain is one such target that is overexpressed by immunosuppressive M2 macrophages [179]. Based on P1-Asn peptidomimetic inhibitors, we have embarked on a journey to develop legumain-targeting radiotracers for PET imaging. In our first approach, we have developed [^{11}C]**1** and [^{11}C]**2**, two strong-affinity radiotracers. However, [^{11}C]**1** and [^{11}C]**2** lacked *in vivo* stability and were not blockable with the respective unlabeled compound in excess. Based on a modified structure of the P1-Asn peptidomimetic scaffold, we introduced [^{11}C]**3**, with improved *in vivo* stability. [^{11}C]**3** showed blocking in the kidney and spleen, tissues with high legumain expression, indicating specificity. Accumulation in the tumor was low and could not be blocked. The specificity of the tracer in other tissues than the tumor led us to conclude that there is some tumor inherent property that prevents legumain-specific tracer accumulation. The large set of endogenous substrates of legumain and their differential expression in tumors compared to healthy tissue may offer an explanation for this observation [35, 182].

In AD, legumain expression has been closely linked to the generation of Aβ plaques and neurofibrillary tangles, the two main hallmarks of the disease [123]. Legumain is highly expressed in activated microglia, the tissue-resident macrophages of the brain [84, 204]. There is a high demand for PET tracers in the setting of AD. Current approaches for legumain imaging are not BBB penetrant [80, 118, 119, 159]. The development of legumain-specific inhibitors for the brain has yielded compounds that ameliorate the pathology in AD mouse models [112, 217]. Our attempt to develop the legumain-targeting radiotracer [^{11}C]CC11m based on these compounds is a first step to image legumain in the brain. In using APP/PS1 mice, a well-established AD mouse model, we showed that legumain is highly expressed in the brain of these mice. However, brain legumain activity was only marginally higher than in the control tissue and might not be sufficient for PET tracer development. The stability of [^{11}C]CC11m remains to be elucidated and the affinity will need to be improved if this route is pursued. Alternatively, one could, based on the P1-Asn peptidomimetic tracers that we have developed and the published, structurally similar inhibitors, develop a legumain PET tracer for the brain [101]. In any case, the conducted pilot study would also have to be supplemented by PET studies comparing APP/PS1 transgenic and wild-type mice.

The development of legumain-targeting radiotracers in AD and cancer shows many commonalities. Competition with endogenous substrates is a major challenge in the development of legumain PET tracers and may also be a concern in other scenarios. To alleviate this problem, one possible attempt is to develop irreversible inhibitors. ^{18}F-labeling might be valid option for the corresponding PET tracers, as the molecules already contain fluorine atoms [101]. Another approach would be to develop molecules with sub-nanomolar affinity to outcompete endogenous substrates. One such molecule is the endogenous inhibitor cystatin M/E which possesses a reported K_i of 1.6 ± 0.5 pM [9]. It is commercially available, could readily be labeled with $^{99\mathrm{m}}$Tc and potentially used for SPECT imaging. It is most likely not BBB-penetrant and would therefore be applied in the context of cancer.

An important consideration that is biologically relevant but not yet fully understood is the role of the legumain localization intra- and pericellularly. Legumain is located in lysosomes at a high concentration including in healthy tissue [182]. Therefore, targeting legumain irrespective of its localization will lead to high background signal. If the role of extracellular and cytosolic legumain turns out to be especially important in cancer progression, one could develop tracers that are not lysosome penetrant. For example, molecules that cannot penetrate cellular membranes due to their size or charge could be used to specifically target extracellular legumain. Another aspect to be taken into account is the role of active legumain. For the development of therapeutic legumain inhibitors, it is less relevant if both pro- and active legumain are targeted. For the development of a PET tracer, it is crucial to target active legumain, as the pro-enzyme is not relevant for the pathology, will distort the signal and is present in high concentrations also in healthy tissue. Legumain activity measurements with tissue samples as the ones performed in our projects, may thus form an integral step in legumain PET tracer development. Legumain is currently being investigated preclinically in the context of cancer, AD and other diseases and the success of some inhibitors coupled with data from human samples might spark the initiation of clinical trials in the near future, amplifying the need for nuclear imaging tracers [153].

M1-polarized macrophages express the co-stimulatory molecule CD80 in the TME [12]. CD80 acts as a modulator of T cell activity and is of clinical relevance in ICI-based cancer immunotherapy [48, 191]. In an effort to detect and monitor CD80 expression *in vivo*, we have evaluated the use of small recombinant proteins based on the extracellular domain of CD80-binding CTLA-4 $^{99\mathrm{m}}$Tc-CACM-1 and $^{99\mathrm{m}}$Tc-CACM-2 for SPECT imaging in CT26 tumor-bearing mice. Both tracers showed accumulation in the tumor. However, high uptake in the liver and kidney and the absence of a blocking effect with the unlabeled compound leaves room for further optimization. Incorporating a modified His-tag might improve pharmacokinetics with regard to hepatic uptake [79]. Renal uptake is a challenging issue often encountered in the development of antibody fragments [196]. Although there exist several strategies to mitigate this issue, the improvement strategy will inevitably be specific to the tracer in question [44]. For CACM-1 and CACM-2, the use of $^{99\mathrm{m}}$Tc is preferable as the physical half life aligns well with the pharmacokinetics of the tracers.

RLM offers the potential to augment existing methods of biological evaluation for tracer development by bridging the gap between autoradiography and IHC methods. It can be applied to many different isotopes and both small and large molecule radiotracers [157]. We showed the straightforward incorporation in the immunohistochemical staining workflow and offered a qualitative readout in conjunction with fluorescence microscopy as a proof-

of-concept. Furthermore, we suggested the implementation of an existing lensless imaging system for RLM with tissue samples [97]. The setup would be cost-effective but would require several adjustments to be applicable to radioluminescence and fluorescence on tissue samples. The implementation of RLM in the tracer development pipeline of a given laboratory is largely dependent on the existing equipment and the fluorescence microscopy requirements.

In this dissertation, we have focused on PET and SPECT tracer development for monitoring legumain and CD80 in cancer and other immune-related conditions. Molecular imaging of targets that are linked to immune-related conditions, offers the possibility for multi-use tracers that can be applied in the clinical setting. This could greatly accelerate the development process of suitable tracers to the benefit of the patient. As companion diagnostics, which are increasingly a requirement for the regulatory approval of therapeutics, such radiotracers are key for a personalized treatment approach [122, 193]. CD80 and legumain are two prominent targets that assume a critical role in understanding the immune response in cancer, AD and beyond.

Bibliography

[1] Abatacept: Uses, interactions, mechanism of action | drugbank online. https://go.drugbank.com/drugs/DB01281.

[2] Belatacept: Uses, interactions, mechanism of action | drugbank online. https://go.drugbank.com/drugs/DB06681.

[3] Bioconductor - flowviz. https://bioconductor.org/packages/release/bioc/html/flowViz.html.

[4] Livechart of nuclides – advanced version | iaea, 2014. https://www.iaea.org/resources/databases.

[5] Aggregated tau measured by visual interpretation of flortaucipir positron emission tomography and the associated risk of clinical progression of mild cognitive impairment and alzheimer disease: Results from 2 phase iii clinical trials. *JAMA Neurology*, 78:445–453, 4 2021. https://doi.org/10.1001/JAMANEUROL.2020.5505.

[6] What is cancer? - nci, 2021. https://www.cancer.gov/about-cancer/understanding/what-is-cancer.

[7] Mohammed H. Ahmed, Isaias Hernández-Verdin, Franck Bielle, Maïté Verreault, Julie Lerond, Agusti Alentorn, Marc Sanson, and Ahmed Idbaih. Expression and prognostic value of cd80 and cd86 in the tumor microenvironment of newly diagnosed glioblastoma. *Canadian Journal of Neurological Sciences*, 50:234–242, 3 2023. https://doi.org/10.1017/CJN.2022.5.

[8] Sepideh Almasi and Guillem Pratx. High-resolution radioluminescence microscopy image reconstruction via ionization track analysis. *IEEE Transactions on Radiation and Plasma Medical Sciences*, 3:660–667, 11 2019. https://doi.org/10.1109/TRPMS.2019.2908219.

[9] Marcia Alvarez-Fernandez, Alan J. Barrett, Bernd Gerhartz, Pam M. Dando, Jian Ni, and Magnus Abrahamson. Inhibition of mammalian legumain by some cystatins is due to a novel second reactive site. *Journal of Biological Chemistry*, 274:19195–19203, 7 1999. https://doi.org/10.1074/JBC.274.27.19195.

[10] Simon M. Ametamey, Michael Honer, and Pius August Schubiger. Molecular imaging with pet. *Chemical Reviews*, 108:1501–1516, 5 2008. https://doi.org/10.1021/CR0782426.

[11] Nicole M. Anderson and M. Celeste Simon. The tumor microenvironment. *Current Biology*, 30:R921–R925, 8 2020.
https://doi.org/10.1016/J.CUB.2020.06.081.

[12] Sreya Bagchi, Robert Yuan, and Edgar G. Engleman. Immune checkpoint inhibitors for the treatment of cancer: Clinical impact and mechanisms of response and resistance. *Annual Review of Pathology: Mechanisms of Disease*, 16:223–249, 1 2021.
https://doi.org/10.1146/ANNUREV-PATHOL-042020-042741.

[13] Weiqi Bao, Fang Xie, Chuantao Zuo, Yihui Guan, and Yiyun Henry Huang. Pet neuroimaging of alzheimer's disease: Radiotracers and their utility in clinical research. *Frontiers in Aging Neuroscience*, 13:624330, 5 2021.
https://doi.org/10.3389/FNAGI.2021.624330.

[14] Gustavo Basurto-Islas, Inge Grundke-Iqbal, Yunn Chyn Tung, Fei Liu, and Khalid Iqbal. Activation of asparaginyl endopeptidase leads to tau hyperphosphorylation in alzheimer disease. *Journal of Biological Chemistry*, 288:17495–17507, 6 2013.
https://doi.org/10.1074/jbc.M112.446070.

[15] Richard Beare, Bradley Lowekamp, and Ziv Yaniv. Image segmentation, registration and characterization in r with simpleitk. *Journal of Statistical Software*, 86:1–35, 9 2018.
https://doi.org/10.18637/JSS.V086.I08.

[16] Laboratoire National Henri Becquerel. 99mtc tables, January 2012.
https://www.nucleide.org/DDEP_WG/Nuclides/Tc-99m_tables.pdf.

[17] Frederike Bensch, Elly L. van der Veen, Marjolijn N. Lub de Hooge, Annelies Jorritsma-Smit, Ronald Boellaard, Iris C. Kok, Sjoukje F. Oosting, Carolina P. Schröder, T. Jeroen N. Hiltermann, Anthonie J. van der Wekken, Harry J.M. Groen, Thomas C. Kwee, Sjoerd G. Elias, Jourik A. Gietema, Sandra Sanabria Bohorquez, Alex de Crespigny, Simon Peter Williams, Christoph Mancao, Adrienne H. Brouwers, Bernard M. Fine, and Elisabeth G.E. de Vries. 89zr-atezolizumab imaging as a non-invasive approach to assess clinical response to pd-l1 blockade in cancer. *Nature Medicine 2018 24:12*, 24:1852–1858, 11 2018.
https://doi.org/10.1038/s41591-018-0255-8.

[18] Matthew J. Bernett, Seung Y. Chu, Irene Leung, Gregory L. Moore, Sung Hyung Lee, Erik Pong, Hsing Chen, Sheryl Phung, Umesh S. Muchhal, Holly M. Horton, Greg A. Lazar, John R. Desjarlais, and David E. Szymkowski. Immune suppression in cynomolgus monkeys by xpro9523. *mAbs*, 5:384–396, 5 2013.
https://doi.org/10.4161/MABS.23976.

[19] Subhra K. Biswas and Alberto Mantovani. Macrophage plasticity and interaction with lymphocyte subsets: cancer as a paradigm. *Nature Immunology 2010 11:10*, 11:889–896, 9 2010.
https://doi.org/10.1038/ni.1937.

[20] David Borchelt. 034829 - app/ps1 strain details, 2024.
https://www.jax.org/strain/004462.

[21] Jordi Borràs, Joan Lecina, Julie Foster, Roxana Kashani, Laura Melendez-Alafort, Jane Sosabowski, and Joan Suades. Bioconjugated technetium carbonyls by transmetalation reaction with zinc derivatives. *Bioorganic & Medicinal Chemistry Letters*, 37:127840, 4 2021.
https://doi.org/10.1016/J.BMCL.2021.127840.

[22] Alizée Bouleau, Vincent Lebon, and Charles Truillet. Pet imaging of immune checkpoint proteins in oncology. *Pharmacology & Therapeutics*, 222:107786, 6 2021.
https://doi.org/10.1016/J.PHARMTHERA.2020.107786.

[23] Morten Busk, Jens Overgaard, and Michael R. Horsman. Imaging of tumor hypoxia for radiotherapy: Current status and future directions. *Seminars in Nuclear Medicine*, 50:562–583, 11 2020.
https://doi.org/10.1053/J.SEMNUCLMED.2020.05.003.

[24] Claudia A Castro Jaramillo. *Targeting legumain and CD80 for molecular imaging of immune responses in chronic inflammatory disease*. PhD thesis, ETH Zurich, 2020.

[25] Andre Maia Chagas, Lucia L. Prieto-Godino, Aristides B. Arrenberg, and Tom Baden. The €100 lab: A 3d-printable open-source platform for fluorescence microscopy, optogenetics, and accurate temperature control during behaviour of zebrafish, drosophila, and caenorhabditis elegans. *PLOS Biology*, 15:e2002702, 7 2017.
https://doi.org/10.1371/JOURNAL.PBIO.2002702.

[26] Cheng Shyong Chang, Julia H. Chang, Nicholas C. Hsu, Hsuan Yu Lin, and Chih Yuan Chung. Expression of cd80 and cd86 costimulatory molecules are potential markers for better survival in nasopharyngeal carcinoma. *BMC Cancer*, 7:1–7, 5 2007.
https://doi.org/10.1186/1471-2407-7-88.

[27] Jinq May Chen, Pam M. Dando, Neil D. Rawlings, Molly A. Brown, Nina E. Young, Richard A. Stevens, Eric Hewittt, Colin Watts, and Alan J. Barrett. Cloning, isolation, and characterization of mammalian legumain, an asparaginyl endopeptidase. *Journal of Biological Chemistry*, 272:8090–8098, 3 1997.
https://doi.org/10.1074/JBC.272.12.8090.

[28] Jinq-May CHEN, Mara FORTUNATO, and Alan J. BARRETT. Activation of human prolegumain by cleavage at a c-terminal asparagine residue. *Biochemical Journal*, 352:327–334, 12 2000.
https://doi.org/10.1042/BJ3520327.

[29] Jinq-May Chen, Mara Fortunato, Richard A. E. Stevens, and Alan J. Barrett. Activation of progelatinase a by mammalian legumain, a recently discovered cysteine proteinase. *bchm*, 382:777–784, 5 2001.
https://doi.org/10.1515/BCHM.2001.382.5.777.

[30] Shanze Chen, Abdullah F.U.H. Saeed, Quan Liu, Qiong Jiang, Haizhao Xu, Gary Guishan Xiao, Lang Rao, and Yanhong Duo. Macrophages in immunoregulation and therapeutics. *Signal Transduction and Targeted Therapy 2023 8:1*, 8:1–35, 5 2023.
https://doi.org/10.1038/s41392-023-01452-1.

[31] Yu Jen Chen, Shou Cheng Wu, Chung Yung Chen, Shey Cherng Tzou, Tian Lu Cheng, Ying Fang Huang, Shyng Shiou Yuan, and Yun Ming Wang. Peptide-based mri contrast agent and near-infrared fluorescent probe for intratumoral legumain detection. *Biomaterials*, 35:304–315, 1 2014. https://doi.org/10.1016/J.BIOMATERIALS.2013.09.100.

[32] Anthos Christofides, Laura Strauss, Alan Yeo, Carol Cao, Alain Charest, and Vassiliki A. Boussiotis. The complex role of tumor-infiltrating macrophages. *Nature Immunology 2022 23:8*, 23:1148–1156, 7 2022. https://doi.org/10.1038/s41590-022-01267-2.

[33] Alexandria P Cogdill, Miles C Andrews, and Jennifer A Wargo. Hallmarks of response to immune checkpoint blockade. *British Journal of Cancer*, 117:1–7, 6 2017. https://doi.org/10.1038/bjc.2017.136.

[34] Maggie S. Cooper, Emmanuelle M. Sabbah, and Stephen J. Mather. Conjugation of chelating agents to proteins and radiolabeling with trivalent metallic isotopes. *Nature Protocols 2006 1:1*, 1:314–317, 6 2006. https://doi.org/10.1038/nprot.2006.49.

[35] Elfriede Dall and Hans Brandstetter. Structure and function of legumain in health and disease. *Biochimie*, 122:126–150, 3 2016. https://doi.org/10.1016/J.BIOCHI.2015.09.022.

[36] Pramod Darvin, Salman M. Toor, Varun Sasidharan Nair, and Eyad Elkord. Immune checkpoint inhibitors: Recent progress and potential biomarkers. *Experimental & Molecular Medicine*, 50:1–11, 12 2018. https://doi.org/10.1038/s12276-018-0191-1.

[37] Julie Douthwaite, Jacques Moisan, Cyril Privezentzev, Blagoje Soskic, Shereen Sabbah, Suzanne Cohen, Andie Collinson, Elizabeth England, Catherine Huntington, Ben Kemp, Li Zhuang, Suzanne Hudak, D. Gareth Rees, Debbie Goldberg, Chris Barton, Linda Chang, Inna Vainshtein, Meina Liang, Laurie Iciek, Philip Ambery, Mark Peakman, Tristan J. Vaughan, Tim I. M. Tree, David M. Sansom, Michael A. Bowen, Ralph R. Minter, and Lutz Jermutus. A cd80-biased ctla4-ig fusion protein with superior in vivo efficacy by simultaneous engineering of affinity, selectivity, stability, and fcrn binding. *The Journal of Immunology*, 198:528–537, 1 2017. https://doi.org/10.4049/JIMMUNOL.1600682.

[38] DrugBank. Decitabine, 2024. https://go.drugbank.com/drugs/DB01262.

[39] William C. Eckelman and Chester A. Mathis. Targeting proteins in vivo: in vitro guidelines. *Nuclear Medicine and Biology*, 33:161–164, 2 2006. https://doi.org/10.1016/J.NUCMEDBIO.2006.01.010.

[40] Sharon L. Eddie, Aaron Gregson, Emma Graham, Stephanie Burton, Timothy Harrison, Roberta Burden, Christopher J. Scott, Paul B. Mullan, and Rich Williams. Identification and sar exploration of a novel series of legumain inhibitors. *Bioorganic & Medicinal Chemistry Letters*, 29:1546–1548, 6 2019. https://doi.org/10.1016/J.BMCL.2019.03.019.

[41] Laura E. Edgington, Martijn Verdoes, Alberto Ortega, Nimali P. Withana, Jiyoun Lee, Salahuddin Syed, Michael H. Bachmann, Galia Blum, and Matthew Bogyo. Functional imaging of legumain in cancer using a new quenched activity-based probe. *Journal of the American Chemical Society*, 135:174–182, 1 2013. https://doi.org/10.1021/ja307083b.

[42] Anastasia G. Efthymiou and Alison M. Goate. Late onset alzheimer's disease genetics implicates microglial pathways in disease risk. *Molecular Neurodegeneration*, 12, 5 2017. https://doi.org/10.1186/S13024-017-0184-X.

[43] Georgios Efthymiou, Angélique Saint, Michaël Ruff, Zeinab Rekad, Delphine Ciais, and Ellen Van Obberghen-Schilling. Shaping up the tumor microenvironment with cellular fibronectin. *Frontiers in Oncology*, 10:537637, 4 2020. https://doi.org/10.3389/FONC.2020.00641.

[44] Torun Ekblad, Thuy Tran, Anna Orlova, Charles Widström, Joachim Feldwisch, Lars Abrahmsén, Anders Wennborg, Amelie Eriksson Karlström, and Vladimir Tolmachev. Development and preclinical characterisation of 99mtc-labelled affibody molecules with reduced renal uptake. *European Journal of Nuclear Medicine and Molecular Imaging*, 35:2245–2255, 12 2008. https://doi.org/10.1007/S00259-008-0845-7/FIGURES/5.

[45] Timothy C. Elzhov, Katharine M. Mullen, Andrej-Nikolai Spiess, and Ben Bolker. minpack.lm: R interface to the levenberg-marquardt nonlinear least-squares algorithm found in minpack, 2016. R package version 1.2-1.

[46] Jonathan H. Esensten, Ynes A. Helou, Gaurav Chopra, Arthur Weiss, and Jeffrey A. Bluestone. Cd28 costimulation: From mechanism to therapy. *Immunity*, 44:973–988, 5 2016. https://doi.org/10.1016/J.IMMUNI.2016.04.020.

[47] Faridoon, Raymond Ng, Guiping Zhang, and Jie Jack Li. An update on the discovery and development of reversible covalent inhibitors. *Medicinal Chemistry Research*, 32:1039–1062, 6 2023. https://doi.org/10.1007/s00044-023-03065-3.

[48] Xing Yu Feng, Lin Lu, Ke Feng Wang, Bao Yan Zhu, Xi Zhi Wen, Rui Qing Peng, Ya Ding, Dan Dan Li, Jing Jing Li, Yong Li, and Xiao Shi Zhang. Low expression of cd80 predicts for poor prognosis in patients with gastric adenocarcinoma. *Future Oncology*, 15:473–483, 2 2019. https://doi.org/10.2217/FON-2018-0420.

[49] J Ferlay, M Ervik, F Lam, M Colombet, L Mery, and M Piñeros. Global cancer observatory: Cancer today, 2020. gco.iarc.who.int/today.

[50] Carlos Elias Conti Filho, Lairane Bridi Loss, Clairton Marcolongo-Pereira, Joamyr Victor Rossoni Junior, Rafael Mazioli Barcelos, Orlando Chiarelli-Neto, Bruno Spalenza da Silva, Roberta Passamani Ambrosio, Fernanda Cristina de Abreu

Quintela Castro, Sarah Fernandes Teixeira, and Nathana Jamille Mezzomo. Advances in alzheimer's disease's pharmacological treatment. *Frontiers in Pharmacology*, 14:1101452, 1 2023.
https://doi.org/10.3389/FPHAR.2023.1101452.

[51] Greg Finak. flowworkspace: a package for importing flowjo workspaces into r. *R Guide*, 2014.

[52] Greg Finak, Jacob Frelinger, Wenxin Jiang, Evan W. Newell, John Ramey, Mark M. Davis, Spyros A. Kalams, Stephen C. De Rosa, and Raphael Gottardo. Opencyto: An open source infrastructure for scalable, robust, reproducible, and automated, end-to-end flow cytometry data analysis. *PLOS Computational Biology*, 10:e1003806, 8 2014.
https://doi.org/10.1371/JOURNAL.PCBI.1003806.

[53] Greg Finak, Wenxin Jiang, and Raphael Gottardo. Cytoml for cross-platform cytometry data sharing. *Cytometry Part A*, 93:1189–1196, 12 2018.
https://doi.org/10.1002/CYTO.A.23663.

[54] Lukas Flatz, Fiamma Berner, David Bomze, Stefan Diem, Omar Hasan Ali, Mirjam Fässler, Sandra Ring, Rebekka Niederer, Christoph J. Ackermann, Petra Baumgaertner, Natalia Pikor, Cristina Gil Cruz, Willem Van De Veen, Mübeccel Akdis, Sergey Nikolaev, Heinz Läubli, Alfred Zippelius, Fabienne Hartmann, Hung Wei Cheng, Gideon Hönger, Mike Recher, Jonathan Goldman, Antonio Cozzio, Martin Früh, Jacques Neefjes, Christoph Driessen, Burkhard Ludewig, Ahmed N. Hegazy, Wolfram Jochum, and Daniel E. Speiser. Association of checkpoint inhibitor–induced toxic effects with shared cancer and tissue antigens in non–small cell lung cancer. *JAMA Oncology*, 5:1043–1047, 7 2019.
https://doi.org/10.1001/JAMAONCOL.2019.0402.

[55] Wolf Herman Fridman, Franck Pagès, Catherine Sauts-Fridman, and Jérôme Galon. The immune contexture in human tumours: impact on clinical outcome. *Nature Reviews Cancer 2012 12:4*, 12:298–306, 3 2012.
https://doi.org/10.1038/nrc3245.

[56] Markus Fridén, Marie Wennerberg, Madeleine Antonsson, Maria Sandberg-Ställ, Lars Farde, and Magnus Schou. Identification of positron emission tomography (pet) tracer candidates by prediction of the target-bound fraction in the brain. *EJNMMI Research*, 2014.
https://doi.org/10.1186/s13550-014-0050-6.

[57] Giovanni B. Frisoni, Daniele Altomare, Dietmar Rudolf Thal, Federica Ribaldi, Rik van der Kant, Rik Ossenkoppele, Kaj Blennow, Jeffrey Cummings, Cornelia van Duijn, Peter M. Nilsson, Pierre Yves Dietrich, Philip Scheltens, and Bruno Dubois. The probabilistic model of alzheimer disease: the amyloid hypothesis revised. *Nature Reviews Neuroscience 2021 23:1*, 23:53–66, 11 2021.
https://doi.org/10.1038/s41583-021-00533-w.

[58] Takeshi Fuchigami, Kohnosuke Itagaki, Natsumi Ishikawa, Sakura Yoshida, and Morio Nakayama. Synthesis and evaluation of radioactive/fluorescent peptide probes for imaging of legumain activity. *Bioorganic & Medicinal Chemistry Letters*,

29:126629, 10 2019.
https://doi.org/10.1016/J.BMCL.2019.126629.

[59] M. E. Gallina, T. J. Kim, J. Vasquez, S. Tuerkcan, P. Abbyad, and G. Pratx. Single-cell analysis of radiotracers' uptake by fluorescence microscopy: direct and droplet approach. *https://doi.org/10.1117/12.2253169*, 10068:67–74, 2 2017.
https://doi.org/10.1117/12.2253169.

[60] Jessica Gawenda, Frank Traub, Hans J. Lück, Hans Kreipe, and Reinhard Von Wasielewski. Legumain expression as a prognostic factor in breast cancer patients. *Breast Cancer Research and Treatment*, 102:1–6, 3 2007.
https://doi.org/10.1007/S10549-006-9311-Z.

[61] Andrew L. Goertzen, Qinan Bao, Mélanie Bergeron, Eric Blankemeyer, Stephan Blinder, Mario Cañadas, Arion F. Chatziioannou, Katherine Dinelle, Esmat Elhami, Hans Sonke Jans, Eduardo Lage, Roger Lecomte, Vesna Sossi, Suleman Surti, Yuan Chuan Tai, Juan José Vaquero, Esther Vicente, Darin A. Williams, and Richard Laforest. Nema nu 4-2008 comparison of preclinical pet imaging systems. *Journal of nuclear medicine : official publication, Society of Nuclear Medicine*, 53:1300–1309, 8 2012.
https://doi.org/10.2967/JNUMED.111.099382.

[62] Jun Gong, Alexander Chehrazi-Raffle, Srikanth Reddi, and Ravi Salgia. Development of pd-1 and pd-l1 inhibitors as a form of cancer immunotherapy: a comprehensive review of registration trials and future considerations. *Journal for ImmunoTherapy of Cancer*, 6:8, 12 2018.
https://doi.org/10.1186/S40425-018-0316-Z.

[63] Jonathan B. Grimm and Luke D. Lavis. Caveat fluorophore: an insiders' guide to small-molecule fluorescent labels. *Nature Methods 2021 19:2*, 19:149–158, 12 2021.
https://doi.org/10.1038/s41592-021-01338-6.

[64] Jürgen Grünberg, Karin Knogler, Robert Waibel, Ilse Novak-Hofer, Piruz Nahreini, Amy J Han-Son, and Kedar N Prasad. High-yield production of recombinant antibody fragments in hek-293 cells using sodium butyrate. *BioTechniques*, 34:968–972, 5 2003.
https://doi.org/10.2144/03345ST02.

[65] Shenrui Guo, Hui Wang, and Yafu Yin. Microglia polarization from m1 to m2 in neurodegenerative diseases. *Frontiers in Aging Neuroscience*, 14, 2 2022.
https://doi.org/10.3389/FNAGI.2022.815347.

[66] Florian Hahne, Nolwenn LeMeur, Ryan R. Brinkman, Byron Ellis, Perry Haaland, Deepayan Sarkar, Josef Spidlen, Errol Strain, and Robert Gentleman. flowcore: a bioconductor package for high throughput flow cytometry. *BMC bioinformatics*, 10, 4 2009.
https://doi.org/10.1186/1471-2105-10-106.

[67] Douglas Hanahan and Robert A. Weinberg. Hallmarks of cancer: The next generation. *Cell*, 144:646–674, 3 2011.
https://doi.org/10.1016/J.CELL.2011.02.013.

[68] Kristian M. Hargadon, Coleman E. Johnson, and Corey J. Williams. Immune checkpoint blockade therapy for cancer: An overview of fda-approved immune checkpoint inhibitors. *International Immunopharmacology*, 62:29–39, 9 2018. https://doi.org/10.1016/j.intimp.2018.06.001.

[69] Charles R. Harris, K. Jarrod Millman, Stéfan J. van der Walt, Ralf Gommers, Pauli Virtanen, David Cournapeau, Eric Wieser, Julian Taylor, Sebastian Berg, Nathaniel J. Smith, Robert Kern, Matti Picus, Stephan Hoyer, Marten H. van Kerkwijk, Matthew Brett, Allan Haldane, Jaime Fernández del Río, Mark Wiebe, Pearu Peterson, Pierre Gérard-Marchant, Kevin Sheppard, Tyler Reddy, Warren Weckesser, Hameer Abbasi, Christoph Gohlke, and Travis E. Oliphant. Array programming with numpy. *Nature 2020 585:7825*, 585:357–362, 9 2020. https://doi.org/10.1038/s41586-020-2649-2.

[70] Theresa M. Harrison, Renaud La Joie, Anne Maass, Suzanne L. Baker, Kaitlin Swinnerton, Laura Fenton, Taylor J. Mellinger, Lauren Edwards, Julie Pham, Bruce L. Miller, Gil D. Rabinovici, and William J. Jagust. Longitudinal tau accumulation and atrophy in aging and alzheimer disease. *Annals of Neurology*, 85:229–240, 2 2019. https://doi.org/10.1002/ANA.25406.

[71] Mads H. Haugen, Kjetil Boye, Jahn Martin Nesland, Solveig J. Pettersen, Eivind Valen Egeland, Tripti Tamhane, Klaudia Brix, Gunhild M. Maelandsmo, and Kjersti Flatmark. High expression of the cysteine proteinase legumain in colorectal cancer – implications for therapeutic targeting. *European Journal of Cancer*, 51:9–17, 1 2015. https://doi.org/10.1016/J.EJCA.2014.10.020.

[72] Mads H. Haugen, Harald T. Johansen, Solveig J. Pettersen, Rigmor Solberg, Klaudia Brix, Kjersti Flatmark, and Gunhild M. Maelandsmo. Nuclear legumain activity in colorectal cancer. *PLOS ONE*, 8:e52980, 1 2013. https://doi.org/10.1371/JOURNAL.PONE.0052980.

[73] Anne Laure Hemonnot, Jennifer Hua, Lauriane Ulmann, and Hélène Hirbec. Microglia in alzheimer disease: Well-known targets and new opportunities. *Frontiers in Cellular and Infection Microbiology*, 9:474803, 8 2019. https://doi.org/10.3389/FNAGI.2019.00233.

[74] Michael T. Heneka, Douglas T. Golenbock, and Eicke Latz. Innate immunity in alzheimer's disease. *Nature Immunology 2015 16:3*, 16:229–236, 2 2015. https://doi.org/10.1038/ni.3102.

[75] Archibald Vivian Hill. The possible effects of the aggregation of the molecules of hemoglobin on its dissociation curves. *j. physiol.*, 40:iv–vii, 1910.

[76] John Hilton, Fuji Yokoi, Robert F. Dannals, Hayden T. Ravert, Zsolt Szabo, and Dean F. Wong. Column-switching hplc for the analysis of plasma in pet imaging studies. *Nuclear Medicine and Biology*, 2000. https://10.1016/S0969-8051(00)00125-6.

[77] Stanley Hirsch, Jonathan M. Austyn, and Siamon Gordon. Expression of the macrophage-specific antigen f4/80 during differentiation of mouse bone marrow cells in culture. *The Journal of Experimental Medicine*, 154:713, 9 1981. https://doi.org/10.1084/JEM.154.3.713.

[78] E. Hochuli, W. Bannwarth, H. Dobeli, R. Gentzi, and D. Stuber. Genetic approach to facilitate purification of recombinant proteins with a novel metal chelate adsorbent. *Bio/Technology 1988 6:11*, 6:1321–1325, 1988. https://doi.org/10.1038/nbt1188-1321.

[79] Camilla Hofström, Mohamed Altai, Hadis Honarvar, Joanna Strand, Jennie Malmberg, Seyed Jalal Hosseinimehr, Anna Orlova, Torbjörn Gräslund, and Vladimir Tolmachev. Hahaha, hehehe, hihihi, or hkhkhk: Influence of position and composition of histidine containing tags on biodistribution of [99mtc(co) 3]+-labeled affibody molecules. *Journal of Medicinal Chemistry*, 56:4966–4974, 6 2013. https://doi.org/10.1021/JM400218Y.

[80] Di Hua, Hongjie Xi, Quan Xie, Shuyue Cai, Yuxuan Zhou, Xin Hu, Ling Qiu, and Jianguo Lin. Lysosome-targeting and legumain-triggered 68ga-labeled probe for enhanced tumor pet imaging. *Biochemical and Biophysical Research Communications*, 703:149646, 4 2024. https://doi.org/10.1016/J.BBRC.2024.149646.

[81] Fangjiao Huang, Xiaoli Han, Xiaohui Xiao, and Jinming Zhou. Covalent warheads targeting cysteine residue: The promising approach in drug development. *Molecules 2022, Vol. 27, Page 7728*, 27:7728, 11 2022. https://doi.org/10.3390/MOLECULES27227728.

[82] John D. Hunter. Matplotlib: A 2d graphics environment. *Computing in Science and Engineering*, 9:90–95, 2007. https://doi.org/10.1109/MCSE.2007.55.

[83] Shin Ichi Ishii. [42] legumain: Asparaginyl endopeptidase. *Methods in Enzymology*, 244:604–615, 1 1994. https://doi.org/10.1016/0076-6879(94)44044-1.

[84] Taku Ishizaki, Agnes Erickson, Enida Kuric, Mehrdad Shamloo, Ikuko Hara-Nishimura, Ana Rita Lourenço Inácio, Tadeusz Wieloch, and Karsten Ruscher. The asparaginyl endopeptidase legumain after experimental stroke. *Journal of Cerebral Blood Flow & Metabolism*, 30:1756, 2010. https://doi.org/10.1038/JCBFM.2010.39.

[85] Clifford R. Jack and David M. Holtzman. Biomarker modeling of alzheimer's disease. *Neuron*, 80:1347–1358, 12 2013. https://doi.org/10.1016/J.NEURON.2013.12.003.

[86] Caitlin V.M.L. Jie, Valerie Treyer, Roger Schibli, and Linjing Mu. Tauvid™: The first fda-approved pet tracer for imaging tau pathology in alzheimer's disease. *Pharmaceuticals 2021, Vol. 14, Page 110*, 14:110, 1 2021. https://doi.org/10.3390/PH14020110.

[87] Harald T. Johansen, C. Graham Knight, and Alan J. Barrett. Colorimetric and fluorimetric microplate assays for legumain and a staining reaction for detection of the enzyme after electrophoresis. *Analytical Biochemistry*, 273:278–283, 9 1999. https://doi.org/10.1006/ABIO.1999.4221.

[88] Seong Su Kang, Eun Hee Ahn, and Keqiang Ye. Delta-secretase cleavage of tau mediates its pathology and propagation in alzheimer's disease. *Experimental & Molecular Medicine 2020 52:8*, 52:1275–1287, 8 2020. https://doi.org/10.1038/s12276-020-00494-7.

[89] Bremer Karl-heinz and Aktiengesellschaft Hoechst. Large-scale production and distribution of tc-99m generators for medical use. *Radiochimica Acta*, 41:73–82, 2 1987. https://doi.org/10.1524/RACT.1987.41.23.73.

[90] L K Keefer, A J Streeter, L Y Leung, W C Perry, H S Hu, and T A Baillie. Pharmacokinetic and deuterium isotope effect studies on the metabolism of formaldehyde and formate to carbon dioxide in rats in vivo. *Drug Metabolism and Disposition*, 15, 1987.

[91] Syamantak Khan, Sungwoo Kim, Yunzhi Peter Yang, and Guillem Pratx. High-resolution radioluminescence microscopy of fdg uptake in an engineered 3d tumor-stoma model. *European Journal of Nuclear Medicine and Molecular Imaging*, 48:3400–3407, 10 2021. https://doi.org/10.1007/S00259-021-05364-6.

[92] Syamantak Khan, June Ho Shin, Valentina Ferri, Ning Cheng, Julia E. Noel, Calvin Kuo, John B. Sunwoo, and Guillem Pratx. High-resolution positron emission microscopy of patient-derived tumor organoids. *Nature Communications 2021 12:1*, 12:1–11, 10 2021. https://doi.org/10.1038/s41467-021-26081-6.

[93] Minkyu Kim, Ming Pan, Ya Gai, Shuo Pang, Chao Han, Changhuei Yang, and Sindy K.Y. Tang. Optofluidic ultrahigh-throughput detection of fluorescent drops. *Lab on a Chip*, 15:1417–1423, 3 2015. https://doi.org/10.1039/C4LC01465K.

[94] Tae Jin Kim, Silvan Türkcan, and Guillem Pratx. Modular low-light microscope for imaging cellular bioluminescence and radioluminescence. *Nature Protocols 2017 12:5*, 12:1055–1076, 4 2017. https://doi.org/10.1038/nprot.2017.008.

[95] Tae Jin Kim, Qian Wang, Mark Shelor, and Guillem Pratx. Single-cell radioluminescence microscopy with two-fold higher sensitivity using dual scintillator configuration. *PLOS ONE*, 15:e0221241, 7 2020. https://doi.org/10.1371/JOURNAL.PONE.0221241.

[96] Louise Kiru, Tae Jin Kim, Bin Shen, Frederick T. Chin, and Guillem Pratx. Single-cell imaging using radioluminescence microscopy reveals unexpected binding target for [18f]hfb. *Molecular Imaging and Biology*, 20:378–387, 6 2018. https://doi.org/10.1007/S11307-017-1144-0.

[97] Justin S. Klein, Tae Jin Kim, and Guillem Pratx. Development of a lensless radiomicroscope for cellular-resolution radionuclide imaging. *Journal of Nuclear Medicine*, 64:479–484, 3 2023.
https://doi.org/10.2967/JNUMED.122.264021.

[98] David S. Knopman, Helene Amieva, Ronald C. Petersen, Gäel Chételat, David M. Holtzman, Bradley T. Hyman, Ralph A. Nixon, and David T. Jones. Alzheimer disease. *Nature Reviews Disease Primers 2021 7:1*, 7:1–21, 5 2021.
https://doi.org/10.1038/s41572-021-00269-y.

[99] Yoshihiro Komohara, Yukio Fujiwara, Koji Ohnishi, and Motohiro Takeya. Tumor-associated macrophages: Potential therapeutic targets for anti-cancer therapy. *Advanced Drug Delivery Reviews*, 99:180–185, 4 2016.
https://doi.org/10.1016/J.ADDR.2015.11.009.

[100] Shohei Koyama, Tsunehiko Maruyama, Shinya Adachi, and Mutsumi Nozue. Expression of costimulatory molecules, b7-1 and b7-2 on human gastric carcinoma. *Journal of Cancer Research and Clinical Oncology*, 124:383–388, 1998.
https://doi.org/10.1007/S004320050187.

[101] Daniela Krummenacher, Weiping He, Bernd Kuhn, Christian Schnider, Angélica Beurier, Virginie Brom, Thulase Sivasothy, Christine Marty, Andreas Tosstorff, David S. Hewings, Stefanie Mesch, Emmanuel Pinard, Mathis Brändlin, Remo Hochstrasser, Paul Westwood, Judith Rothe, Alexandra Kronenberger, Federica Morandi, Simon Gutbier, Angelika Schuler, Dominik Heer, Ludivine Esteves Gloria, Lisa Joedicke, Markus G. Rudolph, Lutz Müller, Fiona Grüninger, Karlheinz Baumann, Senthilvelrajan Kaniyappan, Nenad Manevski, and Björn Bartels. Discovery of orally available and brain penetrant aep inhibitors. *Journal of Medicinal Chemistry*, 66:17026–17043, 12 2023.
https://doi.org/10.1021/ACS.JMEDCHEM.3C01804.

[102] Fabian Krutzek, Cornelius K. Donat, Martin Ullrich, Kristof Zarschler, Marie Charlotte Ludik, Anja Feldmann, Liliana R. Loureiro, Klaus Kopka, and Sven Stadlbauer. Design and biological evaluation of small-molecule pet-tracers for imaging of programmed death ligand 1. *Cancers*, 15:2638, 5 2023.
https://doi.org/10.3390/CANCERS15092638.

[103] Fabian Krutzek, Klaus Kopka, and Sven Stadlbauer. Development of radiotracers for imaging of the pd-1/pd-l1 axis. *Pharmaceuticals 2022, Vol. 15, Page 747*, 15:747, 6 2022.
https://doi.org/10.3390/PH15060747.

[104] B T Kurien and R Hal Scofield. *Western blotting: Methods and protocols. West.* 2015.

[105] James Larkin, Vanna Chiarion-Sileni, Rene Gonzalez, Jean Jacques Grob, C. Lance Cowey, Christopher D. Lao, Dirk Schadendorf, Reinhard Dummer, Michael Smylie, Piotr Rutkowski, Pier F. Ferrucci, Andrew Hill, John Wagstaff, Matteo S. Carlino, John B. Haanen, Michele Maio, Ivan Marquez-Rodas, Grant A. McArthur, Paolo A. Ascierto, Georgina V. Long, Margaret K. Callahan, Michael A. Postow, Kenneth Grossmann, Mario Sznol, Brigitte Dreno, Lars Bastholt, Arvin Yang, Linda M. Rollin,

Christine Horak, F. Stephen Hodi, and Jedd D. Wolchok. Combined nivolumab and ipilimumab or monotherapy in untreated melanoma. *New England Journal of Medicine*, 373:23–34, 7 2015.
https://doi.org/10.1056/NEJMOA1504030.

[106] Joseph Lau, Etienne Rousseau, Daniel Kwon, Kuo Shyan Lin, François Bénard, and Xiaoyuan Chen. Insight into the development of pet radiopharmaceuticals for oncology. *Cancers 2020, Vol. 12, Page 1312*, 12:1312, 5 2020.
https://doi.org/10.3390/CANCERS12051312.

[107] Markus Laube, Maxim Frizler, Robert Wodtke, Christin Neuber, Birgit Belter, Torsten Kniess, Michael Bachmann, Michael Gütschow, Jens Pietzsch, and Reik Löser. Synthesis and preliminary radiopharmacological characterisation of an 11c-labelled azadipeptide nitrile as potential pet tracer for imaging of cysteine cathepsins. *Journal of Labelled Compounds and Radiopharmaceuticals*, 62:448–459, 6 2019.
https://doi.org/10.1002/JLCR.3729.

[108] Jiyoun Lee and Matthew Bogyo. Development of near-infrared fluorophore (nirf)-labeled activity-based probes for in vivo imaging of legumain. *ACS Chemical Biology*, 5:233–243, 2 2010.
https://doi.org/10.1021/cb900232a.

[109] K. L. Leenders, D. Perani, A. A. Lammertsma, J. D. Heather, P. Buckingham, T. Jones, M. J.R. Healy, J. M. Gibbs, R. J.S. Wise, J. Hatazawa, S. Herold, R. P. Beaney, D. J. Brooks, T. Spinks, C. Rhodes, and R. S.J. Frackowiak. Cerebral blood flow, blood volume and oxygen utilization: Normal values and effect of age. *Brain*, 113:27–47, 2 1990.
https://doi.org/10.1093/BRAIN/113.1.27.

[110] Mengjun Li, Linye He, Jing Zhu, Peng Zhang, and Shufang Liang. Targeting tumor-associated macrophages for cancer treatment. *Cell & Bioscience 2022 12:1*, 12:1–13, 6 2022.
https://doi.org/10.1186/S13578-022-00823-5.

[111] Xi Li, Qingzhu Liu, Siqin Ye, Shijie Wang, Ke Li, Gaochao Lv, Ying Peng, Ling Qiu, and Jianguo Lin. A protease-responsive fluorescent probe for sensitive imaging of legumain activity in living tumor cells. *Chemical Biology & Drug Design*, 94:1494–1503, 8 2019.
https://doi.org/10.1111/CBDD.13530.

[112] Jianming Liao, Chun Chen, Eun Hee Ahn, Xia Liu, Hua Li, Laura E. Edgington-Mitchell, Zhonghua Lu, Shuping Ming, and Keqiang Ye. Targeting both bdnf/trkb pathway and delta-secretase for treating alzheimer's disease. *Neuropharmacology*, 197:108737, 10 2021.
https://doi.org/10.1016/J.NEUROPHARM.2021.108737.

[113] E. A. Lim, C. G. Drake, and A. Mintz. Molecular imaging for cancer immunotherapy. *Immuno-Oncology Technology*, 5:10–21, 3 2020.
https://doi.org/10.1016/J.IOTECH.2020.03.001.

[114] Thiago V.M. Lima, Silvano Gnesin, Klaus Strobel, Maria Del Sol Pérez, Justus E. Roos, Cristina Müller, and Nicholas P. van der Meulen. Fifty shades of scandium: Comparative study of pet capabilities using sc-43 and sc-44 with respect to conventional clinical radionuclides. *Diagnostics 2021, Vol. 11, Page 1826*, 11:1826, 10 2021.
https://doi.org/10.3390/DIAGNOSTICS11101826.

[115] Yingying Lin, Yongming Qiu, Cheng Xu, Qiaoling Liu, Baowei Peng, Gunnar F. Kaufmann, Xi Chen, Bin Lan, Chongyang Wei, Desheng Lu, Yueshan Zhang, Yifeng Guo, Zhimin Lu, Biao Jiang, Thomas S. Edgington, and Fang Guo. Functional role of asparaginyl endopeptidase ubiquitination by traf6 in tumor invasion and metastasis. *Journal of the National Cancer Institute*, 106, 4 2014.
https://doi.org/10.1093/JNCI/DJU012.

[116] Yingying Lin, Chongyang Wei, Yuan Liu, Yongming Qiu, Cheng Liu, and Fang Guo. Selective ablation of tumor-associated macrophages suppresses metastasis and angiogenesis. *Cancer Science*, 104:1217–1225, 9 2013.
https://10.1111/CAS.12202.

[117] Bradley C. Lowekamp, David T. Chen, Luis Ibáñez, and Daniel Blezek. The design of simpleitk. *Frontiers in Neuroinformatics*, 7:73735, 12 2013.
https://doi.org/10.3389/FNINF.2013.00045.

[118] Chunmei Lu, Ke Li, Hongjie Xi, Di Hua, Huirong Li, Feng Gao, Ling Qiu, and Jianguo Lin. Dual-targeting pet tracers enable enzyme-mediated self-assembly for the pet imaging of legumain activity. *ACS Applied Materials and Interfaces*, 15:44654–44664, 9 2023.
https://doi.org/10.1021/acsami.3c07479.

[119] Chunmei Lu, Xiuting Wang, Qiqi Wang, Lixia Zhang, Jianguo Lin, and Ling Qiu. Development of a promising 18f-radiotracer for pet imaging legumain activity in vivo. *Pharmaceuticals*, 15:543, 5 2022.
https://doi.org/10.3390/PH15050543.

[120] Severin K. Lustenberger, Claudia A. Castro Jaramillo, Lena A. Bärtschi, Rich Williams, Roger Schibli, Linjing Mu, and Stefanie D. Krämer. Towards imaging the immune state of cancer by pet: Targeting legumain with 11c-labeled p1-asn peptidomimetics carrying a cyano-warhead. *Nuclear Medicine and Biology*, page 108951, 9 2024.
https://doi.org/10.1016/J.NUCMEDBIO.2024.108951.

[121] Izumi Maezawa, Pavel I. Zimin, Heike Wulff, and Lee Way Jin. Amyloid-β protein oligomer at low nanomolar concentrations activates microglia and induces microglial neurotoxicity. *Journal of Biological Chemistry*, 286:3693–3706, 2 2011.
https://doi.org/10.1074/jbc.M110.135244.

[122] David A. Mankoff, Christine E. Edmonds, Michael D. Farwell, and Daniel A. Pryma. Development of companion diagnostics. *Seminars in Nuclear Medicine*, 46:47–56, 1 2016.
https://doi.org/10.1053/J.SEMNUCLMED.2015.09.002.

[123] Colin L. Masters, Randall Bateman, Kaj Blennow, Christopher C. Rowe, Reisa A. Sperling, and Jeffrey L. Cummings. Alzheimer's disease. *Nature Reviews Disease Primers 2015 1:1*, 1:1–18, 10 2015. https://doi.org/10.1038/nrdp.2015.56.

[124] Y. Matsumura and H. Maeda. A new concept for macromolecular therapeutics in cancer chemotherapy: mechanism of tumoritropic accumulation of proteins and the antitumor agent smancs. *Cancer Research*, 46(12 Pt 1):6387–6392, Dec 1986.

[125] Wes McKinney. Data structures for statistical computing in python. *Proceedings of the 9th Python in Science Conference*, pages 56–61, 2010. https://doi.org/10.25080/MAJORA-92BF1922-00A.

[126] Romana Meletta, Adrienne Müller Herde, Patrick Dennler, Eliane Fischer, Roger Schibli, and Stefanie D. Krämer. Preclinical imaging of the co-stimulatory molecules cd80 and cd86 with indium-111-labeled belatacept in atherosclerosis. *EJNMMI Research*, 6:1–12, 12 2016. https://doi.org/10.1186/S13550-015-0157-4/FIGURES/5.

[127] P. Anton Van Der Merwe, Dale L. Bodian, Susan Daenke, Peter Linsley, and Simon J. Davis. Cd80 (b7-1) binds both cd28 and ctla-4 with a low affinity and very fast kinetics. *The Journal of experimental medicine*, 185:393–403, 2 1997. https://doi.org/10.1084/JEM.185.3.393.

[128] Charles D. Mills. M1 and m2 macrophages: Oracles of health and disease. *Critical Reviews™ in Immunology*, 32:463–488, 2012. https://doi.org/10.1615/CRITREVIMMUNOL.V32.I6.10.

[129] Manzoor Ahmad Mir. Introduction to costimulation and costimulatory molecules. *Developing Costimulatory Molecules for Immunotherapy of Diseases*, pages 1–43, 1 2015. https://doi.org/10.1016/B978-0-12-802585-7.00001-7.

[130] Gianni Monaco, Hao Chen, Michael Poidinger, Jinmiao Chen, João Pedro De Magalhães, and Anis Larbi. flowai: automatic and interactive anomaly discerning tools for flow cytometry data. *Bioinformatics (Oxford, England)*, 32:2473–2480, 8 2016. https://doi.org/10.1093/BIOINFORMATICS/BTW191.

[131] Yoshikata Morita, Hisazumi Araki, Toshiro Sugimoto, Keisuke Takeuchi, Takuya Yamane, Toshinaga Maeda, Yoshio Yamamoto, Katsuji Nishi, Masahide Asano, Kanae Shirahama-Noda, Mikio Nishimura, Takashi Uzu, Ikuko Hara-Nishimura, Daisuke Koya, Atsunori Kashiwagi, and Iwao Ohkubo. Legumain/asparaginyl endopeptidase controls extracellular matrix remodeling through the degradation of fibronectin in mouse renal proximal tubular cells. *FEBS letters*, 581:1417–1424, 4 2007. https://doi.org/10.1016/J.FEBSLET.2007.02.064.

[132] Kenneth Murphy and Casey Weaver. *Janeway's immunobiology*. Garland science, 2016.

[133] Peter J. Murray, Judith E. Allen, Subhra K. Biswas, Edward A. Fisher, Derek W. Gilroy, Sergij Goerdt, Siamon Gordon, John A. Hamilton, Lionel B. Ivashkiv, Toby Lawrence, Massimo Locati, Alberto Mantovani, Fernando O. Martinez, Jean Louis Mege, David M. Mosser, Gioacchino Natoli, Jeroen P. Saeij, Joachim L. Schultze, Kari Ann Shirey, Antonio Sica, Jill Suttles, Irina Udalova, Jo A. vanGinderachter, Stefanie N. Vogel, and Thomas A. Wynn. Macrophage activation and polarization: nomenclature and experimental guidelines. *Immunity*, 41:14, 7 2014. https://doi.org/10.1016/J.IMMUNI.2014.06.008.

[134] Raghavendra Vasudeva Murthy, Gunnar Arbman, Jingfang Gao, G. David Roodman, and Xiao Feng Sun. Legumain expression in relation to clinicopathologic and biological variables in colorectal cancer. *Clinical Cancer Research*, 11:2293–2299, 3 2005. https://doi.org/10.1158/1078-0432.CCR-04-1642.

[135] Cristina Müller, Alexander Hohn, P. August Schubiger, and Roger Schibli. Preclinical evaluation of novel organometallic 99mtc-folate and 99mtc-pteroate radiotracers for folate receptor-positive tumour targeting. *European Journal of Nuclear Medicine and Molecular Imaging*, 33:1007–1016, 9 2006. https://doi.org/10.1007/s00259-006-0111-9.

[136] Arutselvan Natarajan, Silvan Türkcan, Sanjiv S. Gambhir, and Guillem Pratx. Multiscale framework for imaging radiolabeled therapeutics. *Molecular Pharmaceutics*, 12:4554–4560, 10 2015. https://doi.org/10.1021/ACS.MOLPHARMACEUT.5B00392.

[137] Victoria Navarro, Elisabeth Sanchez-Mejias, Sebastian Jimenez, Clara Muñoz-Castro, Raquel Sanchez-Varo, Jose C. Davila, Marisa Vizuete, Antonia Gutierrez, and Javier Vitorica. Microglia in alzheimer's disease: Activated, dysfunctional or degenerative. *Frontiers in Aging Neuroscience*, 10:357752, 5 2018. https://doi.org/10.3389/FNAGI.2018.00140.

[138] Kerry A. Ness, Sharon L. Eddie, Catherine A. Higgins, Amy Templeman, Zenobia D'Costa, Kishore K.D. Gaddale, Samira Bouzzaoui, Linda Jordan, Dominic Janssen, Timothy Harrison, Frank Burkamp, Andrew Young, Roberta Burden, Christopher J. Scott, Paul B. Mullan, and Rich Williams. Development of a potent and selective cell penetrant legumain inhibitor. *Bioorganic & Medicinal Chemistry Letters*, 25:5642–5645, 12 2015. https://doi.org/10.1016/J.BMCL.2015.10.001.

[139] Kerry Anne Ness, Sharon L. Eddie, Stephanie Burton, Timothy Harrison, Paul Mullan, and Rich Williams. Flat sar of p3-methylsulphonamide based small molecule legumain inhibitors. *Bioorganic & Medicinal Chemistry Letters*, 26:413–416, 1 2016. https://doi.org/10.1016/J.BMCL.2015.11.101.

[140] Hai M. Nguyen, Eva M. Grössinger, Makoto Horiuchi, Kyle W. Davis, Lee Way Jin, Izumi Maezawa, and Heike Wulff. Differential kv1.3, kca3.1, and kir2.1 expression in "classically" and "alternatively" activated microglia. *Glia*, 65:106, 1 2017. https://doi.org/10.1002/GLIA.23078.

[141] André J. Niestroj, Kirstin Feußner, Ulrich Heiser, Pam M. Dando, Alan Barrett, Bernd Gerhartz, and Hans Ulrich Demuth. Inhibition of mammalian legumain by michael acceptors and azaasn-halomethylketones. *Biological Chemistry*, 383:1205–1214, 7 2002.
https://doi.org/10.1515/BC.2002.133.

[142] Li Niu, Ting Chen, Aodan Yang, Xiwen Yan, Feng Jin, Ang Zheng, and Xinyue Song. Macrophages and tertiary lymphoid structures as indicators of prognosis and therapeutic response in cancer patients. *Biochimica et Biophysica Acta (BBA) - Reviews on Cancer*, 1879:189125, 9 2024.
https://doi.org/10.1016/J.BBCAN.2024.189125.

[143] Isaac Nuñez, Tamara Matute, Roberto Herrera, Juan Keymer, Timothy Marzullo, Timothy Rudge, and Fernán Federici. Low cost and open source multi-fluorescence imaging system for teaching and research in biology and bioengineering. *PLOS ONE*, 12:e0187163, 11 2017.
https://doi.org/10.1371/JOURNAL.PONE.0187163.

[144] Yoshio Ohno, Jun Nakashima, Miki Izumi, Makoto Ohori, Takeshi Hashimoto, and Masaaki Tachibana. Association of legumain expression pattern with prostate cancer invasiveness and aggressiveness. *World Journal of Urology*, 31:359–364, 4 2013.
https://doi.org/10.1007/S00345-012-0977-Z.

[145] Oakley C. Olson and Johanna A. Joyce. Cysteine cathepsin proteases: regulators of cancer progression and therapeutic response. *Nature Reviews Cancer 2015 15:12*, 15:712–729, 11 2015.
https://doi.org/10.1038/nrc4027.

[146] Dmitry A. Ovchinnikov. Macrophages in the embryo and beyond: Much more than just giant phagocytes. *genesis*, 46:447–462, 9 2008.
https://doi.org/10.1002/DVG.20417.

[147] Lizhi Pang, Songlin Guo, Fatima Khan, Madeline Dunterman, Heba Ali, Yang Liu, Yuyun Huang, and Peiwen Chen. Hypoxia-driven protease legumain promotes immunosuppression in glioblastoma. *Cell Reports Medicine*, 4:101238, 11 2023.
https://doi.org/10.1016/j.xcrm.2023.101238.

[148] Neha N. Parayath, Avani Parikh, and Mansoor M. Amiji. Repolarization of tumor-associated macrophages in a genetically engineered nonsmall cell lung cancer model by intraperitoneal administration of hyaluronic acid-based nanoparticles encapsulating microrna-125b. *Nano Letters*, 18:3571–3579, 6 2018.
https://doi.org/10.1021/acs.nanolett.8b00689.

[149] Robert J. Peachi, Jürgen Bajorath, Joseph Naemura, Gina Leytze, Jo Anne Greene, Alejandro Aruffo, and Peter S. Linsley. Both extracellular immunoglobin-like domains of cd80 contain residues critical for binding t cell surface receptors ctla-4 and cd28. *Journal of Biological Chemistry*, 270:21181–21187, 9 1995.
https://doi.org/10.1074/JBC.270.36.21181.

[150] Qi Peng, Xiangyan Qiu, Zihan Zhang, Silin Zhang, Yuanyuan Zhang, Yong Liang, Jingya Guo, Hua Peng, Mingyi Chen, Yang Xin Fu, and Haidong Tang. Pd-l1

on dendritic cells attenuates t cell activation and regulates response to immune checkpoint blockade. *Nature Communications 2020 11:1*, 11:1–8, 9 2020. https://doi.org/10.1038/s41467-020-18570-x.

[151] V. Phu, Wenxin Jiang, Raphael Gottardo, and Greg Finak. ggcyto: next generation open-source visualization software for cytometry. *Bioinformatics*, 34:3951–3953, 11 2018. https://doi.org/10.1093/BIOINFORMATICS/BTY441.

[152] Marcin Poreba. Recent advances in the development of legumain-selective chemical probes and peptide prodrugs. *Biological Chemistry*, 400:1529–1550, 12 2019. https://doi.org/10.1515/HSZ-2019-0135.

[153] Marcin Poreba, Rigmor Solberg, Wioletta Rut, Ngoc Nguyen Lunde, Paulina Kasperkiewicz, Scott J. Snipas, Marko Mihelic, Dusan Turk, Boris Turk, Guy S. Salvesen, and Marcin Drag. Counter selection substrate library strategy for developing specific protease substrates and probes. *Cell Chemical Biology*, 23:1023–1035, 8 2016. https://doi.org/10.1016/J.CHEMBIOL.2016.05.020.

[154] Michael A. Postow, Jason Chesney, Anna C. Pavlick, Caroline Robert, Kenneth Grossmann, David McDermott, Gerald P. Linette, Nicolas Meyer, Jeffrey K. Giguere, Sanjiv S. Agarwala, Montaser Shaheen, Marc S. Ernstoff, David Minor, April K. Salama, Matthew Taylor, Patrick A. Ott, Linda M. Rollin, Christine Horak, Paul Gagnier, Jedd D. Wolchok, and F. Stephen Hodi. Nivolumab and ipilimumab versus ipilimumab in untreated melanoma. *New England Journal of Medicine*, 372:2006–2017, 5 2015. https://doi.org/10.1056/NEJMOA1414428.

[155] G. Pratx, K. Chen, C. Sun, L. Martin, C. Carpenter, and L. Xing. Radioluminescence microscopy: A new tool to characterize heterogeneous radiopharmaceutical uptake in living cells. *International Journal of Radiation Oncology*Biology*Physics*, 84:S668, 11 2012. https://doi.org/10.1016/j.ijrobp.2012.07.1783.

[156] Guillem Pratx, Kai Chen, Conroy Sun, Marian Axente, Laura Sasportas, Colin Carpenter, and Lei Xing. High-resolution radioluminescence microscopy of 18f-fdg uptake by reconstructing the β-ionization track. *Journal of Nuclear Medicine*, 54:1841–1846, 10 2013. https://doi.org/10.2967/JNUMED.112.113365.

[157] Guillem Pratx, Kai Chen, Conroy Sun, Lynn Martin, Colin M. Carpenter, Peter D. Olcott, and Lei Xing. Radioluminescence microscopy: Measuring the heterogeneous uptake of radiotracers in single living cells. *PLOS ONE*, 7:e46285, 10 2012. https://doi.org/10.1371/JOURNAL.PONE.0046285.

[158] Matthew R.B. Puncher and Philip J. Blower. Radionuclide targeting and dosimetry at the microscopic level: the role of microautoradiography. *European Journal of Nuclear Medicine*, 21:1347–1365, 12 1994. https://doi.org/10.1007/BF02426701.

[159] Ling Qiu, Xi Li, Gaochao Lv, Yann Seimbille, Ke Li, Ying Peng, Qingzhu Liu, Minhao Xie, and Jianguo Lin. Radiofluorinated smart probes for noninvasive pet imaging of legumain activity in living subjects. *Analytical Chemistry*, 92:11627–11634, 9 2020.
https://doi.org/10.1021/acs.analchem.0c01253.

[160] R Core Team. R: A language and environment for statistical computing, 2024.
https://www.R-project.org/.

[161] Anujan Ramesh, Anthony Brouillard, Sahana Kumar, Dipika Nandi, and Ashish Kulkarni. Dual inhibition of csf1r and mapk pathways using supramolecular nanoparticles enhances macrophage immunotherapy. *Biomaterials*, 227:119559, 1 2020.
https://doi.org/10.1016/J.BIOMATERIALS.2019.119559.

[162] Loganathan Rangasamy, Bruno Di Geronimo, Irene Ortín, Claire Coderch, José María Zapico, Ana Ramos, and Beatriz De Pascual-Teresa. Molecular imaging probes based on matrix metalloproteinase inhibitors (mmpis). *Molecules 2019, Vol. 24, Page 2982*, 24:2982, 8 2019.
https://doi.org/10.3390/MOLECULES24162982.

[163] Jianghong Rao. Imaging of tumour acidosis with pet. *Nature Biomedical Engineering 2020 4:3*, 4:250–251, 3 2020.
https://doi.org/10.1038/s41551-020-0533-x.

[164] Martin Reck, Delvys Rodríguez-Abreu, Andrew G. Robinson, Rina Hui, Tibor Csőszi, Andrea Fülöp, Maya Gottfried, Nir Peled, Ali Tafreshi, Sinead Cuffe, Mary O'Brien, Suman Rao, Katsuyuki Hotta, Melanie A. Leiby, Gregory M. Lubiniecki, Yue Shentu, Reshma Rangwala, and Julie R. Brahmer. Pembrolizumab versus chemotherapy for pd-l1–positive non–small-cell lung cancer. *New England Journal of Medicine*, 375:1823–1833, 11 2016.
https://doi.org/10.1056/NEJMOA1606774.

[165] R. S. Reiserer, F. E. Harrison, D. C. Syverud, and M. P. McDonald. Impaired spatial learning in the appswe + psen1deltae9 bigenic mouse model of alzheimer's disease. *Genes, brain, and behavior*, 6:54–65, 2 2007.
https://doi.org/10.1111/J.1601-183X.2006.00221.X.

[166] Farzaneh Rezazadeh and Nourollah Sadeghzadeh. Tumor targeting with 99mtc radiolabeled peptides: Clinical application and recent development. *Chemical Biology & Drug Design*, 93:205–221, 3 2019.
https://doi.org/10.1111/CBDD.13413.

[167] Antoni Ribas and Jedd D. Wolchok. Cancer immunotherapy using checkpoint blockade. *Science*, 359:1350–1355, 3 2018.
https://doi.org/10.1126/SCIENCE.AAR4060.

[168] Christopher C. Rowe, Kathryn A. Ellis, Miroslava Rimajova, Pierrick Bourgeat, Kerryn E. Pike, Gareth Jones, Jurgen Fripp, Henri Tochon-Danguy, Laurence Morandeau, Graeme O'Keefe, Roger Price, Parnesh Raniga, Peter Robins, Oscar Acosta, Nat Lenzo, Cassandra Szoeke, Olivier Salvado, Richard Head, Ralph Martins, Colin L. Masters, David Ames, and Victor L. Villemagne. Amyloid imaging

results from the australian imaging, biomarkers and lifestyle (aibl) study of aging. *Neurobiology of Aging*, 31:1275–1283, 8 2010.
https://doi.org/10.1016/J.NEUROBIOLAGING.2010.04.007.

[169] Madiha Saeed, Zhiai Xu, Bruno G. De Geest, Huixiong Xu, and Haijun Yu. Molecular imaging for cancer immunotherapy: Seeing is believing. *Bioconjugate Chemistry*, 31:404–415, 2 2020.
https://doi.org/10.1021/acs.bioconjchem.9b00851.

[170] Gopal B Saha. *Fundamentals of nuclear pharmacy*, volume 6. Springer, 2004.

[171] Takashi Sato, Kiyoshi Takagi, Mitsunori Higuchi, Hiroko Abe, Michie Kojimahara, Miho Sagawa, Megumi Tanaki, Yasuhiro Miki, Takashi Suzuki, and Hiroshi Hojo. Immunolocalization of cd80 and cd86 in non-small cell lung carcinoma: Cd80 as a potent prognostic factor. *ACTA HISTOCHEMICA ET CYTOCHEMICA*, 55:25–35, 2 2022.
https://doi.org/10.1267/AHC.21-00075.

[172] Dirk Schadendorf, F. Stephen Hodi, Caroline Robert, Jeffrey S. Weber, Kim Margolin, Omid Hamid, Debra Patt, Tai Tsang Chen, David M. Berman, and Jedd D. Wolchok. Pooled analysis of long-term survival data from phase ii and phase iii trials of ipilimumab in unresectable or metastatic melanoma. *Journal of Clinical Oncology*, 33:1889–1894, 6 2015.
https://doi.org/10.1200/JCO.2014.56.2736.

[173] Johannes Schindelin, Ignacio Arganda-Carreras, Erwin Frise, Verena Kaynig, Mark Longair, Tobias Pietzsch, Stephan Preibisch, Curtis Rueden, Stephan Saalfeld, Benjamin Schmid, Jean Yves Tinevez, Daniel James White, Volker Hartenstein, Kevin Eliceiri, Pavel Tomancak, and Albert Cardona. Fiji: An open-source platform for biological-image analysis. *Nature Methods 2012 9:7*, 9:676–682, 6 2012.
https://doi.org/10.1038/nmeth.2019.

[174] Ton N. Schumacher and Daniela S. Thommen. Tertiary lymphoid structures in cancer. *Science*, 375, 1 2022.
https://doi.org/10.1126/SCIENCE.ABF9419.

[175] Tina Schwabe, Karpagam Srinivasan, and Herve Rhinn. Shifting paradigms: The central role of microglia in alzheimer's disease. *Neurobiology of Disease*, 143:104962, 9 2020.
https://doi.org/10.1016/J.NBD.2020.104962.

[176] Debanti Sengupta, Stuart Miller, Zsolt Marton, Frederick Chin, Vivek Nagarkar, Guillem Pratx, D Sengupta, G Pratx, S Miller, Z Marton, V Nagarkar, and F Chin. Bright lu2o3:eu thin-film scintillators for high-resolution radioluminescence microscopy. *Advanced Healthcare Materials*, 4:2064–2070, 10 2015.
https://doi.org/10.1002/ADHM.201500372.

[177] Debanti Sengupta and Guillem Pratx. Single-cell characterization of 18f-flt uptake with radioluminescence microscopy. *Journal of Nuclear Medicine*, 57:1136–1140, 7 2016.
https://doi.org/10.2967/JNUMED.115.167734.

[178] Debanti Sengupta and Guillem Pratx. Radioluminescence microscopy: A quantitative method for radioisotopic imaging of metabolic fluxes in living cancer cells. *Methods in Molecular Biology*, 1928:45–53, 2019. https://doi.org/10.1007/978-1-4939-9027-6.

[179] Long Shen, Honghao Li, Yuzhi Shi, Dekun Wang, Junbo Gong, Jing Xun, Sifan Zhou, Rong Xiang, and Xiaoyue Tan. M2 tumour-associated macrophages contribute to tumour progression via legumain remodelling the extracellular matrix in diffuse large b cell lymphoma. *Scientific Reports 2016 6:1*, 6:1–10, 7 2016. https://doi.org/10.1038/srep30347.

[180] Ying Shi, Xiaochuan Ma, Ge Fang, Xin Tian, and Cuicui Ge. Matrix metalloproteinase inhibitors (mmpis) as attractive therapeutic targets: Recent progress and current challenges. *NanoImpact*, 21:100293, 1 2021. https://doi.org/10.1016/J.IMPACT.2021.100293.

[181] Kanae Shirahama-Noda, Akitsugu Yamamoto, Kazushi Sugihara, Noriyoshi Hashimoto, Masahide Asano, Mikio Nishimura, and Ikuko Hara-Nishimura. Biosynthetic processing of cathepsins and lysosomal degradation are abolished in asparaginyl endopeptidase-deficient mice. *Journal of Biological Chemistry*, 278:33194–33199, 8 2003. https://doi.org/10.1074/jbc.M302742200.

[182] Rigmor Solberg, Ngoc Nguyen Lunde, Karl Martin Forbord, Meshail Okla, Moustapha Kassem, and Abbas Jafari. The mammalian cysteine protease legumain in health and disease. *International journal of molecular sciences*, 23, 12 2022. https://doi.org/10.3390/IJMS232415983.

[183] Rigmor Solberg, Robert Smith, Maria Almlöf, Eyassu Tewolde, Hilde Nilsen, and Harald Thidemann Johansen. Legumain expression, activity and secretion are increased during monocyte-to-macrophage differentiation and inhibited by atorvastatin. *Biological Chemistry*, 396:71–80, 1 2015. https://doi.org/10.1515/HSZ-2014-0172.

[184] Mingke Song. The asparaginyl endopeptidase legumain: an emerging therapeutic target and potential biomarker for alzheimer's disease. *International Journal of Molecular Sciences 2022, Vol. 23, Page 10223*, 23:10223, 9 2022. https://doi.org/10.3390/IJMS231810223.

[185] Reisa A. Sperling, Paul S. Aisen, Laurel A. Beckett, David A. Bennett, Suzanne Craft, Anne M. Fagan, Takeshi Iwatsubo, Clifford R. Jack, Jeffrey Kaye, Thomas J. Montine, Denise C. Park, Eric M. Reiman, Christopher C. Rowe, Eric Siemers, Yaakov Stern, Kristine Yaffe, Maria C. Carrillo, Bill Thies, Marcelle Morrison-Bogorad, Molly V. Wagster, and Creighton H. Phelps. Toward defining the preclinical stages of alzheimer's disease: Recommendations from the national institute on aging-alzheimer's association workgroups on diagnostic guidelines for alzheimer's disease. *Alzheimer's & Dementia*, 7:280–292, 5 2011. https://doi.org/10.1016/J.JALZ.2011.03.003.

[186] Reisa A. Sperling, Elizabeth C. Mormino, Aaron P. Schultz, Rebecca A. Betensky, Kathryn V. Papp, Rebecca E. Amariglio, Bernard J. Hanseeuw, Rachel Buckley,

Jasmeer Chhatwal, Trey Hedden, Gad A. Marshall, Yakeel T. Quiroz, Nancy J. Donovan, Jonathan Jackson, Jennifer R. Gatchel, Jennifer S. Rabin, Heidi Jacobs, Hyun Sik Yang, Michael Properzi, Dylan R. Kirn, Dorene M. Rentz, and Keith A. Johnson. The impact of amyloid-beta and tau on prospective cognitive decline in older individuals. *Annals of Neurology*, 85:181–193, 2 2019. https://doi.org/10.1002/ANA.25395.

[187] Marco F. Taddio, Claudia A. Castro Jaramillo, Peter Runge, Alain Blanc, Claudia Keller, Zeynep Talip, Martin Béhé, Nicholas P. van der Meulen, Cornelia Halin, Roger Schibli, and Stefanie D. Krämer. In vivo imaging of local inflammation: Monitoring lps-induced cd80/cd86 upregulation by pet. *Molecular Imaging and Biology*, 23:196–207, 4 2021. https://doi.org/10.1007/S11307-020-01543-3.

[188] Katharina Tarnutzer, Devanarayanan Siva Sankar, Joern Dengjel, and Collin Y. Ewald. Collagen constitutes about 12% in females and 17% in males of the total protein in mice. *Scientific Reports 2023 13:1*, 13:1–12, 3 2023. https://doi.org/10.1038/s41598-023-31566-z.

[189] Christopher Tay, Atsushi Tanaka, and Shimon Sakaguchi. Tumor-infiltrating regulatory t-cells as targets of cancer immunotherapy. *Cancer Cell*, 41:450–465, 3 2023. https://doi.org/10.1016/J.CCELL.2023.02.014.

[190] Bernard Testa and Stefanie D. Krämer. The biochemistry of drug metabolism–an introduction: Part 2. redox reactions and their enzymes. *Chemistry & biodiversity*, 4:257–405, 2007. https://doi.org/10.1002/CBDV.200790032.

[191] Chiara Tuccilli, Enke Baldini, Salvatore Sorrenti, Antonio Catania, Alessandro Antonelli, Poupak Fallahi, Francesco Tartaglia, Susi Barollo, Caterina Mian, Andrea Palmieri, Giovanni Carbotta, Stefano Arcieri, Daniele Pironi, Massimo Vergine, Massimo Monti, and Salvatore Ulisse. Ctla-4 and pd-1 ligand gene expression in epithelial thyroid cancers. *International Journal of Endocrinology*, 2018:1742951, 1 2018. https://doi.org/10.1155/2018/1742951.

[192] Julie Vackova, Ingrid Polakova, Shweta Dilip Johari, and Michal Smahel. Cd80 expression on tumor cells alters tumor microenvironment and efficacy of cancer immunotherapy by ctla-4 blockade. *Cancers*, 13:1935, 4 2021. https://doi.org/10.3390/CANCERS13081935/S1.

[193] Vasiliki Valla, Saba Alzabin, Angeliki Koukoura, Amy Lewis, Anne Ahlmann Nielsen, and Efstathios Vassiliadis. Companion diagnostics: State of the art and new regulations. *Biomarker Insights*, 16, 2021. https://doi.org/10.1177/11772719211047763.

[194] Peter Vaupel, Friedrich Kallinowski, and Paul Okunieff. Blood flow, oxygen and nutrient supply, and metabolic microenvironment of human tumors: A review. *CANCER RESEARCH*, 49:6449–6465, 1989.

[195] Miguel Vaz, Vítor Silva, Cristina Monteiro, and Samuel Silvestre. Role of aducanumab in the treatment of alzheimer's disease: Challenges and opportunities. *Clinical Interventions in Aging*, 17:797–810, 2022. https://doi.org/10.2147/CIA.S325026.

[196] Erik Vegt, Marion De Jong, Jack F.M. Wetzels, Rosalinde Masereeuw, Marleen Melis, Wim J.G. Oyen, Martin Gotthardt, and Otto C. Boerman. Renal toxicity of radiolabeled peptides and antibody fragments: Mechanisms, impact on radionuclide therapy, and strategies for prevention. *Journal of Nuclear Medicine*, 51:1049–1058, 7 2010. https://doi.org/10.2967/JNUMED.110.075101.

[197] Robert Waibel, Roger Alberto, Jörg Willuda, Ricarda Finnern, Roger Schibli, Albert Stichelberger, André Egli, Ulrich Abram, Jean Pierre Mach, Andreas Plückthun, and P. August Schubiger. Stable one-step technetium-99m labeling of his-tagged recombinant proteins with a novel tc(i)–carbonyl complex. *Nature Biotechnology 1999 17:9*, 17:897–901, 9 1999. https://doi.org/10.1038/12890.

[198] Alex D. Waldman, Jill M. Fritz, and Michael J. Lenardo. A guide to cancer immunotherapy: from t cell basic science to clinical practice. *Nature Reviews Immunology 2020 20:11*, 20:651–668, 5 2020. https://doi.org/10.1038/s41577-020-0306-5.

[199] Stéfan Van Der Walt, Johannes L. Schönberger, Juan Nunez-Iglesias, François Boulogne, Joshua D. Warner, Neil Yager, Emmanuelle Gouillart, and Tony Yu. scikit-image: image processing in python. *PeerJ*, 2, 2014. https://doi.org/10.7717/PEERJ.453.

[200] Li Xin Wang, Zhen Yang Mei, Ji Hao Zhou, Yu Shi Yao, Yong Hui Li, Yi Han Xu, Jing Xin Li, Xiao Ning Gao, Min Hang Zhou, Meng Meng Jiang, Li Gao, Yi Ding, Xue Chun Lu, Jin Long Shi, Xu Feng Luo, Jia Wang, Li Li Wang, Chunfeng Qu, Xue Feng Bai, and Li Yu. Low dose decitabine treatment induces cd80 expression in cancer cells and stimulates tumor specific cytotoxic t lymphocyte responses. *PLOS ONE*, 8:e62924, 5 2013. https://doi.org/10.1371/JOURNAL.PONE.0062924.

[201] Lina Wang, Si Chen, Mingna Zhang, Na Li, Yanan Chen, Weijun Su, Yanhua Liu, Dan Lu, Sanglin Li, Yixuan Yang, Zongjin Li, Dwayne Stupack, Pengpeng Qu, Aidong Hu, and Rong Xiang. Legumain: A biomarker for diagnosis and prognosis of human ovarian cancer. *Journal of Cellular Biochemistry*, 113:2679–2686, 8 2012. https://doi.org/10.1002/JCB.24143.

[202] Shan Shan Wang, Zi Kai Liu, Jing Jing Liu, Qing Cheng, Yan Xia Wang, Yan Liu, Wen Wen Ni, Hong Zhuan Chen, and Mingke Song. Imaging asparaginyl endopeptidase (aep) in the live brain as a biomarker for alzheimer's disease. *Journal of Nanobiotechnology*, 19:1–18, 12 2021. https://doi.org/10.1186/S12951-021-00988-0.

[203] Yan Wang, Shilong Zhang, Haiwei Wang, Yuehong Cui, Zhiming Wang, Xi Cheng, Wei Li, Jun Hou, Yuan Ji, and Tianshu Liu. High level of legumain was correlated

with worse prognosis and peritoneal metastasis in gastric cancer patients. *Frontiers in Oncology*, 10:543503, 7 2020.
https://doi.org/10.3389/fonc.2020.00966.

[204] Zhi Hao Wang, Ke Gong, Xia Liu, Zhentao Zhang, Xiaoou Sun, Zheng Zachory Wei, Shan Ping Yu, Fredric P. Manfredsson, Ivette M. Sandoval, Peter F. Johnson, Jianping Jia, Jian Zhi Wang, and Keqiang Ye. C/ebpβ regulates delta-secretase expression and mediates pathogenesis in mouse models of alzheimer's disease. *Nature Communications 2018 9:1*, 9:1–16, 5 2018.
https://doi.org/10.1038/s41467-018-04120-z.

[205] Evita G Weagel, Evita Weagel, Curren Smith, Ping Guo Liu, Richard Robison, and Kim O'neill. Macrophage polarization and its role in cancer. *Article in Journal of Clinical & Cellular Immunology*, 2015.
https://doi.org/10.4172/2155-9899.1000338.

[206] Jeffrey S. Weber, Sandra P. D'Angelo, David Minor, F. Stephen Hodi, Ralf Gutzmer, Bart Neyns, Christoph Hoeller, Nikhil I. Khushalani, Wilson H. Miller, Christopher D. Lao, Gerald P. Linette, Luc Thomas, Paul Lorigan, Kenneth F. Grossmann, Jessica C. Hassel, Michele Maio, Mario Sznol, Paolo A. Ascierto, Peter Mohr, Bartosz Chmielowski, Alan Bryce, Inge M. Svane, Jean Jacques Grob, Angela M. Krackhardt, Christine Horak, Alexandre Lambert, Arvin S. Yang, and James Larkin. Nivolumab versus chemotherapy in patients with advanced melanoma who progressed after anti-ctla-4 treatment (checkmate 037): a randomised, controlled, open-label, phase 3 trial. *The Lancet Oncology*, 16:375–384, 4 2015.
https://doi.org/10.1016/S1470-2045(15)70076-8.

[207] Wolfgang A. Weber, Johannes Czernin, Carolyn J. Anderson, Ramsey D. Badawi, Henryk Barthel, Frank Bengel, Lisa Bodei, Irene Buvat, Marcelo DiCarli, Michael M. Graham, Jan Grimm, Ken Herrmann, Lale Kostakoglu, Jason S. Lewis, David A. Mankoff, Todd E. Peterson, Heinrich Schelbert, Heiko Schoder, Barry A. Siegel, and H. William Strauss. The future of nuclear medicine, molecular imaging, and theranostics. *Journal of Nuclear Medicine*, 61:263S–272S, 12 2020.
https://doi.org/10.2967/JNUMED.120.254532.

[208] Weijun Wei, Zachary T. Rosenkrans, Jianjun Liu, Gang Huang, Quan Yong Luo, and Weibo Cai. Immunopet: Concept, design, and applications. *Chemical Reviews*, 120:3787–3851, 4 2020.
https://doi.org/10.1021/ACS.CHEMREV.9B00738.

[209] Hadley Wickham, Mara Averick, Jennifer Bryan, Winston Chang, Lucy D', Agostino Mcgowan, Romain François, Garrett Grolemund, Alex Hayes, Lionel Henry, Jim Hester, Max Kuhn, Thomas Lin Pedersen, Evan Miller, Stephan Milton Bache, Kirill Müller, Jeroen Ooms, David Robinson, Dana Paige Seidel, Vitalie Spinu, Kohske Takahashi, Davis Vaughan, Claus Wilke, Kara Woo, and Hiroaki Yutani. Welcome to the tidyverse. *Journal of Open Source Software*, 4:1686, 11 2019.
https://doi.org/10.21105/JOSS.01686.

[210] Zhourui Wu, Zhi Hao Wang, Xia Liu, Zhentao Zhang, Xiaohuan Gu, Shan Ping Yu, C. Dirk Keene, Liming Cheng, and Keqiang Ye. Traumatic brain injury triggers

app and tau cleavage by delta-secretase, mediating alzheimer's disease pathology. *Progress in Neurobiology*, 185:101730, 2 2020.
https://doi.org/10.1016/J.PNEUROBIO.2019.101730.

[211] Yan Xing, Gitasha Chand, Changchun Liu, Gary J.R. Cook, Jim O'Doherty, Lingzhou Zhao, Nicholas C.L. Wong, Levente K. Meszaros, Hong Hoi Ting, and Jinhua Zhao. Early phase i study of a 99mtc-labeled anti–programmed death ligand-1 (pd-l1) single-domain antibody in spect/ct assessment of pd-l1 expression in non–small cell lung cancer. *Journal of Nuclear Medicine*, 60:1213–1220, 9 2019.
https://doi.org/10.2967/JNUMED.118.224170.

[212] Ziv Yaniv, Bradley C. Lowekamp, Hans J. Johnson, and Richard Beare. Simpleitk image-analysis notebooks: A collaborative environment for education and reproducible research. *Journal of digital imaging*, 31:290–303, 6 2018.
https://doi.org/10.1007/S10278-017-0037-8.

[213] Zhennan Yuan, Yingpu Li, Sifan Zhang, Xueying Wang, He Dou, Xi Yu, Zhiren Zhang, Shanshan Yang, and Min Xiao. Extracellular matrix remodeling in tumor progression and immune escape: from mechanisms to treatments. *Molecular Cancer 2023 22:1*, 22:1–42, 3 2023.
https://doi.org/10.1186/S12943-023-01744-8.

[214] Fabiana Albani Zambuzi, Priscilla Mariane Cardoso-Silva, Ricardo Cardoso Castro, Caroline Fontanari, Flavio da Silva Emery, and Fabiani Gai Frantz. Decitabine promotes modulation in phenotype and function of monocytes and macrophages that drive immune response regulation. *Cells*, 10:868, 4 2021.
https://10.3390/CELLS10040868.

[215] Bei Zhang, Yi Zheng Wei, Guo Qing Wang, Dai Di Li, Jing Shan Shi, and Feng Zhang. Targeting mapk pathways by naringenin modulates microglia m1/m2 polarization in lipopolysaccharide-stimulated cultures. *Frontiers in Cellular Neuroscience*, 12, 1 2019.
https://doi.org/10.3389/FNCEL.2018.00531.

[216] Yingying Zhang, Ying Ding, Ning Li, Sen Wang, Si Zhou, Ruping Li, Hui Yang, Wenliang Li, and Jinrong Qu. Noninvasive imaging of tumor pd-l1 expression using [99mtc]tc-labeled kn035 with spect/ct. *Molecular Pharmaceutics*, 20:690–700, 1 2023.
https://doi.org/10.1021/ACS.MOLPHARMACEUT.2C00874.

[217] Zhentao Zhang, Obiamaka Obianyo, Elfriede Dall, Yuhong Du, Haian Fu, Xia Liu, Seong Su Kang, Mingke Song, Shan Ping Yu, Chiara Cabrele, Mario Schubert, Xiaoguang Li, Jian Zhi Wang, Hans Brandstetter, and Keqiang Ye. Inhibition of delta-secretase improves cognitive functions in mouse models of alzheimer's disease. *Nature Communications 2017 8:1*, 8:1–17, 3 2017.
https://doi.org/10.1038/ncomms14740.

[218] Zhentao Zhang, Mingke Song, Xia Liu, Seong Su Kang, Duc M. Duong, Nicholas T. Seyfried, Xuebing Cao, Liming Cheng, Yi E. Sun, Shan Ping Yu, Jianping Jia, Allan I. Levey, and Keqiang Ye. Delta-secretase cleaves amyloid precursor protein and regulates the pathogenesis in alzheimer's disease. *Nature Communications*, 6,

11 2015.
https://doi.org/10.1038/NCOMMS9762.

[219] Zhentao Zhang, Mingke Song, Xia Liu, Seong Su Kang, Il Sun Kwon, Duc M. Duong, Nicholas T. Seyfried, William T. Hu, Zhixue Liu, Jian Zhi Wang, Liming Cheng, Yi E. Sun, Shan Ping Yu, Allan I. Levey, and Keqiang Ye. Cleavage of tau by asparagine endopeptidase mediates the neurofibrillary pathology in alzheimer's disease. *Nature medicine*, 20:1254, 11 2014.
https://doi.org/10.1038/NM.3700.

[220] Yue Zhao, Zijuan Hai, Hongyong Wang, Lanhong Su, and Gaolin Liang. Legumain-specific near-infrared fluorescence "turn on" for tumor-targeted imaging. *Analytical Chemistry*, 90:8732–8735, 8 2018.
https://doi.org/10.1021/acs.analchem.8b02704.

[221] Yunlong Zhao, Calvin K. Lee, Chia Hao Lin, Rodrigo B. Gassen, Xiaozheng Xu, Zhe Huang, Changchun Xiao, Cristina Bonorino, Li Fan Lu, Jack D. Bui, and Enfu Hui. Pd-l1:cd80 cis-heterodimer triggers the co-stimulatory receptor cd28 while repressing the inhibitory pd-1 and ctla-4 pathways. *Immunity*, 51:1059–1073.e9, 12 2019.
https://doi.org/10.1016/J.IMMUNI.2019.11.003.

[222] Rong Zhou, Bin Ji, Yanyan Kong, Limei Qin, Wuwei Ren, Yihui Guan, and Ruiqing Ni. Pet imaging of neuroinflammation in alzheimer's disease. *Frontiers in Immunology*, 12:739130, 9 2021.
https://doi.org/10.3389/FIMMU.2021.739130.